INVESTIGATION ON GRAPHENE FUNCTIONALIZED WITH METAL OXIDES AND THEIR SENSING APPLICATIONS

THESIS SUBMITTED FOR THE AWARD OF THE DEGREE
of

Doctor of Philosophy

in

Applied Physics

by

Kuldeep Kumar
M.Sc.
Enrollment No. 403/14

Under the Supervision of

Prof. (Dr.) Bal Chandra Yadav

DEPARTMENT OF APPLIED PHYSICS

SCHOOL FOR PHYSICAL SCIENCES

BABASAHEB BHIMRAO AMBEDKAR UNIVERSITY,

LUCKNOW-226025, U.P., INDIA

December 2020

DECLARATION

I declare that the thesis entitled **"Investigation on Graphene functionalized with metal oxides and their sensing applications"** has been prepared by me under the supervision of Prof. (Dr.) Bal Chandra Yadav, Department of Physics, School of Physical & Decision Sciences, Babasaheb Bhimrao Ambedkar University, Lucknow. No part of this thesis has formed the basis for the award of any degree, diploma, or fellowship previously. Further, I declare that the material embodied in the present work is based on original research work and the indebtedness to others has been duly acknowledged at relevant places. This is also declared that the thesis is essentially free from all kind of plagiarism.

(Kuldeep Kumar)

Department of Applied Physics

School for Physical Sciences, Babasaheb Bhimrao Ambedkar University,

Vidya Vihar, Raebareli Road, Lucknow-226025, U.P., India

Date: 31st December 2020

Place: Lucknow

Dedicated to my parents & family

CERTIFICATE

This is to certify that the thesis titled **"Investigation on Graphene functionalized with metal oxides and their sensing applications"** submitted by **Mr. Kuldeep Kumar** is an original research work and has not been previously submitted in part or full for the award of any other degree or diploma to this or any other University.

This thesis submitted to Babasaheb Bhimrao Ambedkar University Lucknow satisfies all the requirements as stipulated in the *Doctor of Philosophy (Ph.D.) regulations-1999 as amended in 2008/2010/2013* and it is fit for submission and evaluation for the award of the degree of Doctor of Philosophy of the University.

Prof. (Dr.) B. C. Yadav

(Supervisor)

Date: 31st December 2020

Place: Lucknow

Prof. (Dr.) B. C. Yadav

(Head of the Department)

ACKNOWLEDGEMENT

It is my firm belief that any major research work to result in a positive outcome including a worthy thesis requires the culmination of several factors such as a meaningful subject which can motivate a determined researcher to take up the challenge, a learned and sincere guide in the form of a parent, relative, friend, and colleague who selflessly encourage and help the researcher throughout the research. I had the honour and privilege to have **Prof. (Dr.) Bal Chandra Yadav** as an excellent guide and Head, Department of Physics, School for Physical & Decision Sciences, Babasaheb Bhimrao Ambedkar University, Lucknow, U.P., India. I take this opportunity to place on record my heartfelt and sincere gratitude and deep indebtedness to him without whose guidance this work could not have been meaningfully concluded.

I am extremely thankful to my teachers **Prof. Devesh Kumar, Dr. Ramesh Chandra**, **Dr. Anil K. Yadav**, **Dr. Khem B. Thapa** & **Dr. Devendra Singh** for their valuable suggestions and encouragements which have been a great asset to me during the entire course of study. I owe my deep gratitude towards them for their constant motivation and moral support. I feel blessed to have such motivated and talented teachers.

I am very thankful to senior members of my Nanomaterials and Sensors Research Laboratory**, Dr. Ravikant Tripathi**, D.S. Kothari Fellow, **Dr. Ravindra Kumar, Dr. Rakesh Sonker, Dr. Monika Singh, Dr. Saroj Radheysham,** and **Dr. Samiksha Sikarwar** for their constant motivated valued suggestions. And also, I am very much thankful to **Dr. Utkarsh Kumar** for his valuable discussions and experimental knowledge. I would like to thank other lab members; **Ms. Priyanka Chaudhary, Mr. Shakti Singh, Mr. Ajeet Singh, Mr. Nirbhay Singh, and Mr. Arpit Verma** for the joyful and healthy environment around me to work and to be with me throughout the work. I acknowledge to staff members of Physics Department **Mr. Amit Kumar, Mr. Mukesh Tyagi, Mr. Rahul Mishra, and Mr. Shatrughan Lal.** Also, I am thankful to **Dr. Mukesh Kumar,** STA, USIC, BBAU, and **Mr. Asheesh Tiwari**, IIT Kanpur for their technical support in Characterizations. I am much thankful to **Dr. Rajeev Kumar**, INSPIRE Faculty, CSIR-AMPRI, Bhopal, for support in material's characterizations.

I wish to express my reverence and sense of deep gratitude to **Prof. (Dr.) Gulzhian I. Dzhardimalieva**, Head, Laboratory of Metallopolymers, Institute of Problems of Chemical Physics, Russian Academy of Sciences, Chernogolovka, Moscow, Russia for her priceless, insightful comments and suggestions to improve the quality of this work.

Finally, I would like to pay my highest regards to my parents **Mr. Bahoran Lal,** uncle **Mr. Rakesh Kumar**, maternal uncle **Mr. Pramod Kumar** and blessings of my mother **Late Smt. Ranno Devi** for understanding my dreams and always being there in part of up and down phases of life. Finally, I am also thankful to my close friend of my village **Mr. Rajveer Singh** for being a part of this journey. I am thankful to all those helping hands that directly and indirectly encouraged me and helped me to complete my research work.

My final words of thanks will be for almighty God, for his constant support and companionship through all turmoil of my life.

Kuldeep Kumar

(Ph.D. Scholar)

LIST OF PUBLICATIONS

Part of the thesis published and communicated in the refereed journals:

- **Kuldeep Kumar**, A. Singh, U. Kumar, R. K. Tripathi, B. C. Yadav, **The beauty inhabited inside the modified Graphene for moisture detection at different frequencies,** *Journal of Materials Science: Materials in Electronics*, 31 (2020) 10836-10845.
- **Kuldeep Kumar**, U. Kumar, M. Singh, and B. C. Yadav, **Synthesis and characterizations of exohedral functionalized Graphene oxide with iron nanoparticles for humidity detection**, *Journal of Materials Science: Materials in Electronics*, 30 (14) (2019) 13013-13023.
- **Kuldeep Kumar** and B. C. Yadav, **An Overview on the Importance of Chemical Vapour Deposition Technique for Graphene Synthesis**, *Advanced Science Engineering & Medicines*, 10 (2018) 760–763.
- **Kuldeep Kumar,** U. Kumar, B. C. Yadav, Vitaly A. Shershnev, Rose K. Baimuratova, Rajeev Kumar, L. K. Gupta, Gulzhian I. Dzhardimalieva, **Development of Graphene oxide functionalized with PPdAAm/SnO_2 nanocomposite for liquefied petroleum gas sensing,** *Sensors and Actuators B: Chemical* **(Communicated).**
- **Kuldeep Kumar** and B. C. Yadav, **Development of highly sensitive, selective and reduced response-recovery time for LPG sensor based on Graphene functionalized with CuO/SnO_2 nanocomposites**, *Sensors and Actuators B: Chemical* (**Communicated**).
- **Kuldeep Kumar** and B. C. Yadav, **Development of ultra-fast sensitive and selective CO_2 sensor based on Graphene@CuO nanocomposites**, *Sensors and Actuators B: Chemical* (**Communicated**).

Work not included in the Thesis:

- S. Singh, U. Kumar, **Kuldeep Kumar**, R. Tripathi, B. C. Yadav, K. Singh **Development of scattering-based glucose sensor using hydrothermally synthesized cuprous oxide nanoparticles**, Results in Physics 15 (2019) 102772.
- P. Gupta, N. K. Pandey, **Kuldeep Kumar**, B. C.Yadav, **Structural, optical and LPG sensing properties of zinc-doped nickel oxide pellets operated at room temperature** , *Sensors and Actuators A: Physical* **(Accepted with Manuscript Number # SNA-D-20-001182R1).**
- P. Gupta, **Kuldeep Kumar**, N. K. Pandey, B. C. Yadav, Thermal annealing effect on structural, optical and LPG sensing properties of nanostructured nickel oxide synthesized using sol-gel route, *Sensors and Actuators A: Physical* **(Submitted).**
- L. K. Gupta, **Kuldeep Kumar**, Shripal, T. P. Yadav, G. I. Dzhardimalieva, Igor Uflyand, **Comparative study on humidity sensing abilities of synthesized mono and poly rhodium acryl amide tin oxide (RhAAm/SnO_2) nano composites,** *Sensors and Actuators A: Physical* **(Communicated).**
- L. K. Gupta, **Kuldeep Kumar**, S. Sikarwar, B. C. Yadav, G. I. Dzhardimalieva, Shripal, **Preparation of the thin film of Scandium polyacrylamide nanocomposite synthesized via Frontal Polymerization and its electrical humidity sensing,** *Journal of Electronic Materials* **(Communicated).**
- U. Kumar, B. C. Yadav, **Kuldeep Kumar**, T. Haldar, V. V. Ravi Kanth Kumar, **Development of MWCNT/TiO_2 nanocomposite thin films for the detection of LPG and humidity at room temperature with theoretical calculations,** *International Journal of Hydrogen Energy* **(Communicated).**
- M. Singh, U. Kumar, **Kuldeep Kumar**, B. C. Yadav, Manmeet Kaur, **Study of Liquefied Petroleum Gas sensing properties of nanostructured Lanthanum ferrite prepared by sol-gel method,** *Sensors and Actuators A: Physical* **(Communicated).**
- C. Singh, R. Yadav, T. W. Kim, P. Upare, A. Singh, A. K. Gupta, **Kuldeep Kumar**, B. C. Yadav, D. K. Dwivedi, **In-Situ Prepared Solar Light-Driven Flexible Actuated Carbon Cloth Based Nanorod Photocatalyst for**

Markovnikov-Selective Radical-Radical Coupling to Vinyl Sulfides along with its LPG sensing, *Journal of the American Chemical Society* **(under review).**

- P. Singh, R. K. Yadav, T. W. Kim, T. C. Yadav, V. Gole, A. K. Gupta, K. Singh, **Kuldeep Kumar,** B. C. Yadav, D. K. Dwivedi, **Solar Light Activated Carbon Cloth Based Photocatalyst for the Markovnikov-Selective Radical-Radical Cross-Coupling of S-Nucleophiles to Terminal Alkyne and LPG sensing,** *Journal of Chinese Chemical Society* **(under minor revision).**
- S. Chaubey, T. W. Kim, R. K. Yadav, A. Kumar, **Kuldeep Kumar,** B. C. Yadav, P. P. Pandey, **Ultrahigh Sun-Light-Responsive Integrated Catalyst for C-S Arylation and Humidity Sensing,** *Journal of the American Ceramic Society* **(under review).**

Papers presented/published in International Conference/Proceedings:

- **Kuldeep Kumar,** B. C. Yadav, Graphene as an Environmental gas sensor: a review, **International Conference on Renewable Energy for Sustainable Environment: Challenges and Remedies,** March 20-21, 2017**, SMVDU, Katra, Jammu & Kashmir. (Poster)**
- **Kuldeep Kumar,** B. C. Yadav, An overview on importance of Graphene, **International Conference on Nanoscience and Nanotechnology (ICNN-17)** Sept 22-24, 2017**, BBAU Lucknow, Uttar Pradesh, India. (Poster)**
- **Kuldeep Kumar,** B. C. Yadav, Synthesis and characterizations of the modified Graphene for the humidity detection at optimized frequency**, International Conference on Ultrasonics and Materials Science for Advanced Technology (ICUMST-2019),** Nov 16-18, 2019, **VBSPU Jaunpur, Uttar Pradesh, India. (Oral)**

Papers presented/published in National Conference/Proceedings

- **Kuldeep Kumar,** B. C. Yadav, Synthesis and doping of Graphene**:** a review, **National Conference Recent Advance and Innovative Material Science**

(RAIMS 2017), February 22-24, 2017, **DSMNRU, Lucknow, Uttar Pradesh, India. (Poster)**

- **Kuldeep Kumar,** B. C. Yadav, The real beauty inhabited inside the functionalized Graphene Oxide for the sensing application, **National Conference on Advanced Nanomaterials and their Applications (ANA-2018),** Dec 21-23, 2018, MNNIT, **Allahabad, Prayagraj, Uttar Pradesh, India. (Poster)**
- **Kuldeep Kumar,** B. C. Yadav, **लोहे के नैनोकणों के साथ पांच स्तरित ग्रेफीन ऑक्साइड का उपयोग करके वैद्युत धारिता आधारित आर्द्रता संवेदक का निर्माण,** सूक्ष्म पदार्थ एवं सम्बद्ध चेतन ऊर्जा **पर राष्ट्रीय संगोष्टी,** Feb 01 – 03, 2019, **BBAU, Lucknow, Uttar Pradesh, India. (Oral)**
- **Kuldeep Kumar,** B. C. Yadav, Capacitance based humidity sensing of Graphene Oxide functionalized with iron nanoparticles**, National conference on Recent Advances in Chemical Sciences,** March 29-30, 2019, **MMMUT, Gorakhpur, Uttar Pradesh, India. (Oral)**
- **Kuldeep Kumar,** B. C. Yadav, The beauty inhabited inside the Graphene Oxide functionalized with poly palladium acryl amide SnO_2 nanocomposites for LPG detection, **National E-Conference on Interdisciplinary Research in Science and Technology (NCIRST-20),** May 30-31, 2020, **University of Lucknow, Lucknow, Uttar Pradesh, India. (Oral)**
- **Kuldeep Kumar,** B. C. Yadav, Design and fabrication of capacitive type humidity sensor based on Graphene Oxide functionalized with iron nanoparticles**,** National E-Conference on Emerging Trends in Physical Sciences 2020 (NCETPS-20), July, 22th, 2020, **Shivaji University, Kolhapur, Maharashtra,** India. **(Oral)**
- **Kuldeep Kumar,** B. C. Yadav, सूक्ष्म सम्मिश्र पदार्थ पर आधारित रसोई गैस संवेदक का निर्माण , **सूक्ष्म पदार्थ एवं सम्बद्ध चेतन ऊर्जा पर राष्ट्रीय ऑनलाइन संगोष्टी**, Sept 27 – 29, 2020, **BBAU, Lucknow, Uttar Pradesh, India. (Oral)**

ABSTRACT

Today, we stand at the beginning of what looks like a scientific and technological revolution: the age of nanotechnology. Nanotechnology deals with using nanomaterials to develop products for practical application and the miniaturization of electronic devices. This holds the promise of enabling us to manipulate material at the nanometer scale, resulting in tools and technologies never dreamt of in earlier centuries. Nanotechnology opens up new frontiers for innovation in electronics medicine and material, etc. In human history, technology and the gathering of scientific information seems to have advanced in a more exponential in a self-enhancing manner. This has certainly been true after the enlightenment in the world, the gain in scientific knowledge and technology mastery. It has spurred on the development of the natural sciences which itself is helping to create new technologies to better exploit our resources and create new opportunities.

An important thread in the unfolding story of nanotechnology is carbon nanostructures, discovery and research of which has significantly donated to shaping the route that science at the nanoscale have been taken. These carbon nanostructures include fullerenes, carbon nanotube, and Graphene. All of these nanostructures are composed of entirely sp^2 hybridized carbon atoms forming different structures, from carbon nanosheet: Graphene to soccer ball type structure: fullerenes with the inclusion of tubular carbon sheet: carbon nanotube. These materials have a variation in the physical and chemical properties according to their atomic structure. From the earliest theoretical and experimental investigations regarding the electrical property of Graphene, it is found that Graphene has some unusual properties such as very high electrical conductivity with high thermal stability. Now from the last two decades, more and more extraordinary properties of Graphene have come into the light, for example, the high charge carrier mobility of Graphene and exceptional mechanical properties, such as Young's modulus more than 1 Tpa for Graphene. With the discovery of more and more of their exotic properties the incentive for further research and the promise for practical applications of this material become even greater.

Over the past few decades, a great deal of research efforts has been made towards the development of humidity and gas sensing devices for practical applications ranging from toxic/inflammable gas detection to continuous environmental monitoring. In the present Thesis work, efforts have been made for the development of Graphene-metal oxide nanocomposites based sensor having ultrafast detection with low response-recovery time. There are seven chapters in this Thesis and a brief outline of its contents is as follows:

Chapter 1:

This chapter addresses a brief review on synthesis techniques of the Graphene, Graphene Oxides, and their functionalization along with the basics of different types of sensors. Also, this chapter provides the recent literature survey on the humidity and LPG sensors which are based on functionalized Graphene and carbon nanomaterials.

Chapter 2:

Chapter 2 includes the synthesis of the modified Graphene via thermal reduction method and also deals with the impedance-based humidity sensing at the optimized frequency by performing the experiments on different frequencies. The thin film of the synthesized material was investigated with SEM and UV-visible spectroscopy. The very dilute solution of the sample was used in particle size analysis. The BET, FTIR, and Raman spectroscopy were carried out with the help of the powdered sample. The impedance of the sensing element at different frequencies was recorded and optimized. A detailed impedance-based humidity sensing mechanism was also discussed. At optimized frequency, the sensitivity, response–recovery times were calculated. The experiment was repeated to observe its repeatability and long term ageing effects.

Chapter 3:

Chapter 3 details the development of a capacitance-based humidity sensor along with the synthesis of five-layered Graphene Oxide (GO) and GO functionalization with iron oxides (Fe-GO) by chemical route. The thin film of Fe-GO was employed to observe the humidity sensing potential at an optimized frequency (as optimized in Chapter 1). The synthesized materials were characterized by SEM, EDX, BET, XRD, Particle size analysis, UV-Vis. spectroscopy, FTIR, and Raman spectroscopy. The SEM micrographs of Fe-GO deal with a unique flower-like structure. The capacitance of thin-film based on

Fe-GO was recorded. Sensitivity and response-recovery times were calculated, further, the experiment was also repeated after some time to check the repeatability and long-term stability.

Chapter 4:

Chapter 4 describes the designing of highly selective and sensitive room temperature operated LPG and humidity sensors fabricated by a thin film of Graphene functionalized with CuO/SnO_2 nanocomposites (GCS). The GCS was synthesized with the hydrothermal technique. The synthesized material was under observation with SEM, XRD, UV-Visible spectroscopy, Particle size analyzer, FTIR, and Raman spectroscopy for characterization purposes. The constructed sensing element was investigated with humidity and LPG sensor characterization setups. The LPG sensor was inspected with 0.5, 1.0, 1.5, and 2.0 vol.% LPG concentrations. The sensor response, sensitivity, and response-recovery times along with reproducibility and selectivity of the sensor were also reported in this chapter.

Chapter 5:

In this chapter, five-layered GO functionalized with Poly Pd acrylamide SnO_2 nanocomposite metallopolymer (MP-GO) based LPG and humidity sensors have been developed. The GO was functionalized with metallopolymer by using N-Methyl Pyrrolidone (NMP). The synthesized samples were investigated with SEM, XRD, Particle size analyzer, UV-Vis. spectroscopy, FTIR, Raman spectroscopy, and other characterization techniques. The fabricated sensing element was characterized by LPG and humidity sensing characterization setups. The LPG sensing characteristics of the sensor was observed by exposing various concentration of LPG along with detailed LPG sensing mechanism. The sensitivity, %sensor response, reproducibility, and response-recovery times of the sensor were calculated and the sensor was found very selective for the LPG in comparison to humidity, acetone, ethanol, and CO_2 gas.

Chapter 6:

This chapter addresses the development of highly selective and sensitive room temperature operated CO_2 and humidity sensors fabricated by a thin film of Graphene@CuO) nanocomposites synthesized via Chemical Vapor Deposition technique. For characterization purposes, the synthesized Graphene@CuO nanocomposites were

under investigation with SEM, XRD, UV-Visible spectroscopy, Particle size analyzer, FTIR, and Raman spectroscopy. The fabricated sensor was under observation with CO_2, LPG, and humidity sensing characterization setups. The CO_2 sensor was examined with 0.5, 1.0, 1.5, and 2.0 vol.% CO_2 gas concentrations. The sensor response, sensitivity, and response-recovery times along with reproducibility and selectivity of the sensor were also reported in this chapter.

Chapter 7:

The last chapter summarizes the concluding remarks of the entire research work of the Thesis and also deals with the future research scope of the functionalized Graphene nanomaterials in the field of sensors.

PREFACE

The humidity has much importance for the human being as well as non-livings. It refers to the water in the gaseous form which obeys all laws of gases. Humidity is one of the essential biotic factors which adopt the environment of a particular plant or animal. Humidity investigation is important for weather forecasts because it is a climate variable but also affects the other climate variables sturdily. Hyperthermia, fatigue, skin irritation, and some respiratory disorders may be tracked through humidity concentration in a breath at high humidity condition when surrounding is warmer than the body temperature. Also, monitoring moisture levels in agriculture and during food processing are necessary. Moisture content in a fuel decides the uncertainty in its energy content hence moisture sensing of the fuel is important. Also, humidity monitoring is important for human comfort and achieving hygienic conditions. Due to the above described manifold significance of humidity for mankind, researchers are keenly interested to work in the field of humidity sensors.

Liquefied Petroleum Gas (LPG) is a combustible gas and it is widely used as a fuel for domestic heating and industrial purpose. Although it is an extensively used gas and its leakage is very hazardous. Hence, its detection is crucial in the early stages to avoid active destruction.

Global warming is the consequence of continuously increasing the concentration of CO_2 in the atmosphere. Since the mid-20^{th} century, the amplified emission of CO_2 and other greenhouse gases has been understood to be the cause of the increase in the average near-surface air and ocean temperature of the earth, a phenomenon known as global warming. Also, the excess of CO_2 in the natural environment causes suffocation and creates unconsciousness in human beings. Due to day by day increase in air pollution and global warming, there is a great deal of interest in developing a gas sensor for checking air pollution, detecting harmful gases, monitoring other agro-based products, home safety, and handheld breath analyzer etc. A lot of research work has been done on the miniaturization of gas sensors which is economically cheap with high sensitivity, good sensor response, and the least response-recovery time. There are various n-types and p-

types metal oxide semiconductor gas sensors like ZnO, TiO_2, NiO, SnO_2, CuO, In_2O_3, Fe_2O_3, etc available in the market for the detection of harmful gases. However, after a literature survey, I found that there is very less work done on the design and development of LPG and CO_2 sensors operable at room temperature (300 K). The main goal of the present investigation is to design and fabricate Humidity, LPG, and CO_2 gas sensor which would be robust, more sensitive with reduced response time, economically cheap, and easy to fabricate than previously reported sensors.

For this purpose, we have focused on the synthesis of Graphene functionalized with various metal oxides which possess enhanced sensing features for the detection of Humidity, LPG, and CO_2 at room temperature.

The present thesis is divided into seven chapters. **Chapter 1** contains the basics of the sensors along with a brief history of the carbon nanomaterial, review on synthesis techniques of the Graphene, Graphene Oxides and their functionalization. The synthesis of the modified Graphene via thermal reduction method its application as an impedance-based humidity sensor at optimized frequency is depicted in **Chapter 2**. In **Chapter 3**, the development of capacitance-based humidity sensor along with the synthesis of the five-layered Graphene Oxide (GO) functionalized with iron oxides (Fe-GO) by chemical route, are demonstrated. **Chapter 4** describes the design of highly selective and sensitive room temperature operated LPG and humidity sensors fabricated by a thin film of Graphene functionalized with CuO/SnO_2 nanocomposites (GCS). **Chapter 5** presents the GO functionalized with Poly Pd acrylamide SnO_2 nanocomposite metallopolymer (MP-GO) for the LPG and humidity sensors. Development of highly selective and sensitive room temperature operated CO_2 and humidity sensors fabricated by a thin film of Graphene on CuO nanocomposites synthesized via Chemical Vapor Deposition technique are reported in **Chapter 6.** It also reports the enhanced sensitivity and sensor response of the CO_2 gas sensor. A summary of synthesis, characterization of Graphene, and its composites with metal oxides for the humidity, LPG, and CO_2 gas sensing are reported in **Chapter 7**. And also this Chapter contains the future research scope of the metal oxide functionalized Graphene materials in the field of sensors.

LIST OF ABBREVIATIONS

S. No.	Name Compound	Full Name
1.	FLG	Few Layered Graphene
2.	MLG	Multilayered Graphene
3.	NMP	N-Methyl Pyrrolidone
4.	LPG	Liquid Petroleum Gas
5.	LEL	Lower Explosive Limit
6.	NPs	Nanoparticles
7.	XRD	X-Ray Diffraction
8.	SEM	Scanning Electron Microscope
9.	FE-SEM	Field Emission-Scanning Electron Microscope
10.	UV-vis	Ultra Violet-Visible spectroscopy
11.	AFM	Atomic Force Microscope
12.	FTIR	Fourier Transformation Infrared Spectroscopy
13.	EDX	Electron Dispersive X-ray
14.	BET	Brunauer-Emmett-Teller
15.	BJH	Barrett-Joyner-Halenda
16.	GO	Graphene oxide
17.	Fe-GO	Graphene oxide functionalized with iron oxide
18.	CS	CuO/SnO_2 nanocomposites

19.	HRG	Hydrothermally reduced Graphene
20.	GCS	Graphene functionalized CuO/SnO_2 nanocomposites
21.	MP	Metallopolymer
22.	MP-GO	Graphene oxide functionalized with metallopolymer
23.	PVA/WPPy/hBNNP	Poly(vinyl alcohol) (PVA)/ water soluble polypyrrole (WPPy)/ hexagonal boron nitride nanoparticles (hBNNP)

LIST OF TABLES

LIST OF FIGURES

TABLE OF CONTENTS

CHAPTER 1

INTRODUCTION AND AIM OF PRESENT RESEARCH WORK

This chapter contains the basic introduction to Graphene, its properties synthesis and functionalization techniques and their roles in various applications. The chapter also provides the details of the electrochemical sensors. Applications of Graphene in various fields like humidity sensing, gas sensing have been also discussed here. The chapter also introduces the detailed information about the ongoing research on Garphene in the field of sensors.

CHAPTER 1

Introduction and aim of present research work

1. 1 Introduction

The technology and the assembly of scientific information seem to have advanced in an exponential and self-enhancing manner day by day. This has become true definitely after the enlightenment of the scientific knowledge, and technology mystery. Today, we stand at the beginning of what looks like a scientific and technological revolution: the age of nanoscience and nanotechnology. This technology holds the promise of supporting us to handle material at the nanometer scale, resulting in tools and technologies. The nanomaterial-based technology never dreamt of in earlier centuries opens up new frontiers for innovation in electronics, medicine, and material etc.

An important thread in describing the story of nanotechnology is carbon nanostructures. The discovery and significant inquiry have been contributed to shaping the route at the nanometer scale. The carbon nanostructures consist of the fullerenes, carbon nanotubes, and Graphenes. All of these nanostructures are composed entirely of sp^2 hybridized carbon atom creating different structures, from tubular carbon sheet (carbon nanotube) to soccer ball type structure (fullerenes). According to the atomic structures, the physical and chemical properties of these materials get varied. Now from the last two decades, a more and more extraordinary property of Graphene (very high electrical conductivity, high carrier mobility, thermal stability and good stability in acidic and basic medium) has come into the light. With the discovery of more and more

of their mysterious properties the incentive for further research and the potential of practical applications, Graphene becomes even greater.

1.2 Motivation

The challenges of Graphene-based research, in particular, can be addressed on two fronts; one is the preparation of Graphene, the other is the investigation of its sensing application in various fields such as biosensors, electrochemical sensor etc. To explore and harness the rich physics of Graphene, a new method is required to tailor their properties, and current methods of sample investigation need to be adapted. This thesis is a contribution to the advancement of both of these objectives, through the following studies:

- Exploring the cheapest method for synthesis of Graphene using wet chemical methods.
- Introducing a sample preparation technique that solves the sample solubility issues and detection of humidity/Gas at room temperature.

In the introductory chapters, the properties of Graphene, and functionalized Graphene will be presented along with the relevant experimental methods. Further, the challenges faced in the investigation of the above two topics will be explored and answered.

1.3 Background of the Carbon

The origin of the Carbon is from the Latin word “Carbo” which means coal and its symbolic representation in the periodic table is C with atomic number 6. It is the non-metallic tetravalent forming four covalent bonds. The atomic weight, electronic

configuration of the same element has been illustrated in the Fig. 1.1. Carbon attracts the attention of the researchers because it is the 15^{th} most abundant element in the Earth's crust and 4^{th} most abundant element by mass in the universe after the hydrogen, helium and oxygen. It is present in all known life forms, and in the human body carbon is the second most abundant element by mass (about 18.5%) after oxygen [1]. The bonding between the carbon atoms results in several allotropes of the Carbon. The physical properties of the Carbon vary widely with the allotropic form. The allotropes of the Carbon are graphite, diamonds.

P. Marigo et al in July 2020 reported that carbon was formed in white dwarf stars, particularly those bigger than two solar masses [2]. Carbon is abundant in the sun, starts, comets and the atmosphere of most planets.

1.4 Nanomaterials of the Carbon

Nanotechnology is the branch of science and engineering dedicated to materials having at least one dimension in nanoscale 1 to 100 nm. At this dimension, the materials exhibit peculiar and fascinating structural, thermodynamic, electromagnetic, electronic spectroscopic, and chemical properties which are of great interest in the scientific community. Based on the nanoscale size in dimension, the nanomaterials are classified as 0D, 1D, 2D, and 3D. On the basis of the structures, carbon nanomaterials can be classified as Buckminsterfullerene (0D), Carbon nanotubes (1D), Graphene (2D), and Graphite (3D). A short history of the carbon nanomaterials is discussed here.

1.4.1 Fullerene

Fullerene (Buckminsterfullerene) or buckyball was the new form of carbon in 1985. Before it the pure carbon was found on the earth only in two forms one is the graphite and other is diamond. Fullerene was discovered in 1985 by Sir H.W. Kroto (from University of Sussex, Brighton, England) and their co-workers Richard E. Smalley and Robert F. Curl (from Rice University, Houston). During the vaporization of the graphite rod in the atmosphere of the Helium, they find the cage-like molecule consisting of the 60 carbon (C_{60}) atoms joined together with a single and double bond-forming the hollow sphere of the 12 pentagonal and 20 hexagonal structures. This structure has resembled with the football or soccer ball. For this new pioneer effort, they were awarded by the Nobel Prize in the year 1996. The name of the C_{60} structure was proposed as Fullerene with an American engineer and architect R. Buckminster Fuller, whose geodesic dome principle was found on the hollow sphere of the 12 pentagonal and 20 hexagonal structures [3, 4].

1.4.2 Carbon nanotubes (CNTs)

It is an intermediate allotrope of the Fullerene cage and flat Graphene. During the synthesis of the Fullerene with the arc discharge technique, Sumio Iijima of Japan observed the first CNTs structure in the HRTEM in the year 1991. This structure was elongated cousins of buckyballs and also was the Multiwall carbon nanotubes (MWCNT) [5]. After two years in 1993, Sumio Iijima and Ichihasshi of NEC in the Fundamental Research Laboratory, Tsukuba Science City in the Japan [6] and Bethune and their colleagues at Almaden Research Centre in California have been reported the synthesis of the single-wall carbon nanotube (SWCNT) [7].

1.4.3 Graphene

Graphene is a single layer of carbon packed in a hexagonal honeycomb lattice having the carbon-carbon distance of 0.142 nm. It is truly the first 2D crystalline material and it is demonstrative of a whole class of two-dimensional materials e.g. single layer of Boron-Nitride (BN) and Molybdenum-disulphide (MoS_2). After the experimental discovery of Graphene in 2004, the trends in two-dimensional research started [8].

In 1947, P.R. Wallace reported a theoretical study on Graphene. He proposed the electronic structure and observed the linear dispersion relation [9]. J.W. McClure had already written down the wave equation for the excitations in1956 [10], and also G.W. Semenoff discussed the similarity to the Dirac equation in 1984 [11]. Since the 1960's the Graphene-like structures had been already known [12-15] but there were experimental difficulties in isolating single layers in such a way that electrical measurements could be performed on them, and there were doubts that this was practically possible.

Thus, the difficulty was not to fabricate the Graphene structures but to isolate sufficiently large individual sheets to identify and characterize the Graphene and to verify its unique two dimensional (2D) properties. The first mechanical exfoliation method for extracting the thin layers of graphite from a graphite crystal with the Scotch tape and then transferred these layers to a silicon substrate was proposed and tried by the R. Ruoff's group but they were not able to identify the monolayer [16]. That doubtful assumption was put to rest in 2004. Andre K. Geim, in collaboration with Kostya S. Novoselov and his co-workers at the University of Manchester in England, was studying a variety of approaches to making even thinner samples of graphite. Geim, Novoselov, and their collaborators succeeded in doing the same experiment. They published their results in

October of 2004 in Science. In this paper, they described the fabrication, identification and Atomic Force Microscopy (AFM) characterization of Graphene [17].

It is interesting to consider that everyone who has used an ordinary pencil, has probably produced Graphene-like structures without knowing it. A pencil contains graphite, and when it is moved on a piece of paper, the graphite is cleaved into thin layers that end up on the paper and make up the text or drawing that we are trying to produce. A small fraction of these thin layers will contain only a few layers or even a single layer of graphite, *i.e.* Graphene.

Overall, Graphene is the mother of all Graphitic carbon nanomaterials. The structure of Fullerenes, carbon nanotubes (CNTs) and graphite can be produced from the Graphene. It is a monolayer of carbon atoms in graphite, wrapped in fullerene and rolled form in the carbon nanotube as shown in Fig. 1.2 [18]. Graphene derives from two words Graph (Graphite) +ene (carbon-carbon double bond) [19].

Graphene is recently discovered nanomaterial of the Carbon, researchers' focuses on this due to its extraordinary properties. Some of the properties of the Graphene are discussed below:

1.4.3.1 Properties of Graphene

1.4.3.1.1 Band structure of the Graphene

The electronic structure of graphene is rather changed from the usual 3D materials. Its Fermi surface has six double cones, which is shown in Fig. 1.3. The Fermi level in intrinsic (undoped) Graphene is situated at the connection points of these cones. Since the density of states of the material is zero at that point, the electrical conductivity of intrinsic Graphene is quite low and is of the order of the conductance quantum $\sigma \sim e^2/h$; the exact

prefactor is still debated. The Fermi level in materials can however be reformed by an electric field so that it becomes either n-doped (with electrons) or p-doped (with holes) based the polarity of the applied field. In the case of the Graphene the doping is performed by adsorbing, for example, water or ammonia on its surface. The electrical conductivity of the doped Graphene at room temperature is potentially quite high and it may even be higher than that of copper. Near to the Fermi level, the dispersion relation for electrons and holes is linear. Since the effective masses are given by the curvature of the energy bands, this relates to the zero effective mass. The equation relating the excitations in Graphene is formally identical to the Dirac equation for massless fermions that move with a constant speed and therefore the connection points of the cones are named as Dirac points. This gives rise to interesting similarities between Graphene and particle physics, which are valid for energies up to approximately 1 eV, where the dispersion relation starts to be nonlinear. One result of this special dispersion relation is the quantum Hall effect which becomes unusual in Graphene.

The energy (E) for the excitations in Graphene as a function of the wavenumbers, k_x and k_y, in x and y directions. The black line represents the Fermi energy for an undoped Graphene crystal.

1.4.3.1.2 Density

The area of the hexagonal unit cell of Graphene is 0.052 nm^2 along with having two carbon atoms per unit cell. The calculated density is 0.77 mg/m^2.

1.4.3.1.3 Optical transparency

The suspended Graphene does not have any color. Therefore, Graphene is almost transparent and absorbs only 2.3% of the light intensity, independent of the wavelength in

the optical domain. This number is given by $\pi\ \alpha$, where α is the fine structure constant [20].

1.4.3.1.4 Strength

The breaking strength of Graphene is 42 N/m. The range of breaking strength in Steel is 250-1200 MPa = 0.25-1.2x109 N/m^2. A hypothetical steel film of the same thickness as Graphene (the layer thickness of 3.35Å=$3.35x10^{-10}$ m in graphite) would give a 2D breaking strength of 0.084-0.40 N/m. Overall we can say that Graphene is more than 100 times stronger in comparison to the strongest steel [21].

1.4.3.1.5 Electrical conductivity

Formula $\sigma = en\mu$ is used for the sheet conductivity of a 2D material. Theoretically, the mobility is limited to μ = 200,000 $cm^2V^{-1}s^{-1}$ by acoustic phonons at a carrier density of $n = 10^{12}$ cm^{-2}. The resistance per square is called resistivity of the 2D sheet and is calculated as 31 Ω. We get a bulk conductivity of 0.96 x 10^6 $\Omega^{-1}cm^{-1}$ for Graphene by using the layer thickness. This is somewhat higher than the conductivity of copper which is $0.60x10^6$ $\Omega^{-1}cm^{-1}$ [22].

1.4.3.1.6 Thermal conductivity

Thermal conductivity in Graphene is ruled by the phonons and has been observed at approximately 5000 $Wm^{-1}K^{-1}$. At room temperature, Copper has a thermal conductivity of 401 $Wm^{-1}K^{-1}$. Therefore, Graphene conducts heat 10 times better in comparison to copper [23].

1.5 Synthesis techniques of Graphene

Due to keeping mind the extraordinary property of the Graphene, it has been proved as a magic material and also becomes the part of the attraction for the researchers

in the field of nanoscience and nanotechnology. It also attracts attention to 2D materials. There are several techniques for the synthesis of Graphene which have been shown in Fig. 1.4.

1.5.1 Mechanical exfoliation method

Andrei Geim and Kostya Novoselov separated a graphene layer from HOPG for the first time using a mechanical exfoliation method with the help of Scotch tape [17]. In this method, there was a drawback of a tiny surface area of the single-layer Graphene. However, it is not suitable for mass production because of the difficulty in controlling the size of the sheets and the number of layers [24]. Andrei Geim and Kostya Novoselov both Physicists were awarded the Noble Prize for this discovery in 2004.

1.5.2 Liquid phase exfoliation

The production of Graphene through the liquid-based exfoliation of graphite is typically a promising technique for large-scale Graphene synthesis [25]. In this method, the exfoliation of graphite has been done from the dispersion of graphite flakes in a solvent. The ultrasonication process is used to separate individual graphitic layers in the graphite dispersion. Also, using centrifugation or sedimentation the separation of a single-layer Graphene from the remaining multi- and few-layer graphitic layers in the solvent has been achieved. To selecting a solvent, it is important to minimize the aggregation of single-layer Graphene. Therefore, it is necessary to minimize the interfacial tension between the graphite and the liquid [26, 27].

1.5.3 Electrochemical exfoliation

Electrochemical exfoliation of graphite into Graphene comprises carbon sources (graphite or graphite foils or highly oriented pyrolytic graphite rods) as electrodes in an

aqueous or non-aqueous electrolyte solution. M. Coros et al. demonstrated a simple, cost-effective electrochemical approach to synthesize the Graphene with the electrochemical exfoliation of graphite rods in acidic electrolytes. In this technique size of synthesized Graphene flakes and the exfoliation/oxidation level depends upon the electrochemical parameters like electrolyte concentration, applied bias [28, 29].

1.5.4 Epitaxial growth on SiC

The epitaxial growth of the Graphene on SiC substrate involves the fabrication of Graphene by the thermal decomposition on a prepared SiC surface in temperature conditions of up to 1450 °C for 20 min [30]. The thermal decomposition of SiC is a method to produce high-quality Graphene and the epitaxial grown Graphene can be applied to electrical devices directly without transferring to another substrate. It is very much tough to transfer Graphene epitaxially grown on SiC to the other substrate due to the strong binding between the deposited layer and SiC substrate. SiC is well-matched with these applications and also produces films that are electrically continuous at a millimeter scale. This method of fabrication of Graphene has limited applications. The production of uniform epitaxial grown Graphene on C-face 6H-SiC substrates with a sputtered SiC film under the Ar atmosphere by annealing temperatures ranging from 1400 to 1900 °C has been reported [31, 32].

1.5.5 Chemical Vapor Deposition

The Chemical Vapor Deposition (CVD) method comprising chemical gases or vapors react on the substrate surface of nanostructure or coating [33, 34]. A CVD setup consists of a quartz tube, quartz board, heating filament as shown in Fig. 1.5. This method has the advantages of a high degree of control, uniform deposition, high quality

and low cost. The synthesis of Graphene films via the CVD method involves the decomposition of a liquid or gas at high temperatures to form the film on the substrate.

Ni film on SiO_2/Si wafers or copper foils is mostly used substrates for the synthesis of the Graphene. CVD method can be used as a relatively high-through put production method and it has been proved that the deposited Graphene film can be transferred from the one substrate to a wide range of other substrates. Thus, the CVD method is potentially suitable for applications where a Graphene film is mandatory on a flexible or polymeric substrate that could not survive at high-temperature processing. The quality of the film deposited onto a substrate depends on the growth temperature. The opening first attempt to grow the graphitic layers was carried out in 1960 [35, 36]. Hong et al. informed a technique to transfer and measure the Graphene on the nickel (Ni) films using polydimethylsiloxane (PDMS) films as intermediate adhesive layers. This came to be along with the high-speed development of the CVD growth technique of Graphene [37]. One of the anxiety was focused on the production of Graphene, which is a noteworthy and important issue regarding the practical application. In a short time, CVD growth of Graphene has made the revolution in characterization, transfer technique, and growth with high quality and large quantity. Hence CVD has proven one of the more mature and attractive Graphene engineering techniques with the industry applications [38].

In comparison to other methods, CVD growth of Graphene shows the superior features as a large area continuous film, produces in roll to roll way, simple, repeatable and low cast. However, this method also suffers from the quality problem that disadvantaged its application in the area such as electronic devices. The requirement for

the advanced application in the near future, we have to make efforts in the following areas:

1. The high degree controlling of the size of single-crystal Graphene and number of layers of Garphene.
2. Complete transferring technique with low defects, low contamination, and low cast in roll to roll way.
3. Handling of morphology, doping, and functionalization.

1.5.5.1 Mechanism of CVD technique of Graphene production on various substrates

The mechanism of the CVD growth of Graphene depends upon the nature of the substrate used. There are two types of substrates that are used in Graphene production:

1. Precipitation on metal with high solubility of C such as Ni [39].
2. Absorption and nucleation growth on the surface of the metal with low solubility of C such as Cu [40, 41].

Not only Ni, Cu are metal substrates on which Graphene film can be grown but also platinum (Pt), ruthenium (Ru), iridium (Ir), cobalt (Co), palladium (Pd) used [42-46]. For the convenience of cost and feasibility point of view, Ni and Cu are mostly used.

In a typical CVD process growth of the Graphene film on the Ni substrate involves the high-temperature decomposition of liquid or hydrocarbon gas. The carbon source consists of hydrocarbon gases e.g. CH_4, C_2H_2 etc.. These gases decompose and melt into the Ni bulk [47]. The reaction time is preserved shortly for a suitable dissolution of carbon. Then the substrate is cool down and the carbon layers will found on Ni substrate. The cooling rate decides the carbon amount of precipitation. An extremely fast

or very slow cooling rate usually results in no carbon separation. A moderate cooling rate can be producing an appropriate amount of carbon which leads to a few layers of Graphene on the substrate. There is the biggest challenge for the growth of the Graphene on Ni substrate to control the amount of the diffusing carbon and get the monolayer. A schematic of the mechanism of the synthesis of the Graphene on Ni substrate is shown in Fig. 1.6. A. Guermoune and their colleagues reported a paper for the synthesis of the Graphene on Cu substrate via CVD technique using the alcohols. They used the average growth temperature 850°C and the temperature of the quartz board is kept constant for 20 minutes to remove any generated oxide layer on the Cu. The schematic of this is shown in Fig. 1.7. This consists of the four regions as heating, annealing, exposure of the alcohol and formation of the Graphene. The time of the annealing and exposure of the alcohol is 20 and 5 minutes respectively [48].

The recently published reports on the CVD synthesized Graphene have been summarized in Table 1 [49-60].

1.5.6 Unzipping of Carbon nanotubes

To produce a two-dimensional Graphene nanoribbon, it is possible to ‘unzip’ a one-dimensional carbon nanotube (CNT) (i.e., break a continuous line of bonds along its length or in a helical pattern). . The process for producing the CNTs from graphite electrodes by the arc discharge method is well recognized [5]. There are various methods for the unzipping single- and multi-walled CNTs (SWCNTs and MWCNTs respectively) have been described, including suspension first in concentrated sulphuric acid and then in potassium permanganate in mild conditions [61], argon plasma etching [62], and mechanical sonication in an organic solvent. Although the unzipping of CNTs produces

Graphene nanoribbons approximately 10–20 nm in width rather than continuous sheets, it is possible to use these ribbons to produce arrays [63].

1.5.7 Reduction of Graphite oxide

The synthesis procedures along with the history of synthesis of the multilayered Graphene or Graphite oxide has been described as below [64-66]:

1.5.7.1 Brodie method

The first time to elucidate the structure of multilayered Graphene oxide (graphite oxide) in the year 1859 Benjamin Brodie [67] treated the graphite with strong oxidizers. In this experiment, he heated lamellar graphite (with distinction to amorphous) in a mixture of potassium chlorate ($KClO_3$) and fuming nitric acid (HNO_3) at 60 °C for few days (3-4 d). The obtained product (say GO-BR) was a composition of carbon, hydrogen and oxygen and its averaged general formula was estimated to $C_{11}H_4O_5$ (C/O: 2.2). Also, he perceived that the product was soluble in basic or pure water, and tended to flocculate in more acidic media. Furthermore, the material had a feeble acid reaction when placed upon litmus paper.

1.5.7.2 Stunadenmaier-Hofmann method

Almost forty years later, L. Staudenmaier [68] upgraded the Brodie's method. He amended the way potassium chlorate was added to the reaction mixture and by adding sulfuric acid portion-wise during the reaction. More precisely, the $KClO_3$ was added into the small doses to remove the danger linked with the evolution of explosive by-products and heat. The role of the addition of H_2SO_4 was to increase the acidity of the mixture that drives the oxidation of graphite and reduces the reaction time. More significantly, at lower pH value, a smaller amount of fuming nitric acid was required for the oxidation,

believed, escaping the large emission of toxic gases (NO_2, N_2O_4) and controlling a large quantity of corrosive and hazardous materials, which leads to the overall safer process. In such a way, he got the material (say GO-ST) having similar properties with GO-BR.

In 1937, Hofmann also established a safe alternative method to prepare GO-HO using $KClO_3$ and non-fuming nitric acid with having a lower level of oxidation (C/O >2.5) [69]. Nitric acid is known to react strongly with aromatic carbon surfaces, including carbon nanotubes while $KClO_3$ is a powerful oxidant and is used as an in situ source of molecule oxygen [70]. Although the conditions using $KClO_3$ and HNO_3 were reported at the opening of the discovery of GO, they were among the most powerful oxidative methods known in that time and are still used today for the production of GO at the preparative scale.

1.5.7.3 Hummers method

After the discovery of Brodie's method almost 100 years later Hummers and Offeman developed the most imperative achievement in the field of oxidative chemical exfoliation of graphite [71]. They demonstrated the fastest and safest conventional method of preparing GO-HU with a C/O ratio (2.25) very similar to GO-BR (2.20). This method was centered on the action of an excess of potassium permanganate, sulfuric acid and a small amount of sodium nitrate over the graphite. This method was much safer than chlorate-based methods because in this method the evolution of explosive ClO_2 was avoided. Also, the excess of $KMnO_4$ was suitably defused with a diluted solution of H_2O_2 to form non-toxic manganese sulfate salts and gaseous oxygen easily removed during the purification process. However, nitric acid was produced in situ upon acidification of sodium nitrate and some toxic gases (NO_2, N_2O_4) were still generated. So far, the

materials synthesized by Brodie, Staudenmaier or Hummers methods have observed more defects (holes, wrinkles, irregular shape, presence of contaminants, etc.) than those made directly from micromechanical cleavage of graphite. Hummer's method remains a key point of interest because it is an easy reaction appropriate for producing large quantities of graphite oxide that can be fully delaminated into GO using liquid exfoliation techniques. However, it yields GO with traces of sulfur (up to 6%) [72] and nitrogen likely to be due to the covalently bonded sulfates and nitrates or adsorbed sulfuric and nitric acids [73].

1.5.7.4 Tour method

Noteworthy, an improved technique for the preparation of GO with high level of oxidation using a modified Hummers method was developed in 2010 [74]. Phosphoric acid (H_3PO_4), a dispersive and etching agent, were used instead of sodium nitrate to support the oxidative chemical exfoliation of graphite and to make the GO in higher yield. The GO synthesized with the Tour method (GO-TO) has a higher level of oxidation and has a more regular structure along with fewer defects in the basal plane as compared to GO-BR, GO-ST and GO-HU. This one-pot method is very common and is often known as the "fourth" principal method to produce the GO after Brodie, Staudenmaier and Hummers (Fig. 1.8) [75-78]. A detailed study of the mechanism of the intercalation show how sulfuric acid and potassium permanganate intercalate into the graphite's intergalleries [79-81].

1.6 Mechanism of the Graphite exfoliation into the Graphene oxide layers

In the course of the conversion of bulk graphite into the GO, three independent steps can be recognized. The first one is the alteration of graphite into the sulfuric acid graphite intercalation compound (H_2SO_4-GIC), which can be assumed as the first intermediate. The second step is the conversion of the GIC into the oxidized form of graphite, which has expressed as pristine graphite oxide (PGO), constituting the second intermediate. The third step is the conversion of PGO into the GO by the reaction of PGO with water.

Here two possible explanations for the observed stability of the Pristine Graphite Oxide (PGO) structure against its exfoliation into single layer Graphene Oxide (GO) are possible. First, is the GIC-like electrostatic attraction between Graphene and the intercalant within the graphitic domains. The distances between the two neighboring GO flakes are amplified due to the oxidized domains, but the PGO layers persist integrated due to electrostatic forces of attraction within the graphitic domains. For PGO exfoliation, the enthalpy of hydration of the resulting GO layers by water should overcome electrostatic attraction within the GIC. Hydration is driven by hydrogen bonding and by the electrostatic interaction between charged GO layers and water. This results in the formation of a GO in water colloid solution. In concentrated and slightly diluted H_2SO_4, the ionization of GO functional groups is suppressed, and the electrostatic charge of the GO layers is not sufficient to trigger the exfoliation mechanism.

The second explanation for the PGO stability is the crosslinking of two neighboring GO layers by covalent sulfates. PGO consists in its chemical structure with the significant amounts of covalent sulfates as an integral part [82]. Hydrolysis of covalent sulfates is slow, and even well-washed conventional graphite oxide (CGO)

always consists of residual sulfates, these are in part liable for the acidity of GO solutions [83]. These results regarding the covalent sulfates were recently established and further settled by Eigler and co-workers who verified that under certain conditions even CGO might contain up to 5.6 atom % sulfur [84]. Therefore, the existence of covalent sulfates on the GO platform as a part of its chemical composition is well recognized. Reminding that H_2SO_4 molecules and HSO_4^- ions are already present during the oxidation in the graphite galleries as new C-O bond forms on a Graphene layer. The HSO_4^- ions and/or H_2SO_4 molecules can easily respond with the newly formed epoxides immediately after they have formed, leading to covalent sulfates cross-linking two neighboring GO layers. In addition to exfoliation into single atomic layer sheets, this step involves hydrolysis of covalent sulfates serving as protective groups, and additional modification of oxygen functionalities due to reaction with water [82, 83]. Figure 1.9 summarizes and schematically represents these steps constituting the process of conversion of bulk graphite into GO [84].

Diamanganese heptoxide (Mn_2O_7) plays role of the active species during the oxidation of the graphite is which is formed during the reaction of monometallic tetraoxide and MnO_3^+ as shown in the following reaction:

$$KMnO_4 + 3H_2SO_4 \rightarrow K^+ + MnO_3^+ + H_3O^+ + 3HSO_4^-$$

The transformation of MnO_4^- into a more reactive form, Mn_2O_7 will certainly help to oxidize the graphite powder as shown in the reaction below [82, 85]:

$$MnO_3^+ + MnO_4^- \rightarrow Mn_2O_7$$

$$Mn_2O_7 + H_2SO_4 + C\ (Graphite) \rightarrow \begin{pmatrix} C-O-O \\ C-OH \\ C-COOH \end{pmatrix} + MnO_5 + H_2O + SO_4^-$$

But the bimetallic form of manganese oxide has been reported to detonate when heated up to 55 °C temperature or when reacted with organic compounds.

The chemical reduction of graphite oxide is one of the conventional processes to produce the Graphene in large quantities. Another approach to the preparation of Graphene is sonication and reduction of Graphene oxide (GO). At large excess of $NaBH_4$ has been used as a reducing agent for the addition of H_2 occurs across the alkenes, coupled with the extrusion of nitrogen gas [86]. Other reducing agents as include phenyl hydrazine [87], hydroxylamine [88], glucose, [89] ascorbic acid [90], hydroquinone [91], alkaline solutions [92], and pyrrole [93] are also used for the reduction of the graphite oxide. The thermal reduction process is also used for Graphite oxide reduction [94].

1.7 Functionalization of the Graphene

Graphene oxide (GO) and reduced Graphene Oxide (RGO) have most commonly been investigated in terms of creating novel functional materials. Functionalization of Graphene is a process that inserts the functionalizing element in the functional groups on its surface that may favor the material's solubility [95].

1.7.1 Need of functionalization

To trigger some desired effects and to open new avenues for the application of GO and RGO, a chemical functionalization was conducted. Pristine Graphene sheets are hydrophobic, so they cannot be dissolved in polar solvents. This makes the functionalization of Graphene sheets important for their future applications.

1.7.2 Type of functionalization

The functionalization of Graphene can be categorized on the basis of bond structure of the attachment of the functionalizing element. It is classified into two types, one is covalent and other is non-covalent functionalization.

1.7.3 Covalent functionalization

The covalent functionalization of Graphene includes generally two routes: (a) the formation of covalent bonds between free radicals or dienophiles and C=C bonds of pristine Graphene and (b) the formation of covalent bonds between organic functional groups and the oxygen groups of GO [96]. The covalent functionalization is achieved via four different ways: nucleophilic substitution, electrophilic addition, and condensation and addition reactions [97]. The chemistry of the reactive groups of Graphene-family materials covers many areas of research, including colloid chemistry and interface science; nevertheless, the basic rules of organic chemistry should be regarded as playing a leading role in covalent functionalization [98].

1.7.4 Non-covalent functionalization

Non-covalent interactions primarily involve hydrophobic, van der Waals and electrostatic forces and require the physical adsorption of suitable molecules on the Graphene surface. Non-covalent functionalization by π-interactions (as in the case of carbon nanotubes) is an attractive synthetic methods because it offers the possibility of attaching functional groups to Graphene without disturbing the electronic network [99]. To make Graphene soluble in common solvents, and thereby avoid stacking, non-covalent functionalization with different organic compounds is essential. It is achieved by polymer wrapping, adsorption of surfactants or small aromatic molecules [100-103].

1.7.5 Advantages of Graphene functionalization

It prevents the agglomeration of the Graphene layers and maintains the inherent properties of the Graphene during the reduction and facilitates the formation of a stable dispersion. The electrical conductivity of the functionalized Graphene gets decreased compared to the pure Graphene which is good sign of the device fabrication because the Graphene has very high conductivity. The opening of the bandgap in the Graphene is caused by the functionalization process which hints at the device fabrication purpose.

Sensing is the surface-dependent phenomenon so by modifying the surface of the Graphene we may get fruitful results. The surface modification of the Graphene is done with the functionalization process. The functionalizing elements get attached to the Graphene sheets at the oxygen-containing groups which are present at the side edges, corners and in the basal plane. There are many reports have been published regarding the functionalization of the Graphene and Graphene oxides. [104-110]

1.8 Applications of Graphene

Graphene has become the most well-known 2D carbon allotrope in this time due to its exceptional extraordinary properties like fast carrier mobility, lightweight at room temperature, the elastic limit of 1 TPa, and Young's modulus of 0.5 TPa which makes it 100 times stronger in compared to steel. Due to the attractive properties of Graphene, has been estimated to enhance the functionality of various applications. It has become the subject of tremendous research and extensive interest in recent years. Graphene has potential applications in various fields, such as solar cells, fuel cells, lithium-ion batteries, and other energy sources. Besides, electronic tools, water purification membranes,

biosciences and sensors applications and versatility of the applications are shown in the Fig. 1.10 [111].

Carbon-based nanomaterial as Graphene and their derivatives has been reported several applications in the all field of the science [112, 113]. The Graphene is employed in field emission [114], transparent electrodes [115] solar cell [116] energy storage devices [117-119].

Recently the application of nanomaterials in the field of sensor attracts the attention of researchers. The details about the different types of sensors have been discussed here.

1.8.1 Sensor

The sensors are the devices that yield a measurable output as a function of provided input. These are beneficial for in-situ measurements such as daily necessity, homes, offices, scientific applications and industrial processes etc. These act as critical components in all measurements and controlled applications and also responsible for transforming any physical phenomenon such that pressure, temperature, etc. into a measurable quantity through data acquisition (DAQ) system. It does not perform itself but acts as a part of the larger assembled system which may incorporate many other devices such as a transducer, detectors, data recorders, signal conditioners, signal processors, memory devices and actuators etc.

Rapid development in microelectronics and innovation in technology made the machine more autonomous and intellectual day by day. It has motivated the demand for artificial sensing organs that perform independently [120, 121]. Thus people developed

devices according to their requirements and now sensors are universally used in our daily lifestyle. For a good sensor, 3S factor i.e. sensitivity, selectivity and stability plays an important role. Sensors can be categorized into three types:

1- **Physical sensor**- A physical sensor is based on the measurement factor where no chemical reaction occurs. Measurement can be in the form of mass, temperature, absorbance, refractive index, conductivity etc. Temperature sensor, Pressure sensor etc. are well-known physical sensors [122-124].

2- **Biosensor**- Sensor that is used in biological applications is termed as biosensors. Immuno sensor, Microbial potentiometric sensor, etc. are the example of biosensors [125,126].

3- **Chemical sensor** – A chemical sensor is a sensor in which analyte participates to perform a chemical reaction and gives an analytic signal corresponding to the input. Various gas sensors and humidity sensors are well-known chemical sensors [127, 128]. In this Thesis, our focus is only on such type of sensors and the detailed description is discussed in this section

1.8.1 Chemical sensor

Chemical sensors are a special variety of gas sensors, to detect and investigate which substances are present and in what concentration in our environment. With our senses, we can not only see, hear and feel but also smell and taste. Consequently, a chemical sensor is also recognized as artificial noses or artificial tongues. A chemical sensor interacts with the sample and transforms its chemical information to the analyst to produce analytically useful signals. The chemical information may be due to the chemical reaction of the analyte or due to the physical measuring parameters of the system [129-

131]. Many scientists gave their different definitions for a chemical sensor according to their observations. It just concluded that the chemical sensor is an interface between the chemical world and the electronic. Or it is just the primary link of the measuring chain.

Chemical sensors consist of two important units one is the receptor part and other is the transducers part [132-134]. Sometimes few sensors are provided with separator also. The receptor part of a sensor is a chemical interface; there is an occurrence of chemical interaction of the analyte with a surface of the sample creating a change in its physical/ chemical parameters. The chemical information provided by the analyst is converted into a desirable form of energy which is further measured by the transducer. The transducer part is a device that converts one form of energy to another accordingly [135, 136].

1.8.2 Gas sensor

The gas sensor is the subclass of the chemical sensor. In 1927, Oliver W. Johnson presented an explosive gas indicator of a portable gas cylinder which was considered as the first commercial portable sensor which was no lesser than a miracle at those days. This led to the beginning of the fabrication of the sensor and its commercialization all over the world [137]. After that, the researchers developed various types of gas sensors such as electrochemical sensors, catalytic combustion sensors, calorimetric gas sensor, capacitive gas sensor, optical gas sensor, infrared sensors, and acoustic wave-based sensors, metal oxide-based gas sensor etc. These sensors are applicable in various fields such as chemical engineering, research and development, architecture, medical, pharmaceutical, agriculture, etc. [138, 139].

1.8.2.1 Classification of gas sensors

There are six types of gas sensors depending upon their transduction principle. These are as follows:

1. Electrochemical gas sensor
2. Acoustic gas sensor
3. Metal oxide gas sensor
4. Colourimetric gas sensor
5. Capacitive gas sensor
6. Optical gas sensor

An electrochemical gas sensor consists of two major parts; one is the electrolyte/gel used and another is electrodes (i.e anode and cathode). The anode is responsible for all the oxidation processes while the cathode is responsible for the reduction process. Due to this phenomenon, the current is created and also positive and negative ions are developed. Positive ions flow towards the cathode rod while the negative ions flow towards the anode rod. The output is directly proportional to the concentration or partial pressure of the gaseous species. Nowadays in the electrochemical gas sensor, the liquid electrolyte is replaced by solid-state electrolyte but the whole working is the same [140, 141].

The acoustic gas sensors are based on sound effects. These types of sensors consist of a piezoelectric substrate containing inter-digital electrodes. When RF voltage of a particular frequency is given then the mechanical waves are produced in the piezoelectric substrate. These Rayleigh surfaces then propagate and type of acoustic waves are generated and its frequency is determined. The mechanical energy is converted into electrical RF voltage [142].

The metal oxide gas sensor is also named as chemo-resistor gas sensor. Semiconductors are found to be very sensitive to the very low concentration of gas. This type of sensor requires strain gauze, thick film, thin film, etc. The capacitive gas sensor is used to detect a change in the capacitive behavior of the film by volatile analytes which are proportional to the concentration of the target analyte. The capacitive gas sensor gives the output signal by transforming the capacitance of the film in the form of voltage.

The calorimetric gas sensor is used to detect the combustible gas present in the surrounding. Its principle is based on the change in temperature in the presence of gas. Generally, any substance burns at its ignition temperature, similarly the combustible gas also burns at their ignition temperature but the gas begins to ignite in presence of certain catalytic material even at very low temperatures. This type of sensor is also called a catalytic sensor.

This sensor consisting of an optical fiber with palladium and titanium coating and was used for detecting hydrogen gas. The optical gas sensor gives higher sensitivity, stability, and selectivity than the non-optical gas sensor. Photons play an essential role in the optical gas sensor. They have residual mass with no charge so neither charge nor mass-based detection is done through it. This type of sensor is based on the absorption and emission scattering of a gas species. An optical gas sensor consists of a light-emitting element, optical fiber, a gas sensing element, a photodetector, and a filter for picking up fluorescence or phosphorescence phenomenon.

1.8.2.2 Applications of gas sensor

There are many applications of the gas sensor. Some of them are given as below:

1. In process control industries

2. For fire detection to avoid any miss-happening
3. For environmental monitoring
4. For the detection of harmful gases
5. As a breath sensor for the detection of alcohol
6. For grading of agro-based in the coffee industry or tea industry
7. As boiler sensor
8. In Atomic reactors
9. At home for safety purposes

1.8.3 Humidity sensor

Humidity measurement can be done in diverse ways based on the measurement technique used. The most commonly used terms are — Absolute Humidity (AH) and Relative Humidity (RH). Absolute humidity can be measured by two modes: Parts Per Million (ppm) by weight or volume and Dew/Frost Point. Absolute Humidity (vapor density) is defined as the ratio of the mass of water vapor in the air to the volume of air. Its unit is grams per cubic meter or grains per cubic foot (1 grain = 1/7000 pound lb.) and expressed as Eqn. 1.1.

$$\text{Absolute Humidity (AH)} = \frac{m}{V} \qquad (1.1)$$

where m is the mass of water vapor and V is the volume of air.

The relative humidity is defined as the ratio of the amount of moisture content in the air to the maximum (saturated) moisture level that the air can hold at the same

temperature and pressure. The RH measurement is stated as percentage and obtained by the following expression given in Eqn. 1.2:

$$\text{Relative Humidity (\%RH)} = \frac{Q_1}{Q_2} \qquad (1.2)$$

where Q_1 is the amount of water vapor present in a given volume of air at a given temperature and Q_2 is the amount of water vapor required to saturate the same volume of air at the same temperature.

RH being a temperature-dependent quantity hence called the relative measurement. Also, it can be expressed in terms of partial pressure as the ratio of the actual partial pressure of moisture content in the air (P_a) to the saturated pressure of moist air (P_s) at the same temperature (both in Bar or KPa), given in Eqn. 1.3:

$$\text{Relative Humidity (\%RH)} = \frac{P_a}{P_s} \times 100\% \qquad (1.3)$$

Also, RH can be defined as the ratio of absolute humidity (AH) to saturation humidity (SH) as shown in Eqn. 1.4:

$$\text{Relative Humidity (\%RH)} = \frac{\text{AH}}{\text{SH}} \times 100\% \qquad (1.4)$$

Parts Per Million by volume (PPMv) is defined as the volume of water vapor content per volume of dry gas, and Parts Per Million by weight (PPMw) is obtained by multiplying PPMv by the molar weight of water per molar weight of that gas or air. Dew point is defined as the temperature (above 0°C) at which the water vapor content of the gas begins to condense into liquid form, and Frost point is the temperature (below 0°C) at which the water vapor in a gas solidifies into ice. D/F point parameters are functions of

the pressure of the gas, but independent of temperature and are amongst the absolute humidity measurements. In other words, the dew point is the temperature at which the saturation water vapor pressure is equal to the partial pressure of the water vapor (in an air atmosphere). The difference between the ambient temperature and the dew point temperature is a measure of the ambient relative humidity [143-154].

The most commonly used sensors are those that measure the variation in capacitance of a dielectric material [155] or the variation in resistance [156, 157] of a conductive material as a function of RH. The principal sensor groups for humidity sensing thus include many resistive ceramics [158-161], organic polymers [162, 163] and resistive polyelectrolytes [164]. Although polymer sensors are of simple structure and low cost, however, they can measure only a limited range of moisture content and show hysteresis and drift at high humidity and they are relatively sensitive to chemical interference and dust deposition. Electrolytic sensors [165] require a constant flow rate for measurement. Also, the cell in which measurements are to be carried out requires regular-regeneration. This cell may be easily damaged by accidental water immersion. Infrared spectroscopy can also be used to measure RH. In infrared hygrometer [166, 167] absorption due to water vapor takes place at 2.6 μm and the split beam is used to compare sample cell and reference. Some other methods for humidity measurement are based on the surface acoustic wave (SAW) [168-171] and microwave attenuation.

Also, there are certain parameters which decide the efficiency of a particular sensor at a particular place. These parameters depend upon the type of sensing element. Some material that is efficient for a particular place may not be as good for some other place. The parameters of the humidity sensing are defined as below:

Sensitivity: It is the ratio of the change in the output signal (Impedance, capacitance, resistance, optical power etc.) to that of the input signal (%RH).

Accuracy: It is the conformity to a standardized reference signal.

Response time: It is the time required to reach 90% of the final sensor output after stepwise increasing the humidity.

Recovery time: It is the time required to reach 10% of the final sensor output after stepwise decreasing the humidity.

Drift: It is the change of the sensor output signal with time at a constant input signal.

Repeatability: It is the distribution of sensor outputs after when performing consecutive readings under similar conditions.

Reproducibility: It is the distribution of sensor outputs when measuring the same under different conditions.

Hysteresis: It is the difference in the output signal when measured for an up-trace and down-trace of the input signal.

Temperature dependence: It is the variation of sensor output with the temperature at constant humidity.

1.8.3.1 Types of humidity sensors

Humidity sensors are classified into the following groups:

- Electrical sensors

- Mechanical sensors
- Optical sensors
- Integrated sensors

The first group consists of sensors based on capacitive or impedance-type and measures the variation in capacitance or resistance of a dielectric material or conductive material respectively as a function of RH. The second group i.e. mechanical sensors consist of sensors based on strain-effects and mass-loading effects. In the third and the most important group i.e. optical sensors, the variation of the optical signal in terms of transmission, reflection and quenching of electromagnetic waves is considered. The last group contains miscellaneous integrated humidity sensors that contain on-chip passive or electronic components for linearization, calibration, transmission etc. [172].

1.8.3.2 Applications of humidity sensors

Humidity sensors have exposed noteworthy significance in a broad range of applications [173]. Some of them are shown in Fig. 1.11. Various techniques of humidity sensing have been employed to perform humidity measurements depending upon the need and type of applications, some of the important applications are as follows:

- Food processing
- Building and construction
- Agriculture
- Medical and health monitoring
- Fuel

Graphene is used in the electrochemical, electronic, optical and nanopore sensors after the synthesis and functionalization. The overall application of the functionalized Graphene has been shown in Fig. 1.12. Sensing is the surface dependent phenomenon therefore by modifying the surface of the Graphene with the functionalizing species, a sensor can be developed having the high sensitivity and rapid action.

1.9 Outlines of the Thesis

The thesis addresses the development of well-organized sensing elements for the detection of humidity and LPG. In this thesis, attempts to reduce the response-recovery times have been systematically reported at room temperature. This thesis contains seven Chapters:

Chapter 1 introduces the basics of different types of sensors along with a brief history of the carbon nanomaterial. This chapter also addresses a brief review on synthesis techniques of the Graphene, Graphene Oxides and their functionalization. This chapter provides the literature survey on the humidity and LPG sensors which are based on functionalized Graphene and carbon nanomaterials. **Chapter 2** includes the synthesis of the modified Graphene via thermal reduction method and also deals with the impedance-based humidity sensing at the optimized frequency by performing the experiments at different frequencies. **Chapter 3** describes the development of capacitance-based humidity sensor along with synthesis of the five-layered Graphene Oxide (GO) and GO functionalization with iron oxides (Fe-GO) by chemical route. **Chapter 4** describes the design of highly selective and sensitive room temperature operated LPG and humidity sensors fabricated by thin film of Graphene functionalized with CuO/SnO_2 nanocomposites (GCS). **Chapter 5** presents the five-layered GO

functionalized with Poly Pd acryl amide SnO_2 nanocomposite metallopolymer (MP-GO) based LPG and humidity sensors. **Chapter 6** designates the development of highly selective and sensitive room temperature operated CO_2 and humidity sensors fabricated by thin film of Graphene@CuO nanocomposites synthesized via Chemical Vapor Deposition technique. **Chapter 7** summarizes the concluding remarks on the entire research work of the Thesis and also deals with the future research scope of the Graphene functionalized materials in the field of sensors.

References

[1] D. Jariwala, A. Srivastava, P. M. Ajayan, Graphene synthesis and bandgap opening, Journal of nanoscience and nanotechnology 11 (2011) 6621-6641

[2] P. Marigo, J. D. Cummings, J. L. Curtis, J. Kalirai Y. Chen, P. E. Tremblay, E. R. Ruiz, P. Bergeron, S. Bladh, A. Bressan, L. Girardi, G. Pastorelli, M. Trabucchi, S. Cheng, B. Aringer, P. D. Tio, Carbon star formation as seen through the non-monotonic initial–final mass relation, Nature Astronomy (2020) 1-9

[3] H. W. Kroto, J. R. Heath, S. C. O'Brien, R. F. Curl, and R. E. Smalley, C60: Buckminsterfullerene, Nature 318 (6042) (1985) 162-163.

[4] The Nobel Prize in Chemistry 1996. NobelPrize.org. Nobel Media AB 2020. Mon. 12 Oct 2020. https://www.nobelprize.org/prizes/uncategorized/the-nobel-prize-in-chemistry-1996-1996

[5] S. Iijima, Helical microtubules of graphitic carbon, Nature (London) 354 (1991) 56-58.

[6] S. Iijima, and T. Ichihashi, Single-shell carbon nanotubes of 1-nm diameter, Nature (London) 363 (1993) 603-605.

[7] D. S. Bethune, C. H. Kiang, M. S. De Vries, G. Gorman, R. Savoy, J. Vazquez, and R. Beyers, Cobalt-catalysed growth of carbon nanotubes with single-atomic-layer walls, Nature (London) 363 (1993) 605-607.

[8] K. S. Novoselov, D. Jiang, F. Schedin, T. J. Booth, V. V. Khotkevich, S. V. Morozov, and A. K. Geim, Proceedings of the National Academy of Sciences of the United States of America 102 (2005) 10451

[9] P. R. Wallace, The band theory of graphite, Physical Review 71 (1947) 622-634.

[10] J. W. McClure, diamagnetism of graphite, Physical Review 104 (1956) 666-671.

[11] G. W. Semenoff, Condensed-matter simulation of a three-dimensional anomaly, Physical Review Letters 53 (1984) 2449-2452.

[12] S. Stankovich, D. A. Dikin, R. D. Piner, K. A. Kohlhaas, A. Kleinhammes, Y. Jia, Y. Wu, S. T. Nguyen, and R. S. Ruoff, Synthesis of graphene-based nanosheets via chemical reduction of exfoliated graphite oxide, carbon 45 (7) (2007) 1558-1565.

[13] A. V. Bommel, J. Crombeen, and A. V. Tooren, LEED and Auger electron observations of the SiC (0001) surface, Surface Science 48 (1975) 463-472.

[14] I. Forbeaux, J. Themlin, and J. Debever, Heteroepitaxial graphite on 6 H− SiC (0001): Interface formation through conduction-band electronic structure, Physical Review B 58 (1998) 1-11.

[15] C. Oshima, A. Itoh, E. Rokuta, and T. Tanaka, A hetero-epitaxial-double-atomic-layer system of monolayer graphene/monolayer h-BN on Ni (111), Solid State Communications 116 (2000) 37-40.

[16] X. K. Lu, M. F. Yu, H. Huang, and R. S. Ruoff, Tailoring graphite with the goal of achieving single sheets, Nanotechnology 10 (1999) 1-5.

[17] K. S. Novoselov, A. K. Geim, S. V. Morozov, D. Jiang, Y. Zhang, S. V. Dubonos, I. V. Grigorieva, and A. A. Firsov, Electric field effect in atomically thin carbon film, Science 306 (2004) 666-669.

[18] A. K. Geim, K. S. Novoselove, The rise in graphene, Nature Mater. 6 (184) (2007) 11-19.

[19] H. P. Boehm, R. Setton, E. Stumpp, Nomenclature and terminology of graphite intercalation compounds, Carbon 24 (1986) 241–245.

[20] R. R. Nair, P. Blake, A. N. Grigorenko, K. S. Novoselov, T. J. Booth, T. Stauber, N. M. R. Peres, A. K. Geim, Fine structure constant defines visual transparency of Graphene, Science 80 (2008) 1308-1308.

[21] C. Lee, X. Wei, J. W. Kysar, J. Hone, Measurement of the elastic properties and intrinsic strength of monolayer Graphene, Science 321 (2008) 385-388.

[22] S. V. Morozov, K. S. Novoselov, M. I. Katsnelson, F. Schedin, D. C. Elias, J. A. Jaszczak, A. K. Geim, Giant intrinsic carrier mobilities in Graphene and its bilayer, Phys. Rev. Lett. (016602) (2008) 11-14

[23] S. Ghosh , I. Calizo , D. Teweldebrhan , E. P. Pokatilov , D. L. Nika , A. A. Balandin , W. Bao , F. Miao , C. N. Lau , Extremely high thermal conductivity of graphene: Prospects for thermal management applications in nanoelectronic circuits, Appl. Phys. Lett. 92 (2008) 1-3.

[24] H. C. Lee, and A. R. Mohamed, Correction: Review of the synthesis, transfer, characterization and growth mechanisms of single and multilayer Graphene. RSC advances 7 (45) (2017) 28427-28427.

[25] W. Choi, I. Lahiri, R. Seelaboyina and Y. S. Kang, Synthesis of Graphene and Its Applications: A Review, Crit. Rev. Solid State Mater.Sci. 35 (2010) 52–71.

[26] Y. Hernandez, V. Nicolosi, M. Lotya,., F. M. Blighe Z. Y. Sun, S. De, I. T. McGovern,.; B. Holland, M. Byrne, Y. K. Gun'ko, High-yield production of Graphene by liquid-phase exfoliation of graphite. Nat. Nanotechnol. 3 (2008) 563–568.

[27] M. Lotya, Y. Hernandez, P. J. King, R. J. Smith, V. Nicolosi, L. S. Karlsson, F. M. Blighe, S. De; Z. M. Wang, I. T. McGovern, Liquid phase production of Graphene by exfoliation of graphite in surfactant/water solutions. J. Am. Chem. Soc. 131 (2009) 3611–3620.

[28] M. Coroş, F. Pogăcean, L. Măgeruşan, C. Socaci, and S. Pruneanu, A brief overview on synthesis and applications of Graphene and Graphene-based nanomaterials, Frontiers of Materials Science 13 (1) (2019) 23-32.

[29] M. Coroş, F. Pogăcean, M. C. Roşu, Simple and cost-effective synthesis of Graphene by electrochemical exfoliation of graphite rods. RSC Advances 6(4) (2016) 2651–2661.

[30] M. Hernaez, C. R. Zamarreño, S. M. -Espina, L. R. Bird, A. G. Mayes, and F. J. Arregui. Optical fibre sensors using Graphene-based materials: A review, Sensors 17 (1) (2017) 155-170.

[31] X. Qin, X. Chen, F. Zhang, L. Xiao, X. Xie, X. Yang, X. Xu, X. Hu, and P. Yu, Polarized Raman scattering of epitaxial graphene prepared by thermal decomposition of SiC, ECS Journal of Solid State Science and Technology, 7(3) (2018) 35–40.

[32] F. Mitsuhashi, M. Okada, Y. Tateno, T. Nakabayashi, M. Ueno, H. Nagasawa, H. Fukidome, and M. Suemitsu, Extremely uniform epitaxial growth of Graphene from sputtered SiC films on SiC substrates. MRS Advances, 2(1) (2017) 51–56.

[33] A. Reina, X. Jia, J. Ho, D. Nezich, H. Son, V. Bulovic, M. S. Dresselhaus, and J. Kong, Large Area, Few-Layer Graphene Films on Arbitrary Substrates by Chemical Vapor Deposition , Nano Lett. 9 (2009) 30-35.

[34] M. Sprinkle, M. Ruan, Y. Hu, J. Hankinson, M. R.-Roy, B. Zhang, X. Wu, C. Berger, and W. A. D. Heer, Scalable templated growth of Graphene nanoribbons on SiC, Nat. Nanotech (5) (2010) 727-731.

[35] K. L. Choy, Chemical vapour deposition of coatings, Prog. Mat. sci. (48) (2003) 57-170.

[36] A. Y. Tontegode, Carbon on transition metal surfaces, Prog. in Surf. Sci. 38 (1991) 201-429.

[37] K. S. Kim, Y. Zhao, H. Jang, S. Y. Lee, J. M. Kim, K. S. Kim, J.- H. Ahn, P. Kim, J.-Y. Choi, and B. H. Hong, Large-scale pattern growth of Graphene films for stretchable transparent electrodes, Nature 457 (7230) (2009) 706-10.

[38] P. W. Sutter, J.-I. Flege, E. A. Sutter, Epitaxial Graphene on ruthenium, Nature Materials **7** (2008) 406-411.

[39] Y. Lee, S. Bae, H. Jang, S. Jang, S.-E. Zhu, S. H. Sim, Y. I. Song, B. H. Hong, and J.-H. Ahn, Wafer-Scale Synthesis and Transfer of Graphene Films, Nano Lett. 10 (2010) 490-493.

[40] V. Singh, D. Joung , L. Zhai ,S. Das , S. I. Khondaker , S. Seal , Graphene based materials: Past, present and future, Progress in Materials Science 56 (2011) 1178–1271.

[41] X. S. Li, W. W. Cai, J. H. An, S. Kim, J. Nah, D. X. Yang, R. Piner, A .Velamakanni, I. Jung, E. Tutuc, S. K. Banerjee, L. Colombo and R. S. Ruoff, Large-area synthesis of high-quality and uniform Graphene films on copper foils, Science 324 (2009) 1312–1314.

[42] P. Sutter, J. Lahiri, P. Zahl, B. Wang, E. Sutter, Scalable Synthesis of Uniform Few-Layer Hexagonal Boron Nitride Dielectric Films, Nano Lett. 13 (2013) 276−281.

[43] P. W. Sutter, J.- I. Flege & E. A. Sutter, Epitaxial Graphene on ruthenium, Nature Materials **7** (2008) 406 – 411.

[44] Johann Coraux , A. T. N'Diaye, M. Engler, C. Busse, D. Wall , N. Buckanie, F.-J. M.z. Heringdorf, R. V. Gastel , B. Poelsema and T. Michely, Growth of Graphene on Ir (111), New Journal of Physics 11 (2009) 1-23.

[45] L. Gao, W. Ren, H. Xu, L. Jin , Z. Wang, T. Ma, L.-P. Ma, Z. Zhang, Q. Fu, L.-M. Peng, X. Bao & H.-M. Cheng, Repeated growth and bubbling transfer of Graphene with millimetre-size single-crystal grains using platinum, Nature communications 3 (2012) 1-7.

[46] S.-Y. Kwon C. V. Ciobanu, V. Petrova, V. B. Shenoy, J. Bareno, V. Gambin, I. Petrov, and S. Kodambaka, Growth of semiconducting graphene on palladium, Nano letters 9 (12) (2009) 3985-3990.

[47] M. E. Ramón, A. Gupta, C. Corbet, D. A. Ferrer, H. C. P. Movva, G. Carpenter, L. Colombo, G. Bourianoff, M. Doczy, D. Akinwande, E. Tutuc, and Sanjay K. Banerjee, CMOS-Compatible Synthesis of Large-Area, High-Mobility Graphene by Chemical Vapor Deposition of Acetylene on Cobalt Thin Films, ACS Nano 5 (9) (2011) 7198–7204.

[48] A. Guermoune, T. Chari, F. Popescu, S. S. Sabri, J. Guillemette, H. S. Skulason, T. Szkopek, and Mohamed Siaj, Chemical vapor deposition synthesis of

Graphene on copper with methanol, ethanol, and propanol precursors, Carbon 49 (13) (2011) 4204-4210.

[49] B. Liu, N. Xuan, K. Ba, X. Miao, M. Ji, and Z. Sun, Towards the standardization of Graphene growth through carbon depletion, refilling and nucleation, Carbon 119 (2017) 350–354.

[50] A. M. -Barcenas, J. F. Perez-Robles, Y. V. Vorobiev, N. O.-Soto, A. Mexicano, and A. G. García, Graphene synthesis using a CVD reactor and a discontinuous feed of gas precursor at atmospheric pressure, Journal of Nanomaterials 3457263 (2018) 1-11.

[51] S. Yin, X. Zhang, C. Xu, Y. Wang , Y. Wang, P. Li , H. Sun, M. Wang, Y. Xia, C.-T. Lin, P.Zhao, H. Wang, Chemical vapor deposition growth of scalable monolayer polycrystalline Graphene films with millimeter- sized domains, Materials Letters 215 (2018) 259–262.

[52] F. Pogacean, A. R. Biris, C. Socaci, M. Coros, L. Magerusan, M.-C. Rosu, M. D. Lazar, G. Borodi and S. Pruneanuet, Graphene-bimetallic nanoparticle composites with enhanced electro-catalytic detection of bisphenol, A. Nanotechnology 27(48) (2016) 1-11.

[53] M. P. Lavin-Lopez, L. Sanchez-Silva, J. L. Valverde, A. Romero, CVD Graphene growth on different polycrystalline transition metals. AIMS Materials Science, 4(1) (2017) 194–208.

[54] S. Pekdemir, M. S. Onses, M. Hancer, Low temperature growth of Graphene using inductively-coupled plasma chemical vapor deposition, Surface and Coatings Technology 309 (2017) 814–819.

[55] I. V. Vlassiouk, Y. Stehle, P. R. Pudasaini, R. R. Unocic, P. D. Rack, A. P. Baddorf , I. N. Ivano , N. V. Lavrik, F. List, N. Gupta, K. Bets, B. I. Yakobson, and S. Smirnov, Evolutionary selection growth of two-dimensional materials on polycrystalline substrates. Nature Materials, 17(4) (2018) 318–322.

[56] B. J. Park, J. S. Choi, J. H. Eom, H. Ha, H. Y. Kim, S. Lee, H. Shin, and S.-G. Yoon, Defect-free graphene synthesized directly at 150 °C via chemical vapor deposition with no transfer. ACS Nano, 12(2) (2018) 2008–2016.

[57] A. Kasikov, T. Kahro, L. Matisen, M. Kodu, A. Tarre, H. Seemen, and H. Alleset, The optical properties of transferred graphene and the dielectrics grown on it obtained by ellipsometry. Applied Surface Science, 437(2018) 410–417.

[58] X. Xu, Z. Zhang, J. Dong, D. Yi, J. Niu, M. Wu, L. Lin , R. Yine , M. Li, J. Zhou, S. Wang, J. Sun, X. Duand, P.Gaoa, , Y. Jiangg, X. Wua, H. Peng, R. S. Ruoff, Z. Liu, D. Yua , E. Wangg, F. Ding, K. Liu, Ultrafast epitaxial growth of metre sized single-crystal Graphene on industrial Cu foil. Science Bulletin, 62(15) (2017) 1074–1080.

[59] H. T. Chin, J. J. Lee, M. Hofmann, Y. P. Hsieh, Impact of growth rate on Graphene lattice-defect formation within a single crystalline domain. Scientific Reports 8 (2018) 1-6.

[60] C. C. Hsu, J. D. Bagley, M. L. Teague, W.-S. Tseng, K. L. Yang, Y. Zhang, Y. Li, Y. Li, J. M. Tour, and N.-C.. Yeh, High-yield single-step catalytic growth of Graphene nanostripes by plasma enhanced chemical vapor deposition. Carbon 129 (2018) 527–536.

[61] L. Y. Jiao, L. Zhang, X. R. Wang, G. Diankov, H. J. Dai, Narrow Graphene nanoribbons from carbon nanotubes, Nature 458 (2009) 877–880.

[62] D. V. Kosynkin, A. L. Higginbotham, A. Sinitskii, J. R. Lomeda, A. Dimiev, B. K. Price, J. M. Tour, Longitudinal unzipping of carbon nanotubes to form Graphene nanoribbons, Nature 458 (2009) 872–876.

[63] L.Y. Jiao, X. R. Wang, G. Diankov, H. L. Wang, H. J. Dai, Facile synthesis of high-quality Graphene nanoribbons. Nat. Nanotechnol. 5 (2010) 321–325.

[64] M. S. A. Bhuyan, M. N. Uddin, and M. M. Islam, Synthesis of Graphene, Int. Nano Lett 6 (2016) 65–83.

[65] P. Solís-Fernández, M. Bissett, and H. Ago, Synthesis, structure and applications of Graphene-based 2D heterostructures, Chemical Society Reviews 46 (15) (2017) 4572-4613.

[66] P. P Brisebois, and Mohamed Siaj, Harvesting Graphene oxide–years 1859 to 2019: a review of its structure, synthesis, properties and exfoliation, Journal of Materials Chemistry C 8 (5) (2020) 1517-1547.

[67] B. C. Brodie, XIII. On the atomic weight of graphite, Philos. Trans. R. Soc. London, 149 (1859) 249-259.

[68] L. Staudenmaier, Verfahren zur darstellung der graphitsäure, Berichte der Dtsch. Chem. Gesellschaft, 31 (1898) 1481-1487.

[69] V. L. Hofmann and E. Konig, Untersuchungen über graphitoxyd, Z. Anorg. Allg. Chem. 31 (1937) 311-336.

[70] D. R. Dreyer, S. Park, C. W. Bielawski and R.S. Ruof, The chemistry of Graphene oxide Chem. Soc. Rev. 39 (2010) 228-240.

[71] W. S. Hummers and R. E. Offeman, Preparation of graphitic oxide, J. Am. Chem. Soc. 80 (1958) 1339-1339.

[72] S. Eigler, C. Dotzer, F. Hof, W. Bauer, and A. Hirsch, Sulfur species in Graphene oxide., Chem. Eur. J. 19 (2013) 9490-9496.

[73] H. L. Poh F. Šaněk, A. Ambrosi, G. Zhao, Z. Sofer, and M. Pumera, Graphenes prepared by Staudenmaier, Hofmann and Hummers methods with consequent thermal exfoliation exhibit very different electrochemical properties, Nanoscale 4 (2012) 3515-3522.

[74] D. C. Marcano D. V. Kosynkin, J. M. Berlin, A. Sinitskii, Z. Sun, A. Slesarev, L. B. Alemany, W.Lu, and J. M. Tour, Improved synthesis of graphene oxide, ACS Nano 4 (2010) 4806-4814.

[75] S. Eigler and A. M. Dimiev, Graphene Oxide: Fundamentals and Applications, First Edition, John Wiley and Sons, 2017.

[76] W. Gao, Graphene Oxide: Reduction Recipes, Spectroscopy, and Applications, Springer Springer Cham Heidelberg New York Dordrecht London, 2015.

[77] J. Zhao L. Liu, and F. Li., Graphene Oxide: Physics and Applications, Heidelberg New York Dordrecht London, 2015.

[78] A. M. Dimiev and J. M. Tour, Mechanism of graphene oxide formation, ACS Nano 8 (2014) 3060-3068.

[79] G. Shao, Y. Lu, F. Wu, C.Yang, F. Zeng, and Q. Wu, Graphene oxide: the mechanisms of oxidation and exfoliation, J. Mater. Sci. 47 (2012) 4400-4409.

[80] S. Pan and I. A. Aksay, Factors controlling the size of Graphene oxide sheets produced via the graphite oxide route, ACS Nano 5 (2011) 4073-4083.

[81] S. Eigler, C. Dotzer, F. Hof, W. Bauer, A. Hirsch, Sulfur Species in Graphene Oxide. Chem. Eur. J. 19 (2013) 9490 – 9496.

[82] A. Dimiev, D. V. Kosynkin, L. B. Alemany, P. Chaguine, J. M. Tour, Pristine Graphite Oxide. J. Am. Chem. Soc., 134 (2012) 2815 –2822.

[83] A. Dimiev, L. Alemany, J. M. Tour, Graphene Oxide. Origin of Acidity and Dynamic Structural Model, ACS Nano 7 (2012) 576 –588.

[84] A. M. Dimiev, and J. M. Tour, Mechanism of graphene oxide formation, ACS Nano 8(3) (2014) 3060-3068.

[85] T. F. Emiru, and D. W.u Ayele, Controlled synthesis, characterization and reduction of Graphene oxide: A convenient method for large scale production, Egyptian Journal of Basic and Applied Sciences 4 (2017) 74–79.

[86] H.-J. Shin, K. K. Kim, A. Benayad, S.-M. Yoon, H.K. Park, I.-S. Jung, M.H. Jin, H.-K. Jeong, J.M. Kim, , J.-Y. Choi, Y.H. Lee, Efficient reduction of graphite oxide by sodium borohydride and its effect on electrical conductance. Adv. Funct. Mater. 19(12) (2009) 1987-1992.

[87] V.H. Pham, T.V. Cuong, T.-D Nguyen-Phan, H.D. Pham, E.J. Kim, S.H. Hur, E.W. Shin, S. Kim, J. S. Chung, One-step synthesis of superior dispersion of chemically converted graphene in organic solvents, Chem. Commun. 46 (2010) 4375–4377.

[88] X. Zhou, J. Zhang, H. Wu, H. Yang, J. Zhang, S. Guo, Reducing graphene oxide via hydroxylamine: a simple and efficient route to Graphene, J. Phys. Chem. C 115(24) (2011) 11957–11961.

[89] C. Zhu, S. Guo, Y. Fang, S. Dong, Reducing sugar: new functional molecules for the green synthesis of Graphene nanosheets, ACS Nano 4(4) (2010) 2429–2437.

[90] J. Zhang, H. Yang, G. Shen, P. Cheng, J. Zhang, S. Guo, Reduction of Graphene oxide viaL-ascorbic acid. Chem. Commun, 46 (2010) 1112–1114.

[91] G. Wang, J. Yang, J. Park, X. Gou, B. Wang, H. Liu, J. Yao, Facile synthesis and characterization of Graphene nanosheets, J. Phys. Chem. 112(22) (2008) 8192–8195.

[92] X. Fan, W. Peng, Y. Li, X. Li, S. Wang, G. Zhang, F. Zhang, Deoxygenation of exfoliated graphite oxide under alkaline conditions: a green route to preparation, Adv. Mater. 20(23) (2008) 4490–4493.

[93] C.A. Amarnath, C.E. Hong, N.H. Kim, B.-C. Ku, T. Kuila, J.H. Lee, Efficient synthesis of Graphene sheets using pyrrole as a reducing agent, Carbon 49(11) (2011) 3497–3502.

[94] I. Sengupta, S. Chakraborty, and M. Talukdar, S. K. Pal, S. Chakraborty, Thermal reduction of Graphene oxide: How temperature influences purity, Journal of Materials Research 33 (23) (2018) 4113-4122.

[95] E. D. Grayfer, A. S. Nazarov, V. G. Makotchenko, S.-J. Kim, and V. E. Fedorov, Chemically modified graphene sheets by functionalization of highly exfoliated graphite, J. Mater. Chem. 21 (2011) 3410–3414.

[96] A. Kasprzak, A. Zuchowska, and M. Poplawska, Functionalization of Graphene: does the organic chemistry matter? Beilstein J. Org. Chem. 14 (2018) 2018–2026.

[97] T. Kuila, S. Bose, A. K. Mishra, P. Khanra, N. H. Kim, and J. H. Lee, Chemical functionalization of Graphene and its applications, Progress in Materials Science 57 (2012) 1061–1105.

[98] J. M. Englert, C. Dotzer, G. Yang, M. Schmid, C. Papp, J. M. Gottfried, H.-P. Steinrück, E. Spiecker, F. Hauke, and A. Hirsch, Covalent bulk functionalization of Graphene, Nature Chemistry 3 (4) (2011) 279-286.

[99] M, Ioniţă, G. M. Vlăsceanu, A. A. Watzlawek, S. I. Voicu, J. S. Burns, and H. Iovu, Graphene and functionalized graphene: Extraordinary prospects for nanobiocomposite materials, Composites Part B: Engineering 121 (2017) 34-57.

[100] M. W. Lee, T. Y. Wang, J. L. Tsai, Characterizing the interfacial shear strength of graphite/epoxy composites containing functionalized Graphene, Compos Part B-Eng. 98 (2016) 308-13.

[101] M. Hao, M. Tang, W. Wang, M. Tian, L. Zhang, Y. Lu, Silver-nanoparticle-decorated multiwalled carbon nanotubes prepared by poly (dopamine) functionalization and ultraviolet irradiation. Compos Part B-Eng. 95 (2016) 395-403.

[102] T. Kuilla, S. Bhadra, D. Yao, N. H. Kim, S. Bose, J. H. Lee, Recent advances in Graphene based polymer composites. Prog. Polym. Sci. 35 (11) (2010) 1350-75.

[103] A. Kasprzak, A. Zuchowska, and M. Poplawska, Functionalization of graphene: does the organic chemistry matter? Beilstein J. Org. Chem. 14 (2018) 2018–2026.

[104] P. Huang, L. Jing, H. Zhu, X. Gao, Diazonium functionalized Graphene: microstructure, electric, and magnetic properties, Accounts Chem Res. 46(1) (2012) 43-52.

[105] H. Liu, S. Ryu, Chen Z, M. L. Steigerwald, C. Nuckolls, L. E. Brus, Photochemical reactivity of Graphene, J. Am. Chem Soc. 131(47) (2009) 17099-17101.

[106] V. Georgakilas, M. Otyepka, A. B. Bourlinos, V. Chandra, N. Kim, K. C. Kemp, P. Hobza, R. Zboril, and K. S. Kim, Functionalization of Graphene: covalent and non-covalent approaches, derivatives and applications. Chem Rev. 112(11) (2012) 6156-6214.

[107] S. Vadukumpully, J. Gupta, Y. Zhang, G. Q. Xu, S. Valiyaveettil, Functionalization of surfactant wrapped Graphene nanosheets with alkylazides for enhanced dispersibility, Nanoscale 3(1) (2011) 303-308.

[108] X. Zhong, J. Jin, S. Li, Z. Niu, W. Hu, R. Li, and J. Ma, Aryne cycloaddition: highly efficient chemical modification of Graphene, Chem Commun. 46(39) (2010) 7340-7342.

[109] R. R. Nair, W. Ren, R. Jalil, I. Riaz, V. G. Kravets, L. Britnell, P. Blake , F. Schedin, A. S. Mayorov, S. Yuan, M. I. Katsnelson, H. M. Cheng, W. Strupinski, L. G. Bulusheva, A. V. Okotrub, I. V. Grigorieva, A. N. Grigorenko, K. S. Novoselov, A. K. Geim, Fluorographene: Two - Dimensional Counterpart of Teflon, Small 6(24) (2010) 2877-2884.

[110] T. A. Pham, N. A. Kumar, Y.T. Jeong, Covalent functionalization of Graphene oxide with polyglycerol and their use as templates for anchoring magnetic nanoparticles, Synthetic Met. 160(17) (2010) 2028-2036.

[111] N. A. A. Ghany, S. A. Elsherif, and H. T. Handal, Revolution of Graphene for different applications: State-of-the-art, Surfaces and Interfaces 9 (2017) 93–106.

[112] D. Chen, H. Feng, and J. Li, Graphene oxide: preparation, functionalization, and electrochemical applications, Chem. Rev. 112 (2012) 6027−6053.

[113] T. Wang, D. Huang, Z. Yang, S. Xu, G. He, X. Li, N. Hu, G. Yin, D. He, and L. Zhang, A review on graphene-based gas/vapor sensors with unique properties and potential applications, Nano-Micro Lett. 8(2) (2016) 95–119.

[114] G. Eda, H. E. Unalan, N. Rupesinghe, G. A. J. Amartunga, and M. Chhowalla, Field emission from Graphene based composite films, Appl. Phy. Lett., 93 (2008) 1-3.

[115] Y. Xu, J. Liu, Graphene as transparent electrodes: fabrication and new emerging applications, Small 12 (2016) 1400–1419.

[116] X. Wang, L. Zhi, K. Mu, Transparent, conductive Graphene electrodes for dye sensitized solar cells, Nano Lett. 8 (2007) 321–327.

[117] M. M. Atabaki, R. Kovacevic, Graphene composites as anode materials in lithium ion batteries, Electron. Mater. Lett. 9 (2013) 133–153.

[118] J. R. Miller, P. Simon, Electrochemical capacitors for energy management, Science 80 (321) (2008) 651–652.

[119] J. Xia, F. Chen, J. Li, N. Tao, Measurement of the quantum capacitance of Graphene, Nat. Nanotechnol. 4 (2009) 505–509.

[120] J. Cadena, G. J. Riu, F. X. Rius. Gas sensors based on nanostructured materials. Analyst 132 (2007) 1083-1099.

[121] M. Schenk, A. R. Reichelt. An electron microphone as a force sensor for combined scanning probe microscopy, Ultramicroscopy 65 (1996) 109-118.

[122] F. He, Q. Huang, M. Qin, a silicon directly bonded capacitive absolute pressure sensor. Sens. Actuator A: Phy. 35 (2007) 507-514.

[123] C. T. Huang, C. L. Shen, C. F. Tang, S. H. Chang, A wearable yarn-based piezo-resistive sensor. Sens. Actuator A: Phy., 141(2) (2008) 396-403.

[124] C. V. G. Reddy, S. V. Manorama, V. J. Rao, Preparation and characterization of ferrites as gas sensor materials, J. Mater. Sci. Lett. 19 (2000) 775-778.

[125] L. A. Mercante, V. P. Scagion, F. L. Migliorini, L. H. C. Mattoso, D. S. Correa Electrospinning-based (bio) sensors for food and agricultural applications: A review, Trends in Analytical Chemistry 91 (2017) 91-103.

[126] G. Korotcenkov, B. K. Cho. Metal oxide composites in conductometric gas sensors: Achievements and challenges, Sens. Actuators B: Chem. 244 (2017) 182-210.

[127] S. Singh, B. C. Yadav, R. Prakash, B. Bajaj, J. R. Lee. Synthesis of nanorods and mixed shaped copper ferrite and their applications as liquefied petroleum gas sensor, App. Surf. Sci. 257 (2011) 10763-10770.

[128] C. Peng. Principle and Application of Biomedical Sensors, Higher Education Press, Beijing, China, (2000) 157.

[129] L. Gajdosik. Tin oxide Gas Sensors, Encyclopedia of Sensors, 10 (2006) 361.

[130] K. Shimanoe, M. Yuasa, T. Kida, N. Yamazoe. Semiconductor gas sensor using nano-sized oxide for high-sensitive detection of environment-related gases, in Proceedings of the IEEE International Conference on Nanotechnology Materials and Devices (2011) 38-43.

[131] G. Neri. Metal Doping in semiconductor Gas Sensors, Encyclopedia of Sensors, 6 (2006) 1-13.

[132] T. Seiyama, A. Kato, K. Fujiishi, M. Nagatani, A new detector for gaseous components using semiconductive thin films. Anal. Chem. 34 (1962) 1502-1503.

[133] D. E. Williams, Semiconducting oxides as gas-sensitive resistors. Sens. Actuators B: Chem. 57 (1999) 1-16.

[134] A. A. Tomchenko, G. P. Harmer, B. T. Marquis, J. W. Allen, Semiconducting metal oxide sensor array for the selective detection of combustion gases. Sens. Actuators B: Chem.,93 (2003) 126-134.

[135] N. Yamazoe, K. Shimanoe. Theory of power laws for semiconductor gas sensors. Sens. Actuators B: Chem. 128 (2002) 566-573.

[136] C. Massie, G. Stewart, G. M. Gregor, and J. R. Gilchrist, Design of a portable optical sensor formethane gas detection, Sens. Actuators B: Chem. 113 (2) (2006) 830-836.

[137] S. C. Gadkari, M. Kaur, V. R. Katti, V. B. Bhandarkar, K. P. Muthe, S. K. Gupta. Solid State Sensors for H_2, H_2S and NH_3, Encyclopedia of Sensors 10 (2006) 21.

[138] R. Binions, H. Davies, A. Afonja, S. Dungey, D. Lewis, D. E. Williams, D.E, I.P. Parkin. Zeolitemodified discriminating gas sensors, J. Electrochem. Soc. 156 (3) (2009) J46.

[139] R. K. Sonker, M. Singh, U. Kumar, B. C. Yadav, MWCNT doped ZnO nanocomposite thin film and it's sensing, Journal of Inorganic and Organometallic Polymers and Materials 26 (6) (2016) 1434-1440.

[140] T. Takada, T. Fukunaga, and T. Maekawa. New method for gas identification using a singlesemiconductor sensor, Sens. Actuators B: Chem. 66 (2000) 22-24.

[141] J. F. Currie, A. Essalik, J. C. Marusic, Micromachined thin film solid state electrochemical CO_2, NO_2 and SO_2 gas sensors, Sens. Actuators B: Chem. 59 (2–3) (1999) 235-241.

[142] R. Sathiyamoorthi, R. Chandrasekaran, T. Mathanmohan, B. Muralidharan, T. Vasudevan, Study of electrochemical-based gas sensors for fluorine and chlorine, Sens. Actuators B: Chem. 99 (2–3) (2004) 336-339.

[143] I. D. Avramov, M. Rapp, A. Voigt, U. Stahl, M. Dirschka, Comparative studies on polymer coated SAW and STW resonators for chemical gas sensor applications. In Proceedings of 2000 IEE/EIA International Frequency Control Symposium and Exhibition, Kansas City, USA, 7–9 (2000) 58-65.

[144] W. H King, Piezoelectric Absorption Detector, Analytical Chemistry 36 (1964) 1735-1739.

[145] S. Kamekichi, T. Tatsumi, Wet and dry plate dew point Hygrometer, Humidity and Moisture1, Ed. by R. E. Ruskin (1965) 64.

[146] M. Yoshitake, I. Shimizu. Experimental results of the psychrometer constant, humidity and moisture 1, Ed. by R. E. Ruskin (1965) 70.

[147] R. J. Taylor. The response of psychrometer fluctuations in vapour pressure, Humidity and Moisture 1, Ed. by R. E. Ruskin (1965) 76.

[148] W. W. Robert. Psychrometer Determination of relative humidities in the air with dry-bulb temperatures exceeding 212˚F, Humidity and Moisture1, Ed. by R. E. Ruskin (1965) 105.

[149] R. G. Wylie, D. K. Davies, W. A. Caw, The basic process of the dew-point hygrometer, Humidity and Moisture 1, Ed. by R. E. Ruskin (1965) 125.

[150] A. W. Brewer, The dew-or frost-point hygrometer, Humidity and Moisture 1, Ed. by R. E. Ruskin (1965) 136.

[151] C. Y. Lee, G. B. Lee, Micro-machine based humidity sensors with integrated temperature sensors for signal drift compensation. J. Micromech. Microeng.13 (2003) 620.

[152] P. Pascal-Delannoy, B. Sorli, A. Boyer. Quartz Crystal Microbalance (QCM) used as a humidity sensor. Sens. Actuators B: Chem. 84 (2000) 285-291.

[153] W. H. King Jr., The piezoelectric sorption hygrometer, Humidity and Moisture 1, Ed. by R. E. Ruskin (1965) 570.

[154] M. Jose, M. Perez, C. Freyre. A poly(ethyleneterephthalate)-based humidity sensor, Sens. Actuators B: Chem. 42 (1977) 27-30.

[155] I. Hayakawa, Y. Iwamoto, K. Kikuta, S. Hirano. Gas sensing properties of metal organics derived Pt dispersed-TiO_2 thin film fired in NH_3, Sens. Actuators B: Chem. 67 (2000) 270-274.

[156] Y. Sakai, M. Matsuguchi, T. Hurukawa. Humidity sensor using cross-linked poly (chloromethyl styrene), Sens. Actuators B: Chem. 66 (2000) 135-138.

[157] J. Das, S. M. Hossain, S. Chakraborty, U. Gangopadhyay, H. Saha. Capacitive type Humidity Sensor based on Porous Silicon, Proceedings of the Tenth International Workshop on the Physics of Semiconductor Devices 1 (1999) 707.

[158] B. C. Yadav, A. K. Srivastava, P. Sharma. Resistance based humidity sensing properties of TiO_2, Sens. & Trans. J. 81(7) (2007)1348-1353.

[159] W. Qu, W. Wlodarski, U. Jorg. Comparative study on micromorphology and humidity sensitive properties of thin-film and thick-film humidity sensors based on semiconducting $MnWO_4$, Sens. Actuators B: Chem. 64 (2000) 76-82.

[160] B. C. Yadav, R. Srivastava, C. D. Dwivedi, Synthesis of ZnO nanorods and their application as humidity sensors, Synthesis and Reactivity in Inorganic, Metal-Organic and Nano-Metal Chemistry 37 (2007) 417-423.

[161] B. C. Yadav, P. Sharma, A. K. Srivastava, A. K. Yadav. Synthesis of antimony doped tin oxide and it's use as an electrical humidity sensor. Sens. & Trans. J. 92 (5) (2008) 99.

[162] B. C. Yadav, P. Sharma, P. K. Khanna. Morphological and Humidity Sensing Characteristics of SnO_2-CuO, SnO_2-Fe_2O_3 and SnO_2-SbO_2 nano co-oxides, Bull.of Mater. Sci. 34 (1) (2011) 1-10.

[163] W. Qu, M. Jorg-Uwe, A novel thick film ceramic humidity sensor, Sens. Actuators B: Chem. 40 (1997) 175-182.

[164] B. C. Yadav, R. Srivastava, C. D. Dwivedi. Synthesis and characterization of ZnO-TiO2 nano-composite and its application as a humidity sensor, Philosophical Magazine 88 (2008) 1113-1124.

[165] A. K. Srivastava, B. C. Yadav. Humidity sensing properties of TiO_2-Sb_2O_5 nanocomposite, Materials Science 28(2) (2010) 491-502.

[166] Y. Sakai, Y. Sadaoka, Y. Matsuguchi. Humidity sensors based on polymer thin films, Sens. Actuators B: Chem. 35 (1-3) (1996) 85-90.

[167] B. Yang, B. Aksas, Q. Lin, M. Sitti, Compliant and low-cost Humidity Sensors using Nano-porous polymer membranes, Sens. Actuators B: Chem. 114 (2006) 254-262.

[168] Y. Mu-Roug, C. Ko-Shao. Humidity Sensors using polyvinyl alcohol mixed with electrolytes, Sens, Actuators B: Chem. 49 (1998) 240-247.

[169] F. S. Wayne, W. F. Laurence, P. J. Hans, Infrared Absorption Hygrometer, Humidity and Moisture 1, Ed. by R. E. Ruskin (1965) 465.

[170] R. C. Wood. The Infrared Hygrometer-Its application to Difficult humidity measurement Problems, Humidity and Moisture 1, Ed. by R.E. Ruskin (1965) 492.

[171] N. M. Tashtoush, J. D. N. Cheeke, N. Eddy. Surface Acoustic Wave Humidity Sensor based on a thin poly XIO film, Sens. Actuators B: Chem. 49 (1998) 218-225.

[172] R. H. Huang. Sensor Calibration of a SAW Resonator for absolute humidity measurements in microelectronic packages, Sens. Actuators B: Chem.25 (1-3) (1995) 686-688.

[173] D. W. Galipean, J. D. Stroschine, K. A. Snow, K. A. Vetelino, K. R. Hines. A study of condensation and dew point using a SAW, Sens. Actuators B: Chem. 25(1-3) (1995) 696-700.

[174] C. Caliendo, E. Verona, A. D'Amico, A. Furlani, G. Iucci, M. V. Russo. Surface acoustic wave humidity sensor, Sens. Actuators B: Chem. 16 (1993) 288-292.

Figures

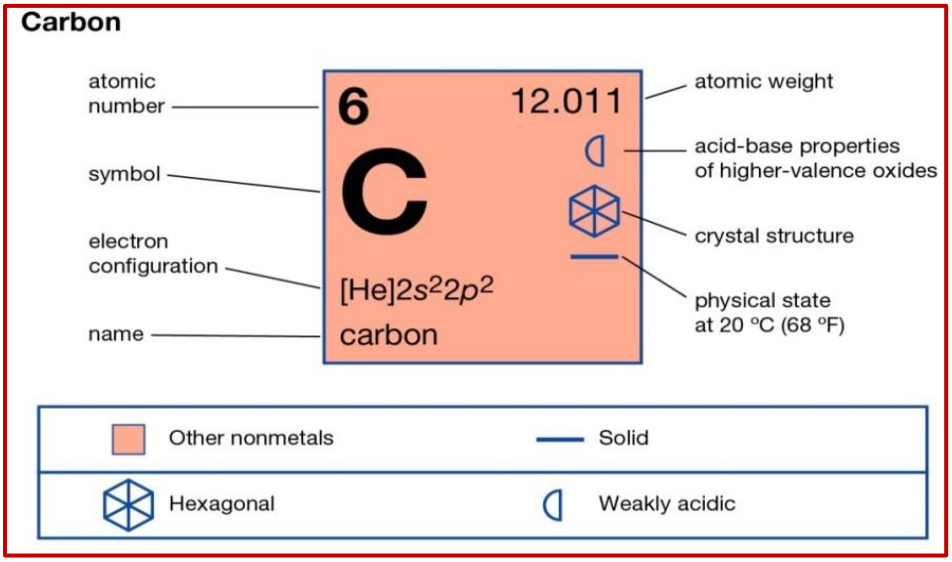

Fig. 1.1 Symbolic representation and electronic configuration of the carbon

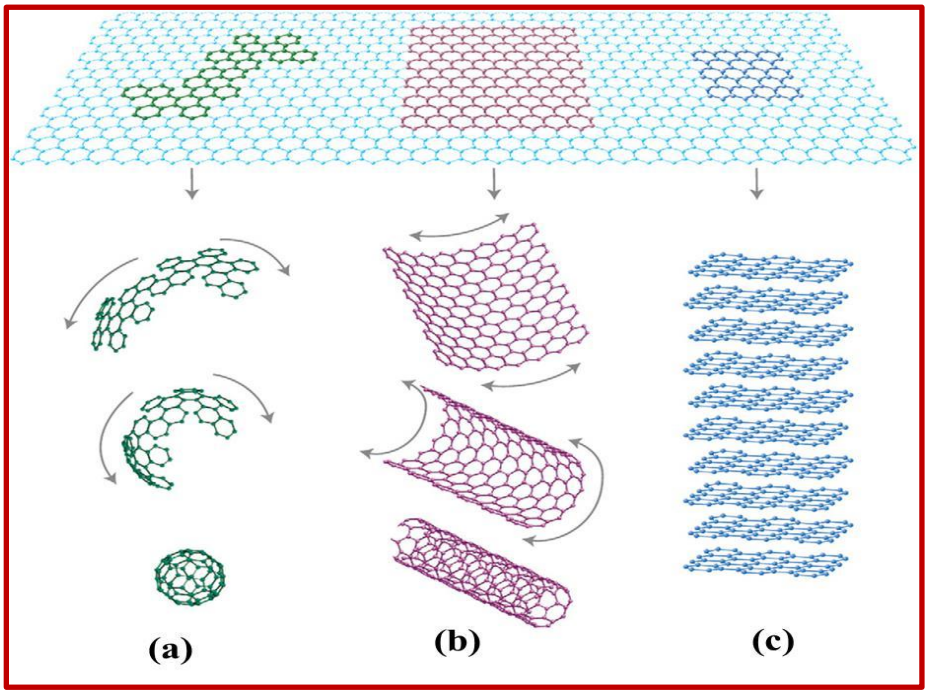

Fig. 1.2 Graphene is the building block for the carbon-based material, which can be wrapped into 0 D buckyballs (a), rolled into 1D nanotube (b) stacked into 3D graphite (c) [18].

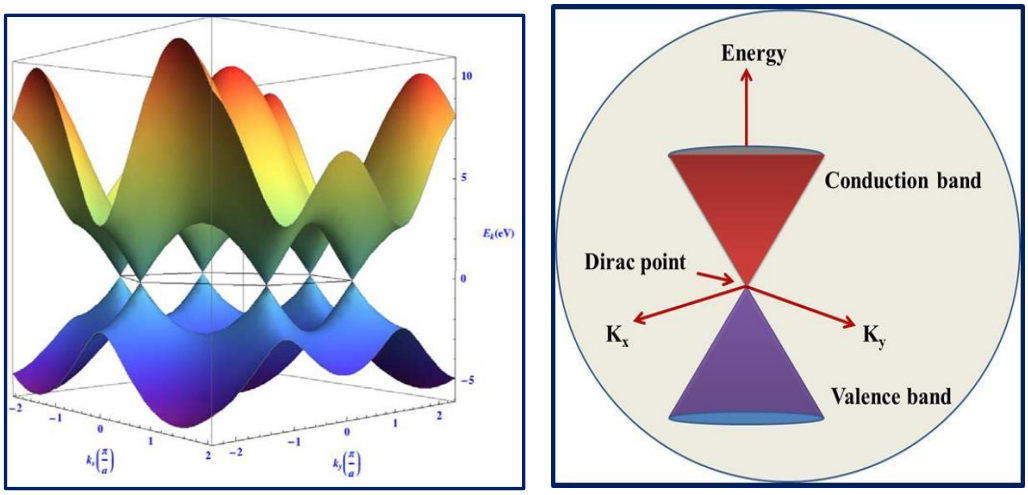

Fig. 1.3 Band structure of the Graphene

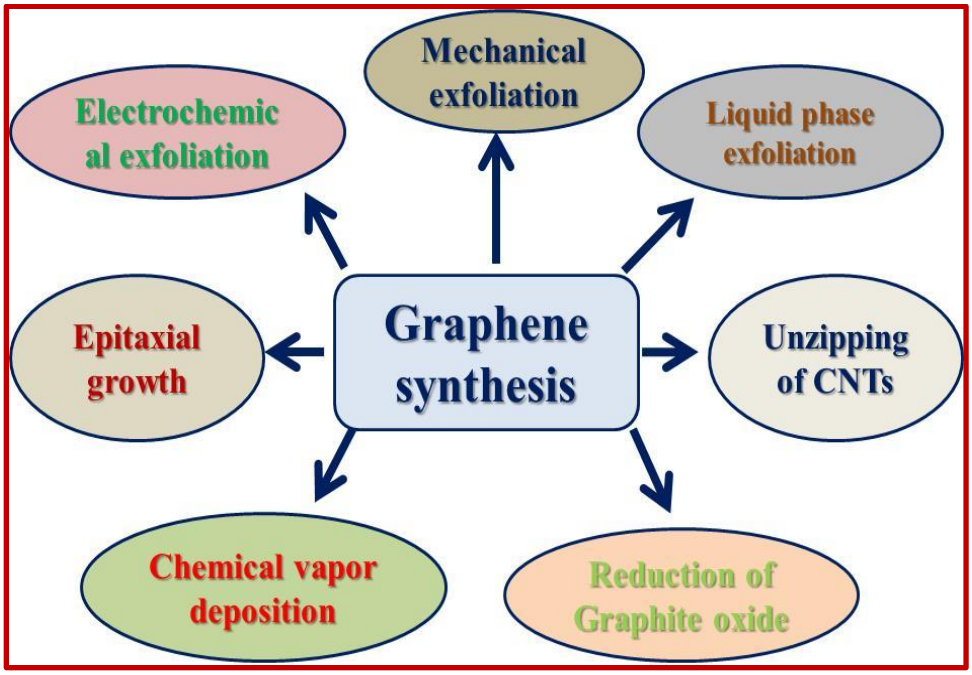

Fig. 1.4 Different synthesis techniques of the Graphene

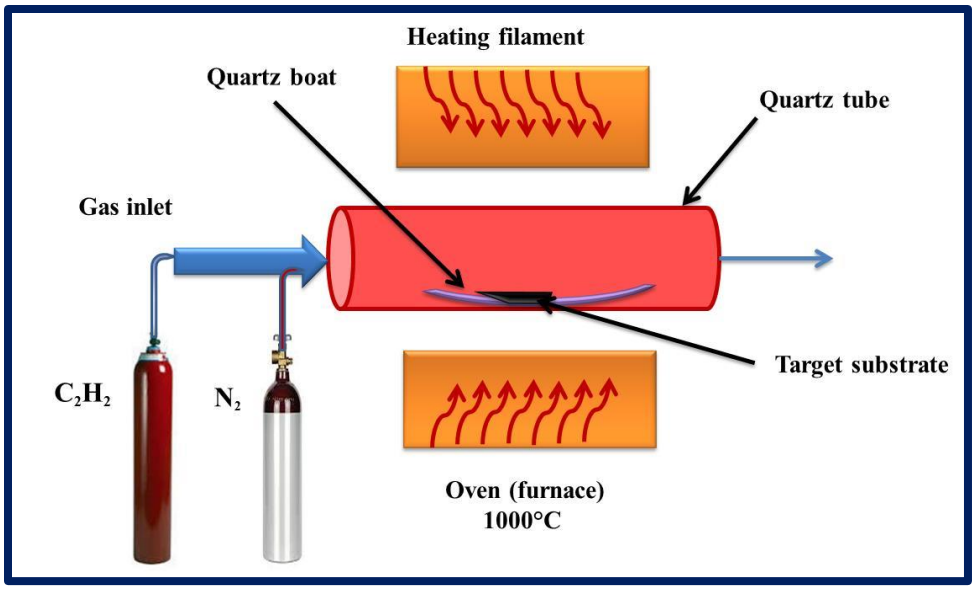

Fig. 1.5 Schematic of the CVD technique setup

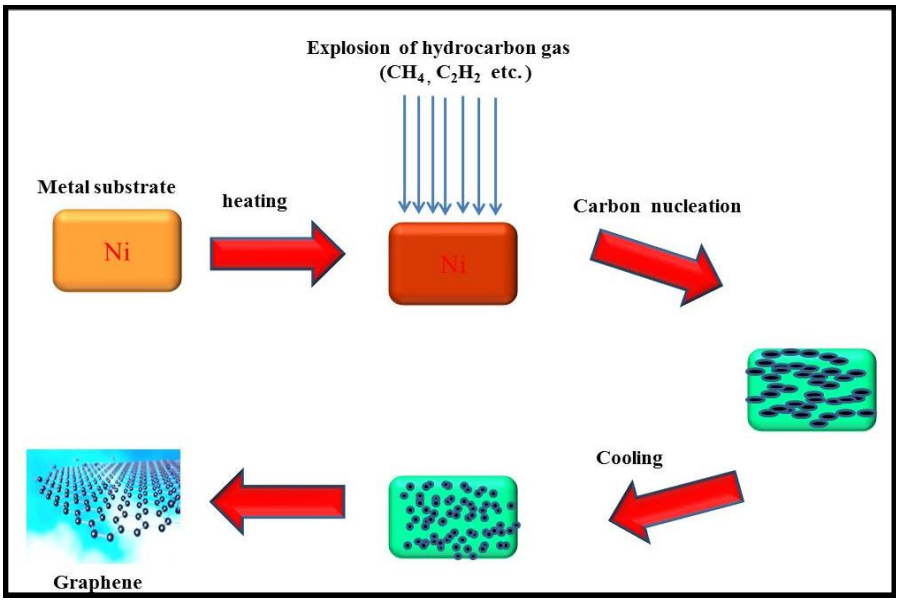

Fig. 1.6 Schematic of the mechanism for CVD Graphene growth on Ni substrate

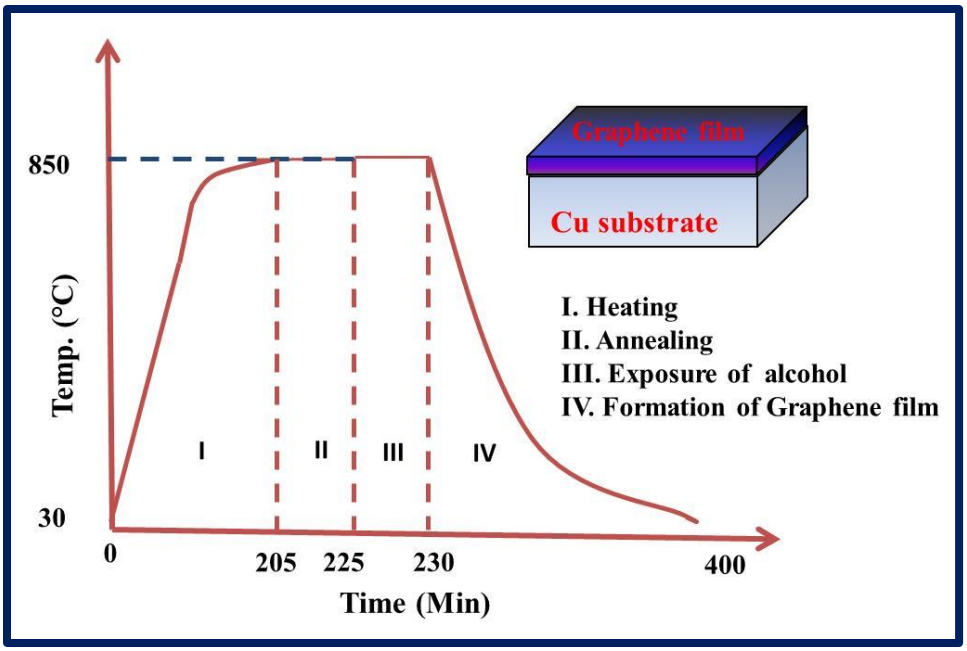

Fig. 1.7 Growth of Graphene on Cu substrate in different regions with the alcohol

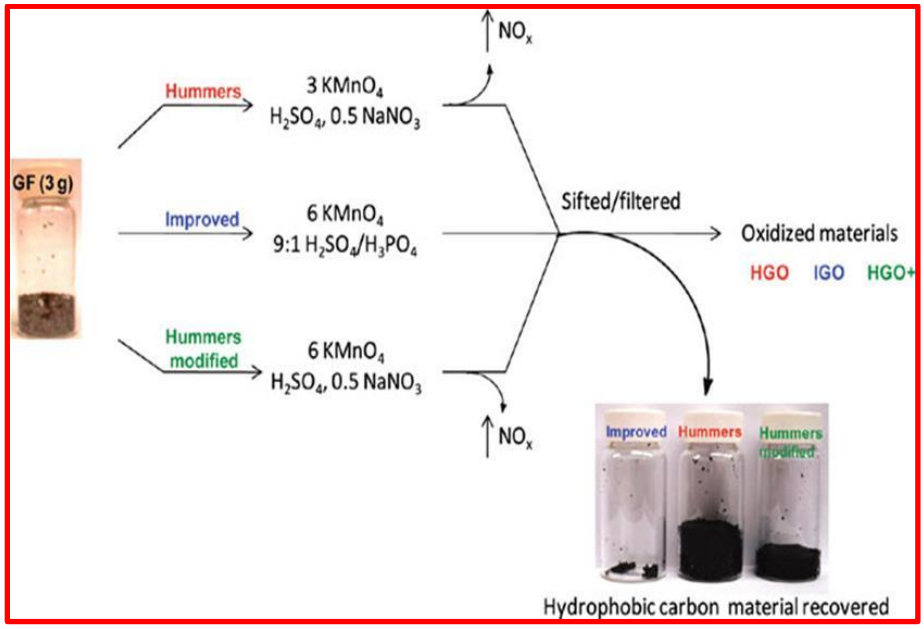

Fig. 1.8 Schematic of the synthesis of GO via different methods

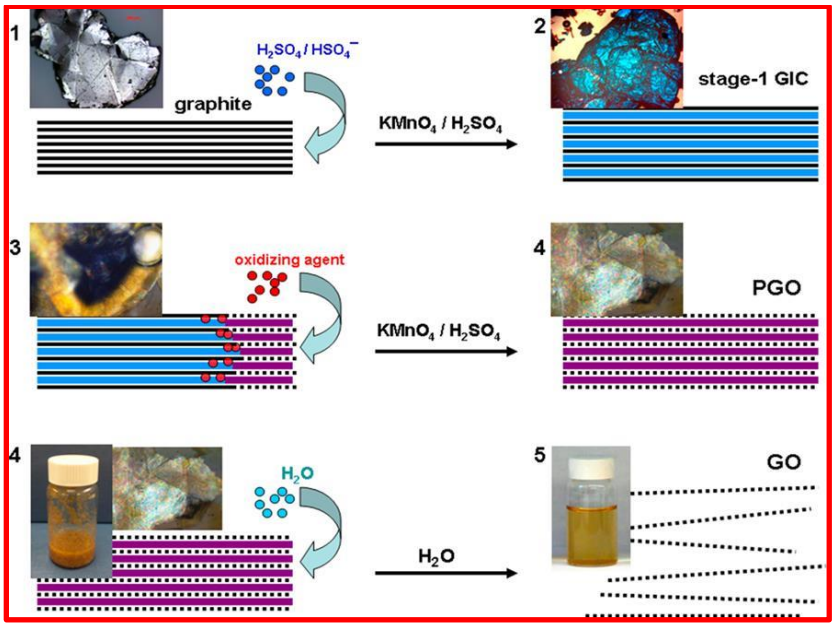

Fig. 1.9 Mechanism of the Graphite exfoliation [84]

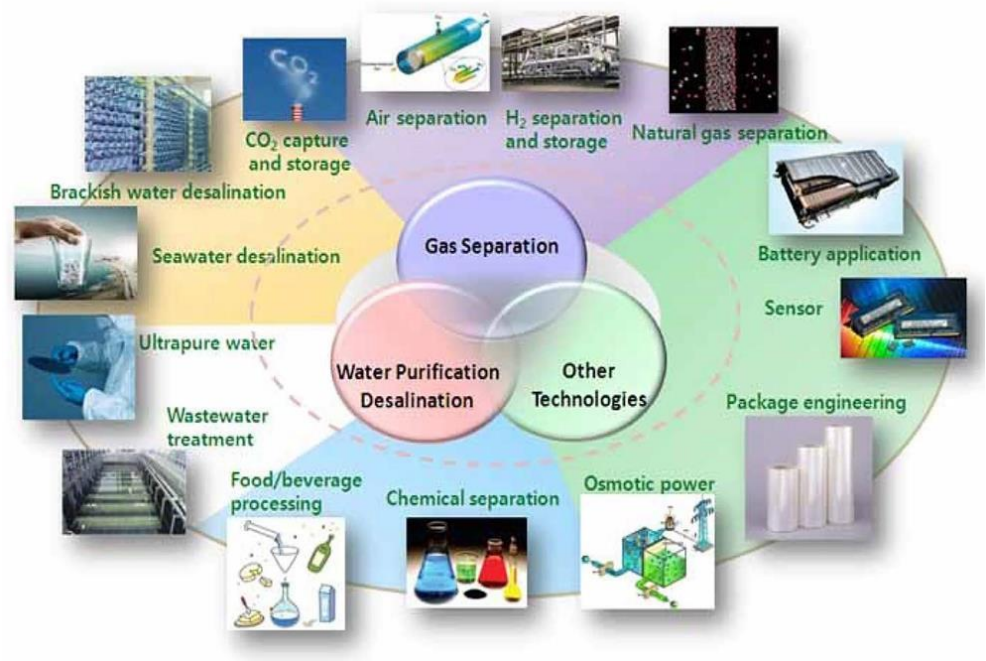

Fig. 1.10 Application of the Graphene in the diverse field of science [111]

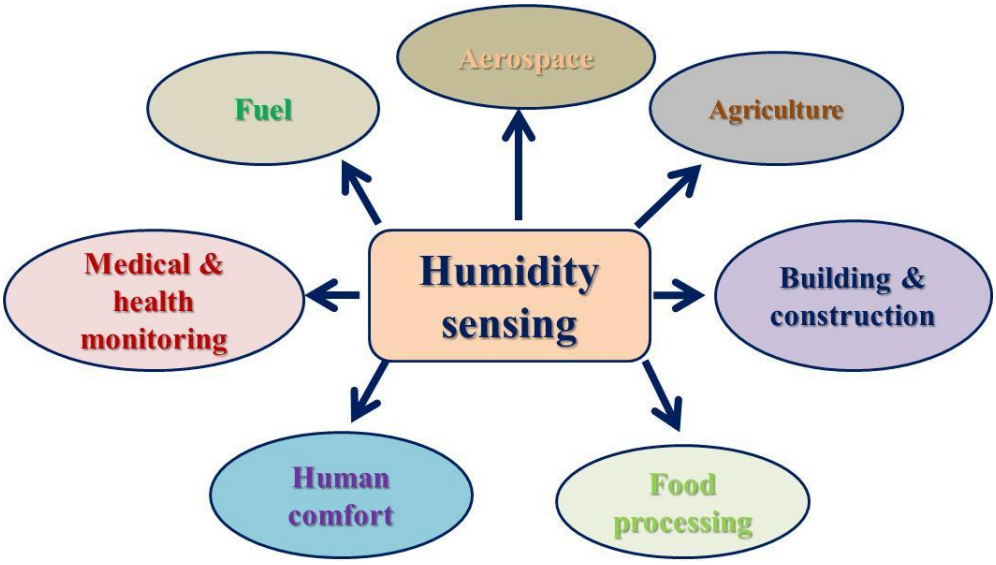

Fig. 1.11 Application of the humidity sensors in the various fields

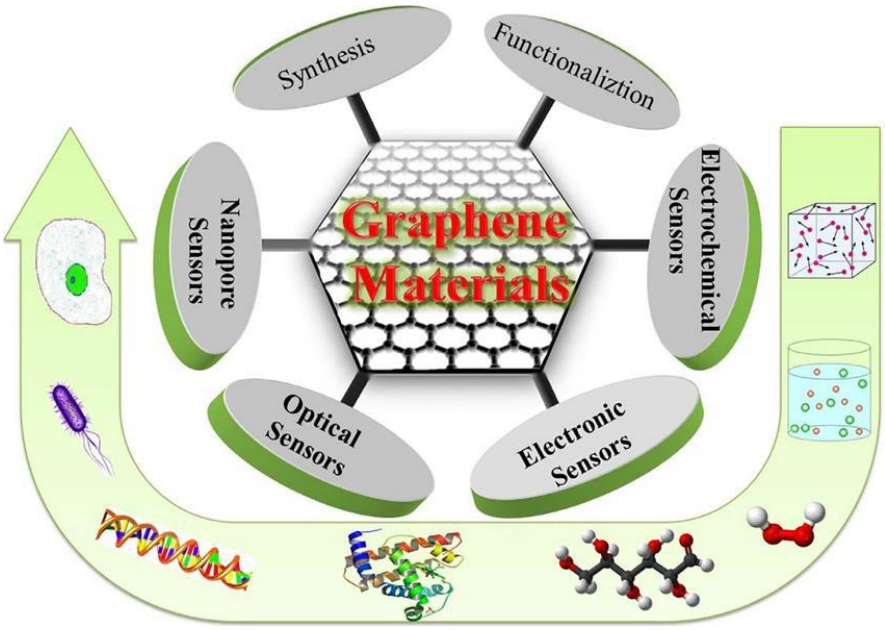

Fig. 1.12 An overview of the role of Graphene and its derivatives in the various types of sensors [111]

Tables

Substrate used/Precursor	Growth temperature	Product	Reference
Cu/(H_2 + CH_4)	1070	Graphene single crystals	[49]
electrolytic Cu (technical grade)/ N_2 (90%):H_2 (10%), C_2H_2	1000	good quality Graphene	[50]
Cu/CH_4	1060	polycrystalline monolayer Graphene	[51]
(AuCu+ MgO or AgCu + MgO)/ CH_4	1000	high quality Graphene decorated with bimetallic nanoparticles (AuCu and AgCu)	[52]
(Ni or Cu)/CH_4	1050 (Cu), 980 (Ni)	high quality Graphene	[53]
Cu/(CH_4 + H_2 + Ar plasma)	300	AB-stacked bilayer Graphene films	[54]
(Cu or NiCu)/CH_4	1050 (Cu), 1100	continuous single	[55]

	(NiCu)	crystal monolayer Graphene	
PET and glass/10 nm thick	150	defect-free Graphene	[56]
Cu/CH_4	1000	single-layer Graphene	[57]
Cu/CH_4	1030	large and high-quality Graphene films with single crystallinity	[58]
Cu/CH_4	1000	high-quality Graphene	[59]
1,2-dichlorobenzene/CH_4	without any active heating	Graphene nanostripes	[60]

Table 1.1 CVD synthesized Graphene published reports

CHAPTER 2

MODIFIED GRAPHENE AS A MOISTURE SENSOR AT OPTIMIZED FREQUENCY

The present chapter details the synthesis and characterization of the modified Graphene and its moisture sensing application. The characterization tools as Brunauer–Emmett–Teller (BET), Scanning Electron Microscopy (SEM), Electron Dispersive X -rays (EDX), Particle size distribution, Fourier-Transform Infra-Red (FTIR), UV-Vis spectrophotometry and Raman are employed for characterizing the synthesized material. The BET demonstrations of the synthesized material have a specific surface area as 10.55 m^2/g together with pores size distribution range from 10.34 to 97.44 nm, confirming mesoporous material. The SEM, EDX, FTIR, UV Vis spectroscopy and Raman analysis of the synthesized material confirmed that it is the modified Graphene (m-Graphene). Presence of the I_D/I_G = 1.55 confirmed the more defects along with many dangling bonds which are more beneficial for the humidity detection. The humidity sensing characteristics of m- Graphene-based sensor have been observed from 100 Hz to 10 kHz frequencies and found the best sensitivity at 100 Hz. The sensor shows the high sensitivity as 2.51 MΩ/%RH along with the calculated repeatability, response and recovery time are 96.05%, 24 and 13 s respectively at room temperature.

CHAPTER 2

Modified Graphene as a moisture sensor at optimized frequency

2.1 Introduction

Nowadays deal of more innovation takes place every day in the area of sensors based on new smart materials. The nanomaterials are the era of attraction due to its size-dependent remarkable properties. In that respect, there are different fabrics which are utilized for the best in the different applications [1-4]. The nanostructured metal oxides, polymers, carbon-based nanomaterials, nanocomposites etc. are employed in the energy storage devices, solar cells, photovoltaic cells, flexible devices, and sensors [5-10]. A humidity sensor along with high sensitivity, high repeatability, low hysteresis, small response and recovery time is desirable. Materials and their size play a key role in the humidity sensing devices [11, 12]. The detection of the humidity in the environment is important not only for the human being but also for non-living bodies. In the field of medicals, agriculture, defense, and food technology the measurement of the humidity is very much important. There are plenty of humidity measurement techniques that are already reported [13, 14]. A variety of fabrics e.g. metal oxides, polymers, nanocomposites and carbon nanomaterials are used to designing the humidity sensors [15, 16]. The carbon-based nanomaterials: Graphene, Graphene Oxide (GO), and reduced Graphene Oxides (rGO) are used in different application due to their remarkable properties and also due to the unique electric transport properties of carbon nanotubes, their use in the manufacture of composite materials significantly enhances microwave

properties [17-20]. Graphene along with its derivatives are 2D materials popularly employed in plenty of applications as energy storage, conversion, photocatalysis, electrocatalysis and sensing platforms. The application of the modified Graphene (m-Graphene) in humidity sensing is because of the large surface to volume (S/V) ratio along with the good conductivity and more dangling bonds formed due to defects [21, 22]. The pure Graphene-based sensors do not give a good response because of the high conductivity, lack of defects and dangling bonds [23, 24]. Zeineb Ben Aziza et al. reported an efficient method to modify the doping level of Graphene and progress its sensitivity to humidity without activating defects to the Graphene [25]. The term "modified" in the modified Graphene is preferred due to the complete reduction of GO to Graphene has not yet been perceived. The reduction of the GO through thermal methods produced conducting modified Graphene [26, 27]. The GO is synthesized by chemical wet using Hummer, modified Hummer and Staundiemer methods. Synthesis of the GO comprises oxidation of the graphite in the presence of the strong acids and oxidizing agents. The oxidation process increases the interlayer spacing between the Graphene layers in GO against the weak Wander Vaal forces present within it. GO consists of the different oxygen-containing functionalities as carbonyl, hydroxyl, epoxy and carboxylic acid groups. To retain the conductivity in the GO we need the reduction of the GO. The chemical reduction of the GO is carried by the $NaHB_4$, hydrazine, ascorbic acids etc. [28-30]. In the reduction process, we exfoliate and reduce the number of Graphene layers in GO. Yunpeng Su et al. developed Graphene/PVA/SiO_2 based surface wave acoustic humidity sensor for respiration monitoring [31]. H. J. Kim et al. reported a Fiber-optic humidity sensor system for the monitoring and detection of coolant leakage in nuclear

power plants [32]. Y. Yao et al. demonstrated renewable cellulose nanocrystals as humidity sensing material which was deposited on the sensing electrode of quartz crystal microbalance (QCM) [33].

The recent literature survey of the humidity sensor has been depicted in Table 2.1. The literature report shows the development of the facile, easy and movable sensor along with wide humidity sensing range, high sensitivity, low response and recovery time which is need of the hour. To overcome these problems, we have reported this article in which the m-Graphene has been synthesized by using the oxidation of the graphite, followed by thermal reduction of GO along with the application in the humidity sensing.

2.2 Experimental procedures

2.2.1 Chemicals used

The Graphite powder was purchased from Triton Graphite, Gujarat, India (98% purity, 200 mesh). The specific surface area of graphite powder was 0.8 m^2/g and other chemicals were purchased from Merck Specialities Private Limited, Mumbai, India and used as these were received. Some other chemicals of analytical grades such as $KMnO_4$, H_3PO_4, H_2SO_4, Hydrogen peroxide, DI water etc. were used without further purifications in the present synthesis.

2.2.2 Synthesis of the m-Graphene

Graphene Oxide (GO) was synthesized through the oxidation of the graphite (2.5 g) by the $KMnO_4$ (15g) in the presence of the mixture H_2SO_4/H_3PO_4 (300/30 ml) shown in Fig. 2.1. Graphite powder was poured in the mixture of H_2SO_4/H_3PO_4 acid and stirred at 500 RPM for 5 h at room temperature. Now the 400cc ice was added to this solution

and stirred for 3 h at 100 RPM. After that, the H_2O_2 (5 ml) has been added dropwise which changes the colour of the solution. This signifies that the reduction of the Graphite into the Graphene oxide (GO) has been completed. Lastly, the obtained solution was washed up to neutral pH (7) and dried it at 40 °C for 24 h in hot air oven. The thermal exfoliation of GO was performed in a temperature-controlled programmable furnace in the presence of 20% oxygen. The temperature of the furnace was fixed at 600 °C for 1h and GO get converted into the modified Graphene in this process [34, 41-43].

2.2.3 Fabrication of the m-Graphene film

For the characterization purpose, the thin film of m-Graphene was fabricated using spin coating technique. The thin film was fabricated on the glass substrate at 3000 RPM in the vacuum insisted chamber. After depositing thin film, it was dehydrated on the hot plate at 40 °C temperature for 30 minutes. The thin film was annealed at 400 °C temperature for 1 hr in the presence of 20% oxygen.

2.3 Characterizations techniques

The synthesized material was characterized using different characterization techniques as Brunauer-Emmett-Teller (BELSORP-mini II), Scanning Electron Microscopy (SEM) (JEOL, JSEM- 6490LV SEM) with Electron Dispersive X -rays (EDX), Particle Size Analysis using Zeta nanosizer, UV-Visible spectra were recorded using UV Visible Spectrophotometer (Evolution 201), Fourier Transform Infra-Red (FTIR Nicolet TM 6700) and Raman spectra were recorded with Raman spectrometer (A Renishaw using $\lambda = 514.5$ nm Ar^+ with power 15 mW).

2.4 Results and Discussions

2.4.1 Brunauer–Emmett–Teller (BET) analysis

Fig. 2.2 is the depiction of the N_2 isotherm and inset the corresponding plot of the nanopore size distribution of the m-Graphene. The BET equation in linear form is represented in Eqn. 2.1. The slope and the intercept of this equation simultaneously with Eqn. 2.2 help to find the specific BET surface area.

$$\frac{P/P_0}{n\{1-(P/P_0)\}} = \frac{1}{n_m C} + \frac{C-1}{n_m C}(P\ /\ P_0) \qquad (2.1)$$

$$a_S(BET) = n_m N_A \sigma \qquad (2.2)$$

Where n is the amount of the gas adsorbed at the relative pressure P/P_0, C is the fitting parameter, n_m is the monolayer coverage, N_A is Avogadro number and σ is the cross-sectional area of the N_2. The surface area of the synthesized material has been calculated using the BET equation and found as 10.55 m^2/g. The isotherm showed the apparent loop ranging from 0.64 to 0.97 P/P_0. The inset of Fig. 2.2 (BJH curve) describing the pore size distributions ranging from 10.34 to 97.44 nm. The distribution of the pore size confirmed that the synthesized material is meso and macroporous which may be fruitful for humidity sensing.

2.4.2 SEM analysis

The surface morphology of the synthesized GO and m-Graphene is shown in Fig. 2.3. The GO has flakes type surface as seen in Fig. 2.3 (a). This figure illustrates that there are many Graphene sheets after overlapping to each other forming the thick layer of

the GO. Fig. 2.3 (b) illustrates the SEM micrograph of m-Graphene. In this micrograph, Graphene sheets have different sizes and are oriented in various directions along with wrinkles. Some of the sheets are getting broken that is why we get the different sizes and shapes of the Graphene sheets. The breakage of the Graphene sheets produces dangling bonds and additional defects. Due to its wrinkled and defects nature, the m-Graphene does not agglomerate and collapse back. The wrinkles, defects and dangling bonds are responsible for the humidity sensing [44, 45].

2.4.3 EDX analysis

EDX analysis confirms the elemental mapping of the synthesized materials. EDX spectrum of the material is as shown in Fig. 2.4. The spectrum illustrates the existence of Carbon and Oxygen with 67 and 29.09 atomic% respectively along with extra elements Ca, Mn, K, Al, P and Si. These extra elements are present due to the glass substrate's constituent elements.

2.4.4 XRD analysis

The XRD pattern of the raw Graphite and synthesized m-Graphene have been shown in Fig. 2.5 (a) and (b) respectively. The raw Graphite shows a very sharp peak at the 2θ~26.65° and 54.57° having the Miller indices (002) and (004) respectively. In the XRD pattern of m-Graphene, the only peak (002) is observed at the 2θ value ~25.01°. The peak (002) in the XRD pattern of m-Graphene shows the broadening and shifting in the postion in the comparison of the raw Graphite. The broadening in the peaks confirms that the Graphite has been oxidized and oxygen species are getting attached to the

Graphitic layers. The shifting in the position and broadening of the peak (002) is the signature that the Graphite has been reduced into m-Graphene.

2.4.5 Dynamic Light Scattering (DLS) analysis

The particle size distribution of the nanomaterials is based on the Dynamic Light Scattering (DLS) technique. In this technique, the particle size is measured by the zig-zag motion of the particles in dilute solution with taking particles as spheres, results in the diameter size distributions [15]. In the case of the Graphene, the sheet size distribution is taken as considering the virtual sphere of diameter along with the thickness, length or breadth and diagonal. Fig. 2.6 illustrates the sheet size distribution of the m-Graphene. The peaks having intensity 16% (106-260 nm), 83% (294-1284 nm) and 2% (4792-6580 nm) are due to the sphere of the diameter along with the thickness, length or breadth and diagonal of the m-Graphene sheet. The average thickness, size in the plane and the diagonal of the Graphene sheet are 180 nm, 627 nm and 5560 nm respectively.

2.4.6 Optical absorption analysis

The optical property of the thin film of the synthesized material was studied by the incidence of the photon having an energy range 1.6-6.5 eV. The material shows maximum absorption of the wavelength range 190-250 nm which reflects the bandgap of material as shown in Fig.2.7. To determine the optical bandgap of the sheets we used the higher absorption range in which excitation of the electrons takes place from lower energy range (valence band) to the higher energy range (conduction band). The variation in the optical absorbance coefficient (α) with the change in corresponding photon energy ($h\upsilon$) is as shown in the Tauc plot inset of Fig.2.7. By extrapolating a tangent we obtained

the bandgap of the synthesized material as 4.6 eV. The wide bandgap is related to the reduction in the number of the graphitic layers and morphological effects of synthesized nanostructures along with the basics of quantum confinement effect which arises due to the small size of nanosheets in the thickness dimension. Such types of bandgaps are much useful for humidity sensing.

2.4.7 FTIR analysis

The FTIR spectrum of the m-Graphene was recorded in the wavenumber range 400-4000 cm^{-1} and the plot is shown in Fig.2.8. This figure illustrates that the absorption bands are obtained at wavenumbers 778, 1088, 1634, 2133 and 3307 cm^{-1} respectively. The valley present at 778, 1088, 1634, 2133 and 3307 cm^{-1} corresponds to -CH, -CO, -C=C, C≡C and –OH stretching vibrations respectively in the synthesized material [46]. The carbonyl, hydroxyl and unsaturated bonds present in the material and hydrophilic groups are responsible for humidity sensing. These bonds provide the medium for the charge carriers present between the sensing species and material of the sensing elements.

2.4.8 Raman analysis

The Raman spectroscopy is the primary characterization tool for differentiating among the carbon nanomaterials. The Raman spectrum of the Graphite and m-Graphene was recorded and plotted as shown in Fig. 2.9 (a) and (b) respectively. In Fig. 2.9 (a) there are two sharp peaks at 1329 and 1593 cm^{-1} Raman shifts, known as D and G-band respectively. The presence of the D-band in Graphite is related to its edge structure i.e. strong armchair and weak zig-zag edge structure. Fig. 2.9 (b) shows the Raman spectrum of m- Graphene consisting of the three bands present at 1326, 1589 and 2780 cm^{-1} Raman shifts are known as D-band, G-band and 2D-band respectively [47]. The D and G–bands

are getting broader and shorter as compared with D and G-bands of Graphite. The broader and shorter D and G-bands lead to an increase in the conductivity of the m-Graphene compared with the raw Graphite. The broadening, shortening and shifting in the position of D and G-bands along with an extra presence of the 2D band are the signatures of the reduction of Graphite into the m-Graphene [48, 49]. The I_D/I_G ratio was 1.55 for the m-Graphene and this is the signature of the synthesized material which has more defective nature as compared to graphitic nature [50]. The I_D/I_G ratio is inversely proportional to the crystalline nature of the materials that is why the m-Graphene has less crystallinity compare to defected nature. The crystallite size of m-Graphene in a plane was calculated using the Tuinstra−Koenig (T. K.) relation as shown by Eqn. 2.3 [51].

$$L_a(nm) = \frac{2.4 \times 10^{-10}\,\lambda^4}{I_D/I_G} \qquad (2.3)$$

Where λ (nm) is the Raman excitation wavelength, the calculated size of the m-Graphene was found as 10.81nm. So we can say that synthesized material has many defects along with dangling bonds which are responsible for humidity detection.

2.5 Humidity sensing application

BET analysis shows the mesoporous nature of the material along with 10.55 m^2/g surface area, SEM micrograph is of planar structure with wrinkles, defects, IR shows the presence of the hydrophilic groups and finally, Raman confirms that synthesized material consists the various defects with crystallite size 10.81 nm. Also, the material consists of dangling bonds and wrinkles. Based on these properties, it was inferred that m-Graphene may be a good humidity detecting material. The measurement of the humidity is not only

beneficial for living beings but also non-living bodies. The Graphene-based sensors give different sensing attributes at different frequencies.

2.5.1 Fabrication of sensing element

A glass substrate of the dimension 1.0 × 0.5 cm^2 was prepared and washed with DI water and acetone followed by sonication for 0.5 h for removing the contaminations associated with it. The sensing element was fabricated with the help of a spin coating technique. In a typical procedure, the thin film of the synthesized m-Graphene was deposited on the silica glass substrate at 1500 RPM and was dried at 50 °C on a hot plate for 0.5 h. Thin-film was annealed at 400 °C for 2 h in the presence of 20% oxygen. Finally, the electrodes on the film were deposited at 25 cm from each side using the silver paste.

2.5.2 Principle of operation

The humidity sensing mechanism of the Graphene-based sensors relies on the charge transfer. The detailed schematic of the Grotthuss chain mechanism is as shown in Fig. 2. 10. In the starting, the dissociation of the water molecules takes place into the H^+ and OH^- ions as shown in Eqn. 2.4. Due to hydrophilic groups present in the synthesized material observed by IR, the OH^- ions are adsorbed to the m-Graphene surface and get chemically bonded with it and the H^+ ion becomes mobile and triggering a drop in the resistance of m-Graphene. This step results in the chemisorbed layer and is known as the chemisorption.

$$H_2O \rightarrow H^+ + OH^- \qquad (2.4)$$

As the relative humidity increases, the hydrogen bonding between the two neighboring hydroxyl groups with each water molecule takes place and forming the first

physisorbed layer. This is known as physisorption and shown by Eqn. 2.5. Again the as relative humidity increases the water molecules become adsorbed to the first physisorbed layer and so forming the second physisorbed layer. Further, as the %RH increases, the formation of the many such physisorbed layers takes place and acting identical to bulk liquid water.

$$2H_2O \rightarrow H_3O^+ + OH^- \quad (2.5)$$

$$H_3O^+ \rightarrow H_2O + H^+ \quad (2.6)$$

In such a way Grotthuss chain reaction mechanism follows that each water molecules combine with each OH^- ions resulting H_3O^+ which further dissociates into the H_2O and H^+ ions shown by Eqn. 2.6. This results in a sudden increase in the mobile H^+ ions and a decrease in the impedance. Lastly, the increment in the relative humidity causes the condensation of water into the m-Graphene film which results in a decrease in impedance [14].

2.5.3 Sensing attributes of the m-Graphene

The sensitivity of the humidity sensor is defined by Eqn. 2.7.

$$Sensitivity = \frac{|Z_1 - Z_2|}{RH_1 - RH_2} \quad (2.7)$$

Where RH_1 and RH_2 are the maximum and minimum values of the %RH and corresponding to these, impedances are Z_1 and Z_2 respectively. The response and recovery time of humidity sensors are defined as the time taken to reach 10% of the final sensor output during the increasing and the decreasing %RH respectively [52]. The hysteresis (H) of the sensor is defined by Eqn. 2.8.

$$H = \frac{Z_D - Z_A}{Sensitivity} \quad (2.8)$$

Where Z_A and Z_D are the measured impedances at a fixed %RH during the adsorption and desorption process [53].

All the data were recorded with the help of a humidity sensor characterization setup which is shown in Fig. 2. 11. This figure consists of a humidity-controlled glass chamber, circuit component analyzer (i.e. impedance analyzer) and connecting wires. The saturated solutions of the K_2SO_4 and KOH were used to humidify and dehumidify the humidity-controlled glass chamber respectively and the humidity within it is measured by a hygrometer. Changes in the impedance with the variation in the %RH (increasing and decreasing both modes) have been recorded at constant 10 kHz, 1 kHz and 100 Hz frequencies of the impedance analyzer. All the recorded readings have been shown in Table 2.2. The graphs between impedance versus %RH at constant 10 kHz, 1 kHz and 100 Hz frequencies are shown in Fig. 2.12 (a), (b) and (c) respectively. At different frequencies, the sensing graphs can be explained as considering the thin film consisting of an equivalent parallel C-R circuit. The impedance of the equivalent parallel C-R circuit is given by Eqn. 2.9.

$$Z = 1/\sqrt{(\omega C)^2 + 1/(R)^2} \qquad (2.9)$$

This depends upon the capacitive reactance ($1/\omega C$) and resistance (R). The capacitive reactance (i.e. $1/\omega C = 1/2\pi X$, f is the frequency and C is capacitance) is inversely proportional to the frequency. At room temperature, there are no adsorbed water molecules and the resistance of the sensing element is high ($1/R << \omega C$) so that impedance is inversely proportional to the frequency and capacitance. So, changes in the impedance of the sensing element can be explained based on the frequency and the capacitance [54, 23, 36]. The curves show the highest change in the impedance at lower

frequency while at higher frequency the change in the impedance is lower. The capacitive reactance offered by film is higher at lower frequency (100 Hz) that is why the change in impedance (226 MΩ – 155 kΩ) is higher with the change in %RH shown in Fig. 2.12 (c) and the inset is showing the variations in impedance with change in %RH from 60 to 100. As the value of the frequency increases (1 kHz), the change in the capacitive reactance decreases and impedance has changed from 29 MΩ to 61 kΩ as shown in Fig. 2.12 (b). The inset of this figure is showing the variations in impedance with change in %RH from 70 to 100. Fig. 2.12 (a) illustrates that if we again increase the value of the frequency upto10 kHz, the change in the impedance are observed lowest, varied from 3.54 MΩ to 76 kΩ.

The impedance is inversely proportional to the capacitance so an increase in capacitance causes the decrease in the impedance. Water is a polar molecule and polarizes into H^+ and OH^- ions. The dielectric constant is directly proportional to polarizability. Capacitance depends upon the dielectric constant. The value of the capacitance increases with the rising %RH [37, 40]. At the lower humidity, polarizability is low, the charge carrier concentration is low, the value of the dielectric constant is low leading the lower capacitance therefore the impedance is higher. As the adsorption of water molecules increases, value of the dielectric constant increases, resulting in the higher value of the capacitance, this results in lower impedances. The sensitivity was calculated with the help of Eqn. 2.4 at different frequencies is depicted in Table 2.3. With the observation of the Fig. 2.12 (a), (b) and (c) we can conclude that at 100 Hz frequency the hysteresis loop is less as compared to two other frequencies and also the Table 2.3 illustrates that the sensitivity of the sensor at the constant 100 Hz frequency results the

best sensitivity. Therefore, the whole experiment was performed at this constant frequency.

The response and recovery time are important parameters of the sensors, having low value demonstrating good sensor. The noted data of the time along with variation in impedance as per increasing and decreasing humidity has been illustrated in Table 2.4. Repeatability and the long term stability of the sensor describe the performance of the sensors. The sensors should have very much repeatability. The data recorded for repeatability and aging are shown in Table 2.5. Figs. 2.13 (a), (b) and (c) illustrate the response- recovery curve, repeatability and long-term stability (ageing effect) of the m-Graphene-based humidity sensor respectively at room temperature. It was found that the sensor has a response, recovery time and repeatability as 24, 13 s and 96.05% respectively along with the negligible ageing effect. Hysteresis is an important parameter for sensing device fabrication. The m-Graphene based sensor hysteresis was calculated using Eqn. 2.8 and has found the maximum hysteresis of 6 %RH during the adsorption and desorption at 40 %RH.

2.6 Conclusion

Using the wet chemical method m-Graphene was successfully synthesized. BET analysis confirmed the synthesis of meso and macro porous material having a surface area 10.55 m^2/g along with the pore size distribution ranging from 10.34 to 97.44 nm, which is the more important for humidity sensing. The SEM, EDX and particle size analysis concluded that synthesized material is the carbon-based sheet structured nanomaterial. The confirmation of m-Graphene was carried out using the IR and Raman

analysis. The m-Graphene was found much defected (I_D/I_G = 1.55) along with more dangling bonds which were proven beneficial for the humidity detection. The crystallite size of m-Graphene was found as 10.81 nm. The humidity sensing for frequency optimization purposes was performed at different frequencies e.g. 100 Hz, 1 kHz, and 10 kHz. The m-Graphene based humidity sensor exhibited the maximum sensitivity as 2.51 MΩ/%RH at an optimized 100 Hz frequency. The other sensing attributes as repeatability, response and recovery time were found as 96.05%, 24 and 13 s respectively.

References

[1] M. A. Almessiere, Y. Slimani, H. Güngüne¸ A. Baykal, S. V. Trukhanov, A. V. Trukhanov, Manganese/yttrium co-doped strontium nanohexaferrites: Evaluation of magnetic susceptibility and Mossbauer spectra, Nanomat. 9 (1) (2019) 1-18

[2] A. V. Trukhanov, M. A. Almessiere, A. Baykal, S. V. Trukhanov, Y. Slimani, D. A. Vinnik, V.E. Zhivulin, A. Yu. Starikov, D. S. Klygach, M. G. Vakhitov, T. I. Zubar, D. I. Tishkevich, E. L. Trukhanova, M. Zdorovetset, Influence of the charge ordering and quantum effects in heterovalent substituted hexaferrite on their microwave characteristics, J. Alloys Compd. 788, (2019) 1193-1202

[3] M. A. Almessiere, Alex V. Trukhanov, Yassine Slimani, K. Y. You, Sergei V. Trukhanov, Ekaterina L. Trukhanova, F. Esa, A. Sadaqati, K. Chaudhary, Maxim Zdorovets, Abdulhadi Baykal, Correlation between composition and electrodynamics properties in nanocomposites based on hard/soft ferrimagnetic with strong exchange coupling, Nanomat. 9(2), (2019) 1-13

[4] D. A. Vinnik, V. E. Zhivulin, A.Yu. Starikov, S. A. Gudkova, E. A. Trofimov, A. V. Trukhanov, S. V. Trukhanov, V. A. Turchenko, V. V. Matveev, E. Lahderanta, E. Fadeev, T. I. Zubar, M. V. Zdorovets, A. L. Kozlovsky, Influence of titanium substitution on structure, magnetic and electric properties of barium hexaferrite $BaFe_{12-x}Ti_xO19$, J. Magn. Magn. Mater. 498, (2020) 1-25

[5] T. Mahmoudi, Y. Wang, Y. B. Hahn, Graphene and its derivatives for solar cells application, Nano Energy 47, (2018) 51-65

[6] V. I. Popov, D. V. Nikolaev, V. B. Timofeev, S. A. Smagulova and I. V. Antonova, Graphene-based humidity sensors: the origin of alternating resistance change, Nanotechnology 28 (355501) (2017) 1-10

[7] B. C. Yadav, A. Yadav, T. Shukla, S. Singh, Experimental investigations on solid-state conductivity of cobaltzincate nanocomposite for liquefied petroleum gas sensing, Sensor Letters 7 (6), (2009) 1119-1123

[8] B. C. Yadav, R. C. Yadav, S. Singh, P. K. Dwivedi, H. Ryu, S. Kang, Nanostructured cobalt oxide and cobalt titanate thin films as optical humidity sensor: a new approach, Optics & Laser Techno. 49, (2013) 68-74

[9] B. C. Yadav, R. Srivastava, C. D. Dwivedi, P. Pramanik, Synthesis of nano-sized ZnO using dropwise method and its performance as a moisture sensor, Sensors & Actuators A: Phys.153 (2), (2009) 137-141

[10] S. Singh, A. Bhaduri, R. K. Tripathi, K. B. Thapa, R. Kumar, B. C. Yadav, Improved sensing behavior of self-healable solar light photodetector based on core-shell type $Ni_{0.2}Zn_{0.8}Fe_2O_4$@ poly (Urea-Formaldehyde), Solar Energy 188, (2019) 278-290

[11] C. Lv, C. Hu, J. Luo, S. Liu, Y. Qiao, Z. Zhang, J. Song, Y. Shi, J. Cai, A. Watanabe, Recent Advances in Graphene-Based Humidity Sensors, Nanomaterials 9 (2019) 1-42

[12] H. Farahani, R. Wagiran and M. N. Hamidon, Humidity Sensors Principle, Mechanism, and Fabrication Technologies: A Comprehensive Review, Sensors 14 (2014) 7881-7939

[13] W. D. Lin, H.- M. Changa, R. J. Wua, Applied novel sensing material graphene/polypyrrole for humidity sensor, Sensors and Actuators B 181 (2013) 326– 331

[14] B. Chethan, H. G. Raj Prakash, Y. T. Ravikiran, S. C. Vijayakumari, CH. V. V. Ramana, S. Thomas and Daewon Kim, Enhancing Humidity Sensing Performance of Polyaniline/Water Soluble Graphene Oxide Composite, Talanta 196, (2019) 337-344

[15] U. Kumar, B. C. Yadav, Development of humidity sensor using modified curved MWCNT based thin film with DFT calculations, Sensors and Actuators B: Chemical 288, (2019) 399-407

[16] U. Kumar, B. C. Yadav, Synthesis of carbon nanotubes by direct liquid injection chemical vapor deposition method and its relevance for developing an ultra-sensitive room temperature based CO_2 sensor, Journal of the Taiwan Institute of Chemical Engineers 96, (2019) 652-663

[17] K. Kumar and B. C. Yadav, An Overview on the Importance of Chemical Vapour Deposition Technique for Graphene Synthesis, Adv. Sci. Eng. Med., 10 (2018) 760–763

[18] O. S. Yakovenko, L.Yu. Matsui, L. L. Vovchenko, A. V. Trukhanov, I. S. Kazakevich, S. V. Trukhanov, Y. I. Prelutsky, U. Ritter, Magnetic anisotropy of the graphite nanoplatelet–epoxy and MWCNT–epoxy composites with aligned barium ferrite filler, J. Mat. Sci. 52 (2017) 5345-5358

[19] O. S. Yakovenko, L.Yu. Matzui, L. L. Vovchenko, O. V. Lozitsky, O. I. Prokopov, O. A. Lazarenko, A. V. Zhuravkov, V. V. Oliynyk, V. L. Launets, S.

V. Trukhanov & A.V. Trukhanov, Electrophysical properties of epoxy-based composites with graphite nanoplatelets and magnetically aligned magnetite, Molecular Crystals and Liquid Crystals 661 (2018) 68-80

[20] L.Yu. Matsui, Alex V. Trukhanov, Olena S. Yakovenko, Ludmila L. Vovchenko, Volodymyr V. Zagorodnii, Victor V. Oliynyk, Mykola O. Borovoy, Ekaterina L. Trukhanova, Ksenia A. Astapovich, Dmitry V. Karpinsky and Sergei V. Trukhanov, Functional magnetic composites based on hexaferrite: Correlation of the composition, magnetic and high-frequency properties, Nanomat. 9(12) (2019) 1-17

[21] E. Llobet, Gas sensors using carbon nanomaterials: A review, Sensors and Actuators B: Chemical 179 (2013) 32-45

[22] Z. Chen and C. Lu, Humidity Sensors: A Review of Materials and Mechanisms, Sensor Letters 3 (2005) 274–295

[23] S. Basu, P. Bhattacharyya, Recent developments on graphene and graphene oxide-based solid-state gas sensors, Sensors and Actuators B 173 (2012) 1– 21

[24] S. Borini, R. White, D. Wei, M. Astley, S. Haque, E. Spigone, N. Harris, J. Kivioja, and T. Ryhanen, Ultrafast Graphene Oxide Humidity Sensors, ACS nano, 7 (12) (2013) 11166–11173

[25] Z. B. Aziza, K. Zhang, D. Baillargeat and Q. Zhang, Enhancement of humidity sensitivity of graphene through functionalization with polyethyleneimine, Applied Physics Letters 107 (2015) 1-7

[26] S. Park, R. S. Ruoff, Chemical methods for the production of graphenes, Nature Nanotechnol. 4(4), (2009) 217-224

[27] H. Kim, A. A. Abdala, C. W. Macosko, Graphene/polymer nanocomposites, Macromolecules 43(16), (2010) 6515-6530

[28] C. N. R. Rao, A. K. Sood, K. S. Subrahmanyam, and A. Govindaraj, Graphene: The New Two-Dimensional Nanomaterial, Angew. Chem. Int. Ed. 48 (2009) 7752 – 7777

[29] H. J. Jeong, Synthesis and Dispersion of Chemically Exfoliated Graphene Nanosheets, AAPPS Bulletin 25(5) (2015) 24-28

[30] T. F. Emiru, D. W. Ayele, Controlled synthesis, characterization and reduction of graphene oxide: A convenient method for large scale production, Egyptian Journal of Basic and Applied Sciences 4 (2017) 74–79

[31] Y. Su, C. Li, M. Li, H. Li, S. Xu, L. Qian, B. Yang, Surface acoustic wave humidity sensor based on three-dimensional architecture graphene/PVA/SiO_2 and its application for respiration monitoring, Sensors & Actuators B. Chemical, 308, (2020) 1-11

[32] H. J. Kim, H. Y. Shin, C. H. Pyeon, S. Kim, B. Lee, Fiber-optic humidity sensor system for the monitoring and detection of coolant leakage in nuclear power plants, Nuclear Engineering and Technology 52 (2020) 1689-1696

[33] Y. Yao, X. Huang, B.-Y. Zhang, Z. Zhang, D. Hou, Z.-K. Zhou, Facile fabrication of high sensitivity cellulose nanocrystals based QCM humidity sensors with asymmetric electrode structure, Sensors & Actuators: B. Chemical 302, (2020) 1-9

[34] H. Saleem, M. Haneef, H. Y. Abbasi, Synthesis route of reduced graphene oxide via thermal reduction of chemically exfoliated graphene oxide, Materials Chemistry and Physics 204 (2018) 1-7

[35] S. Kotresh, Y. T. Ravikiran, H. G. Rajprakash, S. C. Vijayakumari, Polyaniline-Titanium dioxide composite as humidity sensor at room temperature, Nanosyst. Physics, Chem. Math. 7 (2016) 732–739.

[36] W. D. Lin, C. T. Liao, T. C. Chang, S. H. Chen, R. .J. Wu, Humidity sensing properties of novel Graphene/TiO_2 composites by sol-gel process, Sens. Actuators B 209 (2015) 555–561

[37] H. C. Bi, K. B. Yin, X. Xie, J. Ji, S. Wan, L. T. Sun, M. Terrones, M. S. Dresselhaus, Ultrahigh humidity sensitivity of graphene oxide, Sci. Rep. 3 (2013) 2714–2720.

[38] Y. Bai, C. Z. Zhang, B. Chen, H. Sun, Enhanced humidity sensing of functionalized reduced graphene oxide with 4-chloro-3-sulfophenylazo groups, Sensors & Actuators: B. Chemical 287 (2019) 258–266

[39] D. Z. Zhang, J. Tong, B. K. Xia, Humidity-sensing properties of chemically reduced graphene oxide/polymer nanocomposite film sensor based on layer-by-layer nano self-assembly, Sens. Actuators B: Chem.197 (2014) 66-72

[40] K. Kumar, U. Kumar, M. Singh, B. C. Yadav, Synthesis and characterizations of exohedral functionalized graphene oxide with iron nanoparticles for humidity detection, Journal of Materials Science: Materials in Electronics, 30(14) (2019) 13013-1302

[41] D. C. Marcano, Improved Synthesis of Graphene Oxide, ACS Nano, 4(8) (2010) 4806–4814

[42] M. Sohail, M. Saleem, S. Ullah, N. Saeed, A. Afridi, M. Khan, Modified and improved Hummer's synthesis of graphene oxide for capacitors applications, Mod. Electron. Mater. 3 (2017) 110–116

[43] O. Akhavan, The effect of heat treatment on the formation of graphene thin films from graphene oxide nanosheets, Carbon, 48(2), (2010) 509-519

[44] S. J. Choi, H. Yu, J. S. Jang, M. H. Kim, S. J. Kim, H. S. Jeong, I. D. Kim, Nitrogen-doped single graphene fiber with platinum water dissociation catalyst for the wearable humidity sensor, Small, 14(13) (2018) 1-9

[45] Z. Zhen, Z. Li, X. Zhao, Y. Zhong, L. Zhang, Q. Chen, T. Yang, and H. Zhu, Formation of uniform water microdroplets on wrinkled graphene for ultrafast humidity sensing, Small, 14(15) (2018) 1-8

[46] A. C. S. Talari, M. A. G. Martinez, Z. Movasaghi, S. Rehman, I. U. Rehman, Advances in Fourier transform infrared (FTIR) spectroscopy of biological tissues, Appl. Spectrosc. Rev. **52**(5) (2017) 456–506

[47] A. C. Ferrari, J. C. Meyer, V. Scardaci, C. Casiraghi, M. Lazzeri, F. Mauri, S. Piscanec, D. Jiang, K. S. Novoselov, S. Roth, and A. K. Geim, Raman spectrum of graphene and graphene layers, PRL, 97(18), (2006) 1-4

[48] A. C. Ferrari, Raman spectroscopy of graphene and graphite: Disorder, electron-phonon coupling, doping and nonadiabatic effects, Solid State Communications 143, (2007) 47-57

[49] V. B. Mohan, M. Nieuwoudt, K. Jayaraman, and D. Bhattacharyya, Quantification and analysis of Raman spectra of graphene materials, Graphene Technology 2, (2017) 47-62

[50] H. Wang, Z. Maiyalagan, X. Wang, Review on recent progress in nitrogen-doped graphene: synthesis, characterization, and its potential applications, ACS Catal. 2(5), (2012) 781-794

[51] L. G. Cancado, K. Takai, and T. Enok, M. Endo, Y. A. Kim, and H. Mizusaki, A. Jorio, L. N. Coelho, R. Magalhães-Paniago, and M. A. Pimenta, General equation for the determination of the crystallite size L a of nano graphite by Raman spectroscopy, Applied Physics Letters 88(16), (2006) 1-3

[52] S. Sikarwar, B. C. Yadav, Opto-electronic humidity sensor: A review, Sensors & Actuators A: Phys 233, (2015) 54-70

[53] M.-Q. Liu, C. Wang and N.-Y. Kim, High-sensitivity and low-hysteresis porous MIM-type capacitive humidity sensor using functional polymer mixed with TiO_2 microparticles, Sensors 17(2), (2017) 1-11

[54] D. Zhang, X. Zong and Z. Wu, Fabrication of tin disulfide/graphene oxide nanoflower on a flexible substrate for ultrasensitive humidity sensing with ultralow hysteresis and good reversibility, Sensors and Actuators B: Chemical 287, (2019) 398-407

Figures

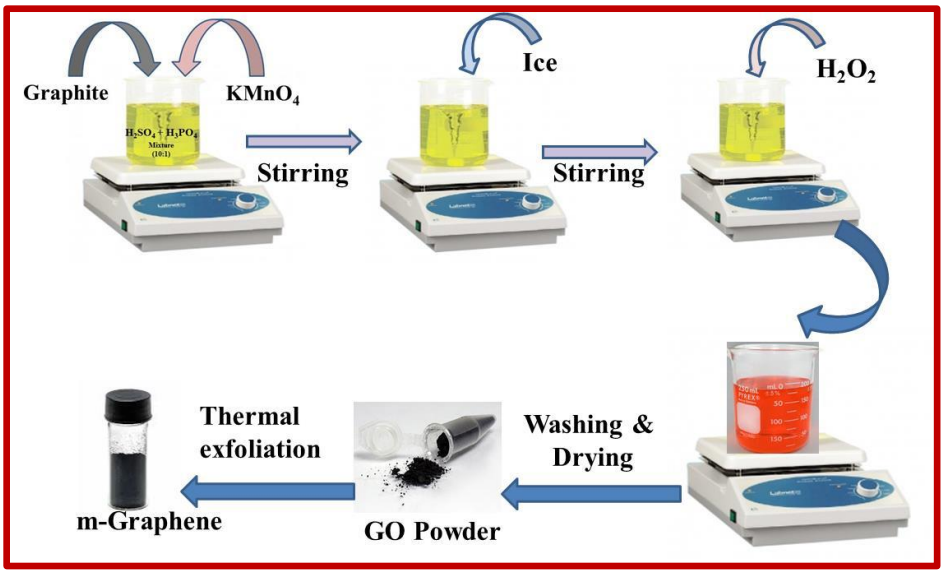

Fig. 2.1 Schematic showing the synthesis process of m-Graphene

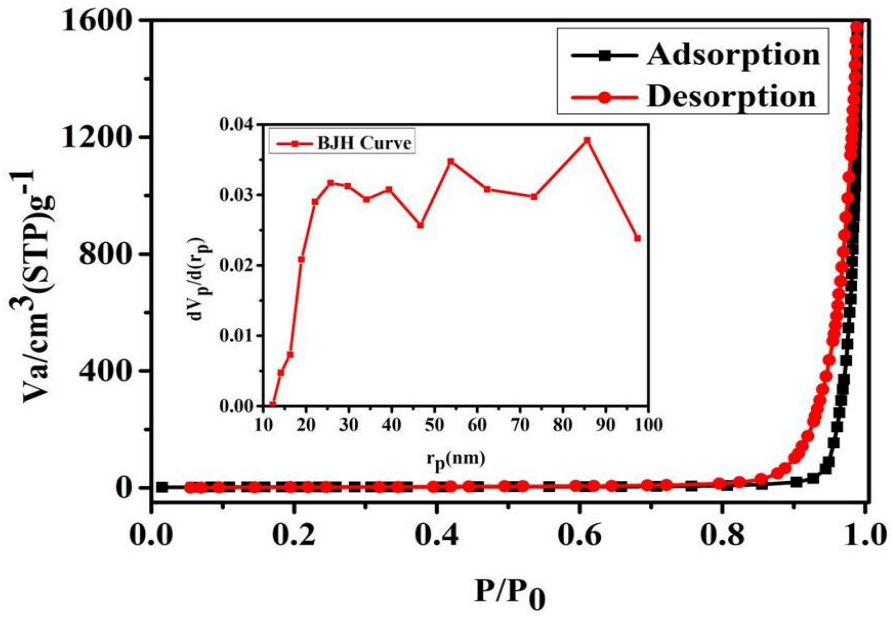

Fig. 2.2 Nitrogen adsorption and desorption isotherm of the m-Graphene along with inset pore size distribution curve

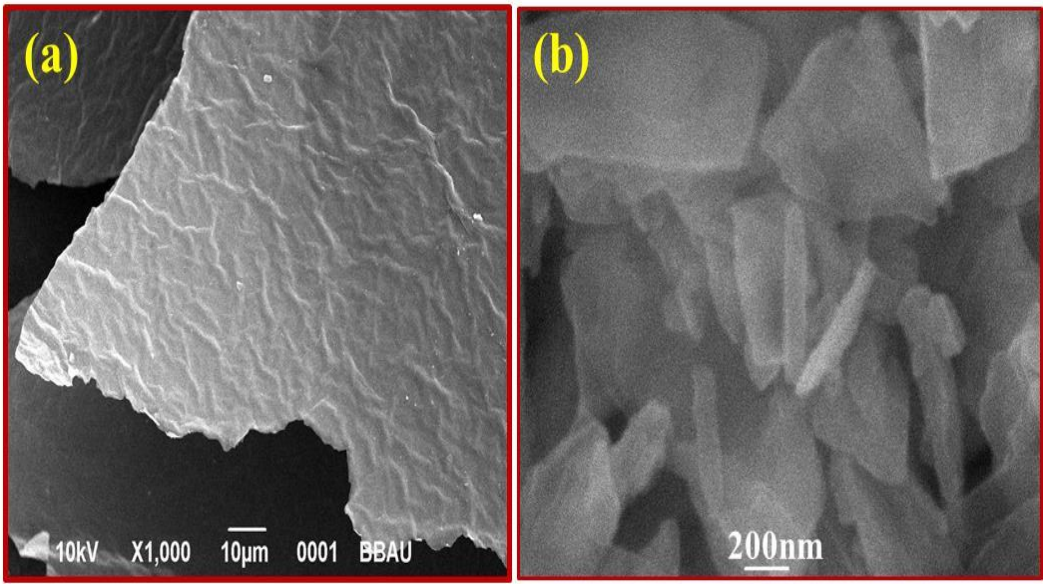

Fig. 2.3 SEM micrographs of (a) GO (b) m-Graphene

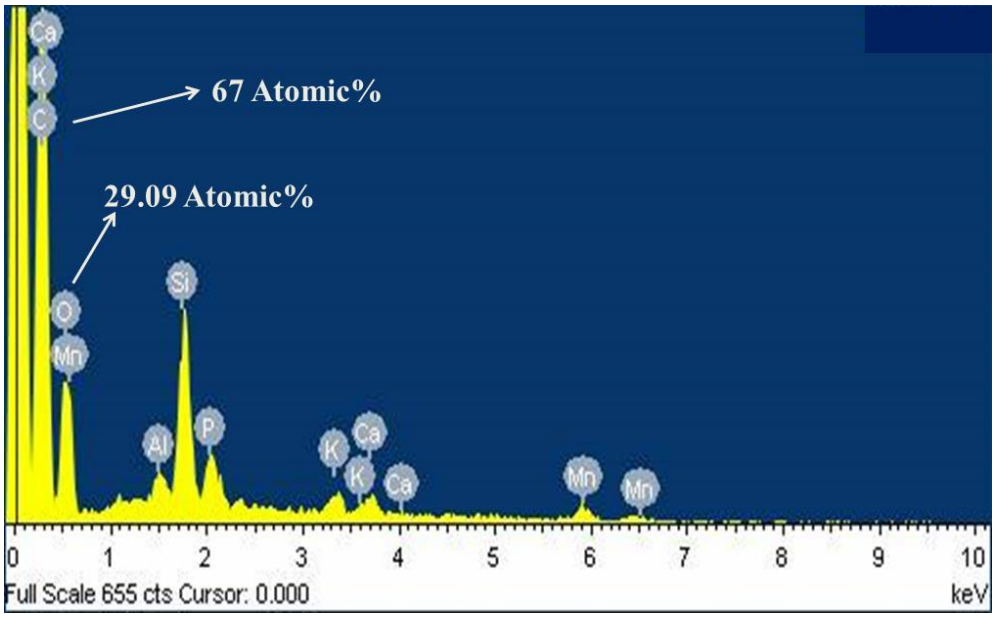

Fig. 2.4 Elemental mapping of the synthesized m-Graphene

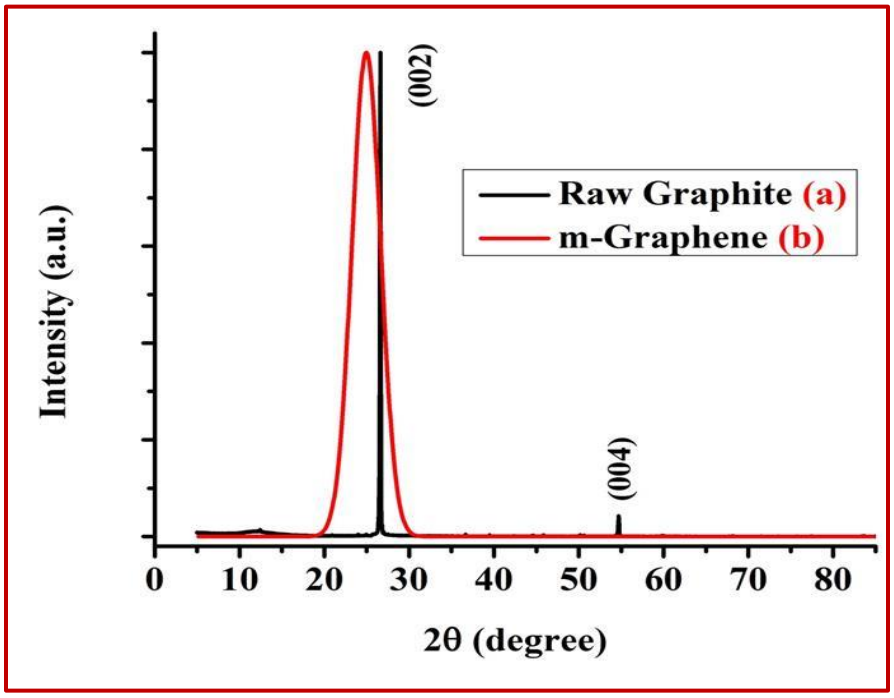

Fig. 2.5 XRD pattern of the raw Graphite and m-Graphene

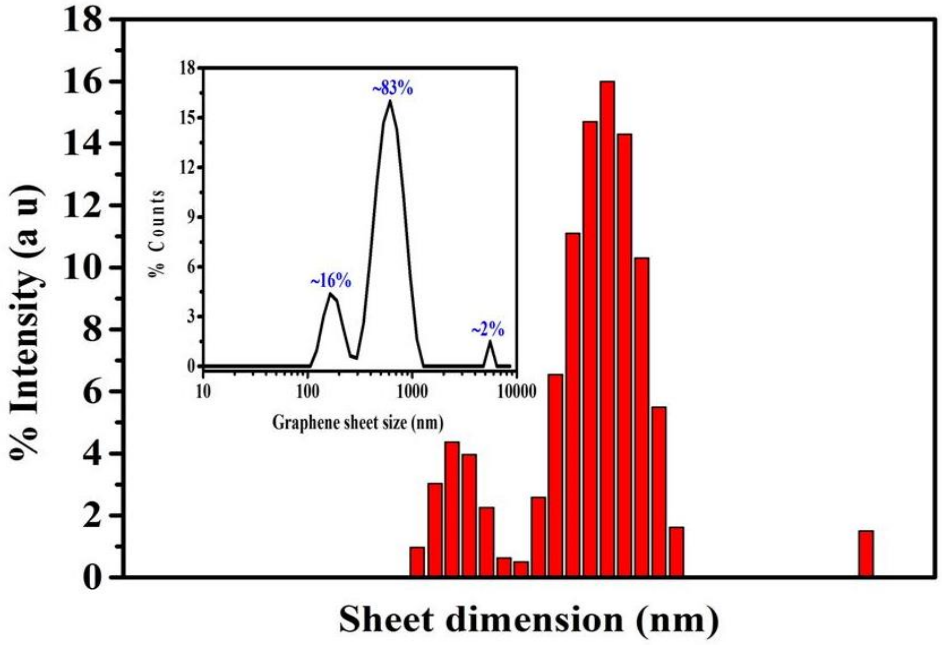

Fig. 2.6 Sheet size distributions of m-Graphene

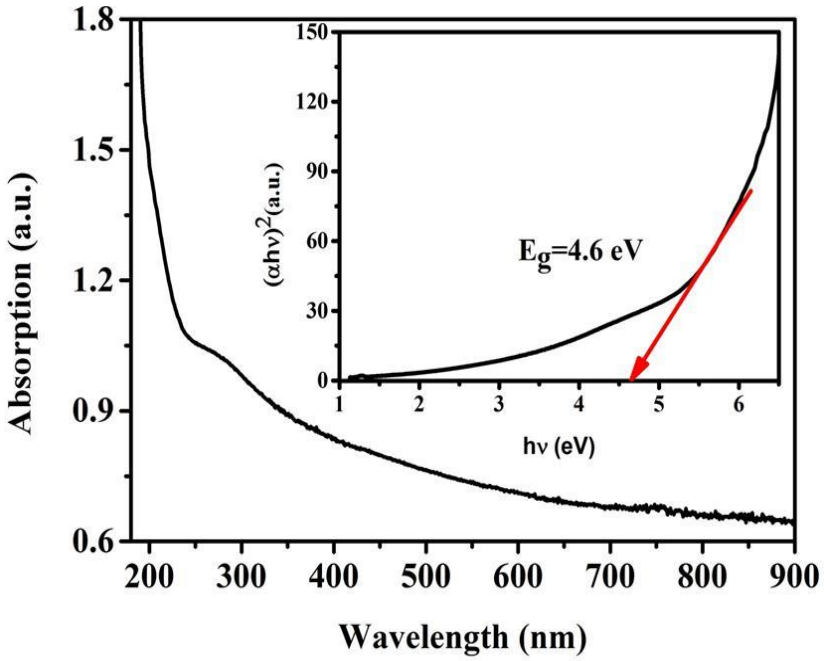

Fig. 2.7 Absorption spectra of m-Graphene and Insitu Tauc plot.

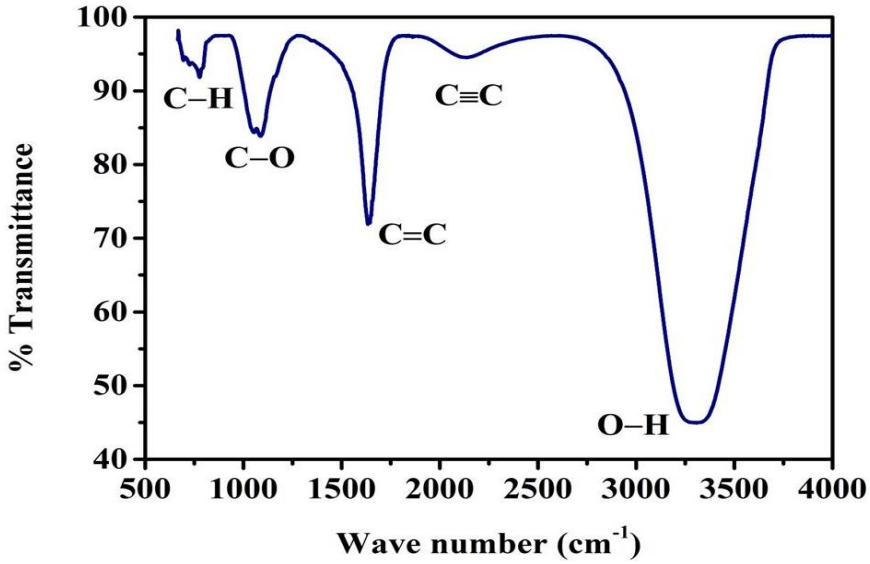

Fig. 2.8 FTIR spectrum of the m-Graphene

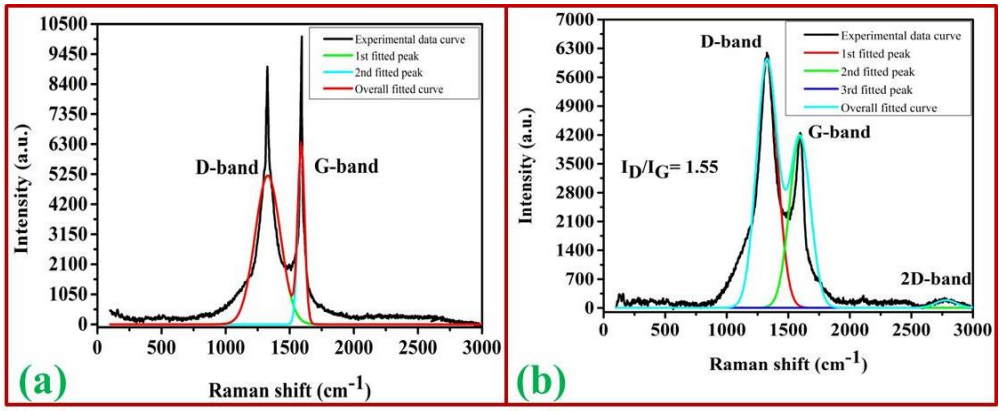

Fig. **2.9** Raman spectrum of the (a) raw Graphite and (b) m-Graphene

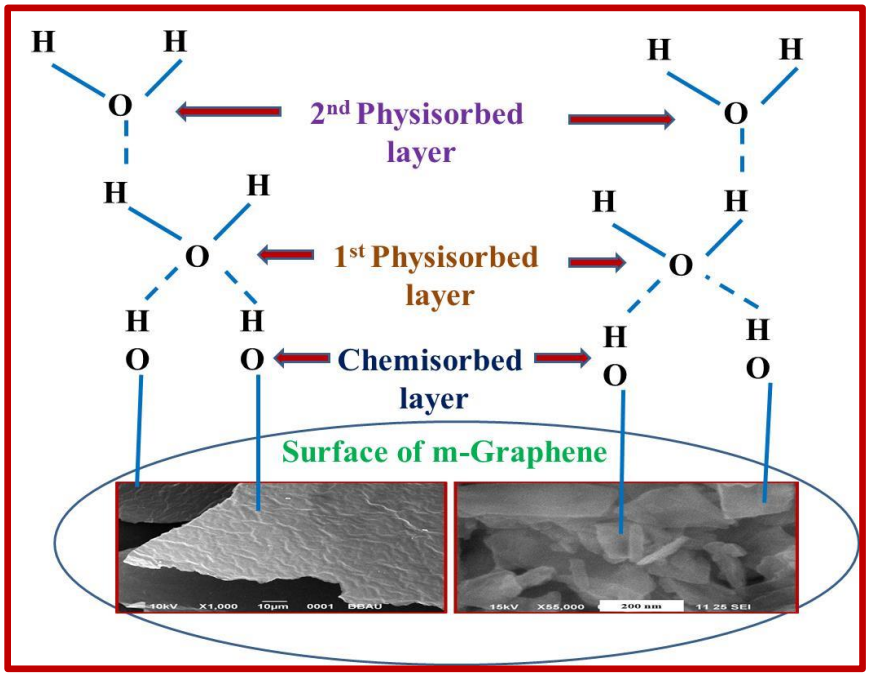

Fig. 2.10 Schematic representing the Grotthuss chain mechanism on the m-Graphene based humidity sensor

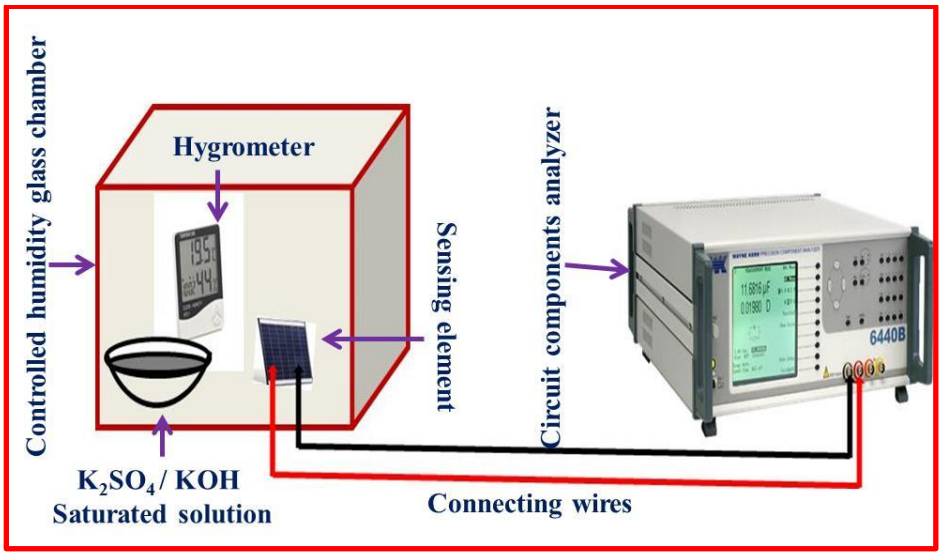

Fig. 2.11 Lab made humidity sensor characterization setup

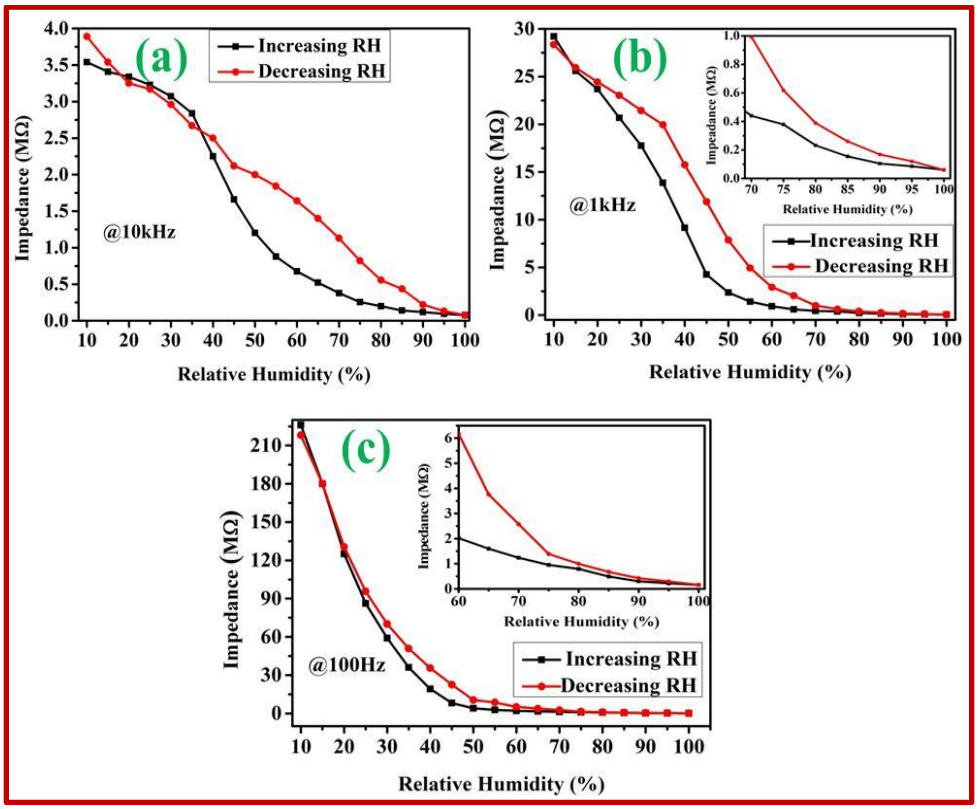

Fig. 2.12 Sensitivity curves of the m-Graphene at (a) 10 kHz, (b) 1 kHz and (c) 100 Hz

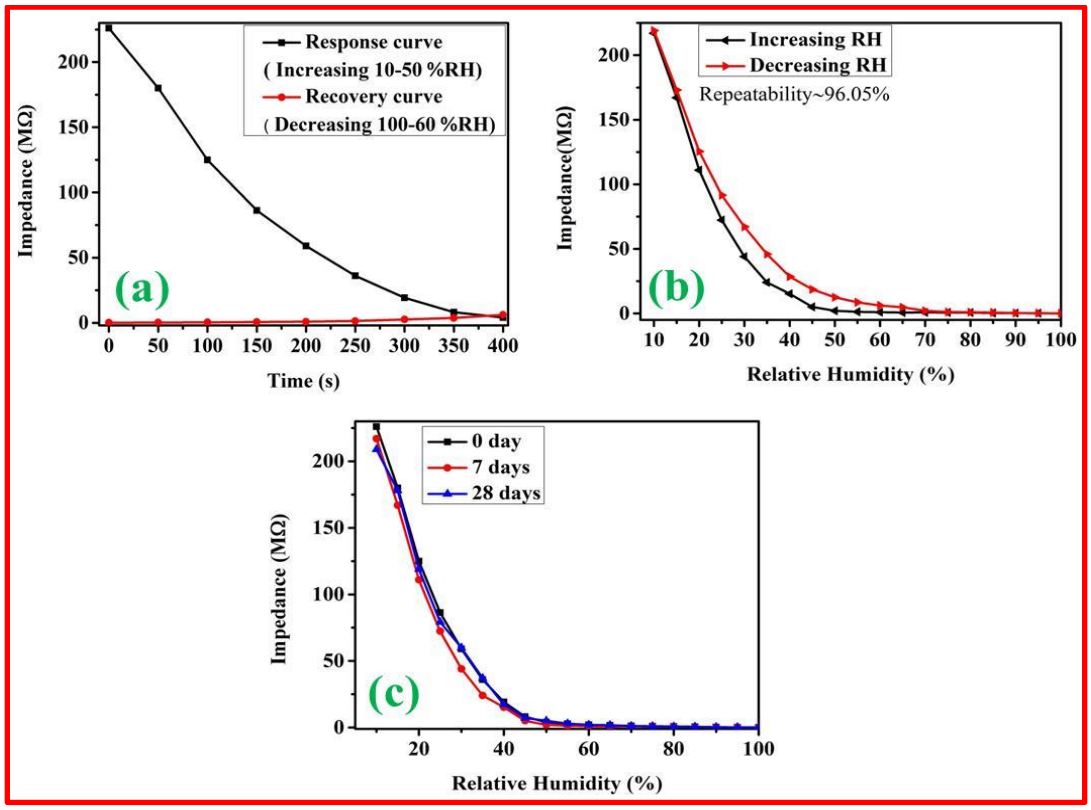

Fig. 2.13 m-Graphene based sensor showing (a) response and recovery curve (b) repeatability and (c) long term stability curve

Tables

S. No.	Materials	Working range	Sensitivity/Sensing response	Response time (s)	Recovery time (s)	References
1	Graphene/polypyrrole	12-90	138/---	15	20	13
2	PANI/ TiO_2	25-95	---/84.21 %	60	100	35
3	Graphene/ TiO_2	12-90	---/151	128	68	36
4	Graphene oxide	23-86	37800% /---	10.5	41	37
5	rGO-SC	11-95	---/2961.39	1.3	23.5	38
6	Modified MWCNT	10-90	0.644 MΩ/%RH---	32	36	15
7	PDDA/rGO	11-97	---/8.69-37.43%	108-147	94-133	39
8	Fe-GO	10-95	5.18 pF/%RH/---	31	11	40
9	**m-Graphene**	**10-99**	**2.51** MΩ/%RH/---	**28**	**13**	**Present Work**

Table 2.1 Literature survey of the Graphene-based humidity sensors

%RH	Impedance (MΩ)					
	100 Hz		1 kHz		10 kHz	
	Increasing mode	Decreasing mode	Increasing mode	Decreasing mode	Increasing mode	Decreasing mode
10	226.00	218.00	29.21	28.35	3.54	3.89
15	180.00	180.00	25.60	25.94	3.41	3.54
20	125.00	130.50	23.69	24.44	3.34	3.25
25	86.30	95.60	20.68	23.03	3.23	3.17
30	59.03	70.15	17.76	21.45	3.07	2.96
35	36.06	50.89	13.87	19.95	2.84	2.67
40	19.23	35.54	9.16	15.75	2.25	2.50
45	8.12	22.62	4.25	11.88	1.66	2.12
50	4.03	10.52	2.36	7.86	1.20	2.00
55	2.84	8.66	1.42	4.94	0.88	1.84
60	2.02	5.17	0.92	2.92	0.68	1.64
65	1.60	3.76	0.605	2.03	0.522	1.40
70	1.24	2.58	0.44	0.99	0.38	1.13
75	0.95	1.39	0.38	0.62	0.26	0.82
80	0.79	0.99	0.23	0.39	0.20	0.56
85	0.49	0.68	0.16	0.26	0.14	0.44
90	0.30	0.42	0.11	0.17	0.12	0.22
95	0.22	0.29	0.09	0.12	0.10	0.13
100	0.16	0.16	0.06	0.06	0.08	0.076

Table 2.2 Variation in the impedance as per increasing and decreasing humidity at 100 Hz, 1 kHz, and 10 kHz frequencies respectively

Serial Number	Constant frequency	Sensitivity
1.	100 Hz	2.51 MΩ/%RH
2.	1 kHz	0.321 MΩ/%RH
3.	10 kHz	0.0384 MΩ/%RH

Table 2.3 Depiction of the sensitivity of sensor at constant frequencies 100 Hz, 1 kHz and 10 kHz

	Impedance (MΩ)	
Time (s)	**Response (10-50 %RH)**	**Recovery (100-60 %RH)**
0	226.00	0.16
50	180.00	0.29
100	125.00	0.42
150	86.30	0.68
200	59.03	0.89
250	36.06	1.39
300	19.23	2.58
350	8.12	3.76

Table 2.4 Time measured along with variation in the impedance as per increasing humidity (10-50 %RH) and decreasing humidity (100-60 %RH) at 100 Hz frequency

%RH	Impedance (MΩ)				
	Repeatability		Ageing effect		
	Increasing mode	Decreasing mode	After 0 days	After 7days	After 28 days
10	217.00	219.00	226.00	217.00	209.00
15	167.00	173.00	180.00	167.00	178.00
20	111.00	125.50	125.00	111.00	119.00
25	72.30	91.60	86.30	72.30	79.30
30	44.03	67.15	59.03	44.03	60.03
35	24.06	45.89	36.06	24.06	37.08
40	15.23	28.54	19.23	15.23	17.23
45	5.12	18.62	8.12	5.12	7.21
50	2.03	12.52	4.03	2.03	5.03
55	1.34	8.66	2.84	1.34	2.97
60	1.00	6.17	2.02	1.00	1.99
65	0.67	4.76	1.60	0.67	1.68
70	0.84	2.08	1.24	0.84	1.04
75	0.75	1.11	0.95	0.75	0.98
80	0.69	0.98	0.79	0.69	0.70
85	0.39	0.77	0.49	0.39	0.50
90	0.29	0.34	0.30	0.29	0.27
95	0.20	0.22	0.22	0.20	0.11
100	0.12	0.11	0.16	0.12	0.13

Table 2.5 Recorded data of repeatability and aging effect after 0, 7 and 28 days

CHAPTER 3

FABRICATION OF HUMIDITY SENSOR BASED ON THIN FILM OF GRAPHENE OXIDE FUNCTIONALIZED WITH IRON OXIDE NANOPARTICLES

This chapter reports the characterizations and humidity sensing properties of Fe-GO. Thin films of GO and Fe-GO have been made by using the spin coating technique at 1500 rpm. After fabrication of thin film, variations in capacitance of the film with relative humidity (%RH) have been recorded. The thin film has been characterized by various techniques and a unique flower-like structure was found after the functionalization of GO with iron. The XRD analysis revealed that the GO consists of a minimum of 5 layers of the Graphene. BET surface analysis confirmed that the synthesized Fe-GO is the mesoporous material pertaining the surface area 45.23 m^2/g together with a mean pore diameter of 32 nm. The sensitivity of the Fe-GO based sensor found as 14.12 pF/%RH for higher humidity (70-95 %RH) region along with average sensitivity, response and recovery time as 5.18 pF/%RH, 31 and 11 s respectively at room temperature.

CHAPTER 3

Fabrication of humidity sensor based on thin-film of Graphene oxide functionalized with iron oxide nanoparticles

3.1 Introduction

The innovative ideas always nourish science and technology by its day by day contributions in various fields. Nanotechnology is one of the most emerging fields of science in this era with a lot of versatile applications by different techniques. In passing days, Graphene has been proved as a "magic material" due to its extraordinary properties like high electrical, thermal conductivity, high mechanical stability, zero bandgap, and thinnest material etc. The tuning bandgap of the GO, tends it as metals and semiconductors, depending upon the parameters like dopant, functionalization etc. [1-4]. Due to its high electrical sensitivity and a large surface to volume ratio, it is used as humidity transductive material [5, 6]. The derivatives of the Graphene and GO contain multiple oxygen-containing groups which mandate us to focus on the thin-film based sensor devices [7-10]. The functional groups with GO proclaim the massive active sites for the moisture acceptors, but such types of functional groups can disrupt the conductive regions for resistive transduction. To overcome this problem the chemical reduction technique is commonly implemented, which restores its conductivity [11].

Humidity is the gaseous state of the water, which is invisible to human eyes. The detection of humidity is very important in fields like agriculture, medical diagnostic, weather, food storage sectors, industries, and environmental monitoring etc. Humidity is an essential factor of the environment, which significantly affects living as well as non-

living organisms also [12, 13]. Therefore, we require to develop a good quality humidity sensor which is economically cost-effective and portable. Nowadays, simple, reliable, sustainable, portable, low-cost humidity sensors are in demand for accurate and precise measurement of humidity [14, 15]. The characteristic features of the good quality sensors are linear response of the sensor, high sensitivity, low response time and low recovery time, good chemical and physical stability at room temperature. There are two types of electrical sensors; a resistive type, and a capacitive type. Since resistive type sensor functions via analyzing the signals in the humid environment, its sensitivity can be increased by functionalizing the hydrophilic groups. These types of groups comprise carboxylic, hydroxylic, sulfonic and phenolic hydroxyl groups etc. which could familiarize with the massive moisture acceptors for humidity sensing. In the commercial field, the capacitive type humidity sensors have been used because of their high sensitivity, low fabrication costs, and low power consumption. The capacitive type sensors have also good performance in the environments which are desirable in various applications. The performances of the sensors are affected by various factors such as materials, its morphology, sensing material and the process of the preparation of the materials etc. For the development of a good humidity sensor, there are many transduction techniques such as capacitance [16], resistance, field-effect transistor (FET) [17], optical fiber, quartz crystal microbalance (QCM) [18, 19], surface acoustic wave (SAW) and photonic crystal etc. [20-22]. To improve the sensitivity of sensors, there are several types of materials such as nanostructured metal oxides, polymers, carbon nanotubes (CNTs) and nanocomposites that have been employed for fulfilling the purpose [23].

Due to the nonappearance of the moisture acceptors, at a high degree of humidity, the pure reduced Graphene Oxide-based sensors demonstrated as the low response sensor (0.27-37.43%) [24-26]. The pure Graphene has a poor response for sensing applications due to high conductivity. In GO, charge carriers have high conductivity and Fermi velocity in the plane. However, the poor interaction of the sensing material and restricted diffusion in the side edges show the poor sensitivity of the sensing material. To overcome this problem, the functionalization of the GO is necessary. The attachment of the metal oxide nanocomposites with the GO is important from the application point of view. The GO-based metal oxides nanocomposites/ nanohybrids are employed in various fields [27-29]. The functionalization of GO with nanostructured metal oxides results in the charge transfer mechanism between the sensing species and functionalized GO and also paying an effective way for the improvement of the sensitivity, fast response, and recovery [30]. There are several techniques for the production of carbon-based metal nanocomposites as hydrothermal, chemical vapor deposition, wet chemical method etc. [31]. For the doping or functionalization of Graphene, researchers used GO or rGO as a precursor. In the literature review, GO-based reported senors neither have a wide range of the %Relative Humidity (%RH) nor low response time. To overcome these problems we successfully come with an idea to functionalize GO with the metal-oxide nanoparticle. In this research article, GO was functionalized with iron nanoparticles (Fe-GO) and further, it was used for the detection of humidity. The recent literature review of the GO-based electrical humidity sensors has been depicted in Table 3.1.

3.2 Experimental details

3.2.1 Materials

All the chemicals used in the synthesis such as sulphuric acid, graphite, potassium nitrate, potassium permagnet, hydrogen peroxide, and ferric chloride, were purchased from Merck Specialities Private Limited, Mumbai, India. These were of analytical grade and used as received. During the entire experiment, di-ionized (DI) water having a pH value of 7 was used for making the aqueous solution.

3.2.2 Synthesis of GO and Fe-GO

GO was synthesized by the chemical oxidation process of the graphite. 1.0 g of natural graphite powder and 1.0 g of potassium nitrate were taken in a glass beaker which was further placed in an ice bath (0-5 ˚C) and 50 ml sulfuric acid was added under dynamic magnetic stirring. Then $KMnO_4$ (6 g) was gradually added to this solution after 20 min. The beaker was then moved from the ice bath to a water bath (30 ˚C) and after the stirring 2 h, a thick paste was obtained. Now, 200 ml distilled water was added to the solution and the solution was stirred for 35 min at 100 ˚C, later hydrogen peroxide was added drop by drop to the solution, which turns the color of the solution to dark brown. Further, the obtained solution was filtered and washed with DI water until neutral pH (7). After filtration, the cakes were formed and those were dispersed in the warm water for sonication and after 2 h sonication, it was converted into the suspension which was centrifuged at 4500 RPM (two times for 15 min). The supernatant (small pieces of GO /water-soluble derivatives) was unwanted while GO films were found from the residue under dry air [32, 33]. The exohedral functionalization method was used for functionalizing GO. In this method, Iron nanoparticle was directly deposited on the GO surface, side edges using the wet chemical deposition method. The diagram of the full synthesis process is shown in Fig. 3.1.

3.2.3 Fabrication of the sensing element

The sensing element was fabricated by the spin coating method. For this purpose, the thin film of the functionalized sample (Fe-GO) was deposited on the silica glass substrate of the dimension 1.0 × 0.5 cm^2 at 1500 rpm. The electrodes on the film at 0.25 cm from each edge were grown using silver paste. Also, the film was annealed at 400˚C in the presence of 20% oxygen for 2 h.

3.3 Characterization techniques

Various characterization techniques were employed to characterize the synthesized materials. The elemental analysis (EDX) and surface morphological analysis of the film was carried out at various magnifications and scales by scanning electron microscope (JEOL, JSEM- 6490LV). UV-Vis absorption spectrum of the aqueous solution was recorded using UV-Vis spectrophotometer (Evolution 201). XRD pattern recorded using PAN analytical X-ray diffractometer at scan rate 0.01°/s using CuKα (λ = 1.540598 Å) and FTIR (Nicolet TM 6700), Raman spectra recorded with Raman spectrometer (A Renishaw using λ = 514.5 nm Ar^+ with power 15 mW).

3.4 Results and Discussion

3.4.1 Scanning Electron Microscopy (SEM) analysis

The surface morphological investigation was carried out using Scanning Electron Microscopy (SEM). This characterization technique deals with the surface morphological study and 3D imaging of the samples.

Fig. 3.2 (a) shows the surface morphological diagram of the GO-based thin film. Flakes of the approximate thickness of 26.22 nm on the film might be observed. Effects of functionalization on the surface morphology of GO have been observed as shown in

Fig. 3.2 (b-c). Fe-GO has unique flake type structures which have not been reported till now. These structures are very similar to Gulmohar petals (Tabebuia angustata or Trumpet flower) (Fig. 2 (d)). The encircled part shows that the GO layers are overlapping to each other and iron nanoparticles are present between the GO layers. A GO sheet of dimension 500 nm is covering the lower GO sheet and iron nanoparticles are trapped between these two dimensional GO sheets. At the corners, there are large numbers of active sites (gaps or empty spaces) that are more responsible for the sensing purpose.

3.4.2 Energy Dispersive X-ray (EDX) analysis and elemental mapping

EDX technique was used for the analysis of the chemical and elemental composition in the sensing species at 10 keV accelerating voltage. An EDX spectrum of the Fe-GO is shown in Fig. 3.3. The observations deal with the presence of the C, O and iron particles along with chlorine as a foreign element. The analyzed elements C, O, Fe and Cl were present in the sample with weight % 41.90, 25.87, 8.12 and 2.24 respectively. Cl is the foreign element present due to the source of the ferric chloride.

3.4.3 BET surface analysis

The surface area of the synthesized Fe-GO was measured using the BET surface measurement. The nitrogen adsorption and desorption isotherms of the GO and Fe-GO are as shown in Fig. 3.4. The GO exhibiting macroporous material having the BET surface area 44.28 m^2/g and mean pore diameter is 129.8 nm as shown in Fig. 3.4 (a). Fig. 3.4 (b) illustrates that the Fe-GO exhibits a porous material containing narrow capillary pores. The BET surface area and mean pore diameter of Fe-GO were found 45.23 m^2/g. and 32.022 nm respectively. After the functionalization of the GO with the iron nanoparticles, the surface area of Fe-GO gets increased and the material gets a

transition from the macroporous to mesoporous material which is more beneficial for the sensing purpose. The functionalization of GO with iron nanoparticles increases the surface area as well as the porous nature of the Fe-GO.

3.4.4 X-Ray Diffraction (XRD) analysis

XRD is the characterization technique that is employed for the determination of crystal structure and lattice parameters. This is based on Bragg's diffraction condition as shown in Eqn. 3.1.

$$2dsin\,\theta = \mathrm{n}\lambda \tag{3.1}$$

where d is the interplanar spacing, n is the order of the plane, λ is the wavelength of the radiation used and θ is the Bragg's angle. The crystallite size can also be calculated using Debye-Scherer formula [34, 35] which is given as Eqn. 3.2.

$$D = \frac{\mathrm{k}\,\lambda}{\beta\cos\theta} \tag{3.2}$$

where D is the thickness in which direction the graphite patterning occurs, k is the Scherer's constant and β is the full-width half maxima. The crystallite size (L) in the plane (shown in Fig.3.5) can be calculated using the Eqn. 3.3 [36]

$$L = \frac{1.84\lambda}{\beta\cos\theta} \tag{3.3}$$

Fig. 3.6 (a) reveals the XRD pattern of the GO sheets. It shows that the highest Bragg's peaks appear at 24.37˚. The synthesized GO comprises amorphous and semi-crystalline behavior. The hump at 2θ = 11.5˚ with interplanar spacing 7.68 Å corresponded to the existence of oxygen-containing functional groups (-O-, -COOH, -C=O, -OH). A wide peak at 2θ = 24.37˚ with an interlayer spacing 3.65 Å is attributed to the lower grade of the crystallization and also indications of the existence of imperfection

and CO_2 molecules generated during the oxidation of graphite. This peak is found due to the diffraction of X-rays with (002) Bragg's plane. There are some Bragg's peaks at 2θ = 43.42˚ and 49.19˚ with 2.08 and 1.85 Å interlayer spacing corresponding to the Bragg's plane (100) and (102) respectively which shows the decrease in the crystallinity. These may be due to the presence of some of the un-oxidized graphite flakes during the oxidation [33].

The average thickness (D in the graphite patterning direction) and crystallite size in the plane (L) for the GO was calculated as 7.24 and 14.81 nm respectively. The number of layers (n) in GO can be calculated by using the formula as given in Eqn. 3.4 [36]

$$n = \frac{D}{d} + 1 \tag{3.4}$$

The minimum and maximum numbers of the Graphene layers in GO were obtained 5 and 13 respectively. The Fig. 3.6 (b) shows the XRD pattern of the Fe-GO sheets consisting of the 10 Bragg's peaks. This shows that Fe-GO has crystalline nature. The Bragg's planes (002), (100) and (102) represented by the black colors are of the GO while (012), (104), (110), (202), (116), and (018) represented by the red are of the iron nanoparticles. There is one un-indexed peak at 2θ = 31.87˚ that may be due to the phase change of the ferric oxide nanoparticles during the annealing of the Fe-GO. The average thickness (D) and crystallite size in the plane (L) of the synthesized Fe-GO sheets was calculated 26.09 and 52.67 nm respectively, these were increased in comparison of GO. The increase in thickness is the signature of iron nanoparticles acting as a connecting bridge among the basal planes of the GO sheets and an increase in crystallite size (i.e. the

size of the Fe-GO sheet in the plane) shows the iron nanoparticles were bonded with the side edges.

3.4.5 Fourier Transform Infra-Red spectroscopy analysis

The synthesized materials were characterized by FTIR spectroscopy to determine the reactivates and functional groups attached to them. The presence of the functional groups in the synthesized materials was confirmed by IR spectroscopy. An IR spectrum of a molecule is obtained by absorbing the IR radiation frequency which matches the bond frequency within the molecule. This spectrum was studied in the wavenumber range 4000 - 500 cm^{-1}. Fig. 3.7 (a) and (b) shows the IR spectrum of the GO and Fe-GO respectively. The absorption bands found at 3740, 2920, 2850, 1440 cm^{-1} are due to the oxygen functionalities present in the material shown in Fig. 3.7 (a). The peak at 3435 cm^{-1} was assigned to hydroxyl (OH) stretching of the C-OH groups [37]. The C=O stretching vibrations of the carboxylic acid (COOH) groups were assigned vibrations as the valley present at 1710 cm^{-1} [37]. The valleys assigned at 1550 and 1151 cm^{-1} were due to C=C and C-O stretching vibrations. There are some additional valleys at 2398, 1619, 545 cm^{-1} in Fig. 3.7 (b) which reveals that the Fe nanoparticles were single-bonded with the GO sheet [38]. There are some other valleys at range 800-900 cm^{-1} due to Fe-OH stretching vibrations and at peak 450 cm^{-1} is due to O-Fe-O stretching vibrations present in the Fe-GO [39].

3.4.6 UV-Visible absorption analysis

The optical characterization of the film was done by UV-Visible spectrophotometer. Fig. 3.8 signifies the variation of the optical absorbance for the film with the wavelength. Insets of Fig. 3.8 (a) & (b) show that the graphs between $(\alpha hv)^2$ and

energy (eV). We found that extrapolations of tangents on these curves give direct bandgap energy of GO and Fe-GO as 2.4 and 4.2 eV respectively. The bandgap energy of the nanomaterial after functionalization increases from 2.4 to 4.2 eV. This shift in the optical band gap shows the blue shift, which is a better indication of humidity sensing. The higher bandgap is credited to the size and morphological effect of nanostructures. Thus the increase of bandgap in comparison to pure GO is more clear based on the quantum size effect which arises due to the very small size of nanosheets in two dimensions. In the functionalization process the GO sheets get functionalized with Fe nanoparticles, these nanoparticles have lower conductivity so they capture free electrons from the Graphene sheets so the conduction band of the nanocomposites shifts upwards, and a higher bandgap has been observed.

3.4.7 Raman spectroscopy

Raman spectroscopy is the primary characterization of carbon-based nanomaterials. This technique plays a significant character in the study of differentiating carbon-based materials [40]. The Raman spectra of the GO and Fe-GO were recorded and plotted as shown in Fig.3.9. Fig. 3.9 (a) shows the Raman spectra of the GO in which two Raman peaks were obtained, among those, one is at 1331 cm^{-1} and the other is at 1589 cm^{-1}. These are known as D - band and G - band respectively. The intensity of the D-band is higher compared to the G – band [41]. The I_D/I_G ratio was 1.53 for the GO. Raman plot of Fe-GO as shown in Fig. 3.9 (b), Raman peaks indexed at wavenumber 1327 and 1587 cm^{-1} corresponded to D - band and G - band respectively. The I_D/I_G ratio was 1.41 for the Fe-GO. The decrease in I_D/I_G ratio from 1.53 to 1.41 exhibits that the crystalline nature increases as the I_D/I_G is inversely proportional to the crystallite size

[42]. The shifting in the position of the D, G - bands and decrease in I_D/I_G were the signatures of the reduction of the GO into the Graphene Layers. At the higher energy in the Raman spectra, there is a peak at wavenumber 2610 cm^{-1} [43]. This peak confirmed that the GO has been reduced into the Graphene Layers. Wavenumber range 220-610 cm^{-1} consists of four peaks. These peaks confirm the existence of iron nanoparticles in the synthesized material [44].

3.5 Humidity sensing application

Graphene-based materials have a charge-transfer sensing mechanism. In such type of mechanism, the transfer of electrons between the sensing species and materials takes place. The foundation of this mechanism is a transfer of the charge carriers from the chemisorbed and physisorbed water molecules to the material surface being predisposed by the porosity and surface area. The Fe functionalization tends to the porous material and active sites in the sensing process. In the case of Fe-GO, many layers are present and oriented in different directions as shown in Fig. 3.10 (a). The orientations of the Fe-GO layers form the capacitor. In the absence of moisture, the value of the capacitance is related to the geometry of the Fe-GO layers. Many capacitors are formed due to the different orientations of the sheets having a capacitance

$$C = \frac{KA}{d} \tag{3.5}$$

Where $K = \epsilon_r \epsilon_0$ is the dielectric constant of the water, ϵ_r and ϵ_0 are the relative permittivity of the material and permittivity of the free space between the Fe-GO sheets respectively, A is the area and d is the spacing between the sheets. The capacitance not only relies on the area of the exposure and the distance between the layers but also on the dielectric constants of the material. The increase in the value of dielectric constant results

in increases in the capacitance. Water is the polar molecule that polarizes into H^+ and OH^- ion. The polarizability is directly proportional to the dielectric constant. Therefore, capacitance directly relies on polarizability [24, 25]. As the humidity increases, the OH^- ion concentration also increases so the value of the capacitance will also increase [45].

At lower humidity, less number of adsorbed water molecules is chemisorbed to the Fe-GO surface. At this level, the OH^- ion chemically bonded to the Fe-GO layers at the surface i.e. chemisorption takes place as shown in Fig. 3.10 (b). As the humidity increases, the number of water molecules increases, and the layers of the water molecules are formed over the chemisorbed layers. In this way, the physisorption takes place as shown in Fig. 3.10 (c). Further, the number of the adsorbed water molecules also increases and so OH^- concentration increases which increase the capacitance.

3.5.1 Experimental setup

A controlled humidity chamber has been designed as shown in Fig. 2.10 of **Chapter 2**. Saturated solutions of KOH and K_2SO_4 in distilled water were used as a humidifier and dehumidifier respectively. Variations in capacitance were noted by using the Impedance Analyzer (Wayne Kerr Precision Component Analyzer, 6440B) through connecting cables. The variations in relative humidity were recorded using a standard hygrometer (HTC-1). The humidifier or dehumidifier was kept in a steel bowl over flat support. During the experiment, the temperature of the chamber remains the same and the frequency is kept at 100 Hz throughout the experiment. A thin film of Fe-GO prepared and depicted in section 2.3 was inserted within a capacitive measuring holder, after that it was exposed to the humidity inside a humidity testing setup. As humidity inside the

testing chamber increases, the capacitance of the thin film increases for the entire range of humidity i.e. from 10% to 95% was observed at room temperature.

3.5.2 Results & Discussion

The changes in capacitance with the variation of %RH for the sensing film of Fe-GO at room temperature are recorded as shown in Table 3.2 and plotted in Fig. 3.11 (a-d). It can be seen that as %RH increases, the capacitance of film increases. The curve has been divided into three segments, Ist for low humid (10–40 %RH), IInd for mid humid (40–70 %RH) and IIIrd for the high humid region (70–95 %RH) respectively.

The slope of the curve defines the sensitivity [23]. Mathematically,

$$Sensitivity = \frac{\text{change in capacitance}}{\text{change in \%RH}} \quad \text{pF/\%RH} \qquad (3.6)$$

The sensitivity of the sensor investigated for three regions of %RH has been depicted in Table 3.3. The sensor shows a lower sensitivity in the low humidity region and improved sensitivity in the mid humid region while drastic enhancement was observed in the higher humidity range i.e. from 70 to 95 %RH. It is 14.66 pF/%RH, which is the maximum among the reported values (Table 3.3). The average sensitivity was calculated as 5.18 pF/%RH by taking the slope of the curve in Fig. 3.11 (a) in different regions. The functionalization, unique, and beautiful porous surface morphology comprises good sensitivity. The time of humidity sensor with the increasing and decreasing humidity has been recorded which is shown in Table 3.4. The response and recovery time of the sensor have been shown in Fig. 3.11 (b) and these were found as 31s and 11s respectively. The observed data for repeatability and aging has been shown in Table 3.5. The experimentally obtained data is plotted as shown in Fig. 3.11 (c) which

shows that results are repeatable up to 97.2%. The aging effect on the sensing material was also tested after one week and three weeks which is shown in Fig. 3.11 (d). It is quite observable that there is very less or negligible aging effect on the results obtained. The data of the real-time versus change in capacitance with increasing humidity is shown in Table 3.6. Fig.3.12 is illustrating the real-time capacitance change at various %RH. As the time of exposure to humidity increases the concentration of the hydroxyl ions also increases and finally we get an increase in the capacitance. The variation in the capacitance has been found because of the generation of new dangling bonds and the conversion of dangling bonds into covalent bonds. Fig. 3.13 shows the comparisons of the sensitivity in three regions (low, mid and high) after 3, 7 and 21 days ageing and the corresponding data is depicted in Table 3.7. The bars demonstrate that the sensor gives negligible deviations in the high and mid humid regions. The sensor gives the same average sensitivity after 3, 7, and 21 days.

3.6 Conclusion

The GO and Fe-GO have been synthesized successfully. The BET technique analyzed that the Fe-GO is the mesoporous material having a surface area 45.23 m^2/g along with mean pores diameter of 32 nm. The surface morphological and XRD investigations of the GO and Fe-GO demonstrate that after the functionalization of GO with the Fe nanoparticles leads the increase in surface area of the sheets, creating more dangling bonds, porous and unique morphology (i.e. Gulmohar petal-like structures); these are responsible for the humidity sensing. The functionalization with iron nanoparticles enhances the crystalline nature of the Fe-GO as compare to GO. The minimum numbers of Graphene layers in GO were found as 5. The iron nanoparticles

were attached to the oxygen-containing functionalities at the side edges, corners, and the basal plane of the GO sheets because the size in the plane (i.e. L) of Fe-GO has been increased as compared to GO. The iron nanoparticles are mostly attached to the oxygen functionalities of the GO, so we can say that GO is functionalized exohedrally with the iron. The decrease in I_D/I_G ratio (from 1.53 to 1.41) also shows that iron nanoparticles are attached to defects in GO sheets. The iron nanoparticles are single bonded with GO sheets and are attached at side edges, corners, and in the basal planes of the GO sheets. Fe-GO shows the best sensitivity in the higher humidity region as compared to the lower and mid humid region. So this is a good sensor for the higher humidity (70–95 %RH) range at room temperature. The sensing attributes as average sensitivity, response, and recovery time are 5.18 pF/%RH, 31 s, and 11 s respectively in the humidity range 10-95 %RH at room temperature. The sensor has the same average sensitivity after 3, 7, and 21 days. The sensitivity in this chapter has been found to be increased and the recovery time also reduced in comparison to previous **Chapter 2**.

References

[1] C. Zhu, D. Du, Y. Lin, Graphene and graphene-like 2D materials for optical biosensing and bioimaging: a review, 2D Mater. 2 (2015) 1-40.

[2] Q. Etienne, , Frédéric Roux, Fabrice Emieux , Pascal Faucherand , Emmanuel Kymakis, George Volonakis, Feliciano Giustino, Beatriz Martín-García, Iwan Moreels, Selmiye Alkan Gürsel, Ayşe Bayrakçeken Yurtcan, Vito Di Noto, Alexandr Talyzin, Igor Baburin, Diana Tranca, Gotthard Seifert, Luigi Crema, Giorgio Speranza, Valentina Tozzini, Paolo Bondavalli, Grégory Pognon, Cristina Botas, Daniel Carriazo, Gurpreet Singh, Teófilo Rojo, Gunwoo Kim, Wanjing Yu, Clare P Grey and Vittorio Pellegrini, Graphene-based technologies for energy applications, challenges and perspectives, 2D Mater. 2 (2015) 1-17.

[3] T. Palaniselvam, J. B. Baek, Graphene-based 2D-materials for supercapacitors 2D Mater. 2 (2015) 1-15.

[4] F. Qing, R. Jia, B. W. Li, C. Liu, C. Li, B. Pong, L. Deng, W. Zhang, Y. Li, R. S. Ruoff, X. Li, Graphene growth with 'no' feedstock, 2D Mater. 4 (2017) 1-30.

[5] W. Xuan, M. He, N. Meng, X. He, W. Wang, J. Chen, T. Shi, T. Hasan, Z. Xu, Y. Xu, J. K. Luo, Fast response and high sensitivity ZnO/glass surface acoustic wave humidity sensors using graphene oxide sensing layer, Sci. Rep. 4 (2014) 1-9.

[6] D. Zhang, J. Tong, B. Xia, Q. Xue, Ultrahigh performance humidity sensor based on layer-by-layer self-assembly of graphene oxide/polyelectrolyte nanocomposite film, Sens. Act. B: Chemical 203 (2014) 263–270.

[7] D. Zhang, H. Chang, R. Liu, Humidity-sensing properties of one-step hydrothermally synthesized tin dioxide-decorated graphene nanocomposite on polyimide substrate, J. Electron. Mater. 45 (2016) 4275–4281.

[8] U. Kumar, B. C. Yadav, Synthesis of carbon nanotubes by direct liquid injection chemical vapor deposition method and its relevance for developing an ultra-sensitive room temperature based CO_2 sensor, J. Tiwan Inst. Chem. Eng. 96 (2019) 652-663.

[9] P. G. Su, Z. M. Lu, Flexibility and electrical and humidity-sensing properties of diamine-functionalized graphene oxide films, Sens. Act. B: Chemical 211 (2015) 157–163.

[10] Q. Huang, D. Zeng, S. Tian, C. Xie, Synthesis of defect graphene and its application for room temperature humidity sensing, Mater. Lett. 83 (2012) 76–79.

[11] K. Kumar and B. C. Yadav, An Overview on the Importance of Chemical Vapour Deposition Technique for Graphene Synthesis, Adv. Sci. Eng. Med., 10 (2018) 760–763.

[12] C. Y. Lee, G. B. Lee, Humidity sensors: a review, Sens. Lett. 3 (2005)1–15.

[13] A. Nag, A. Mitra, S. C. Mukhopadhyay, Graphene and its sensor-based applications: A review, Sen. Act. A: Physical 270 (2018) 177–194.

[14] F. Tudorache, I. Petrila, T. Slatineanu, A. M. Dumitrescu, A. R. Iordan, M. Dobromir, M. N. Palamaru, Humidity sensor characteristics and electrical properties of Ni–Zn–Dy ferrite material prepared using different chelating-fuel agents, J. Mater. Sci.: Mater. Electron 27 (2016) 272 -278.

[15] A. E. Dessler, S. C. Sherwood, A matter of humidity, Science 323 (2009) 1020–1021.

[16] C. L. Zhao, M. Qin, W.H. Li, Q.A. Huang, Enhanced performance of a CMOS interdigital capacitive humidity sensor by Graphene oxide, Proceedings of the 16th International Solid-State Sensors, Actuators and Microsystems Conference, (2011) 1954–1957.

[17] S. H. Song, H. H. Yang, C. H. Han, S. D. Ko, S. H. Lee, J. B. Yoon, Metal-oxide-semiconductor field-effect transistor humidity sensor using surface conductance, Appl. Phys. Lett. 100 (2012) 1-4.

[18] X. Wang, B. Ding, J. Yu, M. Wang, F. Pan, A highly sensitive humidity sensor based on a nanofibrous membrane coated quartz crystal microbalance, Nanotechnology 21 (2009) 1-7.

[19] Y. Yao, X. D. Chen, H. H. Guo, Z. Q. Wu, Graphene oxide thin film coated quartz crystal microbalance for humidity detection, Appl. Surf. Sci. 257 (2011) 7778–7782.

[20] M. M. Hawkeye, M. J. Brett, Optimized colorimetric photonic-crystal humidity sensor fabricated using glancing angle deposition, Adv. Funct. Mater. 21 (2011) 3652–3658.

[21] S. M. Balashov, O. V. Balachova, A. P. Filho, M. C. Q. Bazetto, M. G. de Almeida, Surface acoustic waves humidity sensors based on Graphene oxide thin films deposited with the surface acoustic wave atomizer, ECS Trans. 49 (2012) 445–450.

[22] R. Fenner, E. Zdankiewicz, Micromachined water vapor sensors: a review of sensing technologies, IEEE Sens. J. 1 (2001)309–317.

[23] J. Chu, X. Y. Peng, P. Feng, Y. Sheng, J. T. Zhang, Study of humidity sensors based on nanostructured carbon films produced by physical vapor deposition, Sens. Act. B: Chemical 178 (2013) 508–513.

[24] H. Bi, K. Yin, X. Xie, J. Ji, S. Wan, L.Sun, M. Terrones, M. S. Dresselhaus, Ultrahigh humidity sensitivity of graphene oxide, Sci. Rep. 3 (2714) (2013) 1-4.

[25] U. Kumar, B. C. Yadav, Development of humidity sensor using modified curved MWCNT based thin film with DFT calculations, Sens. Actuat. B: Chemical 288 (2019) 399-407.

[26] D. Z. Zhang, J. Tong, B. Xia, Humidity-sensing properties of chemically reduced graphene oxide/polymer nanocomposite film sensor based on layer-by-layer nano self-assembly, Sens. Actuat. B: Chemical 197 (2014) 66–72.

[27] Y. Chen, Y. Wang, H. B. Zhang, X. Li, C.X.Gui, Z. Z. Yu, Enhanced electromagnetic interference shielding efficiency of polystyrene/graphene composites with magnetic Fe_3O_4 nanoparticles, Carbon 82 (2015) 67 –76.

[28] X. He, Tunable terahertz graphene metamaterials, Carbon 82 (2015) 229 –237.

[29] R.F. Albers, R.A. Bini, J. B. Souza Jr., D. T. Machado, L. C. Varanda, A general one-pot synthetic strategy to reduced graphene oxide (rGO) and rGO-nanoparticle hybrid materials, Carbon 143 (2019) 73-84.

[30] C. Chen, X. Wang, M. Li, Y. Fan, R. Sun, Humidity sensor based on reduced graphene oxide/lignosulfonate composite thin-film, Sen. Act. B: chemical 255 (2018) 1569–1576.

[31] R. K. Mishra, S. B. Upadhyay, A. Kushwaha, T. H. Kim, G. Murali, R. Verma, M. Srivastava, J. Singh, P.P. Sahay, S.H. Lee, SnO_2 quantum dots decorated on RGO: A superior sensitive, selective and reproducible performance for H_2 and LPG sensor, Nanoscale 7 (2015) 11971-11979.

[32] B. Paulchamy, G. Arthi and B. D. Lignesh, A Simple Approach to Stepwise Synthesis of Graphene Oxide Nanomaterial J. Nanomed. Nanotechnol. 6 (2015) 1-4.

[33] M. Sohail, M. Saleem, S. Ullah, N. Saeed, A. Afridi, M. Khan, Modified and improved Hummer's synthesis of graphene oxide for capacitors applications Mod. Elec. Mat. 3 (2017) 110-116.

[34] D. Zhang, H. Chang, P. Li, R. Liu, Q. Xue, Fabrication and characterization of an ultrasensitive humidity sensor based on metal oxide/graphene hybrid nanocomposite, Sen. and Act. B: Chemical 225 (2016) 233–240.

[35] M. Y. Wang, T. Shen, M. Wang, D. E. Zhang a, Z. Tong, J. Chen , One-pot synthesis of α-Fe_2O_3 nanoparticles-decorated reduced Graphene oxide for efficient nonenzymatic H_2O_2 biosensor, Sen. and Act. B 190, (2014) 645-650.

[36] R. Sharma, N. Chadha and P. Saini, Determination of defect density, crystallite size and number of graphene layers in graphene analogs using X-ray diffraction and Raman spectroscopy, Indian J. of Pure & App. Phy. 55 (2017) 625-629.

[37] Z. Movasaghi, S. Rehman & Dr. I. U. Rehman, Fourier transform infrared (FTIR) spectroscopy of biological tissues, Applied Spectroscopy Reviews, 43 (2008) 134–179.

[38] A. C. S. Talari, M. A. G. Martinez, Z. Movasaghi, S. Rehman, and I. U. Rehman, Applied Spectroscopy Reviews, 52 (5) (2017) 456–506.

[39] S. Khelifi, F. Ayari, Chehimi, D. B. Hassan, M. Trabelsi-Ayadi, Synthesis and Characterization of Heterogeneous Catalysts and Comparison to Iron-ore, J. Chem. Eng. Process Technol. 7 (5) (2016) 1-9.

[40] M. S. Dresselhaus, A. Jorio, M. Hofmann, G. Dresselhaus and R. Saito, Perspectives on Carbon Nanotubes and Graphene Raman Spectroscopy, Nano Lett. 10 (2010) 751–758.

[41] S. Claramunt, A. Varea, D. López-Díaz, M. M. Velázquez, A. Cornet, Albert Cirera, The importance of interbands on the interpretation of the Raman spectrum of graphene oxide.J. Phys. Chem. C 119 (2015) 10123−10129.

[42] A. A. K. King, B. R. Davies, N. Noorbehesht, P. Newman, T. L. Church1, A. T. Harris, J. M. Razal & A. I. Minett, A New Raman Metric for the Characterisation of Graphene oxide and its Derivatives, Scientific Reports 6 (2016) 1-6.

[43] J. B. McManus, A. Hennessy, C. P. Cullen, T. Hallam, N. McEvoy, G. S. Duesberg, Controlling defect and dopant concentrations in graphene by remote plasma treatments Phys. Status Solidi (b) 254 (2017) 1-6.

[44] I. Chourpa, E. L. Douziech, O. L. Ngaboni, J. F. Fouquent, J. S. Cohen, M. Souce, H. Marchais, P. Dubois, Molecular composition of iron oxide nanoparticles, precursors for magnetic drug targeting, as characterized by confocal Raman microspectroscopy, Analyst 130 (2005) 1395–1403.

[45] C. L. Zhao, M. Qin, Q. A. Huang, A fully packaged CMOS interdigital capacitive humidity sensor with polysilicon heaters, IEEE Sensors Journal, 11(11) (2011) 2986-2992 .

Figures

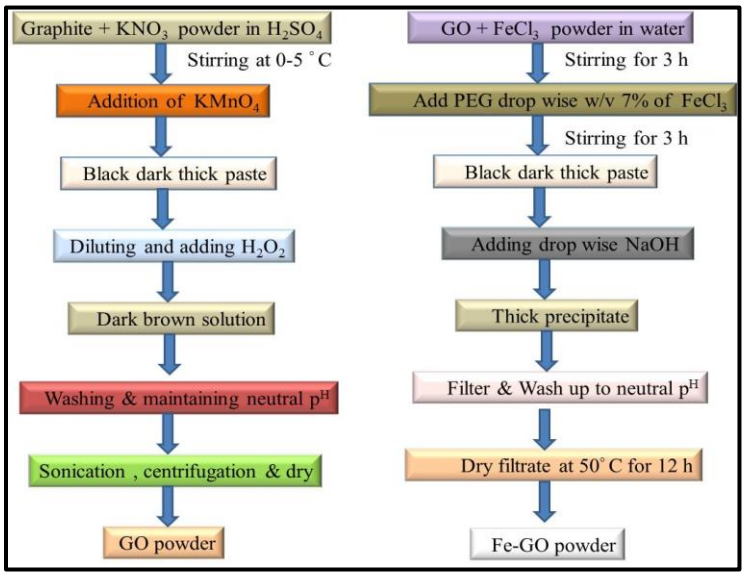

Fig. 3.1 Flow chart of the synthesis process of GO and Fe-GO

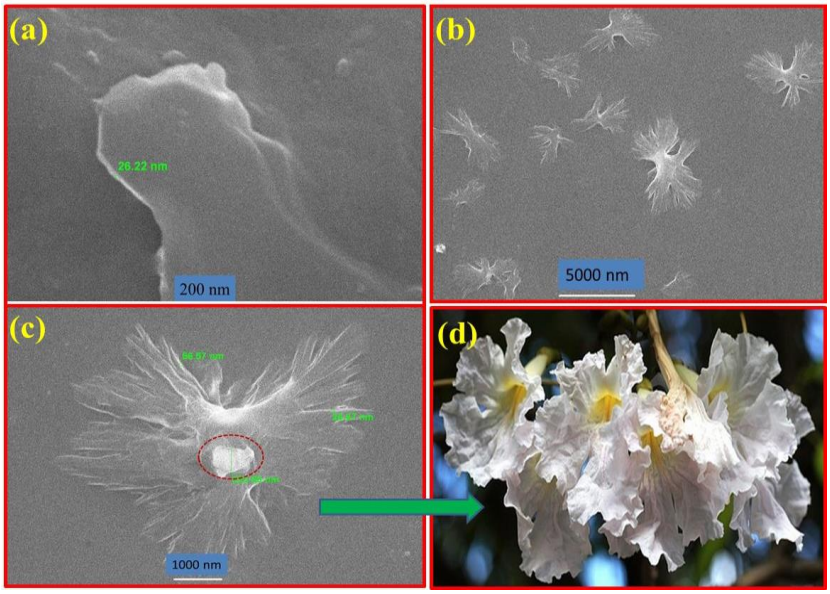

Fig. 3.2 Surface morphology of the (a) pristine GO and (b, c) Fe-GO (d) photograph of Gulmohar flower

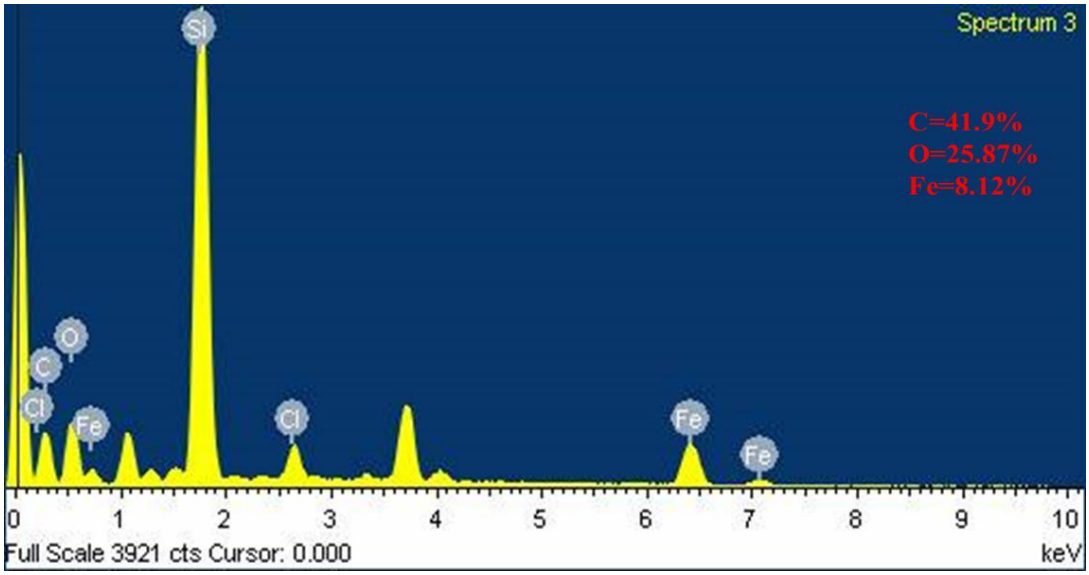

Fig. 3.3 EDX spectra of the Fe-GO

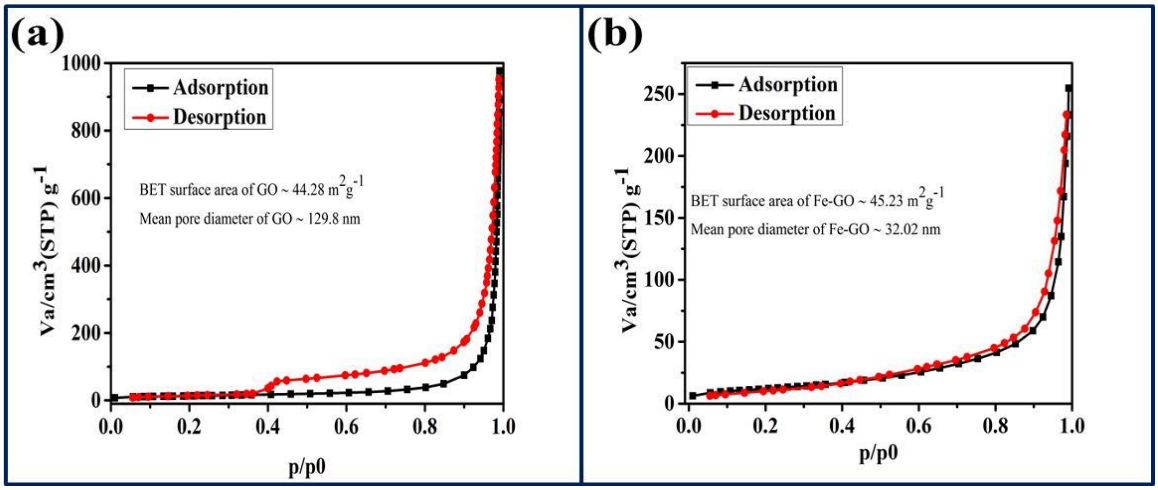

Fig. 3.4 N_2 adsorption-desorption isotherm of (a) GO and (b) Fe-GO at 77 ˚K temperature

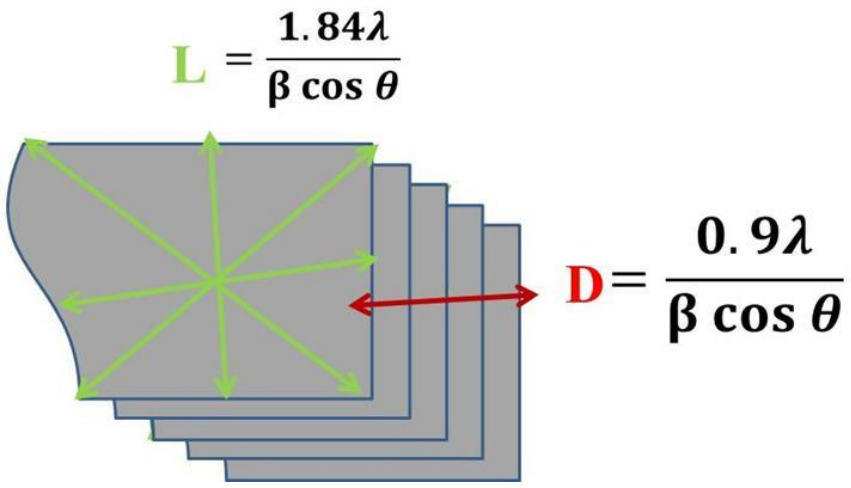

Fig. 3.5 Schematic showing the synthesized GO consists of the minimum 5 layered Graphene

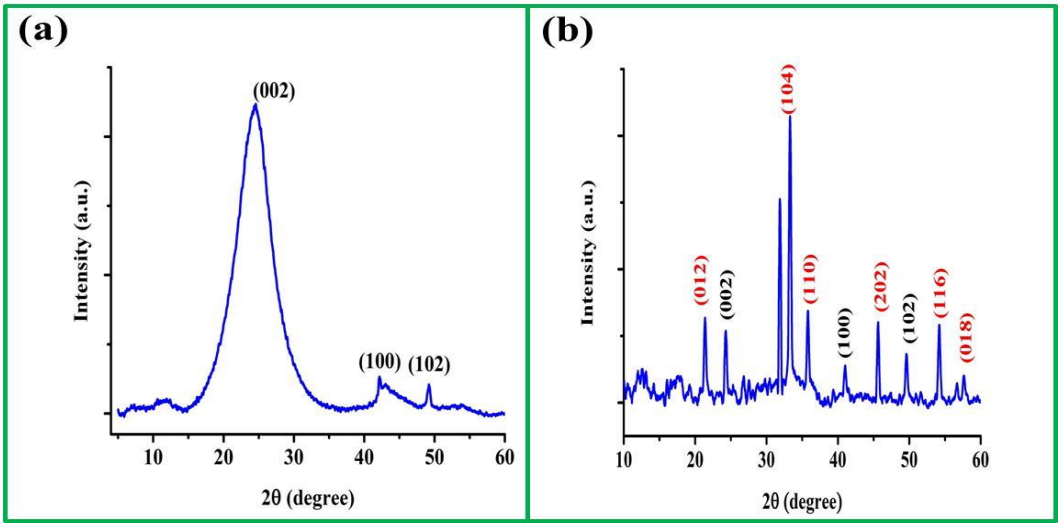

Fig. 3.6 XRD pattern of (a) GO and (b) Fe-GO

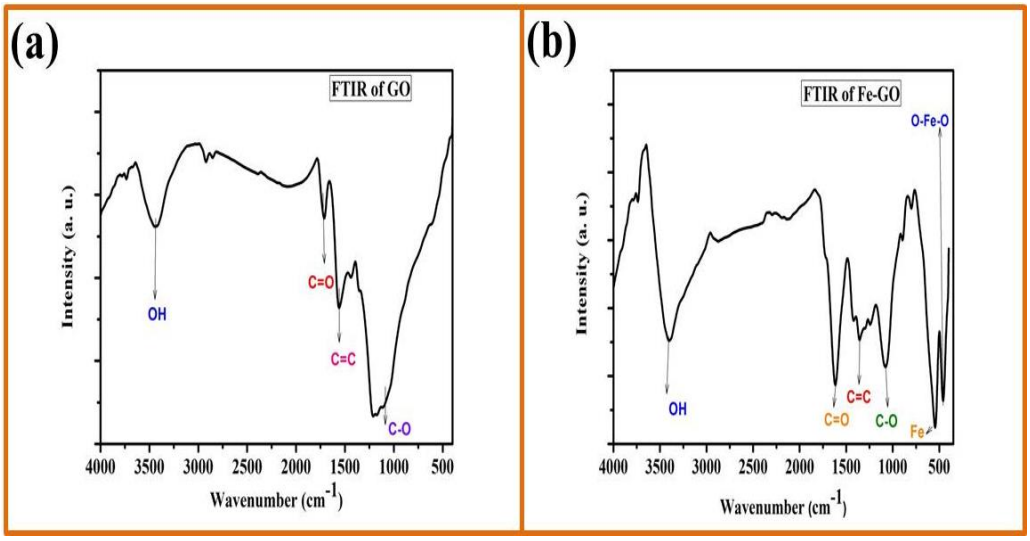

Fig. 3.7 IR spectra of (a) GO (b) Fe-GO

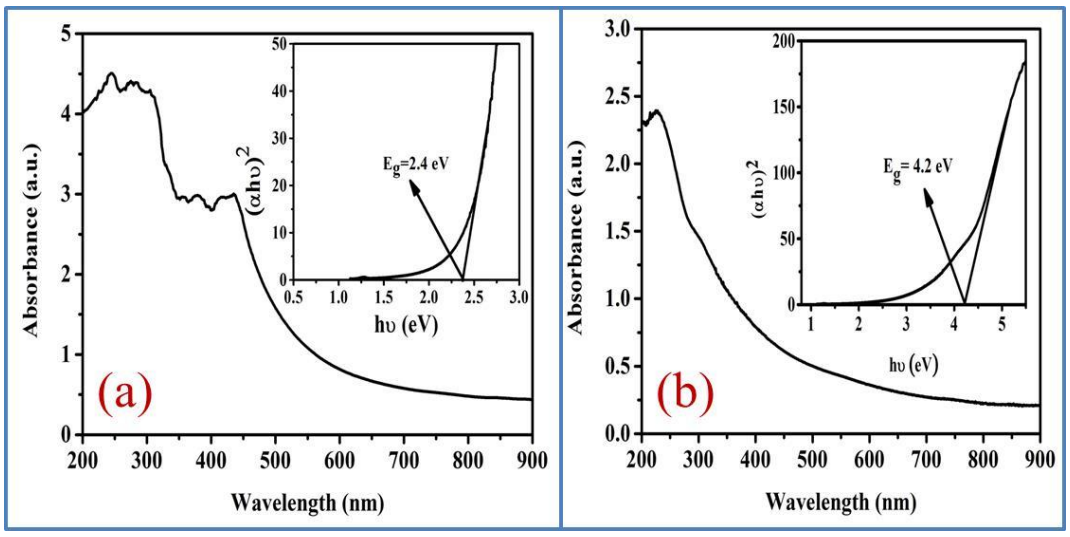

Fig. 3.8 Absorption spectra of (a) GO and (b) Fe-GO, Insets are the Tauc plots showing optical band gaps of GO and Fe-GO as 2.4 and 4.2 eV respectively

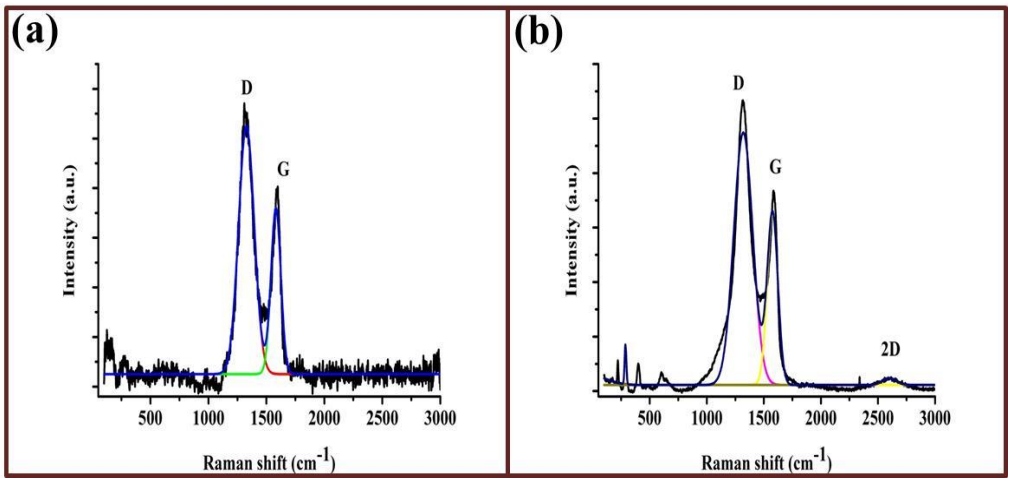

Fig. 3.9 Raman spectra of (a) GO (b) Fe-GO

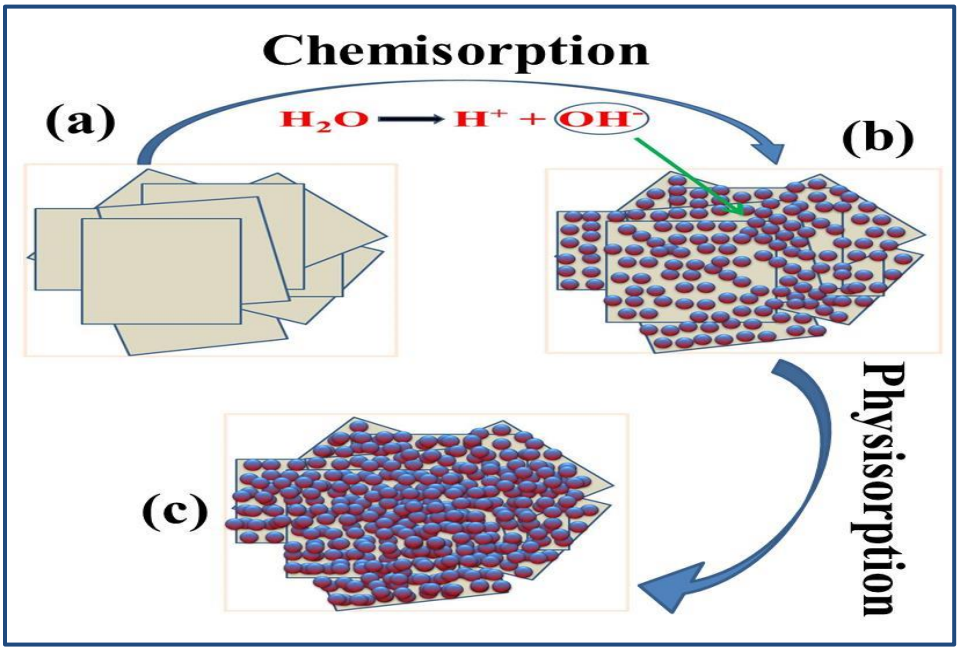

Fig. 3.10 Schematic showing capacitance-based humidity sensing mechanism of Fe-GO

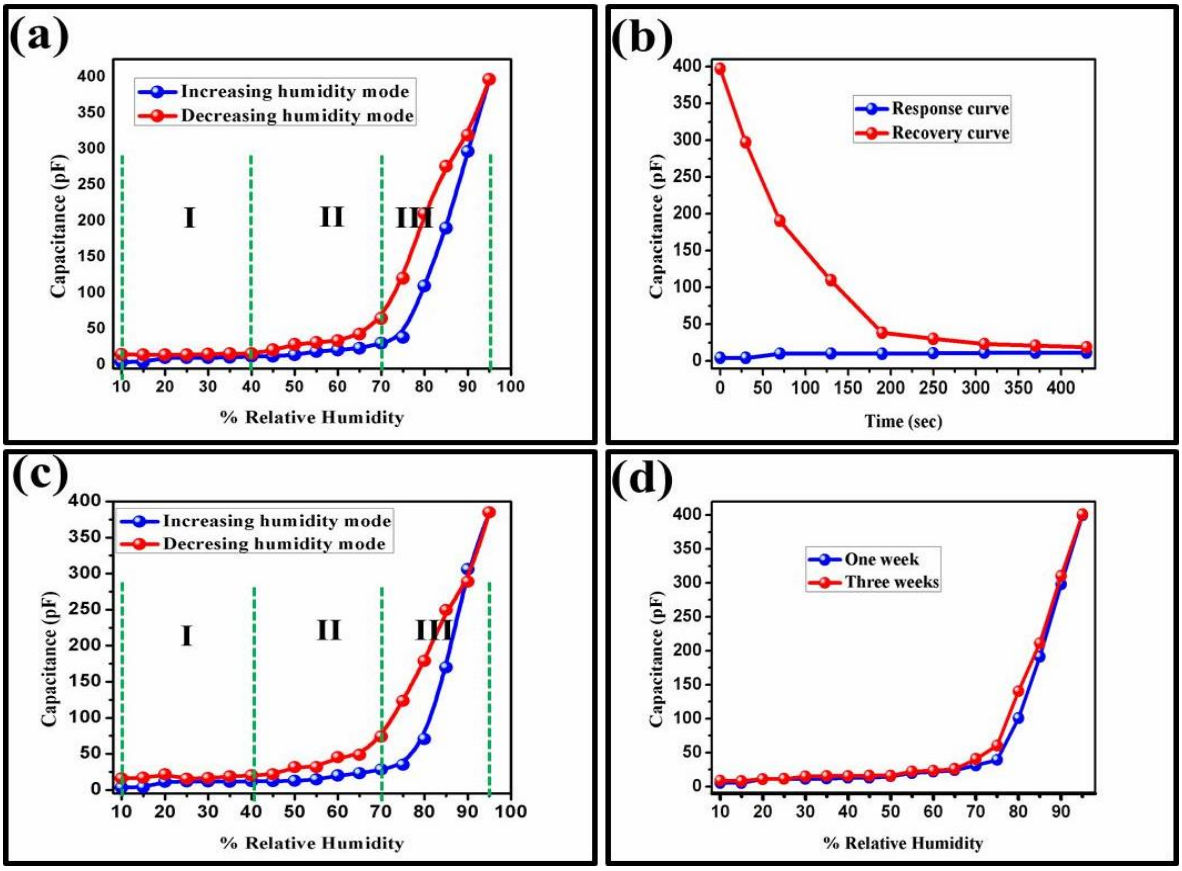

Fig. 3.11 Sensing characteristics: (a) sensitivity, (b) response, recovery curve, (c) repeatability and (d) ageing effect

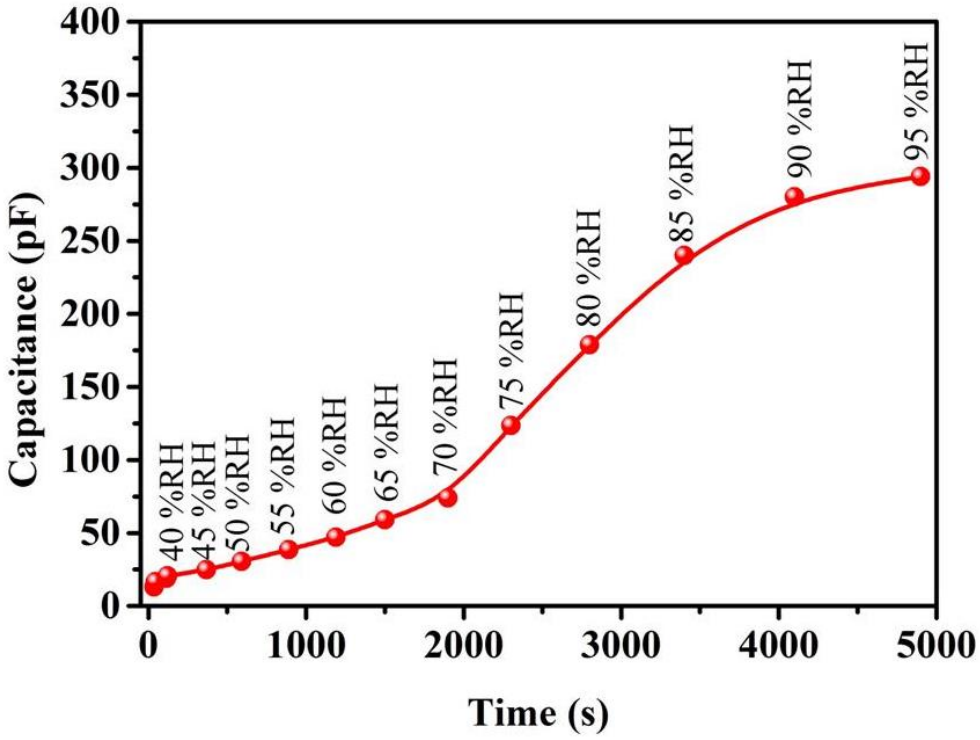

Fig. 3.12 Real-time capacitance change at various %RH

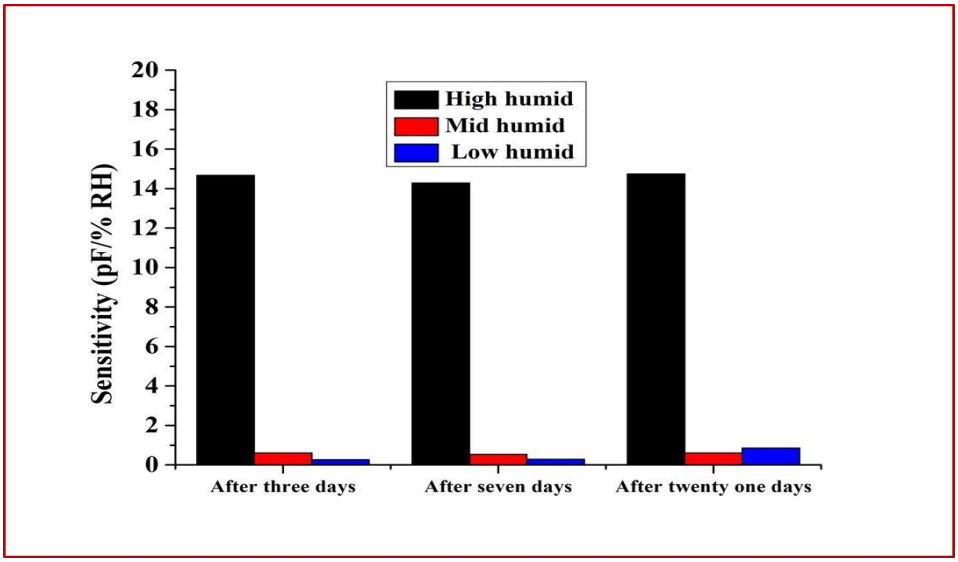

Fig. 3.13 Sensitivity versus %RH of Fe-GO in 3 different regions after 3, 7, and 21 days

Tables

Sensing material	Sensor type	Measurement range	Response/sensitivity	Response time (s)	Recovery time (s)	References
Defected Graphene	Conductive type	3-30 %RH	0.27- 2.33 /%RH	-	-	10
GO	Surface acoustic wave type	8-18 %RH	1.54 kHz / %RH	38	21	21
GO	Capacitive type	25-65 %RH	-9.5 fF / %RH	5	-	16
GO	Quartz crystal microbalance type	6.4- 93.5 %RH	22.1 Hz / %RH	45	24	19
GO	Capacitive type	15-95 %RH	37800%/	10.5	41	24
Fe-GO	Capacitive type	10-95 %RH	5.18 pF/%RH	31	11	Present work

Table 3.1 Literature review for Fe-GO based humidity sensors

%RH	Capacitance (pF)	
	Increasing mode	Decreasing mode
10	4.33	14.97
15	4.36	14.12
20	10.21	14.21
25	10.21	14.35
30	10.14	15.05
35	10.75	15.92
40	11.98	15.71
45	12.14	20.96
50	14.29	28.56
55	19.02	31.47
60	20.93	33.67
65	23.33	42.98
70	30.27	64.68
75	38.43	120.61
80	109.7	210.51
85	190.34	276.06
90	296.89	319.3
95	396.9	396.9

Table 3.2 The recorded data of variation in the capacitance with increasing and decreasing humidity in the range 10-95 %RH

Regions	**I**	**II**	**III**
Humidity range (%RH)	10-40	40–70	70–95
Sensitivity (pF/ %RH)	0.26	0.61	14.66

Table 3.3 Variation of the sensitivity of Fe-GO based sensor for the three regions of %RH

Time (s)	**Capacitance (pF)**	
	Increasing humidity (10-50 %RH)	**Decreasing humidity (95-55 %RH)**
0	4.33	396.90
30	4.36	296.89
70	10.21	190.34
130	10.21	109.7
190	10.14	38.43
250	10.75	30.27
310	11.28	23.33
370	11.44	20.93
430	11.71	19.02

Table 3.4 The data of the measured time versus variation in the capacitance with increasing (10-50 %RH) and decreasing humidity (95-55 %RH)

%RH	Capacitance (pF)			
	Repeatability		Ageing effect	
	Increasing mode	Decreasing mode	After 1 week	After 2 week
10	3.20	15.86	4.25	20.35
15	3.80	16.89	5.87	23.98
20	11.40	21.52	16.75	24.21
25	11.61	15.60	16.58	24.21
30	11.60	16.50	16.45	23.54
35	11.40	18.66	16.32	27.75
40	12.00	20.20	17.89	31.98
45	12.20	21.57	18.20	39.94
50	12.61	31.68	18.70	32.29
55	14.30	31.67	22.54	49.02
60	19.90	45.20	24.92	54.93
65	23.11	48.58	29.13	66.33
70	28.15	73.98	34.14	71.27
75	34.82	123.52	44.85	125.43
80	70.49	178.90	70.52	198.70
85	170.00	249.28	188.00	246.34
90	306.00	288.62	304.00	310.89
95	385.00	385.00	388.89	410.90

Table 3.5 The recorded readings of the repeatability and ageing effect

Real-time (s)	Capacitance
36	12.94
45	16.65
114	18.90
122	20.72
367	24.75
590	30.45
890	38.59
1190	47.01
1500	59.01
1900	73.98
2300	123.52
2800	178.90
3400	240.00
4100	280.00
4900	294.00

Table 3.6 The data of the real-time versus capacitance with increasing humidity

No. of days	Sensitivity (pF/%RH)		
	Low humid (10-40 %RH)	**Mid humid (40-70 %RH)**	**High humid (70-95 %RH)**
After three days	0.26	0.61	14.67
After seven days	0.29	0.53	14.28
After twenty one days	0.85	0.609	14.74

Table 3.7 The data of the calculated sensitivity after 3, 7, and 21 days in low, mid, and high humid regions

CHAPTER 4

DESIGN AND FABRICATION OF GRAPHENE FUNCTIONALIZED WITH CuO/SnO_2 NANOCOMPOSITES BASED LPG AND HUMIDITY SENSORS

The present chapter addresses the design and fabrication of the LPG sensor at room temperature based on the Graphene functionalized with CuO/SnO_2 (GCS) nanocompoistes synthesized with temperature controlled hydrothermal technique. The synthesized material is being characterized with several characterization techniques as scanning electron microscopy (SEM), Electron dispersive X-rays (EDX), Ultraviolet visible (UV-Vis.) spectroscopy, Particle size analysis, X-ray Diffraction (XRD), Fourier Transform Infrared (FTIR) and Raman spectroscopy. The surface morphological investigations as well as elemental mapping analysis details as the metal nanoparticles are attached with Graphene sheet at the side edges, corners and basal plane. Confirmation of the nano sized distribution has been completed with the particle size analysis. The band gap of the synthesized nanomaterials is 4.1 eV. The presence of the oxygen containing functional groups in the material is confirmed with the FTIR. The Raman spectrum is used to describe the nature of the synthesized Graphene as well as GCS. The % maximum sensor response of the LPG sensor is 11.76 for the 2.0 vol.% LPG and also the response and recovery time for the 0.5 vol.% LPG is 1.7 and 1.2 s respectively. The effect of the relative humidity at room temperature on LPG sensing has been well discussed.

CHAPTER 4

Design and fabrication of Graphene functionalized with CuO/SnO_2 nanocomposites based LPG and humidity sensors

4.1 Introduction

Nowadays the Nanotechnology is a growing field in the research era. Nanomaterials are growing the attention of researchers due to their smaller size and larger surface area. The tuning of size of the material leads to extraordinary mechanical, electrical, and optical properties [1]. Due to such properties in nanomaterials, these are applied in different applications in Physics, Chemistry, Biology, Environmental and medical sciences. There are plenty of nanomaterials as pure nanomaterials (e.g. metal oxides, polymers, carbon nanotubes, Graphene, Graphene Oxide etc.), nanocomposites, nanohybrids, nanometallopolymers etc. Due to their specific property (surface morphology, electrical, optical) these materials are used in solar cells, wastewater treatment, light-dependent resistors (LDR), electrical devices, biosensing and electrochemical sensing [2].

Carbon is abundant material on the earth in different forms. Based on structure the carbon nanomaterials are classified as Fullerene, Carbon Nanotubes, Graphene, Graphene Oxides etc. Out of these nanomaterials, each has its importance in the mechanical, chemical, optical properties and electrical properties [3]. Graphene is the most recent nanomaterial of the carbon discovered by Novoselove and being awarded the Nobel Prize in 2010. The bandgap of the Graphene can be tuned with doping, surface modification, or

functionalization. The surface of the Graphene can be altered with the functionalization of the Graphene via different nanomaterials, nanocomposites or polymers.

Nanocomposites reveal different properties compared to constituents nanomaterials. There is very huge literature available about the synthesis and different applications of the nanocomposites materials [4,5]. The synthesis process leads to the different surface morphology of the nanocomposites. Sensing is a surface dependent phenomenon. The surface of the material will be responsible for the sensing mechanism. The materials having a large surface area, more dangling bonds, defects, wrinkles with porous surface morphology are the fruitful sensing materials [6].

Graphene is a promising magic material having a large surface area. With the modification in the surface of the Graphene, we can generate more dangling bonds, defects, wrinkles and porous surface morphology. So by using material engineering for modifying the surface of the Graphene, we can make it a better sensing material. A lot of research papers are available in the sensor area of the Graphene doped/chemically or physically modified/decorated/functionalized with different material species [7-11].

The nanocomposites have been investigated by different groups of researchers worldwide for engineering the novel properties of material architectures at the nanoscale. There are carbon nanotubes, polymers, metallopolymers and a number of the metals present in the periodic table having large applications in the various fields of science [12, 13]. The nanostructured metal oxides as WO_3, Fe_3O_4, ZnO, TiO_2, In_2O_3, CuO, NiO, CeO_2 and SnO_2 may be accepted as potential candidates because of large applications in the diverse area of the research [14]. Due to the application of the SnO_2 in solar cells, light

emission diode, lithium-ion batteries, photocatalytic activity and gas sensors, it attracts the great attention of the researchers. Copper is another promising element of the periodic table. Due to the promoter activity of the copper, it is used in the catalyst in the various chemical processes. The nano composition of the CuO/SnO_2 plays an important role in different applications [15, 16, 17].

Various Graphene functionalized nanocomposites are studied in different applications. Some of the metal oxide synthesized by the hydrothermal technique at different temperatures for various time intervals such as Graphene nanocomposites as Co_3O_4-Graphene, α-Fe_2O_3/rGO, $Ni(OH)_2$/GS (GO), TiO_2-rGO, Co_3O_4/rGO, RGO/SnO_2, ZnO/rGO etc. which are used in the different application areas [18-25]. Sh. Nasresfahani et al demonstrated a methane gas sensor based on the Pd doped SnO_2/ rGO nanocomposite synthesized by the hydrothermal method [26].

Due to the inflammable and explosive nature of the LPG, it is very much hazardous for human beings as well as living or non-living environments. Its leakage causes many serious problems due to which its detection is much important. The LPG is a hydrocarbon gas with a mixture of propane and butane gases which belongs to the family of alkanes. In the industrial sector and to protect human health there are gas sensors which are used to detect LPG leakages. Many reports have been published by researchers to detect the LPG with the use of semiconductors metals oxide and polymer nanocomposites [27]. The previously reported LPG sensors based on Graphene with metal as SnO_2, CdO, SrO, Bi_2O_3 and MnO_2 nanocomposites via different research groups have been shown in Table 4.1 [28-35].

As per open literature, it is found that a LPG sensor generally works at high operating temperatures with large consumption of electric power. Still, there is much possibility to develop a LPG sensor for the low cost, highly sensitive, having fast sensor response and low response-recovery time along with stability operable at room temperature. To overcome these problems, we have developed a LPG sensor that is based on the thin film of Graphene functionalized with CuO/SnO_2 nanocomposites. In this Chapter, modification of the surface of Graphene with the CuO/SnO_2 nanocomposites has been described. The functionalization of CuO/SnO_2 nanocomposites with the Graphene may result in a large surface area, porous surface morphology along with metallic dangling bonds which may be fruitful for the sensing applications.

4.2 Experimental methods used

4.2.1 Chemicals used

The chemical used in our synthesis are Graphite powder, KNO_3, $KMnO_4$, H_2SO_4, H_2O_2, $CuCl_2$, $SnCl_2.2H_2O$, and DI water. The entire used chemical are analytical grade and was used as received from the Sigma Aldrich.

4.2.2 Synthesis of Graphene-CuO/SnO_2 nanocomposites

Graphene Oxide was synthesized according to the Modified Hummer method [10]. In a typical procedure, Graphite powder (1 g) and potassium nitrate (1 g) was poured into a conical flask of 500 ml and later this flask was placed in an ice-filled box. Then the sulfuric acid (50 ml) was added to this mixture and after that, this box was transferred on a stirrer @ 700 RPM for 1 h. This reaction was controlled at 0-5 ˚C

temperature and the $KMnO_4$ (6 g) powder was added gradually to this solution during the stirring. The prepared solution was transferred in the water bath at 35 ˚C with stirrings for 2 h, a greenish paste was obtained. After that, the 200 ml DI water was added to the solution and heated at 95 ˚C along with stirring for 0.5 h. Then at reflux condition, the few drops of H_2O_2 were added dropwise to the solution until its color changes to yellowish. The obtained solution was filtered and multiple washed with the DI water up to the neutral pH. The filtrate was employed for the sonication for 2 h then centrifuged at 4000 RPM for 20 minutes. The obtained supernatant was removed and the remaining sample was collected and dried at 50 ˚C for 8 h and ground with mortar Pestel into a fine powder of Graphene oxide (GO).

Now the 0.2 M solution of the $CuCl_2$ and $SnCl_2.2H_2O$ was made in the 50 ml DI water with stirring at the rate of 500 RPM. In this solution, the above synthesized GO was added gradually as 5 weight % of the taken metal powders. After stirring 1 h and sonicating 30 minutes the above solution was transferred into the Teflon liner. The autoclave was placed in a hot air oven at 180 °C for 12 h. The obtained solution was dried at 50 °C for the 8 h and was ground with the mortar pestle into the fine powder. The obtained powder was annealed at 500 °C in a programmable temperature-controlled furnace. The schematic for the synthesis of the Graphene functionalized with CuO/SnO_2 nanocomposite (GCS) with the hydrothermal technique is shown in Fig. 4.1. Implementing the same hydrothermal technique for pure GO and CuO/SnO_2 nanocomposites at the same conditions separately we obtained hydrothermally reduced Graphene (HRG) and CuO/SnO_2 (CS) nanocomposite.

4.2.3 Fabrication of thin films for the sensor

A thin film of the functionalized sample (Graphene/CuO/SnO_2) was deposited on a cleaned silica glass substrate of the dimension 1.0 × 0.5 cm^2 at 1500 rpm in a vacuum-assisted spin coater. The film was dehydrated on a hot plate at 50 ˚C for 30 minutes. Also, the films were annealed at 400˚C in the presence of 20% oxygen for 2 h in a temperature-controlled microprocessor assisted furnace. The electrodes on one of the films were grown with the silver paste. After pasting the electrodes on film, it was ready for the LPG sensing characterization.

4.2.3 LPG sensing measurement

According to the IUPAC, the sensitivity of the LPG sensor is defined as the slope of the calibration curves i.e. slope of sensor response versus target LPG concentration. Mathematically, the sensitivity of the sensor is calculated by Eqn 4.1:

$$\text{Senstivity} = \frac{Change\ in\ Sensor\ response}{Target\ gas\ concentration}\ \text{/vol.\%} \qquad (4.1)$$

The percentage sensor response (%S.R.) of the sensor was calculated using the formula given by Eqn.4.2:

$$\%\ Sensor\ Response = \frac{R_g \sim R_a}{R_a} \times 100 \qquad (4.2)$$

The response-recovery time of the sensor is defined as 90% of the final sensor output during the adsorption and desorption of the gas respectively [17]. The response-recovery of the sensor has been calculated by applying the exponential fitting for every concentration cycle. The exponential fitting for the growth and decay has been done with the Eqn. 4.3 and 4.4 respectively.

$$R_m = R_0 \exp(\frac{-t}{t_{res}}) \quad (4.3)$$

$$R_m = R_0\{1 - \exp(\frac{-t}{t_{rec}})\} \quad (4.4)$$

Where R_0 and R_m are the initial and measured values of the resistance, t_{res} and t_{rec} are the response and recovery time respectively [26]. The lab model of the LPG sensing setup is shown in Fig. 4.2. This setup consists of a LPG cylinder with a measuring unit, the vacuum-assisted chamber having a gas inlet, outlet, and sample holder. The sensing element was connected to the Keithley electrometer through the connecting wires which are further connected to a computer for the data recording.

4.3 Used characterization instruments

The Scanning Electron Microscopy (SEM) (JEOL, JSEM- 6490LV) with Electron Dispersive X-rays (EDX), Particle Size Analysis (Zeta nanosizer), UV-Visible Spectrophotometer (Evolution 201) were used as the characterization tools for the synthesized materials. The crystal and phase were investigated by powder X-ray Diffractometer (XRD) (Bruker D8 Advance, using Cu Kα radiation) λ=0.15418 nm (at a scan rate of 0.2°/s. A Raman spectrometer (model: Airix Corporation, Japan with laser excitation at 514 nm) was used.

4.5 Results and Discussion

4.5.1 Surface morphology and elemental analysis

The scanning electron microscopy (SEM) was used for the surface morphological investigations. Fig. 4.3 is illustrating the SEM micrographs of the synthesized GCS along

with the elemental mapping of the same material. At the 1000 and 500 nm scale, the SEM images are shown in Fig. 4.3 (a) and (b) respectively. In Fig. 4.3 (a) metal nanoparticles are shown in the encircled part while inside the rectangle there are the two Graphene sheets attached with the metallic nanoparticles. These metallic nanoparticles form the dangling bonds which have a major significance in LPG sensing. Fig. 4.3 (b) is the SEM micrograph of the GCS at 500 nm scale showing the porous surface morphology along with the encircled metallic nanoparticles. The metallic dangling bonds, porous surface morphology and defects in the Graphene are responsible for a good LPG sensor application. Fig. 4.3 (c) is showing the elemental mapping analysis with the presence of the carbon, oxygen, Sn and Cu metals. EDX confirms the presence of the metallic nanoparticles as CuO and SnO_2 which are earlier observed in the SEM micrographs already shown encircled in Fig. 4.3 (a) and (b). The SEM investigation confirms that metal nanoparticles are attached with the Graphene sheet at the side edges, corners and in the basal plane. These metal nanoparticles form the metallic dangling bonds which are useful in the sensing application.

4.5.2 Optical absorption analysis

The optical absorption analysis of the synthesized materials was performed with the help of the UV-Vis. spectrophotometer in the wavelength range of 190-1100 nm. Fig. 4.4 (a) shows the absorption spectrum of the Hydrothermally reduced Graphene (HRG), CuO/SnO_2 (CS) and Graphene functionalized with CuO/SnO_2 (GCS) while Fig. 4.4 (b) is the Tauc plots of the same materials. The maximum absorption was observed in the 290-320 nm wavelength range. Also, it was found that all the materials have almost the same absorption in the same wavelength range so these materials can form a good composite

material for the electronic device application purpose. The maximum absorption of the synthesized materials reflects the optical energy band gaps. In Fig. 4.4 (b) the Tauc plots are shown, extrapolation on tangent cuts on X-axis which gives the optical bandgap of the synthesized materials. The optical band gaps of the materials are the same and are equal to the 4.1 eV.

4.5.3 Functional group analysis

The FTIR is used to obtain information about the molecular fragment, specifically functional groups in the synthesized materials. This technique uses the Infrared radiation having a wavenumber range 400-4000 cm^{-1} of the electromagnetic spectrum. The FTIR spectrum of the synthesized HRG, CS and GCS is shown in Fig. 4.5 (a), (b) and (c) respectively. The bands present in 400-780 cm^{-1} wavenumber range corresponds to the metallic bond vibrations present in the CS and GCS. The valley observed at 1016 cm^{-1} relates to the –C=O bonds vibrations present in the HRG shown by the circle in Fig. 4.5 (a). The C=C bond stretching vibrations are corresponded to in wavenumber range 1500-1700 cm^{-1}. The broadband of the -O-H bonds stretching vibration has been investigated in the wavenumber range 3412-3420 cm^{-1} [36].

4.5.4 Dynamic Light Scattering (DLS) analysis

The measurement of the particle size distribution is based on dynamic light scattering. By measuring the Brownian motion of the particles in a dilute solution, the technique estimates the particle size distributions. Figure 4.6 (a), (b) and (c) illustrate the particle size distribution curve for the HRG, CS and GCS nanocomposites respectively. Fig. 4.6 (a) shows that the HRG has an average sheet size of 255 nm with the distribution

range 219-295 nm. From Fig. 4.6 (b), it is clear that the synthesized CS metal nanocomposites have the particle size distribution in the range of 21-32 nm and the average particle size is 28 nm having an intensity of 89.71%. Fig. 4.6 (c) shows the particle size distribution of the synthesized GCS with the distribution range 255-397 nm and the average particle size is 342 nm with an intensity of 63.23%. After the functionalization of the Graphene with the CS metal nanocomposites, the size distribution and average size have been increased in comparison to the HRG, it means that the metal nanoparticles are get attached with the Graphene sheet at the corner, side edges and basal plane which one is already observed in the SEM analysis.

4.5.5 X-Ray Diffraction (XRD) analysis

XRD characterization was used for the structural and phase analysis of the materials. Fig. 4.7 illustrates the XRD patterns of the synthesized HRG, CS and GCS nanocomposites. Fig. 4.7 (a) shows the XRD pattern of the synthesized Graphene having the two Bragg's plane (002), (004) along with square placed at 26.35°, 54.49° 2θ values respectively and these planes are well-matched with the JCPDS # 075-1621. The average crystallite size (L) of the Graphene-based nanomaterials in the plane is calculated with the help of the Debye-Scherer formula given by Eqn 4.5;

$$L = \frac{1.84\lambda}{\beta \cos \theta} \qquad (4.5)$$

Where λ is the wavelength of the X-rays used (0.1541 nm for Cu Kα lines), β is the Full-width half maxima (FWHM) and θ is the Bragg's diffraction angle. The average crystallite size of the Graphene in the plane is calculated as 12.10 nm. The XRD pattern

of the CS nanocomposites having several planes is shown in Fig. 4.7 (b) and the average crystallite size of the material was calculated as 12.88 nm. Present planes are well-matched with the standard JCPDS #088-287 and JCPDS #004-0836 and have been shown by the triangle and asterisk respectively. Fig. 4.7 (c) is the XRD diffractogram of the synthesized GCS nanocomposite illustrating the existence of the crystalline phase of the material due to the presence of several Bragg's peaks. The average crystallite size of the synthesized GCS was 15.19 nm.

From the deep observation of the XRD pattern of the synthesized materials, it can easily be said that the average crystallite size of the synthesized GCS gets decreased in comparison to the HRG. The average crystallite size of the GCS gets decreased because the GO sheets get breakage during the hydrothermal reduction and metal nanoparticles get attached to it.

4.5.6 Raman analysis

The Raman analysis is a very important characterization tool in the case of the different allotropes of carbon nanomaterials (Buckminster fullerenes, carbon nanotubes, carbon nanoribbons, and Graphene etc). This technique is a vibrational technique, extremely sensitive to the bonding and geometrical structure within the molecule. The experimental and peaks fitted plots of the Raman spectrum of synthesized HRG and GCS have been illustrated in Fig. 4.8 (a) and (b) respectively. In Fig. 4.8 (a), there are two sharp peaks present at 1348, 1607 cm^{-1} and one broad peak at 2678 cm^{-1} Raman shift are known as D, G and 2D bands respectively. These obtained bands are the characteristics of the reduced Graphene and the disorder parameter (I_D/I_G ratio) for the same was calculated

as 1.23. In the Raman spectrum of GCS, there are some extra peaks observed below 500 cm^{-1} Raman shift. These peaks represent the bond stretching vibrations with the presence of Sn and Cu metal nanoparticles. In this spectrum the D, G and 2D bands are observed at 1317, 1588 and 2712 cm^{-1} Raman shift with the sharper than the HRG and also the calculated I_D/I_G ratio was 1.09 for the same. The presence of some extra peaks below 500 cm^{-1} Raman shift and shifting in the positions of the D, G and 2D bands are the signatures of the Graphene has been successfully functionalized with the CuO/SnO_2 nanoparticles [37, 38]. The decrease in the I_D/I_G ratio of the GCS in comparison to the HRG confirmed that the GCS has more crystalline nature than that of the HRG.

4.6 Performance of the LPG sensor and its attributes

The sensing device for the GCS based thin film has been prepared accordingly to 4.2.3 section. This sensing device is placed in the lab-made model of the LPG sensor characterization setup as shown in Fig. 4.2. All the connections were completed among the Keithley electrometer; a vacuum-assisted sensing chamber and a computer for data recording. The vacuum is created inside the gas sensing chamber. Now a potential of 50 V was applied between the electrodes of the sensing device to obtain the stable or saturation state of the resistance of the sensing device. Now the 0.5 vol.% LPG is exposed inside the gas sensing chamber, the resistance of the sensing device rises to a stable state. As the gas is released from the chamber the resistance of the sensing device gets starts decreasing. This experiment is performed for the 1.0, 1.5 and 2.0 vol.% concentration of the LPG. LPG plots of the recorded data for every concentration has been shown in Fig. 4.9. In this figure, there are four response-recovery cycles with resistance versus exposure time corresponding to 0.5, 1.0, 1.5, and 2.0 vol.% LPG

concentration respectively. In the first cycle of response (for 0.5 vol.%), the resistance (R_a) of the sensing material in absence of the LPG was found as 1.77×10^9 Ω while the as LPG was exposed the resistance rises to 1.87×10^9 Ω. As the LPG was removed from the chamber (recovery cycle for 0.5 vol.%), the resistance started decreasing and not achieved the initial state of the resistance (R_a) because few LPG molecules get trapped into the pores of the sensing material and may not be removed. As the LPG concentration was increased to 1.0 vol.%, the response-recovery cycle (second cycle) shown in Fig. 9 is obtained and the resistance rises from 1.81×10^9 Ω (R_a) to 1.93×10^9 Ω (R_g) with LPG exposure. Similarly, for the 1.5 vol.% concentration the resistance of the sensing device rises from 1.82×10^9 Ω to 2.01×10^9 Ω while the change in the resistance was observed from 1.87×10^9 Ω to 2.09×10^9 Ω for the 2.0 vol.% concentration of the LPG.

4.6.1 LPG sensing principle

The gas sensing principle is based on the variation in the electrical properties of the sensing material after exposing the gas. The LPG sensing operation is based on the charge transfer between the target LPG molecules and sensing materials. At room temperature due to electrostatic potential applied through the electrodes of the sensor, the equilibrium occurs between the oxygen present on the surface of the sensing material and atmospheric oxygen forming the ionic oxygen species which are shown by Eqn 4.6 and 4.7. As the LPG interacts with the sensing material, the formed ionic oxygen captured the electron from the sensing material. This results in a decrease in the density of the electron and the resistance of the sensing material get increasing. LPG mainly consists of methane, propane, and butane generally can be written as C_nH_{2n+2}. As C_nH_{2n+2} interacted

with ionic oxygen species, it forms the complex $C_nH_{2n}O$ along with water which is shown in Eqn 4.8.

$$O_2(gas) \leftrightarrow O_2(ads) \quad (4.6)$$

$$O_2(ads) + e^- \rightarrow O_2^- \quad (4.7)$$

$$C_nH_{2n+2} + O_2^- \rightarrow C_nH_{2n}O + H_2O + e^- \quad (4.8)$$

4.6.2 LPG sensor attributes

The main attributes of a sensor are sensitivity, sensor response, repeatability, selectivity, and response-recovery time. Good sensors exhibit large sensitivity, high response and low response-recovery time. The sensitivity, sensor response of the sensor was calculated according to Eqn. 4.1 and 4.2 respectively and the response-recovery times were found using Eqns 4.3 & 4.4 respectively. All the parameters were calculated using the data of Fig. 4.9 and are tabulated in Table 4.2.

Fig. 4.10 is illustrating the LPG sensor attributes for the GCS based sensor. In Fig. 4.10 (a), %S.R. versus LPG concentration has been plotted and it illustrates the linear variation in the %S.R. concerning LPG concentration. Such types of characteristics are required for the sensing device fabrication purpose. As the concentration of gas gets increasing, the sensor response will be increasing. The % sensor respose of the sensor was found maximum 11.76 for the 2.0 vol.% concentration LPG. The response-recovery time of the sensor is a very important parameter. The calculated response-recovery time for each concentration of the gas has been shown in Table 4.2. The response-recovery

time concerning LPG concentration is shown in Fig. 4.10 (b) and this investigates that as the concentration of the LPG increases the response-recovery time also increases. The response-recovery time was calculated with exponential decay and growth fittings. The exponential decay and growth fitted curves for the 0.5 and 1.0 vol.% are shown in Fig. 4.10 (c) and (d) respectively. The response and recovery time were found as 1.2 and 3.5 s for the 0.5 and 1.0 vol.% concentration of LPG respectively. The repeatability analysis for the 1 vol.% LPG concentration had been performed and is shown in Fig. 4.11.

4.7 Humidity sensing application

The humidity sensor characterization of the thin film based on the GCS had been also performed. The experimental setup for the humidity sensor characterization has been already described in **Chapter 2**. All the data related to it has been recorded using this setup and plots of the same are shown in Fig. 4.12. Fig. 4.12 (a) is showing the impedance versus %RH curve and the related data is shown in Table 4.3. The slope of this curve is defined as the sensitivity of the humidity sensor and all other humidity sensor attributes are defined already in our previous **Chapters 2 and 3**. The detailed descriptions about the sensing mechanism of the impedance-based humidity sensor have been already discussed in the previous **Chapter 2**. The experiment was performed in the 10-95 %RH range and the calculated sensitivity of the sensor was 1.20 MΩ/%RH in the same range of the humidity. The response-recovery time of a sensor is an important parameter of the sensor and the calculated response and recovery time for the GCS based humidity sensor was 18 and 6 s respectively. The response and recovery time curve has shown in Fig. 4.12 (b) and related data has been shown in Table 4.4. Fig. 4.12 (c) is illustrating the repeatability curve for the GCS based humidity sensor and is showing the

94.17 % repeatable nature of the sensor. The long term stability of a sensor shows the life of the sensor as well as its accuracy after a long time. The stability analysis curve after the 3, 7, and 15 days for the GCS based humidity sensor has been shown in Fig. 4.12 (d) and this results in good stability after these days. The related data of the repeatability and ageing effect has been shown in Table 4.5.

4.8 Selectivity of the sensor

The selectivity of the sensor is an important parameter. A sensor may not be best for each gas or other sensing species but it may be best for a particular. The process of the selection of the best sensor for a particular sensing species is known as the selectivity of the sensor. The selectivity of the LPG sensor for 2.0 vol.% LPG concentration has been studied towards the humidity (50 %RH), acetone (2.0 vol.%), ethanol (2.0 vol.%) and CO_2 gas (2.0 vol.%) and is shown in the Fig. 4.13. The sensor shows the maximum %sensor response for the LPG and it confirms that this sensor is selective for the LPG in comparison to studied cases. The selectivity of the LPG sensor can be explained based on the variations in the electrical resistance of the sensor with the charge transfer between the sensing material and sensing species. In our case, the charge transfer between the LPG and synthesized GCS is responsible for the maximum change in the resistance of the sensor.

4.9 Effect of humidity on the LPG sensor

The effect of relative humidity (RH) at 30, 50, 60 and 70 %RH on the LPG sensor for 2 vol.% concentration at room temperature has been studied and the plot is shown in Fig. 4.14. The plotted data of LPG sensing performance in the presence of 30, 50, 60 and

70 %RH is shown in Fig. 4.14 (a), (b), (c) and (d) respectively. The change in the resistance from the 1.61×10^9 to 1.66×10^9 Ω was observed in the presence of the 30 %RH and the %S.R. was found as 3.11. At the 50 %RH, the change in the resistance was observed from 1.22×10^9 to 1.34×10^9 Ω with the exposure of the LPG and the calculated %S.R. was found 9.85. In the presence of the 60 %RH the LPG sensor has the %S.R. 16.33 with the variation in the resistance from the 9.53×10^8 to the 1.1×10^9 Ω. Lastly, at 70 %RH the sensor shows the %S.R. as 18.77 with a maximum change in the resistance from 7.5×10^8 to 8.90×10^9 Ω. A close look at the data obtained from LPG sensing reveals that with increasing %RH, the resistance (or conductivity) gets decreasing (or increasing) and the %S.R. also gets increasing. The increase in the %S.R. and conductivity of the sensing material can be explained by the interaction of the humidity with sensing material. The dissociation of the water molecule on the surface of the sensing material generates the hydroxyl ions which donates the electron and are used to decrease or increase the resistance or conductivity of the sensing material. The oxygen atoms of the hydroxyl group get attached to the surface of the material and surface interaction sites of the sensor get enhanced which increases the sensor response.

4.10 Conclusion

We have successfully designed and fabricated the LPG sensor based on the Graphene functionalized with CuO/SnO_2 (GCS) nanocomposites synthesized by using a temperature-controlled hydrothermal technique. The particle size analysis confirmed that the synthesized materials have the range of nanometers. The surface morphological investigation along with elemental mapping analysis confirmed the metal nanoparticles

are attached with the Graphene sheet at the side edges, corners and basal plane. The optical absorption in the UV-Visible range shows the maximum in the range 290-320 nm and results in the bandgap of the synthesized nanomaterials as 4.1 eV. The presence of the oxygen-containing functional groups in the material is confirmation of the porous material. The Raman spectrum is used to well describe the nature of the synthesized Graphene as well as GCS. The % sensor response of the sensor is maximum (11.76) for the 2.0 vol.% LPG and minimum response and recovery time are 1.7 and 1.2 s for the 0.5 vol.% LPG. The selectivity of the sensor shows good results for the LPG in comparison to the ethanol, acetone, and relative humidity, and CO_2 gas. The effect of the relative humidity on the LPG sensor exhibited a relative increase in the sensor response of the sensor increases with increasing the relative humidity. In this chapter, the sensitivity of the humidity sensor was found decreased in comparison to the previous chapters while an improved LPG sensor based on the GCS was reported here. So the GCS-based LPG sensor can be developed for commercial as well as industrial purposes for fast detection as it has a lower response-recovery time for the 0.5 vol.% concentration.

References

[1] G. Mandal and T. Ganguly, Applications of nanomaterials in the different fields of photosciences, Indian J. Phys. 85 (8) (2011) 1229-1245.

[2] Jaise Mariya George, Arun Antony, and Beena Mathew, Metal oxide nanoparticles in electrochemical sensing and biosensing: a review, Microchimica Acta 185(7) (2018) 1-26.

[3] K. Kumar and B. C. Yadav, An Overview on the Importance of Chemical Vapour Deposition Technique for Graphene Synthesis, Adv. Sci. Eng. Med., 10 (2018) 760–763.

[4] Z. Liu, L. Zhang, S. Poyraz, and X. Zhang, Conducting polymer-metal nanocomposites synthesis and their sensory applications, Current Organic Chemistry 17 (20) (2013) 2256-2267.

[5] P. H. C. Camargo, K. G. Satyanarayana, and F. Wypych, Nanocomposites: synthesis, structure, properties and new application opportunities, Materials Research 12 (1) (2009) 1-39.

[6] Anindya Nag, Arkadeep Mitra, Subhas Chandra Mukhopadhyay, Graphene and its sensor-based applications: A review, Sensors and Actuators A: Physical 270 (2018) 177–194.

[7] K. P. Prathish, M. M. Barsan, D. Geng, X. Sun, and C. M. A. Brett, Chemically modified graphene and nitrogen-doped graphene: electrochemical characterization and sensing applications, Electrochimica Acta 114 (2013) 533-542.

[8] M. Kaur, M. Kaur, and V. K. Sharma, Nitrogen-doped graphene and graphene quantum dots: A review onsynthesis and applications in energy, sensors and environment., Advances in colloid and interface science 259 (2018) 44-64.

[9] P. A. Pandey, N. R. Wilson, and J. A. Covington, Pd-doped reduced graphene oxide sensing films for H_2 detection, Sensors and Actuators B: Chemical 183 (2013) 478-487.

[10] K. Kumar, U. Kumar, M. Singh, and B. C. Yadav, Synthesis and characterizations of exohedral functionalized graphene oxide with iron nanoparticles for humidity detection, Journal of Materials Science: Materials in Electronics, 30(14) (2019) 13013-1302.

[11] K. Kumar, A. Singh, U. Kumar, R. K. Tripathi, B. C. Yadav, The beauty inhabited inside the modified Graphene for moisture detection at different frequencies, Journal of Materials Science: Materials in Electronics, 31 (2020) 10836-10845.

[12] U. Kumar and B. C. Yadav, Synthesis of carbon nanotubes by direct liquid injection chemical vapor deposition method and its relevance for developing an ultra-sensitive room temperature based CO_2 sensor, Journal of the Taiwan Institute of Chemical Engineers, 96 (2019) 652-663.

[13] U. Kumar and B. C. Yadav, Development of humidity sensor using modified curved MWCNT based thin film with DFT calculations, Sensors and Actuators B: Chemical, 288 (2019) 399-407.

[14] S. Singh, U. Kumar, B. C. Yadav, K. Kumar, R. Tripathi and K. Singh, Development of scattering based glucose sensor using hydrothermally synthesized cuprous oxide nanoparticles, Results in Physics 15 (2019) 1-28.

[15] M. K. Mishra, N. Singh, V. Pandey, and F. Z. Haque, Synthesis of SnO_2 Nanoparticles and Its Application in Sensing Ammonia Gas Through Photoluminescence, Journal of Advanced Physics 5, (2015) 1–5.

[16] M. R. Kumar, G. Murugadoss, A. N. Pirogov, and R. Thangamuthu, A facile one-step synthesis of SnO_2/CuO and CuO/SnO_2 nanocomposites: photocatalytic application, Journal of Materials Science: Materials in Electronics 29 (16) (2018) 13508-13515.

[17] S. Singh, N. Verma, A. Singh, and B. C. Yadav, Synthesis and characterization of CuO–SnO_2 nanocomposite and its application as liquefied petroleum gas sensor, Materials science in semiconductor processing 18 (2014) 88-96.

[18] E. M. Kamar and S. I. El-Dek, 2018 IOP Conf. Ser.: Mater. Sci. Eng. 464 012010.

[19] M.-Y. Wang, T. Shen, D.-E. Zhang, Z.-W. Tong, J. Chen, One-pot synthesis of Fe_2O_3 nanoparticles-decorated reduced graphene oxide for efficient nonenzymatic H_2O_2 biosensor, Sensors and Actuators B: Chemical 190 (2014) 645-650.

[20] H. Wang, H. S. Casalongue, Y. Liang and H. Dai, $Ni(OH)_2$ Nanoplates Grown on Graphene as Advanced Electrochemical Pseudocapacitor Materials, Journal of the American Chemical Society 132 (21) (2010) 7472-7477.

[21] H. H. Mohamed, I. Hammami, H. A. Baghdadi, and S. S. Al-Jameel, Multifunctional TiO_2 microspheres-rGO as highly active visible light photocatalyst and antimicrobial agent, Mater. Express, 8 (4) (2018) 345-352.

[22] A. Mishra, B. K. Kuanr, and T. Mohanty Co_3O_4/reduced graphene oxide nanocomposite for removal of organic pollutants fromaqueous medium, AIP Conference Proceedings 1832 (2017) 050006.

[23] D. Zhang, H. Chang, and R. Liu, Humidity-Sensing Properties of One-Step Hydrothermally Synthesized Tin Dioxide-Decorated Graphene Nanocomposite on Polyimide Substrate, Journal of Electronic materials, Vol. 45 (8) (2016) 4275-4281.

[24] L. Zhang, N. Li, H. Jiu, G. Qi, and Y. Huang, ZnO-reduced graphene oxide nanocomposites as efficient photocatalysts for photocatalytic reduction of CO_2, Ceramics International 41 5 (2015) 6256-6262.

[25] A. Jana, E. Scheer and S. Polarz, Synthesis of graphene–transition metal oxide hybrid nanoparticles and their application in various fields, Beilstein J. Nanotechnol. 8 (2017) 688–714.

[26] Sh. Nasresfahani, M. H. Sheikhi, M. Tohidi, and A. Zarifkar, Methane gas sensing properties of Pd-doped SnO_2/reduced graphene oxide synthesized by a facile hydrothermal route, Materials Research Bulletin 89 (2017) 161-169.

[27] M. Singh, B. C. Yadav, A. Ranjan, M. Kaur and S. K. Gupta, Synthesis and characterization of perovskite barium titanate thin film and its application as LPG sensor, Sensors and Actuators B: Chemical, 241 (2017) 1170–1178.

[28] K. R. Nemade, S.A. Waghuley, Chemiresistive gas sensing by few-layered graphene. J. Electron. Mater., 42(10) (2013) 2857–2866.

[29] S. Goutham, S. Bykkam, K. K. Sadasivuni, D. S. Kumar, M. Ahmadipour, Z. A. Ahmad, and K. V. Rao, Room-temperature LPG resistive sensor based on the use of a few-layer graphene/SnO_2 nanocomposite, Microchimica Acta 185 (1) (2018) 1-8.

[30] S. Goutham, N. Jayarambabu, C. Sandeep, K. K. Sadasivuni, D. S. Kumar, K. V. Rao, Resistive room temperature LPG sensor based on a graphene/CdO nanocomposite, Microchimica Acta, 186 (2019) 62 1-8.

[31] K. R. Nemade, S.A. Waghuley, in situ synthesis of graphene/SnO_2 quantum dots composites for chemiresistive gas sensing, Materials Science in Semiconductor Processing 24 (2014) 126–131.

[32] K. R. Nemade, and S. A. Waghuley, Strontium oxide quantum dot decorated graphene composites for liquid petroleum gas sensing, Journal of the Chinese Advanced Materials Society 1 (3) (2013) 219-228.

[33] K. R. Nemade, S.A. Waghuley, LPG sensing application of graphene/Bi_2O_3 quantum dots composites, Solid State Sciences 22 (2013) 27-32.

[34] K. R. Nemade, S.A. Waghuley, Preparation of MnO_2 immobilized graphene nanocomposite by solid state diffusion route for LPG sensing, J. Lumin. 153 (2014) 194–197.

[35] J. G. Thangamani, K. Deshmukh, K. K. Sadasivuni, D. Ponnamma, S. Goutham, K. V. Rao, K. Chidambaram, M. B. Ahamed, A. N. Grace, M. Faisal, S. K. Khadheer Pasha,White graphene reinforced polypyrrole and poly(vinyl alcohol)

blend nanocomposites as chemoresistive sensors for room temperature detection of liquid petroleum gases, Microchimica Acta, 184 (2017) 3977-3987.

[36] M. R. Kumar, G. Murugadoss, A. N. Pirogov, and R. Thangamuthu, A facile one-step synthesis of SnO_2/CuO and CuO/SnO_2 nanocomposites: photocatalytic application, Journal of Materials Science: Materials in Electronics 29 (16) (2018) 13508-13515.

[37] A. Gupta, R. Jamatia, R. A. Patil, Y.-R. Ma, and A. K. Pal, Copper oxide/reduced graphene oxide nanocomposite-catalyzed synthesis of flavanones and flavanones with triazole hybrid molecules in one pot: a green and sustainable approach, ACS Omega 3, (7) (2018) 7288-7299.

[38] S. Sagadevan, Z. Z. Chowdhury, M. R. B. Johan, F. A. Aziz, E. M.Salleh, A.Hawa and R. F. Rafique, A one-step facile route synthesis of copper oxide/reduced graphene oxide nanocomposite for supercapacitor applications, Journal of Experimental Nanoscience 13 (1) (2018) 284-296.

Figures

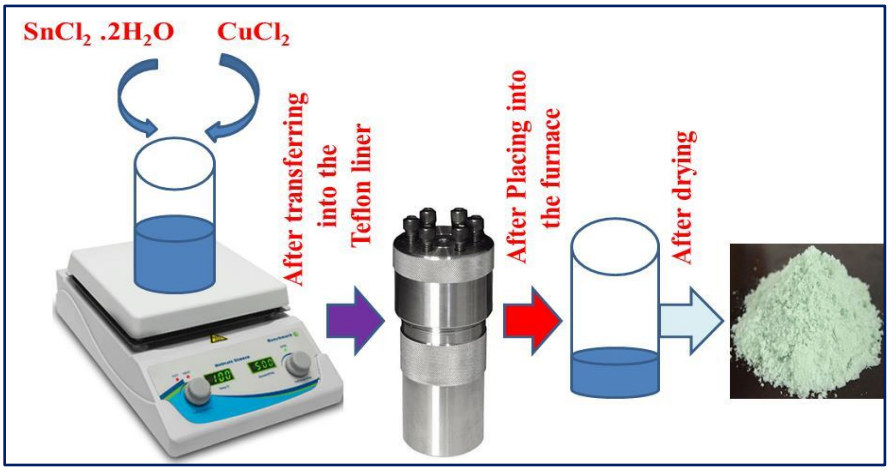

Fig. 4.1 Schematic of synthesis of Graphene functionalized with CuO/SnO_2 nanocomposite using the hydrothermal technique.

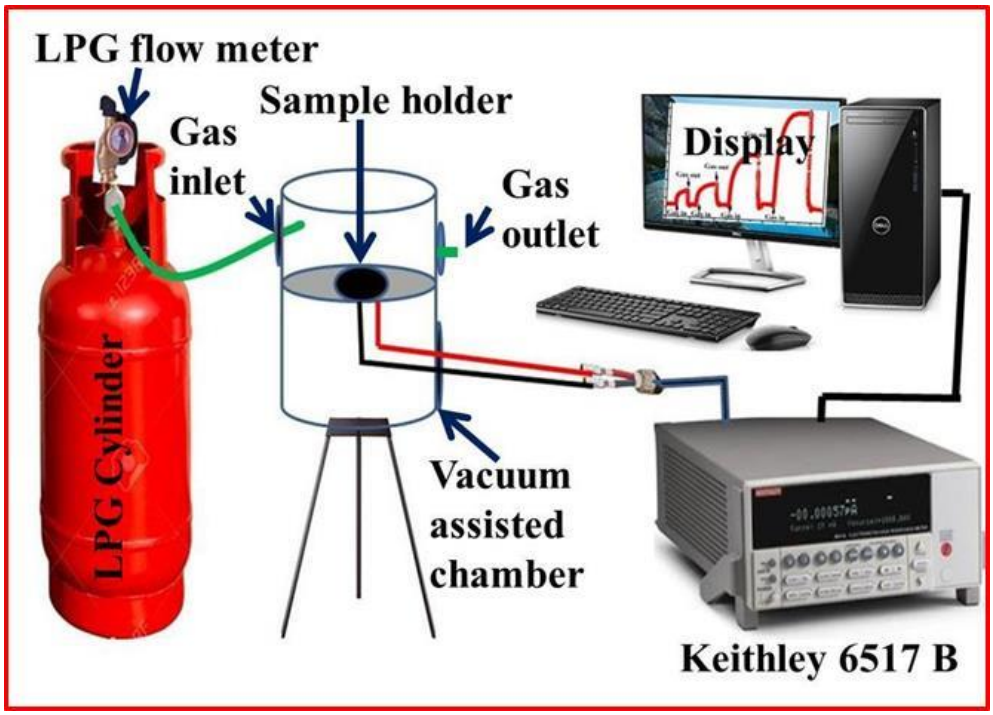

Fig. 4.2 Lab model of the LPG sensing setup

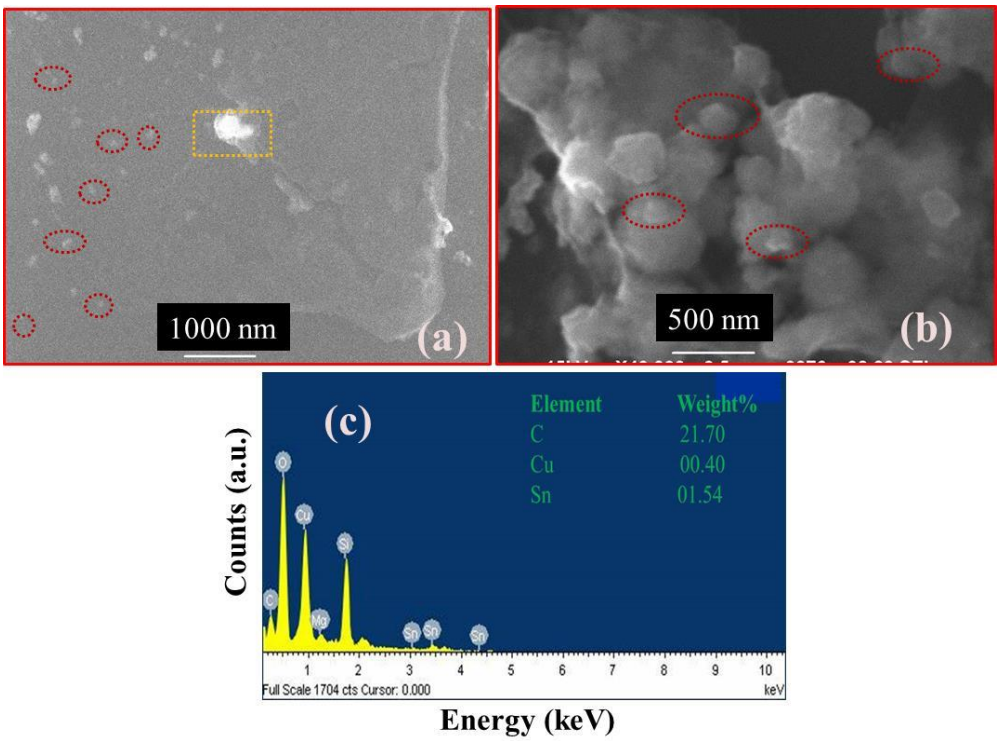

Fig. 4.3 (a) and (b) are the SEM micrographs of the Graphene functionalized with CuO/SnO_2 nanocomposite at 1000 and 500 nm scale respectively and (c) is the EDX spectrum.

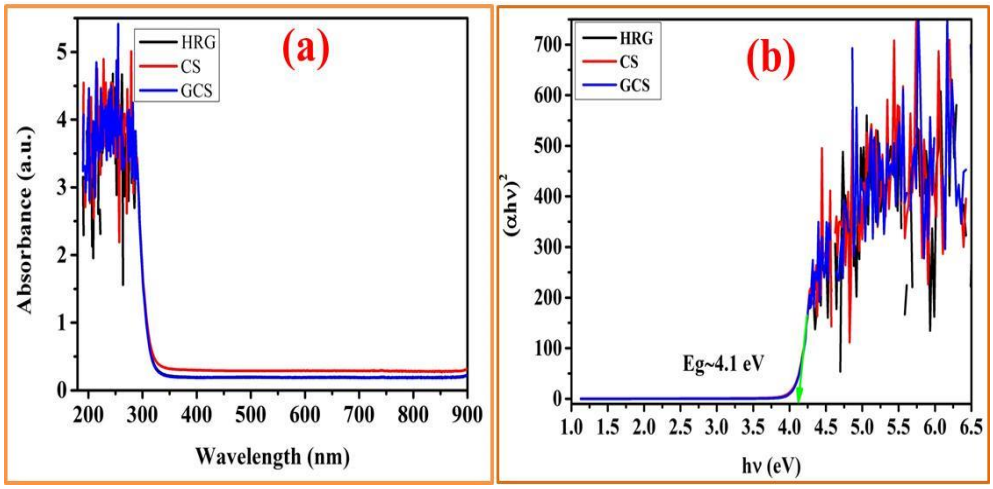

Fig. 4.4 (a) is showing the absorption spectrum of the HRG, CS, and GCS while (b) is the Tauc plot of the same

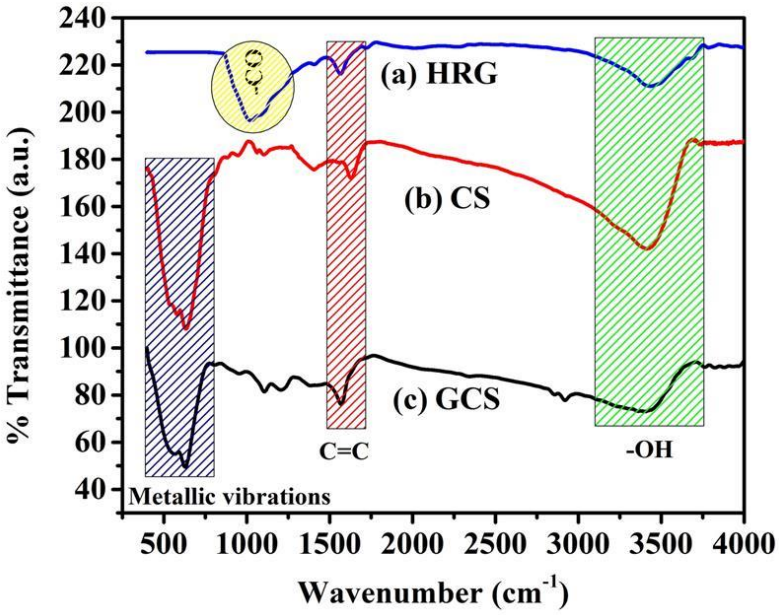

Fig. 4.5 FTIR spectrum of the synthesized HRG, CS and GCS

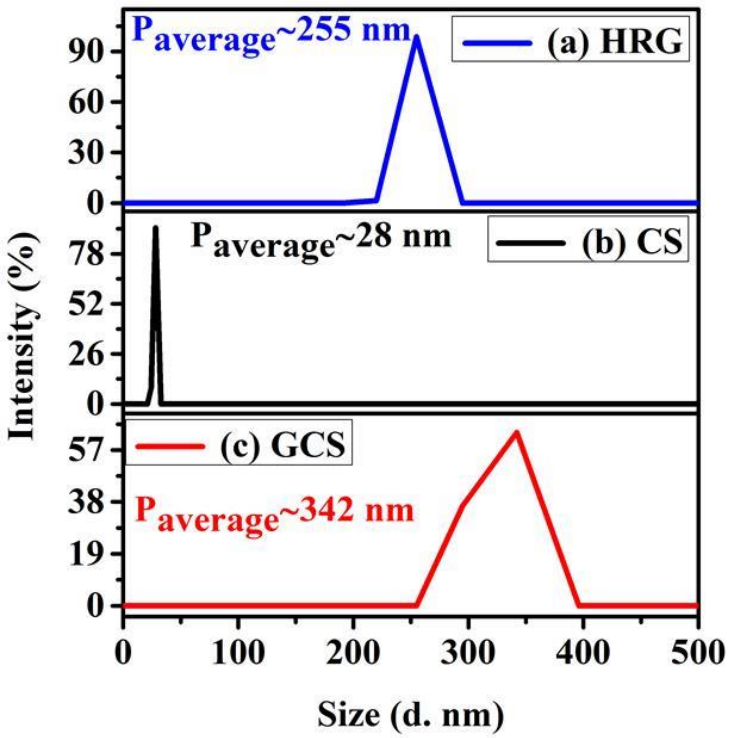

Fig. 4.6 Particle size distribution curve for the synthesized HRG, CS, and GCS nanocomposites

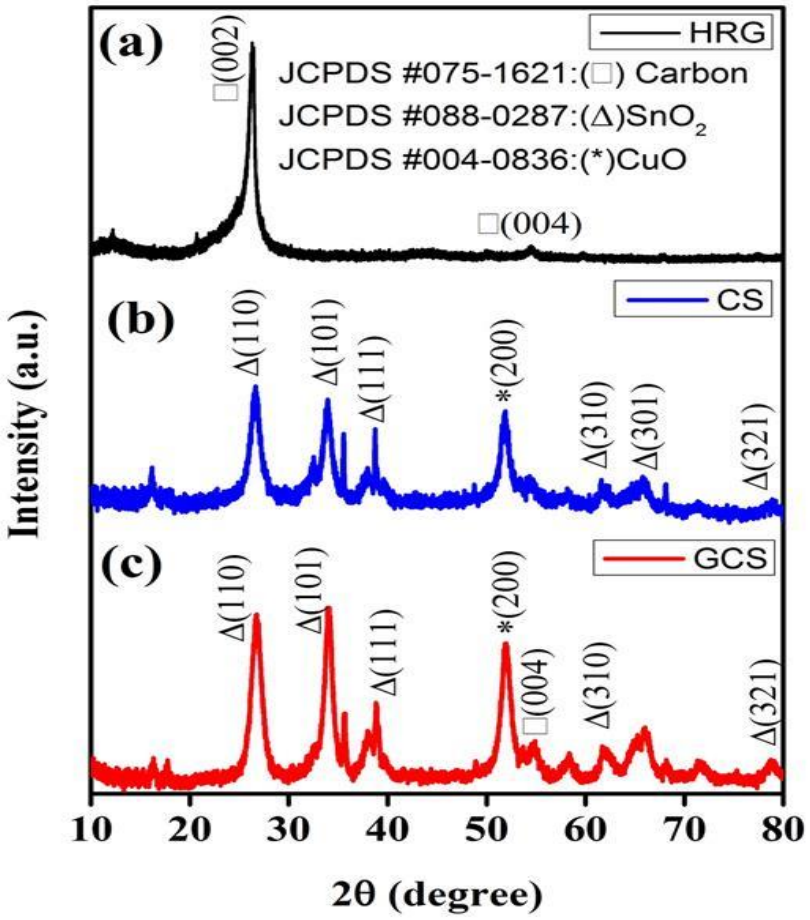

Fig. 4.7 XRD pattern of the synthesized HRG, CS and GCS

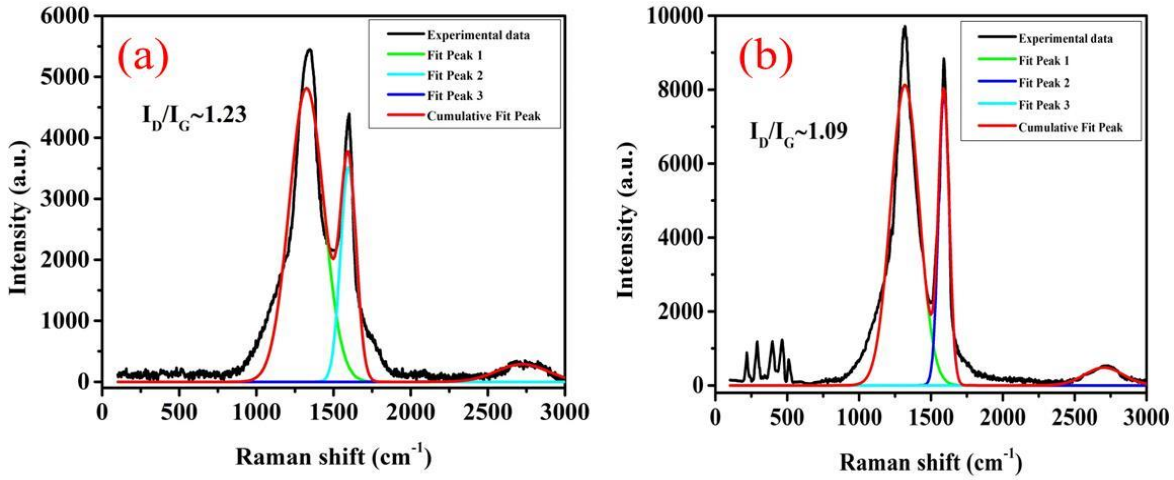

Fig. 4.8 Raman spectrum of the synthesized (a) HRG and (b) GCS

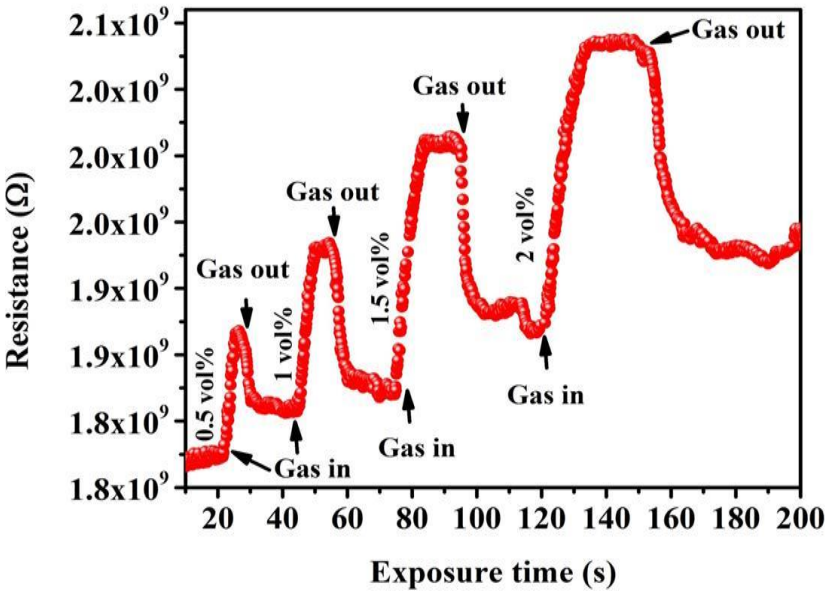

Fig. 4.9 LPG sensing characteristics of the synthesized GCS based sensor

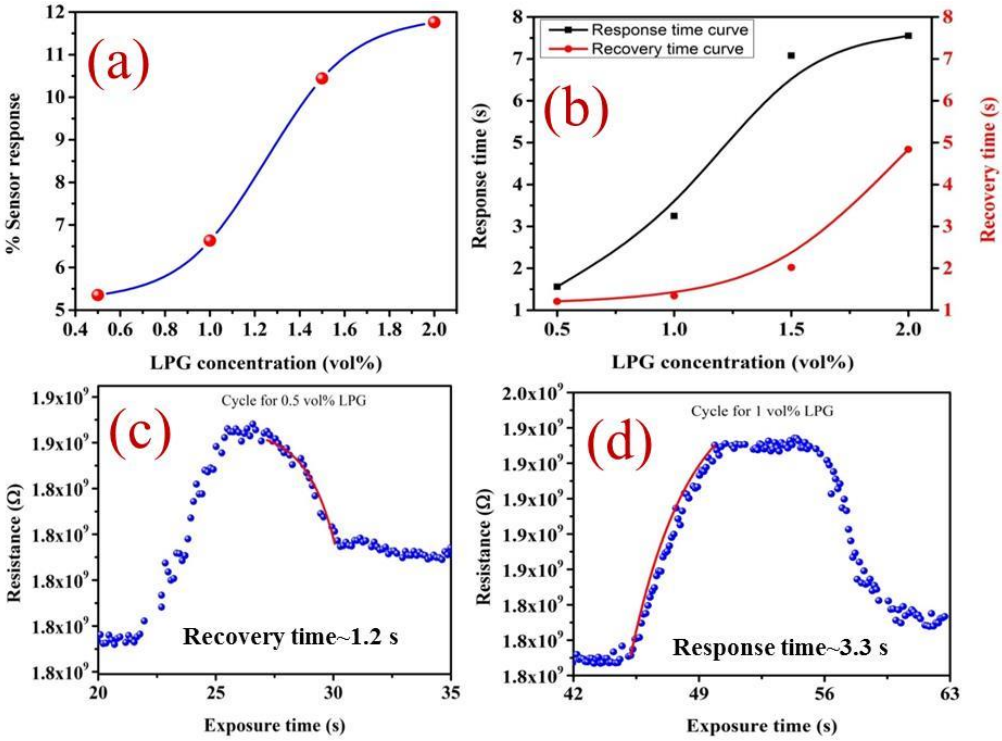

Fig. 4.10 LPG sensor attributes based on the equipped GCS sensor

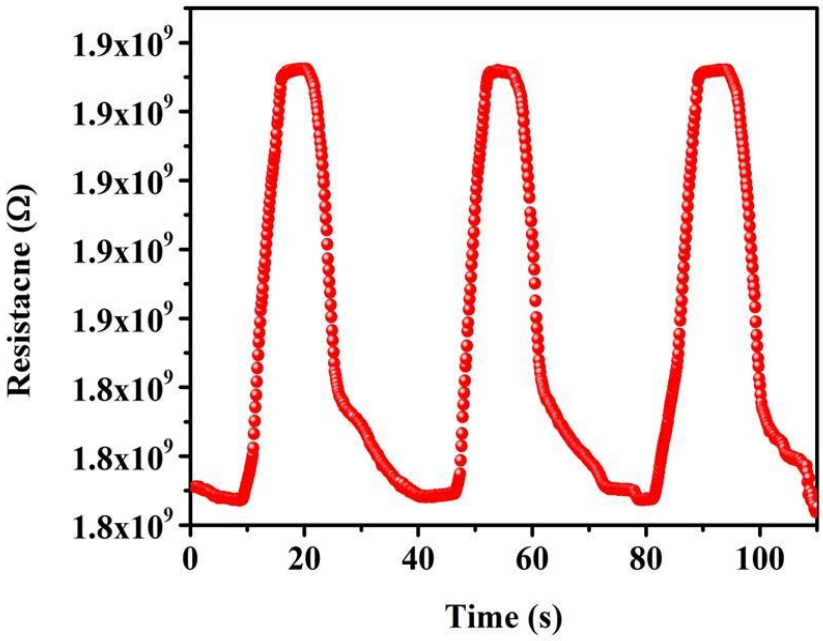

Fig. 4.11 Repeatability curve for the GCS based LPG sensor for 1.0 vol.% concentration

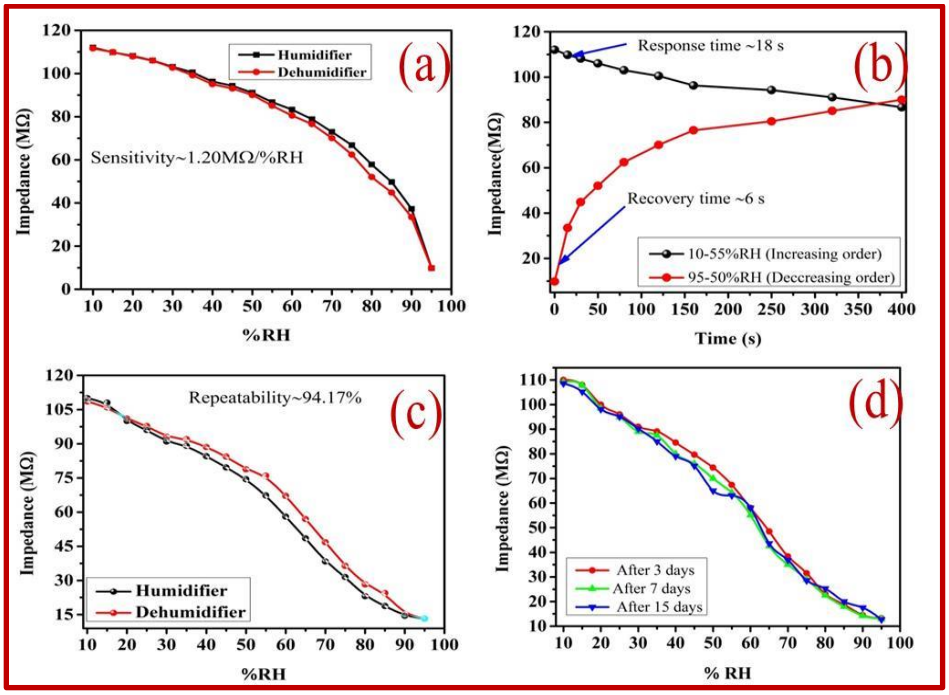

Fig. 4.12 Humidity sensor characteristics of GCS based sensor

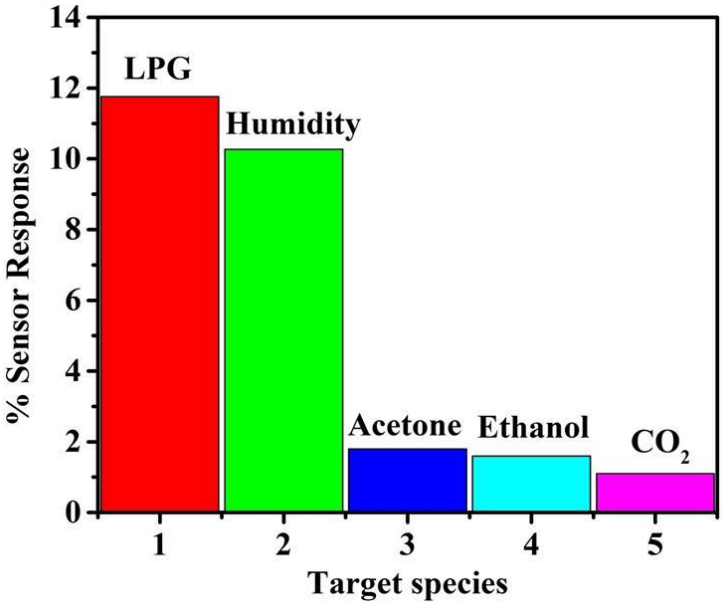

Fig. 4.13 Selectivity curve for the LPG sensor

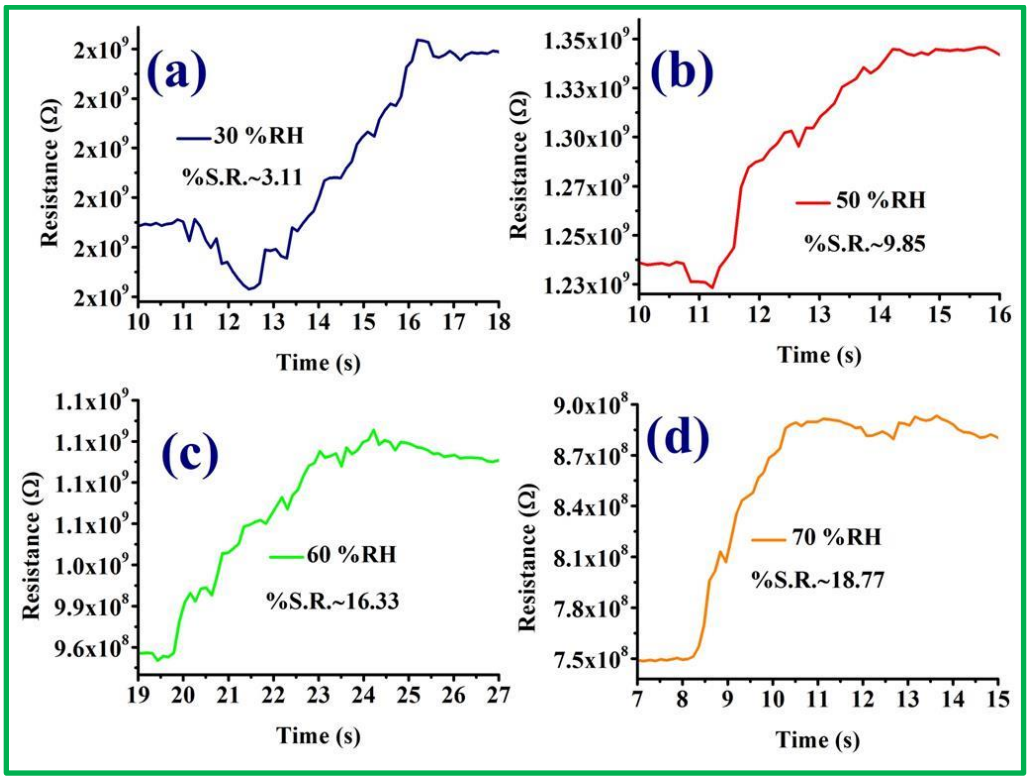

Fig. 4.14 Effect of relative humidity on LPG sensor

Tables

Materials	**Target Gas**	**Limit of detection**	**% S.R.**	**T_{res}/ T_{rec}**	**Reference**
Few layered Graphene	LPG	4 ppm	0.92	5/18	[23]
Few layer Graphene /SnO_2	LPG	25 ppm	-	-	[24]
Graphene/CdO	LPG	600 ppm	77	-	[25]
Graphene/SnO_2 quantum dot	LPG	50 ppm	-	16/20	[26]
Graphene/SrO quantum dots	LPG	50 ppm	-	16/22	[27]
Graphene/Bi_2O_3 qunatum dots	LPG	100 ppm	-	16/20	[28]
MnO_2/Graphene	LPG	25 ppm	-	17/19	[29]
White Graphene (PVA/WPPy/hBNNP nanocomposite)	LPG	600 ppm	0.25	30/32	[30]
Graphene/CuO/SnO_2	LPG	0.5 vol.%	5.35	1.7/1.2	Present study

Table 4.1. Graphene-based LPG sensor's attributes

LPG Conc. **Sensor Attributes**	**0.5 vol.%**	**1 vol.%**	**1.5 vol.%**	**2 vol.%**
Sensitivity (/vol.%)	10.70	6.63	6.96	5.88
%S.R.	5.35	6.63	10.44	11.76
Response time (s)	1.7	3.3	7.1	7.6
Recovery time (s)	1.2	1.3	2.0	4.8

Table 4.2 LPG sensor attributes based on the synthesized GCS

%RH	**Impedance (MΩ)**	
	Increasing mode	**Decreasing mode**
10	112.01	111.60
15	109.78	109.90
20	108.14	107.89
25	106.02	105.98
30	103.04	102.70
35	100.51	99.20
40	96.27	95.05
45	94.25	93.05
50	91.12	90.06
55	86.69	85.09
60	83.27	80.50

65	78.83	76.55
70	72.99	70.05
75	66.81	62.44
80	57.87	52.01
85	49.71	44.84
90	37.28	33.45
95	9.81	9.81

Table 4.3 Variation in the impedance as per increasing and decreasing humidity at 100 Hz

	Impedance (MΩ)	
Time (s)	**Response (10-55 %RH)**	**Recovery (95-50 %RH)**
0	112.013	9.808
15	109.779	33.45
30	108.1409	44.84
50	106.0183	52.009
80	103.0392	62.44
120	100.507	70.05
160	96.268	76.55
250	94.25	80.5
320	91.122	85.09
400	86.691	90.06

Table 4.4 Time measured along with variation in the impedance as per increasing humidity (10-55 %RH) and decreasing humidity (95-50 %RH) at 100 Hz frequency

%RH	Impedance (MΩ)				
	Repeatability		Ageing effect		
	Increasing mode	Decreasing mode	After 3 days	After 7 days	After 15 days
10	110	108.6	110	109	108.56
15	108	106	108	107.8	105.23
20	100	101.00	100.00	98.50	98.11
25	96	97.80	96.00	94.87	95.05
30	91	93.00	91.00	88.97	90.23
35	89.09	92.00	89.09	87.45	85.05
40	84.55	88.60	84.55	80.00	79.04
45	79.62	84.40	79.62	76.01	75.08
50	74.44	78.80	74.44	70.00	65.00
55	67.35	75.95	67.35	64.23	63.06
60	58.06	67.15	58.06	55.12	58.06
65	48.49	56.97	48.49	42.61	43.57
70	38.36	46.80	38.36	35.00	36.85
75	31.54	36.40	31.54	29.05	28.56
80	23.08	28.30	23.09	22.50	25.30
85	18.79	24.45	18.79	17.98	20.01
90	14.48	15.10	14.48	14.23	17.56
95	13.23	13.23	13.23	13.00	12.65

Table 4.5 Recorded data of repeatability and ageing effect after 3, 7 and 15 days

CHAPTER 5

DEVELOPMENT OF GRAPHENE OXIDE FUNCTIONALIZED WITH POLY PALLADIUM ACRYLAMIDE SnO_2 NANOCOMPOSITES FOR LPG AND HUMIDITY SENSING

The present chapter reports the synthesis and characterization of Graphene oxide (GO) functionalized with poly Pd acryl amide SnO_2 (PPdAAm/SnO_2) nanocomposites and its relevance for detecting the liquefied petroleum gas at room temperature. For surface morphological observation and elemental mapping, a thin film of the material has been investigated through Scanning Electron Microscope and further, for optical characterization UV-Vis spectrophotometer and Particle size analyzer have been used. Minimum crystallite size of the material was found as 19.14 nm from the X-Ray Diffraction analysis and also confirmed the presence of the Palladium (Pd) nanoparticles. The peaks corresponding at 465 and 507 cm^{-1} in Raman spectrum confirmed the stretched bond vibrations of the SnO_2 nanoparticles. Average size of the synthesized material was found as 118 nm through the Dynamic Light Scattering technique and the Tauc plot gave the bandgap as 5.3 eV. The N-H vibrations of the amide group present in the FTIR spectrum confirmed the formation of acrylamide in the synthesized material. The LPG detection was studied for 0.5, 1.0, 1.5 and 2.0 vol.% concentration with typical operable voltage of 40 V at 27 °C. The maximum %sensor response of the sensor was found as 570.58 for 2.0 vol.% of LPG.

CHAPTER 5

Development of Graphene oxide functionalized with poly palladium acrylamide SnO_2 nanocomposites for LPG and humidity sensing

5.1 Introduction

The coordination of the nano-structured transition metals with the polymers is not only used in material science, environmental science, nanoscience, and nanotechnology but also in the diverse field of biology and medicals [1]. After dispersing the nanoscopic inorganic materials in the polymer matrix, polymer nanocomposites were synthesized. The insertion of metals in the polymer causes changes in the electrical properties which is a very important parameter for the device fabrication purpose. Adopting this property any metal-polymer nanocomposite can be recognized in the various field of science. The nanostructured metals within the polymer matrix lead the multiple advantages compared to the pure polymer [2]. There are a variety of polymers (polyaniline, polypyrrole, polythiophene, polyacrylamide and their derivatives etc.) and several transition metals (Ni, Ti, Cu, Co, Pd etc.) which had been reported in the literature [3-8]. The acrylamide molecule has a planar and structure consistent with the amide functional group. It is a polyfunctional compound that consists of the vinylic amide group and carbon-carbon double-bonded chain. The electron-deficient (C=C) bond in acrylamide is susceptible to a wide range of reactions including nucleophilic, addition substitution, and free radical reactions. The acrylamide is capable to coordinate with the transition metals.

Acrylamide is a white crystalline compound having a solubility in water, alcohol, and acetone but the metal-doped polyacrylamide is partially soluble in the same [9].

Graphene has been proven a magic material depending upon its properties as bandgap and number of layers [10]. The functionalization process leads to its solubility and from conductor to semiconductor. The Graphene oxide (GO) consists of hydrophilic groups like hydroxyl, epoxy, and carboxylic acid groups. These promote the Graphene sheets detached from each other via sonication. These GO sheets or functionalized Graphene are used in the desired applications [11-13]. GO can be functionalized with metal oxides nanomaterials, nanocomposites, polymers, and metallopolymers. Such type of GO has been already used in the various field of nanotechnology as biophysics, medical, sensors, touch screens, solar cells, wastewater treatment, field emission and energy conversion device fabrications etc. [14-18].

Sensing is an important field of nanomaterials from the application point of view. There are various nanomaterials as nanostructured metal oxides, nanocomposites, polymers, metallopolymers that have been applied to detect the various species as CO_2, NH_3, NO_2, relative humidity (RH), alcohol, liquefied petroleum gas (LPG), and others[19-22]. Among these, our focus is on the detection of the LPG because it is highly flammable and has a versatile use in India and other developing countries. Recently, Fe_2O_3, $ZnFe_2O_4$, $BaTiO_3$, CdO, ZnO rods, and Pd doped ZnO nanorods were reported for the LPG sensing [23-28]. The literature review on the LPG sensors has been summarized in Table 5.1 [29-39].

As per the open literature review, the existing LPG sensors have low sensitivity, sensor response, and long response - recovery time. Therefore as of now, it is a basic requirement to overcome these problems associated with sensor development. In this chapter, we have reported the GO functionalized with a metallopolymer-based LPG sensor with better sensitivity, sensor response, and repeatability along with low response-recovery time.

5.2 Experimental details

5.2.1 Materials used

Graphite powder (98% purity, 200 mesh) was purchased from Triton Graphite, Gujarat, India and other chemicals used were $KMnO_4$, KNO_3, H_2SO_4, H_2O_2, Pd(II) nitrate, SnO_2, DI water, N-Methyl pyrrolidone (NMP), etc.. All these chemicals were of AR grade and used as without any further purification.

5.2.2 Synthesis procedure

The synthesis process is divided into three steps. One of which is a synthesis of the GO second consists of synthesis of the PPdAAm/SnO_2 metallopolymer (MP) and finally synthesis of MP-GO nanocomposite has been reported in the third step. The detailed synthesis has been discussed in the following subsections 5.2.3, 5.2.4, and 5.2.5.

5.2.3 Synthesis of GO

The method of the synthesis of GO has already been reported in Chapter 3 and also published [38]. The synthesis of GO was carried out with the modified Hummer method.

Typically in this method, the Graphite powder (1 g) and potassium nitrate (1 g) were poured into a beaker containing sulfuric acid (50 ml) at 0-5 °C under continuous magnetic stirring. $KMnO_4$ (6 g) was gradually added to this solution. For appropriate dilution, H_2O_2 was dropped wisely added accordingly.

5.2.4 Synthesis of the PPdAAm/SnO_2 nanocomposite metallopolymer (MP)

Flowchart of the synthesis of the PPdAAm/SnO_2 nanocomposites involves a stepwise process that has been discussed in Fig. 5.1. The synthesis of the AAm was carried out according to the published paper of Pomogailo et al [39]. In a typical procedure, a mixture of calculated amounts of Pd(II) nitrate, AAm, and SnO_2 was ground in an agate mortar within a box having an inert atmosphere to the pasty state, washed with benzene and ether, and dried in vacuum for at least 12 h at 30 °C. As a result, PdAAm/SnO_2 nanocomposite was formed. The frontal polymerization process was implemented after this step. In a typical procedure, PdAAm/SnO_2 samples were pressed as pellets having the range of diameter d = 0.5-0.8 cm, height h = 1.2-1.5 cm, and density ρ =1.45±0.02 g/cm^3, further, these were placed in a glass ampule. To start the polymerization, the bottom region of the ampule with the sample was immersed by 0.2 cm into the bath with the heat carrier (Wood alloy) for 10-15 s. The powdered polymeric nanocomposite products were washed with methanol and ether and then dried in a vacuum at room temperature to a constant weight. The details of the chemical compositions of the Pd(II) nitrate, AAm, and SnO_2 are according to Table 5.2.

5.2.5 Synthesis of the GO functionalized with PPdAAm/SnO_2 (MP-GO)

The above-synthesized GO and PPdAAm/SnO_2 nanomaterials were mixed with the wet chemical method as shown in Fig. 5.2. First of all, GO was dissolved in the N-Methyl Pyrrolidone (NMP), stirred for 30 minutes, and sonicated for 1 h. Now the PPdAAm/SnO_2 was added gradually according to 1:1 weight ratio of GO during the stirring for 3 h. After that, the solution was dried at 40 °C for 8 h in a hot air oven and we obtained the MP-GO.

5.2.6 Fabrication of sensing device

The sensing device was prepared using a photoresist spinner. The thin film of the synthesized material was fabricated on the silica glass substrate of the dimension 2.5 × 1.5 cm^2 and then it was dehydrated on the hot plate for 30 min at 50 °C temperature. The electrodes on the film were deposited at a distance 0.25 cm from each edge using silver paste. Now, this sensing device is ready for the characterizations.

5.2.7 LPG sensing measurements

According to the IUPAC definition, sensitivity is the slope of the calibration curve i.e. slope of sensor response versus target LPG concentration as mentioned in **Chapter 4** in section 4.2.3. The percentage sensor response of the sensor was calculated using the formula given by Eqn. 4.2 in same Chapter.

$$\%\ Sensor\ Response = \frac{R_g \sim R_a}{R_a} \text{ x } 100 \qquad (5.1)$$

The response-recovery time of the sensor is defined as 90% of the final sensor output during the adsorption and desorption of the gas respectively [1]. The response

and recovery times were calculated according to procedure discussed in section 4.2.3 in **Chapter 4.**

The lab-made LPG sensing setup is shown in Chapter 4. This setup consists of a LPG cylinder attached along with the LPG measuring unit connected to a vacuum-assisted chamber having a gas inlet, outlet, and sample holder. The sensing element was connected to the Keithley electrometer through the connecting wires which are further connected to a computer for the data recording and analysis.

5.3 Characterization techniques

The synthesized materials were characterized using different characterization techniques like Scanning Electron Microscopy (SEM) (JEOL, JSEM- 6490LV) with Electron Dispersive X-rays (EDX), Particle Size Analysis using Zeta nanosizer, UV-Visible spectra were recorded using UV-Visible Spectrophotometer (Evolution 201). The crystal and phase were investigated by powder X-ray Diffractometer (XRD) (Bruker D8 Advance, using Cu-Kα radiation) λ=0.15418 nm at a scan rate of 0.2°/s. A Raman spectrometer (model: Airix Corporation, Japan with laser excitation at 514 nm) was used.

5.4 Results and Discussion

5.4.1 SEM Analysis

Fig. 5.3 (a) and (b) shows the SEM micrographs of the synthesized PPdAAm/SnO_2 nanocomposite metallopolymer at X 27 k and X 20 k magnifications having at 500 nm and 1000 nm scale respectively with an electron beam energy of 15 kV. In Fig. 5.3 (a) and (b) the metal nanoparticles, nanoparticles wrapped with polymer are attached with

each other and forming the bunch/cluster of these. The metal nanoparticles wrapped with polymer are spherical and elliptical shaped showing the porous surface morphology.

Fig. 5.3 (c) and (d) are the SEM micrographs of the synthesized MP-GO at 500 nm scale. In these two micrographs, GO sheets are completely covered with the metallopolymers forming the cavities, pores on the surface of the GO wrapped with metallopolymers. The formed cavities in the surface of the synthesized material are shown by en-circled, the spherical-shaped metal nanoparticles are represented by en-triangled in Fig. 5. 3 (c) & (d) and the square is showing the two GO sheets wrapped with polymer placed neighboring to each other as shown in Fig. 5.3 (c)**.** The metallic dangling bonds are also formed during the functionalization. Cavities, dangling bonds, and pores create active center sites for oxygen adsorptions. Such types of nanostructures may be fruitful for LPG detection.

5.4.2 EDX Analysis

The elemental mapping of the synthesized MP-GO is illustrated by the EDX spectrum in Fig. 5.4. In this spectrum, the Y-axis represents the counts while X-axis is the energy in (keV). This spectrum illustrates that the synthesized material consists of C, O, Sn elements along with the Na, Mg, and Si foreign elements. The Na, Mg, and Si elements are obtained due to the glass substrate on which the thin film of the material was deposited. The percentage weight of C, O, and Sn are 45.87, 41.46, and 6.44 wt% respectively.

5.4.3 UV-Vis. Analysis

The absorption spectrum of the synthesized material in the wavelength range from 190 to 900 nm was recorded and the plot is illustrated in Fig. 5.5. The absorption spectrum represents the fluctuations in the wavelength range from 190 to 220 nm, which is due to the glass substrate used for the film fabrication through the spin coating technique. The inset figure shows the Tauc plot. Extrapolation of a tangent on Tauc plot gives the optical bandgap of the material as 5.3 eV [40]. This wide bandgap of material is due to the functionalization and the quantum confinement in the nano range which may be appropriate for LPG sensing.

5.4.4 Particle Size Analysis

The size distribution measurement of the nanoparticles relied on the Dynamic Light Scattering (DLS) technique [41]. The particle size distributions of the synthesized material in dilute solution were recorded and the plot of percentage counts versus size distributions have been shown in Fig. 5.6. The inset plot represents that material consists of different nano range in size (diameter) 50-210 nm. The average size of the synthesized MP-GO is found as 118 nm.

5.4.5 XRD Analysis

Figs. 5.7 (a), (b) and (c) show the XRD diffractographs of the synthesized material GO, metallopolymer and MP-GO respectively. Fig. 5.7 (a) i.e. XRD pattern of the GO has been shown in chapter 3 [38]. In Fig.5.7 (b), there are several Bragg's peaks showing the insertion of nano metals and are resulting in the crystalline nature due to the presence of their metallic nanoparticles. The plane °(110), °(101), °(200), °(111), °(210), °(211), °(220), °(002), °(310), °(112), °(301), °(202), °(321), °(400), °(222) and °(330) are of the

SnO_2 nanoparticles. These planes are well-matched with the JCPDS#88-0287. The plane *(111) and *(200) are of the Pd metals well matched with the JCPDS# 05-0681. The minimum and average crystallite size of the metallopolymer was calculated as 14.60 and 33.38 nm respectively with the help of the Debye Scherer formula. Fig. 5.7 (c) is showing some extra peaks due to the functionalization of the metallopolymer with the GO. The extra peak #(001) present at 21° is due to the GO. The minimum and average crystallite sizes of the MP-GO were calculated as 17.16 and 19.14 nm respectively. The average crystallite size of the MP-GO gets decreased because some of the GO sheets, as well as polymeric chain of MP, are broken during the functionalization process and these will create the metallic dangling bonds. The functionalized GO shows some peaks shift in the position and few extra peaks compared to that of the polymer. The peak shifting is obtained due to the atomic radii of the constituents atoms present in the synthesized material.

5.4.6 FTIR Analysis

The transmittance versus wavenumber data has been recorded and the plot is as shown in Fig. 5.8. The FTIR spectrum consists of several bands corresponding to functional groups present in the synthesized material. The wideband at 3420 cm^{-1} corresponds to the hydroxyl group showing the vibrations of O-H bonds. The bands present at 2924, 1385, 788 and 641 cm^{-1} belong to stretching and bending of C-H bonds respectively. Bands at 1710 and 1098 cm^{-1} assigned to the carbonyl bonds present in the carboxylic and alcoholic groups respectively. The N-H bending vibrations of the amide group, which is present in the acrylamide, relates to the valley present at 1579 cm^{-1} wavenumber. The band at 470 cm^{-1} equates with vibrations of Sn-O bonds [42, 43].

5.4.7 Raman Analysis

The Raman spectrum of the synthesized material is shown in Fig. 5.9 which consists of several peaks. The peaks corresponding to 1355, 1588, and 2658 cm^{-1} are known as D, G and 2D bands respectively. These bands are the characteristics of Graphene. The disorder parameter, in this case, was found 1.03 (i.e. I_D/I_G=1.03). The peaks in the range 100-200 cm^{-1} is due to the lattice vibrational modes occurring in the crystal. The peak present at 275 cm^{-1} corresponds to the stretching modes of C-C aliphatic chain formed because of the linkage of the polymer and Graphene oxide. The peaks corresponding at 465 and 507 cm^{-1} are due to the SnO_2 nanoparticles [44]. The peak is corresponding to 915 cm^{-1} for the C-O-O bond vibrations present in the synthesized MP-GO. The peaks present below 1000 cm^{-1} are representing the characteristics of the metal oxide nanoparticles.

5.5 LPG Sensing Application

Nowadays LPG is being much important part of human being's life and others, especially in developing countries. LPG is a hydrocarbon flammable gas consisting of a mixture of butane, propane etc.. It is used as fuel in heating appliances as cooking equipment and vehicles. It has huge use in the kitchens as fuel in India and other Asian countries for cooking the food. As the use of the LPG is friendly but its leakage in the kitchens or storages is the enemy of the environment because of the highly flammable and toxic nature. Detection of LPG is not important only for human beings and animals but also for the environment. The detailed literature of the LPG sensor has been given in Table 5.1. Due to the small sensor response, sensitivity, and long response-recovery time,

our need is to develop good quality, reliable, and a cost-effective sensor having a large sensor response, sensitivity with small response-recovery time. The thin film of MP-GO possesses pores inside the cavities on its surface along with metallic dangling bonds and was employed for the LPG sensing.

5.5.1 Principle of the LPG sensing

Sensing is the surface phenomenon depending upon the dangling bonds, defects, wrinkles, functionalizations, and surface modification in the sensing material. The LPG sensing mechanism relies on the charge transfer mechanism between the surface of the sensing material and LPG. The center of the oxygen chemisorption may be present at dangling bonds, wrinkles, oxygen vacancies, and localized acceptor and donor states. The sensing device is placed on the sample holder in the gas sensing chamber. Before starting the experiment the thin film was placed in the atmosphere in which the pores of the nanomaterial have interacted with the oxygen present in the atmosphere. By applying the voltage of 40 V in between the electrodes of the sensing device, at room temperature, the equilibrium is obtained by the chemisorption and charge transfer between the thin film and oxygen species. In such a way at room temperature, the ionic oxygen species (O_2^-, O^-) are formed on the surface of the sensing material. The kinematics involve during the chemisorption of the oxygen is given by Eqns. 5.4, 5.5 & 5.6. The immovability of ionic species resulting in the stable state of the resistance and is denoted by R_a.

$$O_2(air) \leftrightarrow O_2(ads) \quad (5.4)$$

$$O_2(ads) + e^- \leftrightarrow O_2^-(ads) \quad (5.5)$$

$$O_2^-(ads) + e^- \leftrightarrow 2O^-(ads) \quad (5.6)$$

When the sensing gas interacts with the sensing material the resistance of the sensing material may get an increase or decrease depending upon the nature of the gas (either reducing or oxidizing). As the LPG is the reducing gas due to which with the explosion of LPG, the resistance of the sensing material gets increased, known as the resistance of the sensing element in presence of the gas and denoted as R_g. The increase in the resistance is caused due to the capture of the electron by the chemisorbed oxygen (ionic oxygen) from the surface of the sensing element. In this work, GO is wrapped with the metallopolymer which is containing Pd and SnO_2 nanoparticles. When the LPG interacted with the sensing material, the free electrons have been captured by ionic oxygen species formed on the sensing material's surface from the sensing element. These electrons may be of either Pd or Sn metal. The electron density in the sensing element gets decreased and so the resistance of the sensing material gets increased. The gaseous species are formed after the removal of the adsorbed oxygen as hydrocarbons present in the LPG (C_nH_{2n+2}) interact with the sensing material. The reaction involved in this step is shown by Eqn.5.7:

$$C_nH_{2n+2} + O_2^- \rightarrow C_nH_{2n}O + H_2O + e^- \quad (5.7)$$

The LPG sensing of MP-GO had been studied by exposing the different concentrations of the LPG. For this purpose, the sensing device was put in the sample holder and was connected with the cable of the Keithley electrometer. The sensor was functional at 27 °C at a typical voltage of 40V. Now the LPG of different concentrations was exposed in the vacuum assisted chamber and also removed from the chamber by opening the outlet. The related data of the exposing and removing the LPG have been recorded. Initially, when the LPG was exposed to the sensing element the resistance of the material gets increased and after a certain time, it became saturated or stable. After that, the gas was let out and the resistance gets decreased and finally got a constant or stable value. Fig. 5.10 shows the plot of the variation in resistance with LPG exposure time. After exposing the gas, resistance getting increases up to a constant or stable value which represents the response study of the sensor for each concentration. For the recovery study, the exposed LPG was removed from the vacuum assisted chamber and the resistance of the sensing material gets started decreasing and reaches a stable value in every concentration of LPG. In such a way there are four cycles in the resistance-exposure time graph, which corresponds to 0.5, 1.0, 1.5, and 2.0 vol.% of LPG concentrations as shown in Fig. 5.10.

The %sensor response of the sensor was calculated with the help of Eqn. 5.1 for the 0.5, 1.0, 1.5, and 2.0 vol.% concentrations of the LPG and were found as 120.90, 163.33, 373.25, and 570.575 respectively. The sensor shows the minimum and maximum response for the 0.5 and 2.0 vol.% of the LPG. As the concentration of the LPG increases the %sensor response also increases as shown in Fig. 5.11 having a linear nature, which is the unique characteristic of a good LPG sensing material. The

sensitivities were calculated taking the slope in Fig. 5.11 (i.e. slope of the sensor response versus LPG concentration) for each concentration of LPG. The sensitivities for the 0.5, 1.0, 1.5, and 2.0 vol.% of LPG concentrations were found as 240.58, 163.33, 248.83, and 285.29 /vol.% respectively. The reproducible nature of the LPG for 0.5 vol.% is shown in Fig. 5.12.

The response-recovery time has been calculated by applying the exponential fitting according to Eqn. 5.2 & 5.3. Fig. 5.13 (a) and (b) illustrate the exponential decay and growth fitted curves for the 1 and 1.5 vol.% LPG. For each concentration of LPG, the calculated response-recovery time is shown in Table 5.3. The sensor shows the lowest response recovery time for the 0.5 vol.% LPG and highest for the 2.0 vol.% LPG.

5.6 Humidity sensing application

The sensing setup for the humidity sensor characterization has been shown in previous Chapter 2. The whole experiment was performed at the optimized frequency of 100 Hz in and the impedance-based sensing mechanism also had been discussed in the same chapter for the Graphene-based humidity sensors. With the variation in the relative humidity, the corresponding change in the impedances has been recorded and the plot of all the data is illustrated in Fig. 5.14. The changes in the impedance have been observed from 170 to 0.052 MΩ corresponding to variation in relative humidity from 10 to 99 %RH. The recorded data has been presented in Table 5.4. Figs. 5.14 (a), (b), (c) and (d) show the sensitivity, repeatability, response recovery time, and aging effect curves respectively and all these humidity sensor attributes are defined in Chapter 2. The noted

data related to repeatability, response-recovery times, and ageing effect have been depicted in Tables 5.5, 5.6, and 5.7 respectively.

The sensitivity of the sensor in the 10-99 %RH humidity range is calculated as ~2.01 MΩ/%RH. The sensor shows repeatable nature having repeatability of 97.5%, which is shown in Fig. 5.14 (b). The response recovery time of a sensor is an important parameter. A sensor having possible less response recovery time leads to a good sensor. The response- recovery curve is as shown in Fig. 5.14 (c) having response and recovery time 6.0 s and 112.0 s respectively. Fig.5.14 (d) is showing the aging effect of the sensor within one month at 25, 30, 45, and 70 %RH. The variation in the impedance values is observed due to the dangling bonds formed during the adsorption and desorption of the relative humidity.

5.7 Selectivity of the sensor

The selectivity of the MP-GO sensor was studied toward the LPG (2.0 vol.%) humidity (95 %RH), ethanol (2.0 vol.%), acetone (2.0 vol.%) and CO_2 gas (2.0 vol.%) and was found the maximum sensor response for the LPG sensor which is illustrated in the Fig.5.15. The selectivity of LPG can be explained based on the variations in the electrical resistance of the sensor with the charge transfer between the sensing material and sensing species. LPG exhibited good diffusivity, interaction with MP-GO compared with the others.

5.8 Effect of the humidity on the LPG sensing

To study the effect of the relative humidity on the sensing response of the sensor experiment has been performed at different values of the humidity for the 0.5 vol.%

concentration of the LPG. Fig. 5.16 illustrates the LPG sensing characteristics at different %RH. Fig. 5.16 (a) shows the variations in the resistance by exposing the 0.5 vol.% LPG at 30 %RH. The sensor shows the variation in the resistance from 1.64×10^7 to 3.48×10^7 Ω and the calculated %S.R for the same was 112.20. In Fig. 16 (b), the sensor shows the change in the resistance from the 1.55×10^7 to 3.58×10^7 Ω at the 50 %RH along with %S.R. 130.97 and Fig. 16 (c) is at the 60 %RH showing the variation in the resistance from the 1.25×10^7 to 3.31×10^7 Ω having the %S.R. as 164.80. The %S.R. was calculated as 187.25 at 70 %RH with varying the resistance from 1.02×10^7 to 2.93×10^7 Ω.

Overall with the above observation, it can be concluded that the % sensor response of the sensor was increased with the increasing humidity. The increase in the %S.R. and conductivity of the sensing material can be explained by the interaction of the humidity with the sensing material. The dissociation of the water molecules on the surface of the material generates hydroxyl species which act as electron donors and are used to enhance the conductivity of the sensing material. As the humidity increases the resistance of the sensing material gets decreasing. The oxygen atoms of the hydroxyl species get attached to the surface of the sensing material and the surface interaction sites of the material get increased which leads the enhancement in the sensor response. As the level of the humidity gets increasing the surface interaction sites of the sensor's material and gas interaction get increasing, this increases the sensor response [45].

5.9 Conclusions

The Graphene oxide was successfully functionalized with Pd doped polyacrylamide SnO_2 nanocomposites. The confirmation of the functionalization was insured with the different characterization techniques as SEM, EDX, Particle size analysis, UV-Visible spectroscopy, XRD, FTIR, and Raman etc.. Based on the characterizations, the synthesized material was employed as the LPG sensing at room temperature and found improved manifold with the previously reported LPG sensors. The sensor was attributed as sensitivity, sensor response, repeatability, response-recovery time, and selectivity successfully. The exposure of LPG has been studied for 0.5, 1.0, 1.5, and 2.0 vol.% concentrations. The MP-GO based LPG sensor showed the maximum % sensor response (570.58) for the 2.0 vol.% concentration while the response/recovery time was found minimum (7.8/7.3 s) for the 0.5 vol.% concentration. The sensor was operable at room temperature with 40 V operating voltage. Also, the results were found reproducible and no aging effect was observed. Thus the lab model of sensor developed here may be proven robust for outdoor applications and can be fabricated at the commercial level. In this chapter, the % sensor response of the LPG sensor was found to increase in comparison to previous chapters.

Reference

[1] S. Singh, M. Singh, B. C. Yadav, P. Tandon, S. I. Pomogailo, G. I. Dzhardimalieva, A. D. Pomogailo, Experimental investigations on liquefied petroleum gas sensing of $Cd(NO_3)_2 \cdot (AAm)_4 \cdot 2H_2O$ and CdS/polyacrylamide synthesized via frontal polymerization, Sensors and Actuators B, 160 (2011) 826–834.

[2] R. K. Sonker, B. C. Yadav, V. Gupta, M. Tomar, Fabrication and characterization of ZnO-TiO_2-PANI (ZTP) micro/nanoballs for the detection of flammable and toxic gases, Journal of Hazardous Materials, 370 (2019) 126-137.

[3] U. Kumar and B. C. Yadav, Development of humidity sensor using modified curved MWCNT based thin film with DFT calculations, Sensors and Actuators B: Chemical, 288 (2019) 399-407.

[4] N. D. Golubeva, S. Sikarwar, A. Kumar, B. C. Yadav, G.I. Dzhardimalieva, Nanostructured spherical-shaped Sc(III) Polyacrylate for monitoring the moisture level, IEEE Sensors Journal,18 (11) (2018) 4384 – 4391.

[5] R. K. Sonker, B. C. Yadav, Development of Fe_2O_3–PANI nanocomposite thin film based sensor for NO_2 detection, Journal of the Taiwan Institute of Chemical Engineers, 77 (2017) 1–6.

[6] R. Kumar and B. C. Yadav, Fabrication of polyaniline (PANI)—tungsten oxide (WO_3) composite for humidity sensing application Journal of Inorganic and Organometallic Polymers and Materials, 26(6) (2016) 1421-1427.

[7] K. B. Girma, V. Lorenz, S. Blaurock, F. T. Edelmann, Review Coordination chemistry of acrylamide, Coordination Chemistry Reviews, 249 (2005) 1283-1293.

[8] G. I. Dzhardimalieva, V. G. Dorokhov, N. D. Golubeva, S. I. Pomogailo, A. M. Lyakhovich, V. I. Savchenko and A. D. Pomogailo, Reactivity of metal-containing monomers 66. Hydrogenation of nitrotoluene derivatives in the presence of polymer immobilized Pd nanoparticles, Russ. Chem. Bull., Int. Ed., 58(10) (2009) 2070-2076.

[9] R. Kumar, S. Singh, B. C. Yadav, Conducting polymers: synthesis, properties and applications, Inter. Adv. Res. J. in Sci., Eng. and Techno., 2(11) (2015) 110-124.

[10] K. Kumar and B. C. Yadav, An Overview on the Importance of Chemical Vapour Deposition Technique for Graphene Synthesis, Adv. Sci. Eng. Med., 10 (2018) 760–763.

[11] A. Kasprzak, A. Zuchowska and M. Poplawska, Functionalization of graphene: does the organic chemistry matter?, Beilstein J. Org. Chem., 14 (2018) 2018–2026.

[12] D. Chen, H. Feng and J. Li, Graphene Oxide: Preparation, Functionalization, and Electrochemical Applications, Chem. Rev., 112 (2012) 6027−6053.

[13] T. Kuila, S. Bose, A. K. Mishra, P. Khanra, N. H. Kim, J. H. Lee, Chemical functionalization of graphene and its applications, Progress in Materials Science, 57 (2012) 1061–1105.

[14] R. K. Layek, A. K. Nandi, A review on synthesis and properties of polymer functionalized graphene, Polymer, 54 (2013) 5087-5103.

[15] M. Fang, K. Wang, H. Lu, Y. Yang and S. Nutt, Covalent polymer functionalization of graphene nanosheets and mechanical properties of composites, J. Mater. Chem., 19 (2009) 7098–7105.

[16] J. R. Potts, D. R. Dreyer, C. W. Bielawski, R. S. Ruoff, Graphene-based polymer nanocomposites, Polymer, 52 (2011) 5-25.

[17] X. Ji, Y. Xu, W. Zhang, L. Cui, J. Liu, Review of functionalization, structure and properties of graphene/polymer composite fibers, Composites: Part A, 87 (2016) 29–45.

[18] Y. Huang, M. Zeng, J. Rena, J. Wang, L. Fan, Q. Xu, Preparation and swelling properties of graphene oxide/poly(acrylic acid-co-acrylamide) super-absorbent hydrogel nanocomposites, Colloids and Surfaces A: Physicochem. Eng. Aspects, 401 (2012) 97– 106.

[19] A. Naga, A. Mitra, S. C. Mukhopadhyaya, Graphene and its sensor-based applications: A review, Sensors and Actuators A, 270 (2018) 177–194

[20] R. K. Sonker, B. C. Yadav, A. Sharma, M. Tomar and V. Gupta, Experimental investigations on NO_2 sensing of pure ZnO and PANI–ZnO composite thin films, RSC Advances, 6 (61) (2016) 56149-56158.

[21] U. Kumar and B. C. Yadav, Synthesis of carbon nanotubes by direct liquid injection chemical vapor deposition method and its relevance for developing an ultra-sensitive room temperature based CO_2 sensor, Journal of the Taiwan Institute of Chemical Engineers, 96 (2019) 652-663.

[22] S. Singh, U. Kumar, B. C. Yadav, K. Kumar, R. Tripathi and K. Singh, Development of scattering based glucose sensor using hydrothermally synthesized cuprous oxide nanoparticles, Results in Physics 15 (2019) 1-28.

[23] B. C. Yadav, S. Singh and A. Yadav, Nanonails structured ferric oxide thick film as room temperature liquefied petroleum gas (LPG) sensor, Appl. Surf. Sci., 257 (2011) 1960–1966.

[24] S. Singh, N. Verma, A. Singh and B. C. Yadav, Synthesis and characterization of $CuO\text{-}SnO_2$ nanocomposite and its application as liquefied petroleum gas sensor, Materials Science in Semiconductor Processing, 18(1) (2014) 88–96

[25] M. Singh, B. C. Yadav, A. Ranjan, M. Kaur and S. K. Gupta, Synthesis and characterization of perovskite barium titanate thin film and its application as LPG sensor, Sensors and Actuators B: Chemical, 241 (2017) 1170–1178.

[26] U. T. Nakate, P. Patil, B. Ghule, Y. T. Nakate, Satish Ekar, Revan C. Ambare, and R. S. Mane, Room temperature LPG sensing properties using spray pyrolysis deposited nanocrystalline CdO thin films, Surfaces and Interfaces 17 (2019) 1-7.

[27] M. Jabeen, A. Iqbal, R. V. Kumar, and M. Ahmed, Pd-doped zinc oxide nanostructures for liquefied petroleum gas detection at low temperature, Sensing and Bio-Sensing Research 25 (2019) 1-8.

[28] S. Choudhary, S. Annapoorni, and R. Malik, Evolution and growth mechanism of hexagonal ZnO nanorods and their LPG sensing response at low operating temperature, Sensors and Actuators A: Physical 293 (2019) 207-214.

[29] K. R. Nemade, and S. A. Waghuley, Strontium oxide quantum dot decorated graphene composites for liquid petroleum gas sensing, Journal of the Chinese Advanced Materials Society 1 (3) (2013) 219-228.

[30] K. R. Nemade, S.A. Waghuley, Chemiresistive gas sensing by few-layered graphene. J. Electron. Mater., 42 (10) (2013) 2857–2866.

[31] N. V. Hieu, N. A. P. Duc, T. Trung, M. A. Tuan, N. D. Chien, Gas-sensing properties of tin oxide doped with metal oxides and carbon nanotubes: A competitive sensor for ethanol and liquid petroleum gas Sensors and Actuators B 144 (2010) 450–456.

[32] N. G. Shimpi, D. P. Hansora, R. Yadav, and S. Mishra, Performance of hybrid nanostructured conductive cotton threads as LPG sensor at ambient temperature: preparation and analysis, RSC Advances 5 (120) (2015) 99253-99269.

[33] S. Goutham, S. Bykkam, K. K. Sadasivuni, D. S. Kumar, M. Ahmadipour, Z. A. Ahmad, and K. V. Rao, Room-temperature LPG resistive sensor based on the use of a few-layer graphene/SnO 2 nanocomposite, Microchimica Acta 185 (1) (2018) 1-8.

[34] J. G. Thangamani, K. Deshmukh, K. K. Sadasivuni, D. Ponnamma, S. Goutham, K. V. Rao, K. Chidambaram, M. B. Ahamed, A. N. Grace, M. Faisal, S. K. Khadheer Pasha, White graphene reinforced polypyrrole and poly(vinyl alcohol) blend nanocomposites as chemo resistive sensors for room temperature detection of liquid petroleum gases, Microchimica Acta, 184 (2017) 3977-3987.

[35] B. Chaitongrat and S. Chaisitsak, Fast-LPG Sensors at Room Temperature by α-Fe_2O_3/CNT Nanocomposite Thin Films, Journal of Nanomaterials 2018 (2018) 1-12.

[36] S. Goutham, N. Jayarambabu, C. Sandeep, K. K. Sadasivuni, D. S. Kumar, K. V. Rao, Resistive room temperature LPG sensor based on a graphene/CdO nanocomposite, Microchimica Acta, 186 (2019) 1-8.

[37] K. R. Nemade, S.A. Waghuley, LPG sensing application of graphene/Bi2O3 quantum dots composites, Solid State Sciences 22 (2013) 27-32.

[38] K. Kumar, U. Kumar, M. Singh, and B. C. Yadav, Synthesis and characterizations of exohedral functionalized graphene oxide with iron nanoparticles for humidity detection, J. of Mater. Sci.: Mater. in Electr., 30 (14) (2019) 13013-13023.

[39] A. D. Pomogailo, G. I. Dzhardimalieva, Frontal polymerization of metal-containing monomers: achievements and problems, Polym. Sci., Ser. A, 46(3) (2004) 250-263.

[40] S. K. Suram, P. F. Newhouse, and John M. Gregoire, High Throughput Light Absorber Discovery, Part 1: An Algorithm for Automated Tauc Analysis, ACS Comb. Sci., 18 (2016) 673−681.

[41] J. Stetefeld, S. A. McKenna & T. R. Patel, Dynamic light scattering: a practical guide and applications in Biomedical Sciences, Biophys. Rev., 8 (2016) 409–427.

[42] B. Nandan, B. Venugopal, S. Amirthapandian, B. K. Panigrahi, and P. Thangadurai, Effect of Pd ion doping in the band gap of SnO_2 nanoparticles:

structural and optical studies, Journal of Nanoparticle Research 15, (10) (2013) 1-11.

[43] J. Coates, Interpretation of infrared spectra, a practical approach, Encyclopedia of Analytical Chemistry: Applications, Theory and Instrumentation (2006).

[44] S. A. Saleh, A. A. Ibrahim and S. H. Mohamed, Structural and Optical Properties of Nanostructured Fe-Doped SnO_2, Acta Physica Polonica A,129 (6) (2016) 1220-1225.

[45] D. S. Vlachos, P. D. Skafidas, and J. N. Avaritsiotis, The effect of humidity on tin-oxide thick-film gas sensors in the presence of reducing and combustible gases, Sensors and Actuators B: Chemical 25 (1995) 491-494.

Figures:

Fig. 5.1 Flowchart of synthesis of frontal polymerization of PdAAm@SnO_2 nanocomposite

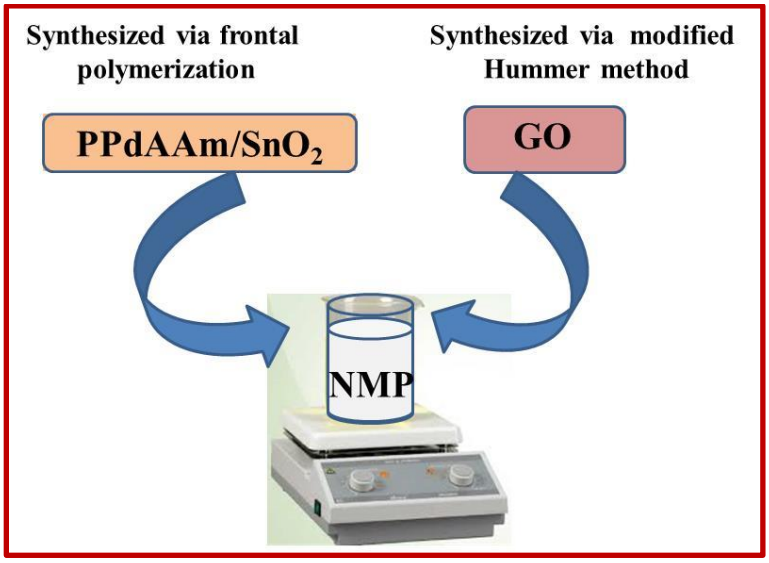

Fig. 5.2 Flowchart of the synthesis of MP-GO

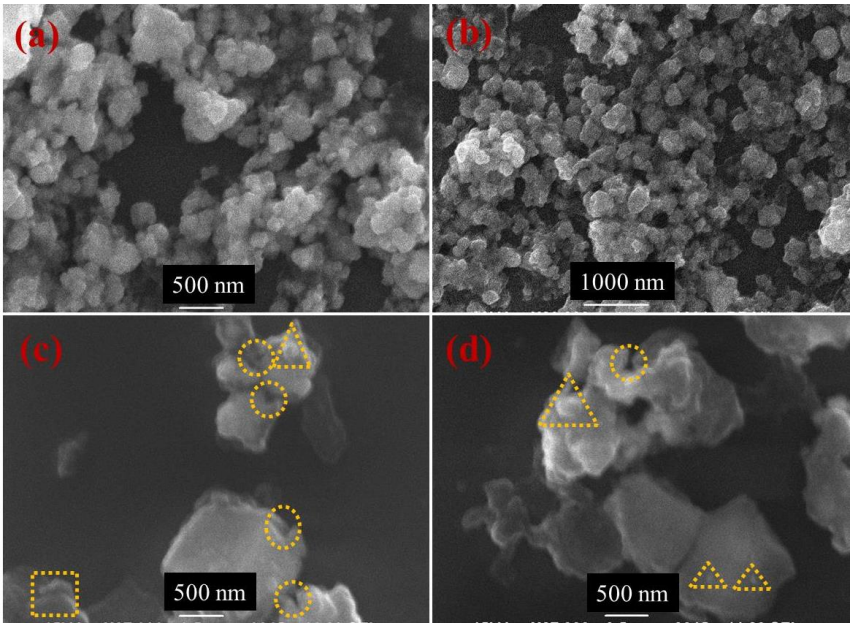

Fig. 5.3 SEM micrographs at various scales (a) 500 nm (b) 1000 nm are of metallopolymer, while (c) & (d) are of MP-GO at 500 nm.

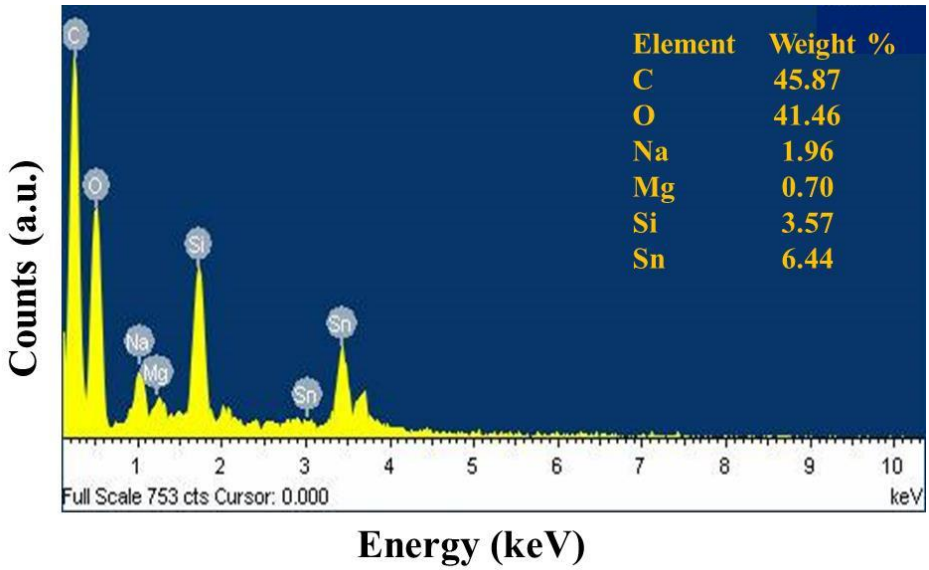

Fig. 5.4 Elemental mapping of MP-GO

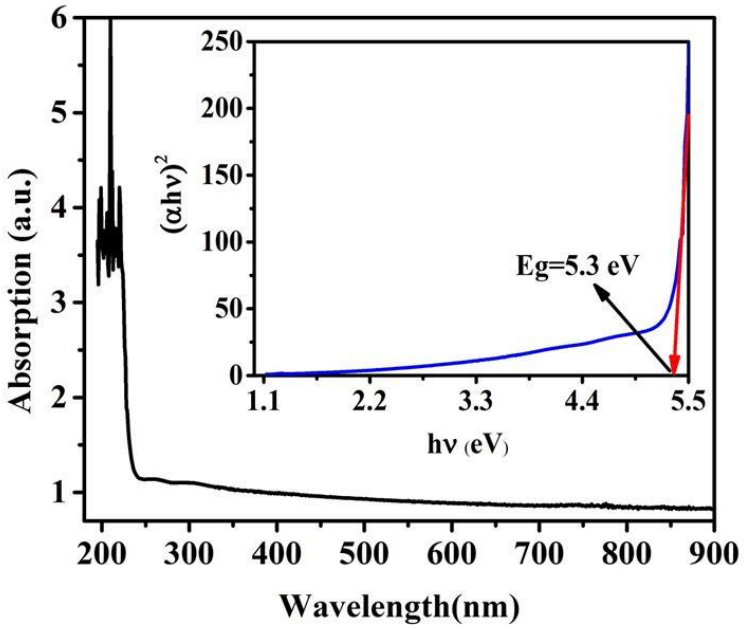

Fig.5. 5 UV -Vis. Absorption along with the Tauc plot of the synthesized materials showing the optical band gap 5.3 eV

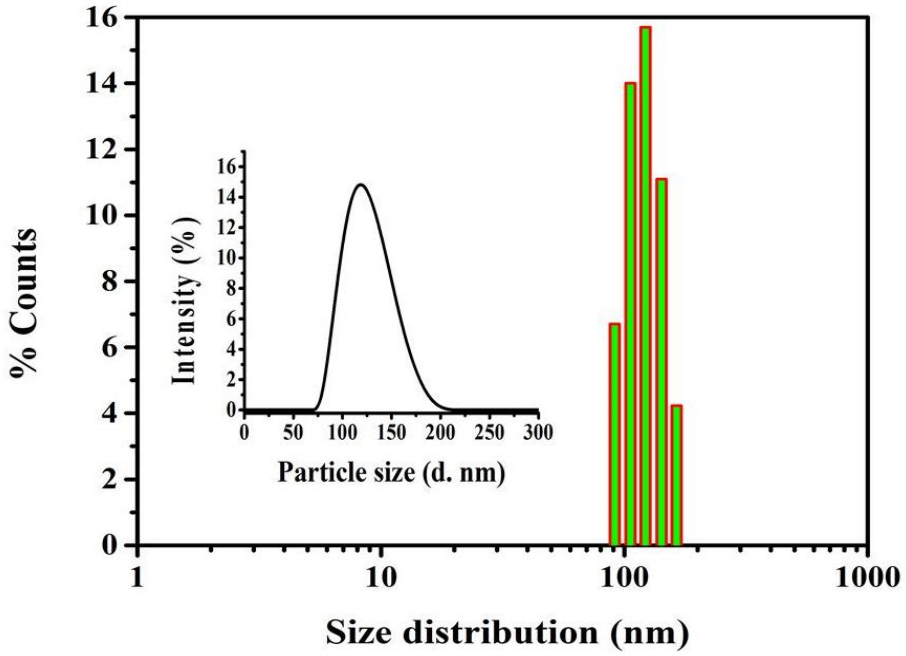

Fig. 5.6 Particle size distribution of the MP-GO showing in the nano range

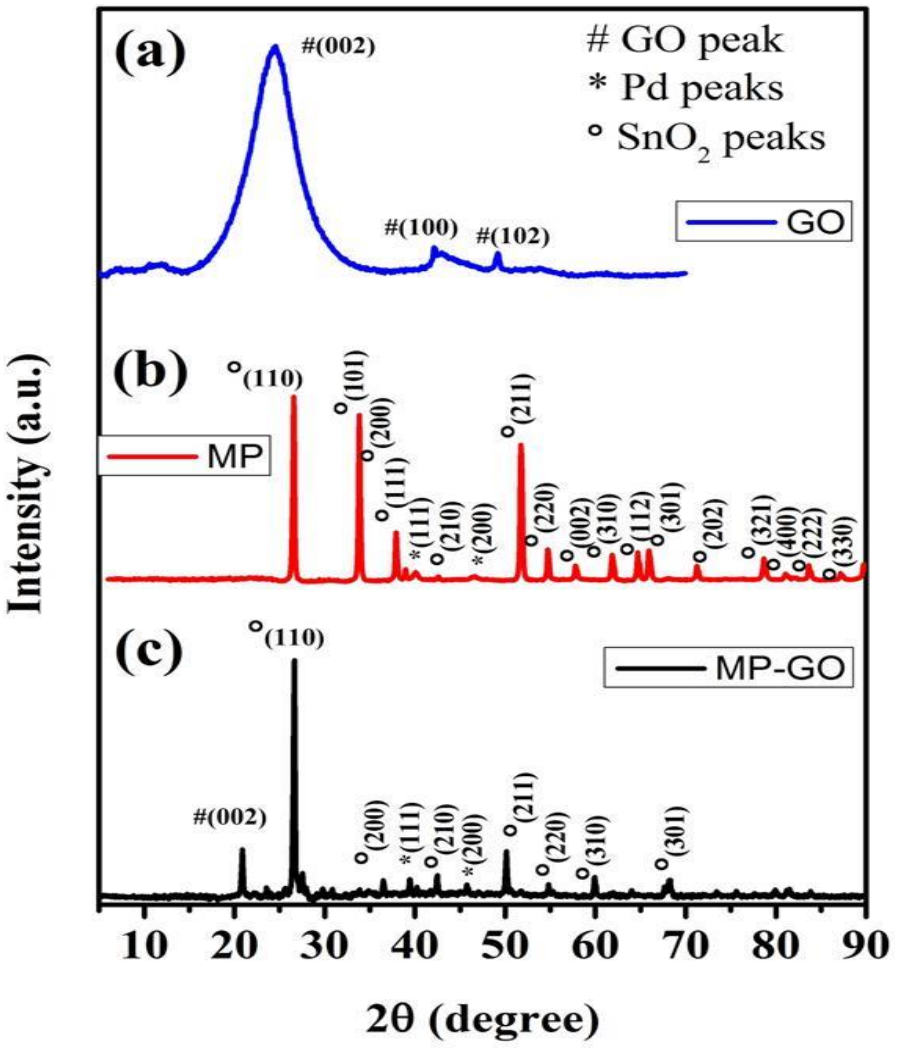

Fig. 5.7 XRD spectrum of (a) GO [38], (b) PPdAAm@SnO_2 nanocomposites (MP) and (c) MP-GO

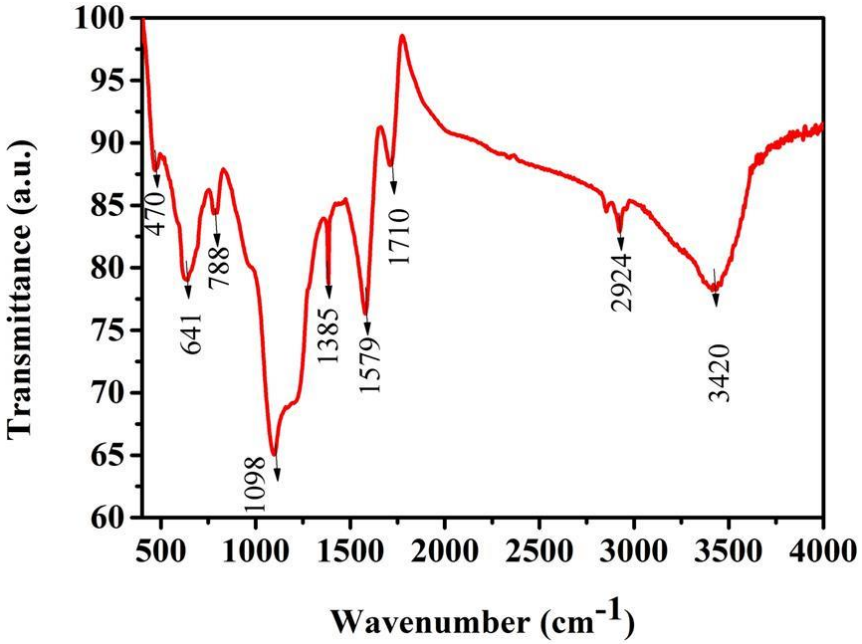

Fig. 5.8 FTIR spectrum of the MP-GO

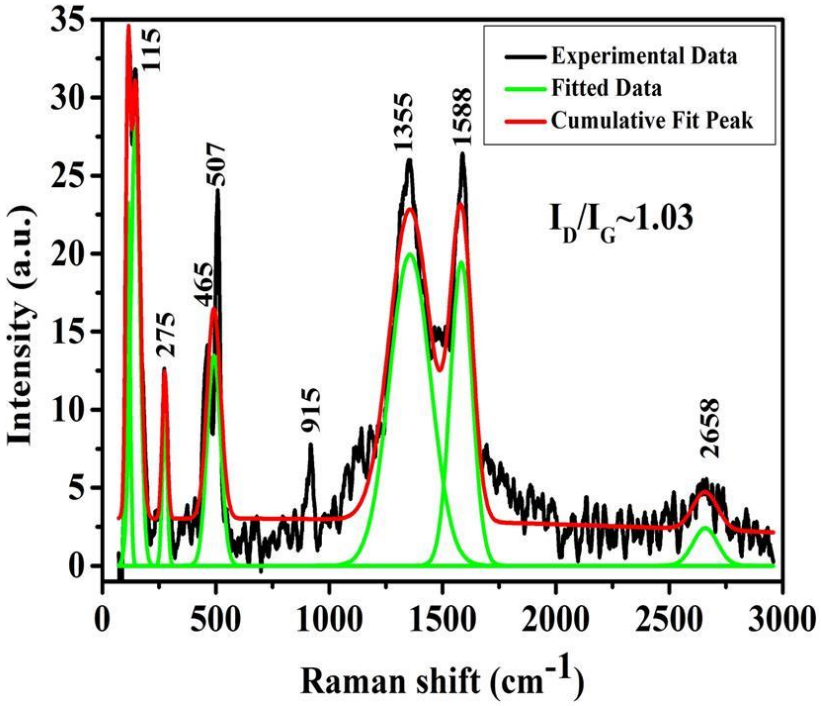

Fig. 5.9 Raman spectrum of the MP-GO

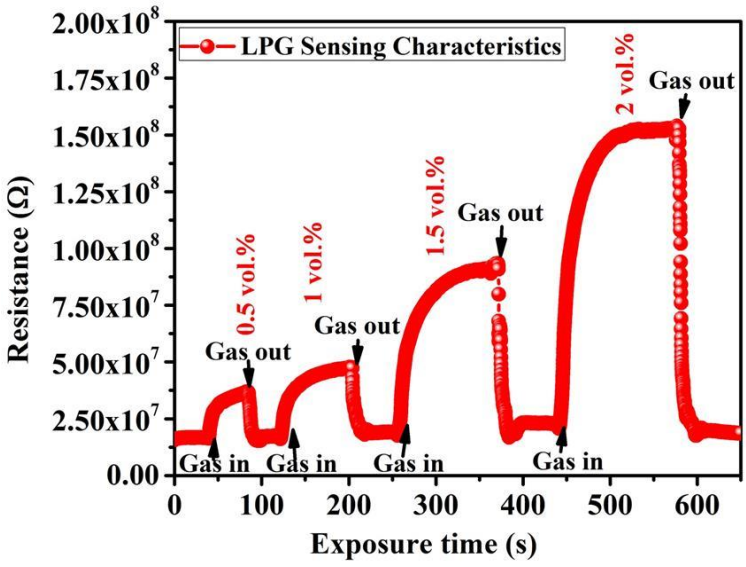

Fig. 5.10 Variations in the resistance of the sensing material versus time in the presence and absence of LPG

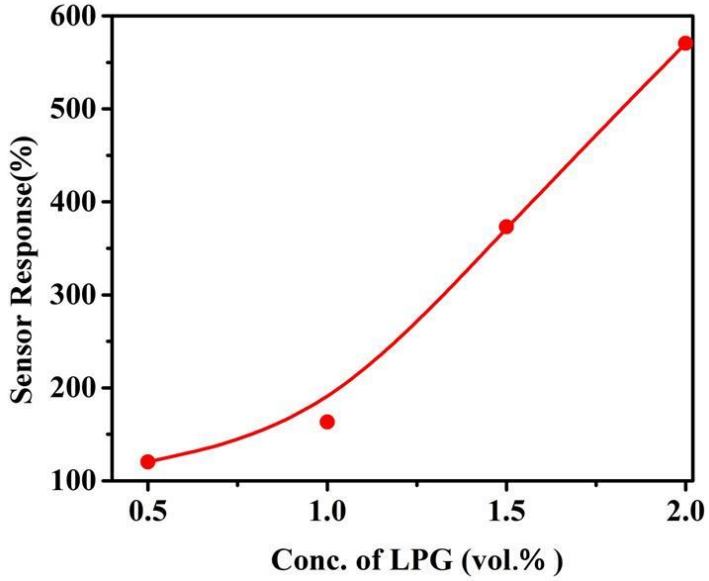

Fig. 5.11 Variation in the sensor response with the LPG concentration

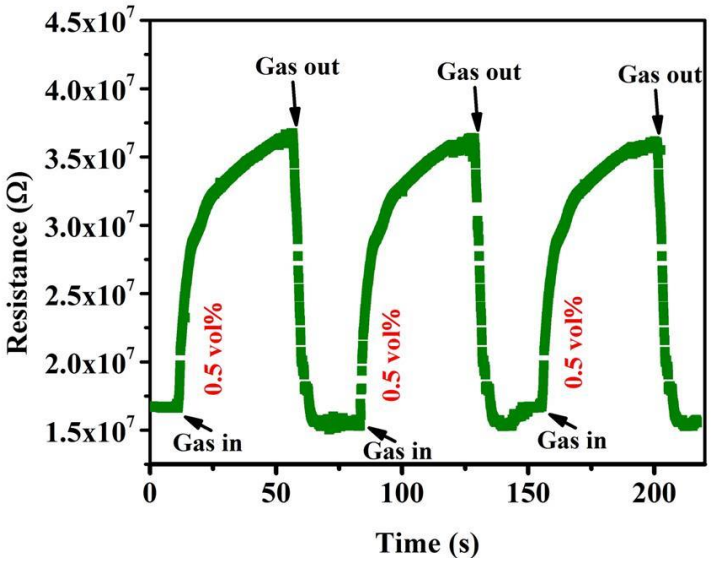

Fig.5.12 showing the repeatable nature of MP-GO based sensor at 0.5 vol.% LPG concentrations

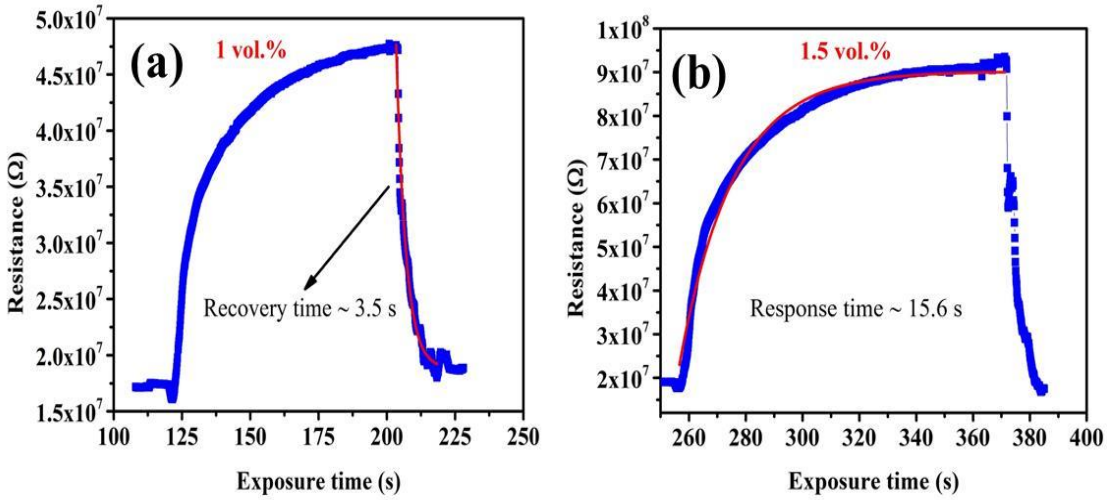

Fig. 5.13 (a) and (b) showing the exponential decay and growth fitted curves for 1.0 and 1.5 vol.% LPG concentration respectively.

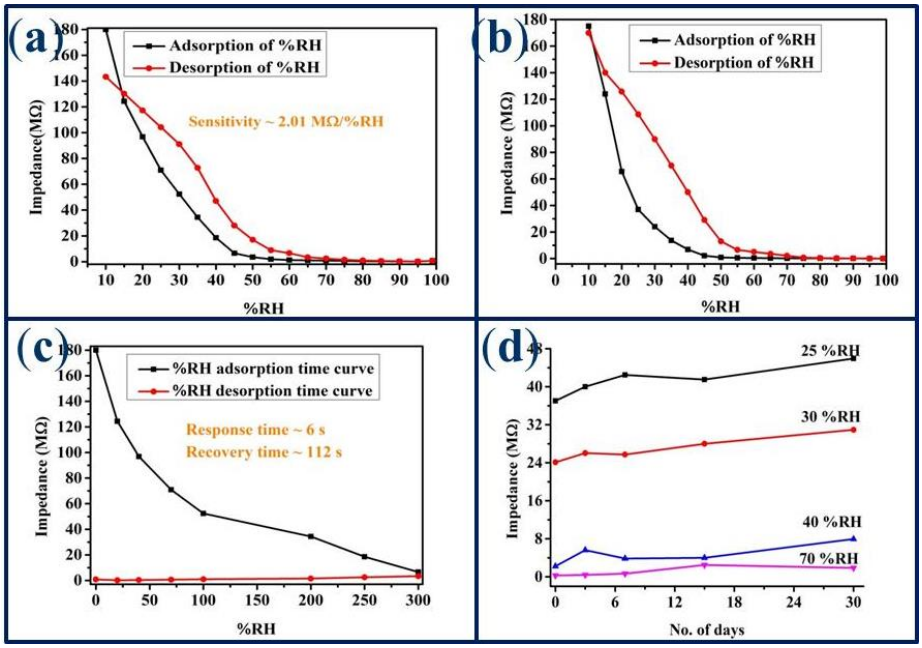

Fig. 5.14 MP-GO based humidity sensor attributes

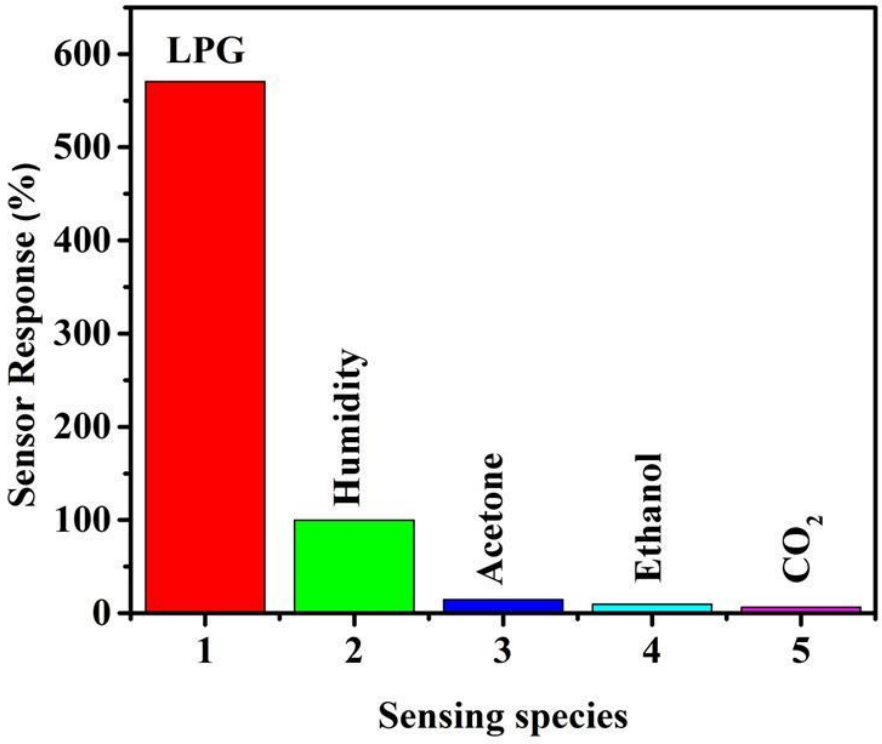

Fig. 5.15 Selectivity investigation for MP-GO based LPG sensor

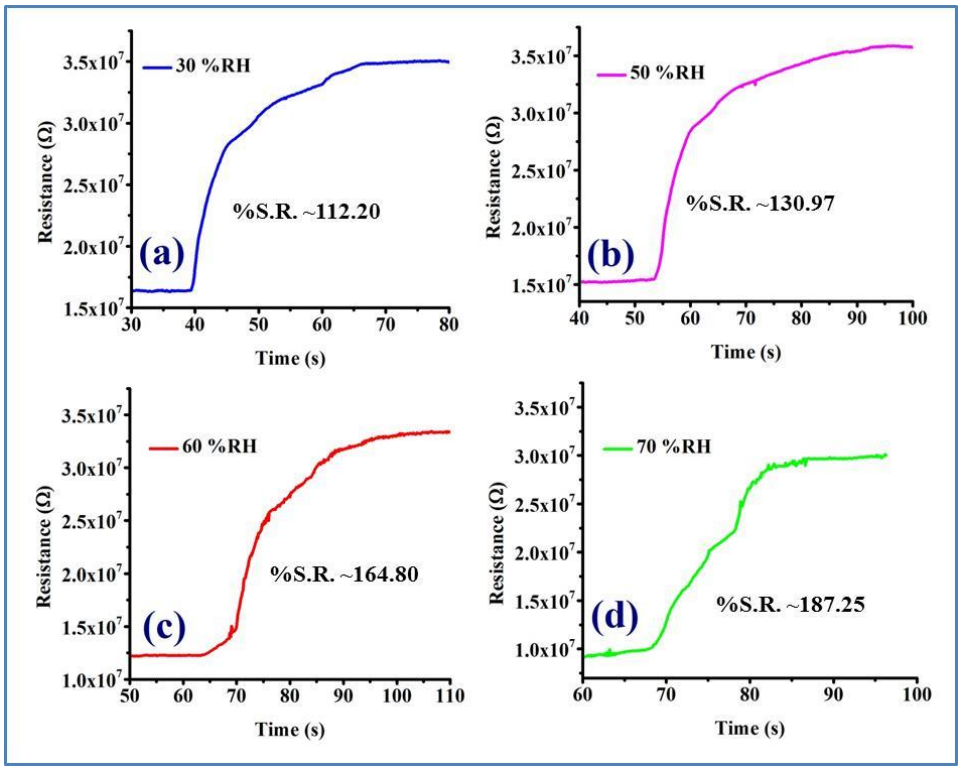

Fig. 5.16. Variation in resistance (Ω) with time(s) at 30, 50, 60 and 70 %RH for the 0.5 vol.% LPG sensor with calculated %S.R.**.**

Tables

Materials	Target Gas	Limit of detection	% S.R.	T_{res}/ T_{rec}	Reference
Graphene/SrO quantum dots	LPG	50 ppm	-	16/22	[29]
Few layered Graphene	LPG	4 ppm	0.92	5/18	[30]
MWCNTs doped SnO_2	LPG	2500 ppm	-	21/36	[31]
CNT/PAni/γ-Fe_2O_3 nanostructured thread	LPG	50 PPM	0.91	20-25/35-40	[32]
Few layer Graphene /SnO_2	LPG	25 ppm	-	-	[33]
White Graphene (PVA/WPPy/hBNNP nanocomposite)	LPG	600 ppm	0.25	30/32	[34]
Purified CNT	LPG	5 vol.%	0.25	20/45	[35]
α-Fe_2O_3/CNTs	LPG	0.1–5vol.%	1–6	25/13 s/-30/80 s	
Graphene/CdO	LPG	600 ppm	77	-	[36]
Graphene/Bi_2O_3 qunatum dots	LPG	100 ppm	-	16/20	[37]

Table 5.1 Literature review on Carbon/Graphene based LPG sensors

Complex	Found/calculated wt%			
	C	H	N	Pd
$Pd(NO_3)_2 \cdot 2H_2O$	-	1.4/1.5	10.2/10.5	40.4/39.9
PdAAm	20.1/19.4	3.5/2.7	15.1/15.0	29.4/28.6
PdAAm/SnO_2	-	-	-	5.2

Table 5.2 Elemental analysis data of Pd(II)complexes

S.No.	LPG Concentration	Sensitivity (/vol.%)	% S.R.	Response/Recovery time (s)
1	0.5 vol.%	40.40MΩ/vol.% 240.58	120.90	7.8/3.3
2	1.0 vol.%	29.48 MΩ/vol.% 163.33	163.33	14.3/3.5
3	1.5 vol.%	48.02 MΩ/vol.% 248.83	373.25	15.6/4.1
4	2.0 vol.%	64.64 MΩ/vol.% 285.29	570.58	18.9/5.2

Table 5.3 Calculated LPG sensing attributes for the synthesized MP-GO based sensor

%RH	Impedance (MΩ)	
	Increasing mode	Decreasing mode
10	175	170
15	124	140
20	65.55	125.8
25	37.03	108.64
30	24.1	89.9
35	13.72	70.09
40	6.9	50.05
45	2.22	29.12
50	0.9	13.07
55	0.565	6.58
60	0.447	5.047
65	0.37	3.63
70	0.288	2.21
75	0.226	0.802
80	0.224	0.455
85	0.196	0.282
90	0.145	0.177
95	0.0985	0.133
99	0.052	0.052

Table 5.4 The recorded data of variation in the impedances with increasing and decreasing humidity in range 10-99 %RH

%RH	Repeatability	
	Impedance (MΩ)	
	Increasing mode	Decreasing mode
10	180	143.30
15	124.34	130.25
20	96.80	117.21
25	70.90	104.17
30	52.35	91.12
35	34.40	72.70
40	18.52	47.05
45	6.61	28.01
50	3.55	16.94
55	1.96	8.90
60	1.30	6.57
65	1.06	3.38
70	0.84	2.48
75	0.59	1.52
80	0.32	0.96
85	0.27	0.60
90	0.15	0.33
95	0.11	0.21
99	0.77	0.77

Table 5.5 The recorded readings of the impedances to study the repeatability

Time (s)	Impedance (MΩ)	
	Increasing humidity (10-50 %RH)	Decreasing humidity (95-55 %RH)
0	180.00	0.77
20	124.34	0.21
40	96.80	0.33
70	70.90	0.60
100	52.35	0.96
200	34.40	1.52
250	18.52	2.48
300	6.61	3.38

Table 5.6 The data of the measured time versus variation in impedances with increasing (10-45 %RH) and decreasing humidity (99-65 %RH)

No. of days	Impedance (MΩ)			
	25 %RH	30 %RH	45 %RH	70 %RH
0	37.03	24.10	2.22	0.29
3	40.00	26.04	5.62	0.41
7	42.50	25.73	3.85	0.67
15	41.50	28.01	4.00	2.50
30	45.95	30.94	7.95	1.87

Table 5.7 The data of the measured impedances at the 25, 30, 45, and 70 %RH for the ageing effect

CHAPTER 6

DEVELOPMENT OF ULTRA-FAST SENSITIVE AND SELECTIVE CO_2 GAS AND HUMIDITY SENSOR BASED ON THIN FILM OF GRAPHENE@CuO NANOCOMPOSITES

The present chapter deals with the development of the CO_2 gas and humidity sensor at room temperature based on the Graphene@CuO nanocompoistes, synthesized through Chemical Vapor Deposition (CVD) route. The synthesized materials have been characterized with several techniques such as Scanning electron microscopy (SEM), Electron dispersive X-rays (EDX), Ultraviolet-Visible (UV-Vis.) spectroscopy, X-ray Diffraction (XRD), Fourier Transform Infrared (FTIR) and Raman spectroscopy. The surface morphological investigations as well as elemental mapping analysis confirmed that the CuO metal nanoparticles are attached with Graphene sheet at the side edges, corners and basal plane. Investigation of the nano size distribution has been carried out with the particle size analysis. The band gap of the synthesized nanomaterials was estimated as 4.1 eV. The presence of the oxygen containing functional groups in the material is confirmed with the FTIR. The Raman spectrum describes the nature of the synthesized Graphene as well as Graphene@CuO nanocomposites. The % sensor response of the CO_2 sensor is maximum (1178.31) for the 2.0 vol.% and also the response and recovery time for the 0.5 vol.% are 1.3 and 1.5 s respectively.

CHAPTER 6

Development of ultra-fast sensitive and selective CO_2 gas and humidity sensor based on thin film of Graphene@CuO nanocomposites

6.1 Introduction

Nowadays environmental pollution has become a very serious problem in the world. The prevention of the same is a very challenging problem for the researchers. The major environmental pollutants as CO and CO_2 are produced from the burning of fossil fuels in the motor vehicle, volcanic eruption, and industries. Global warming is the result of continuous increase in the concentration of CO_2 in the atmosphere. Since the mid-20^{th} century, the amplified emission of CO_2 and other greenhouse gases have been understood to be the cause of the increase in the average near-surface air and ocean temperature of the earth, a phenomenon known as global warming. Also, the excess of CO_2 in the natural environment causes suffocation and creates unconsciousness in human beings. Many sensors have been developed to detect the presence of toxic gases like NO_2, NH_3, CO, and CO_2 in the environment [1-7].

Recently, Graphene has been used as a promising material because it is being applied in terahertz devices. The Graphene-based devices have very low Johnson noise due to their resistivity. The Pd [8], Ru [9, 10], Ir [11], Ni [12-15], Cu [16-19], and Co [20, 21] are the catalysts that may be recently used for the synthesis of Graphene with the Chemical Vapor Deposition (CVD) method [22, 23]. Mostly the Cu metal is used for the synthesis of the Graphene due to the low solubility of the carbon on the Cu metal which

is explained by the self-limiting mechanism. The recent literature review on Graphene-based CO_2 sensors has been summarized in Table 6.1 [24-29].

Mostly, Graphene metal nanocomposites have been chosen for different applications because Graphene has extraordinary properties as mechanical, chemical, optical, and electrical properties and metal can be used as the bandgap tuning in the same material. The gas sensing response is generally attributed due to the electron transfer between the sensing materials and chemisorbed gaseous molecules. This is a redox reaction, results a change in the depletion layer which may cause the variation in the electrical resistance. Several sensing mechanisms have been proposed but most commonly the variation in resistance/conductance by the adsorption of a gaseous molecule on the sensing material is being used. Since Graphene has a larger surface area and its metal composites possess good electrical conductivity so the interactions of the sensing species have the same surface area and this leads to the maximum sensing response. Metal oxides like SnO_2, ZnO, TiO_2, and In_2O_3 are the most efficient CO_2 gas sensing materials. Normally, metal oxide gas sensors are operated at high temperatures [30-34].

In the recent scenario, plenty of the metal oxides are widely used for sensing applications but there is a drawback of these sensors that they require high operating temperature (200-400°C) [35-38]. Therefore, the development of a CO_2 gas sensor with rapid detection, low response-recovery time, and operable at room temperature has been undertaken. The thin-film based sensors operable at room temperature is the most emerging technique for environmental sensing. In the present work, we have focused on the thin film of Graphene@CuO nanocomposites for CO_2 gas sensing.

6.2 Experimental details

6.2.1 Synthesis procedure

For the synthesis of the Graphene and Graphene@CuO nanocomposites, here Direct Liquid Injection Chemical Vapor Deposition (DLICVD) technique has been used. The schematic of a typical DLICVD is shown in Fig. 6.1. First of all, the CuO nanoparticles were synthesized with the sol-gel technique. The catalytic growth of the Graphene was performed on CuO nanoparticles. The CuO nanopowder was spread on the quartz board and this board was put inside the quartz tube of the CVD. The programmable furnace was calibrated for the temperature up to 850 °C for 30 min. Now the 25 ml ethanol was injected into the quartz tube @ 1 ml/min in presence of Ar atmosphere [22]. The Graphene was grown on the CuO nanoparticles. In such a way we got Graphene@CuO nanocomposites. Later, the synthesized Graphene@CuO nanocomposites were dissolved into the nitric acid, the colored solution was obtained. Now this solution was filtered and the obtained filtrate was found as the Graphene. Such a way, we got two synthesized materials one is Graphene and the other is Graphene@CuO nanocomposites.

6.2.2 CO_2 gas sensing measurement

According to the IUPAC, the sensitivity is the slope of the gas calibration curve i.e. slope of sensor response versus target gas concentration.

The %sensor response (%S.R.) of a sensor was calculated using the formula given by Eqn.6.1:

$$\% S.R. = \frac{R_g \sim R_a}{R_a} \times 100 \qquad (6.1)$$

The response and recovery time of the sensor is defined as 90% of the final sensor output during the adsorption and desorption of the gas respectively. The exponential fitting for every concentration cycle was used for the calculation of the response-recovery times of the sensor. The exponential fitting for the growth and decay has been done in accordance with Eqn. 6.2 and 6.3 respectively.

$$R_m = R_0 \exp(\frac{-t}{t_{res}}) \qquad (6.2)$$

$$R_m = R_0\{1 - \exp(\frac{-t}{t_{rec}})\} \qquad (6.3)$$

Where the R_0 and R_m are the initial and measured values of the resistance of the sensing material and t_{res} and t_{rec} are the response and recovery time respectively [39].

The lab-made CO_2 gas sensor characterization setup is shown in Fig.6.2. This setup consists of a CO_2 gas cylinder attached along with the gas measuring unit connected to a vacuum-assisted chamber having a gas inlet, outlet, and sample holder. The sensor was connected to the Keithley electrometer through the connecting wires which are further connected to a computer for the data recording and analysis.

6.3 Characterizations

The characterization techniques used to characterize synthesized materials were Scanning Electron Microscopy (SEM) (JEOL, JSEM- 6490LV) with Electron Dispersive X-rays (EDX), Particle Size Analysis using Zeta nanosizer, UV-Visible Spectrophotometer (Evolution 201). The crystal and phase were investigated by powder

X-ray Diffractometer (XRD) (Bruker D8 Advance, using Cu Kα radiation) λ=0.15418 nm (at a scan rate of 0.2°/s). A Raman spectrometer (model: Airix Corporation, Japan with laser excitation at 514 nm) was used.

6.4 Results and Discussion

6.4.1 Morphological and elemental analysis

The SEM micrographs of the synthesized Graphene@CuO nanocomposites are shown in Figs. 6.3 (a)-(c) and (d) is showing the EDX spectrum of the same. Fig. 6.3 (a) illustrates the highly porous structure of the synthesized material at 1000 nm scale. SEM micrographs at 500 nm scale presented in Fig. 6.3 (b) and (c) are showing the clear morphology of the synthesized material. From these two micrographs, it is investigated that spherical shaped CuO nanoparticles are attached to Graphene sheets. The attached CuO nanoparticles and porous structure of the material may be useful for sensing application.

The EDX spectrum of the synthesized Graphene@CuO nanocomposites is shown in Fig. 6.3 (d). This shows the presence of the carbon, oxygen, and Cu elements having weight% 26.85, 14.30, and 44.68% respectively. The presence of the Zr and Si is observed due to the coating on the glass substrate during the sample preparation for the SEM.

The planar sheet structure of the multilayered Graphene has been observed in the SEM micrographs at 500, 500, and 200 nm scales which are shown in Figs. 6.4 (a), (b) and (c) respectively. The presence of the elements in the material is investigated via EDX

spectrum which is shown in Fig. 6.4 (d) and this confirms the presence of the C and O elements with weight% as 70.27 and 8.56% respectively. The presence of the Na, Zr, and Si elements is due to the sample preparation process for the SEM micrographs and constituents of the glass substrate.

6.4.2 Particle size distribution analysis

The particle size distribution of the synthesized materials has been illustrated in Fig. 6.5. The intensity (in %) versus the size of diameter (in nm) of the particles of the synthesized materials in isopropyl alcohol has been investigated. There are two peaks present in Fig. 6.4 corresponding with Graphene and Graphene@CuO nanocomposites respectively. The synthesized Graphene has a sheet size range of 142–219 nm with an average sheet size of 190 nm while 295-456 nm and 342 nm are sheet size range and average sheet size for the Graphene@CuO nanocomposites. The observation confirms that the size of the Graphene sheets has smaller in comparison to Graphene@CuO nanocomposites. When the Graphene is grown on the spherical-shaped CuO nanoparticles, some of the particles get attached to the Graphene sheets and vice versa, and also the observed sheet size gets increased in comparison to the Graphene.

6.4.3 Structural analysis

The structural analysis of the synthesized materials has done with the X-ray diffraction (XRD) analysis. The XRD pattern of the synthesized Graphene and Graphene@CuO nanocomposites have been shown in Fig. 6.6 (a) and (b) respectively. In XRD pattern of the Graphene, there is one Bragg's peak at 2θ~25.72° values corresponding to *(002) plane. In the XRD pattern of the Graphene@CuO, there are

sharp peaks present and showing the crystalline nature due to the presence of the CuO nanoparticles. The peaks present at 2θ~23.39°, 43.08°, 50.26°, and 74.08° values correspond with the *(002), #(111), #(200) and #(220). The *(002) is of the graphitic plane while #(111), #(200), and #(220) relate with the presence of the CuO in the synthesized material. The *(002) well matches with JCPDS# 075-1621 while all other planes with the JCPDS# 004-0836. The average crystallite size of the Graphene and Graphene@CuO were calculated and found as 1.29 and 26.07 nm respectively. The increase in average size shows that CuO nanoparticles are attached to the Graphene sheet.

6.4.4 Optical absorption analysis

The optical absorption spectra of the synthesized Graphene and Graphene@CuO both materials have shown in Fig. 6.7. In these spectra, the variation in optical absorption was observed in the wavelength range of 190-800 nm. Both synthesized materials have almost equal absorption getting overlapped to each other and also showing the maximum absorption with the fluctuations in the 190-290 nm wavelength range. The fluctuations are observed due to the glass substrate used on which the thin film was spin-coated. Inset of this figure, Tauc plots of both materials getting overlapped and the extrapolation of the tangent to this curve evaluated the optical energy gap of both materials as 4.1 eV. Such a wide energy gap may be fruitful for sensing applications.

6.4.5 Functional group analysis

The bond vibrations, bending, stretching, and also the functional groups present in the synthesized materials were investigated with the Fourier transform infrared (FTIR) spectroscopy technique. The FTIR spectrum of the synthesized Graphene and

Graphene@CuO has been illustrated in Fig. 6.8 (a) and (b) respectively. In this spectra several valleys correspond to different bond vibrations, stretching, and bending present between constituent elements. The wide valley present at 3344 cm^{-1} wavenumber relates with the hydroxyl group representing the vibrations of O-H bond present in the synthesized materials. The bands present in 2850-2990 and 1270-1483 cm^{-1} wavenumber range resembles the stretching and bending of C-H bonds respectively within the materials. The unsaturated C=C bond presence corresponds to the valley at 1645 cm^{-1} in the materials. The presence of C-O bond vibrations may be seen at 1123 cm^{-1}. There are two extra bands present in the range 792-1117 cm^{-1} in the Graphene@CuO in comparison to the Graphene, showing the presence of the metallic bond vibrations due to the Cu metal [40].

6.4.6 Raman analysis

Fig. 6.9 (a) and (b) show the Raman spectra of the synthesized Graphene and Graphene@CuO nanocomposites respectively. In Fig. 6.9 (a), peaks appearing at 1335, 1597, and 2859 cm^{-1} are known as D, G, and 2D bands respectively. These peaks define the characteristics of the Graphene. The presence of the D-band is related to its edge structure i.e. strong armchair and weak zig-zag edge structure. The calculated disorder parameter for the Graphene was 1.1 (i.e. I_D/I_G= 1.1). The peaks appearing in the 200-1100 cm^{-1} range are due to the lattice vibrational modes occurring in the CuO crystal were observed in the Raman spectrum of the Graphene@CuO nanocomposites in Fig. 6.9 (b). Here peaks present below 1100 cm^{-1} exhibit the characteristics of the metal oxide nanoparticles. The position of the D, G, and 2D bands in the case of Graphene@CuO nanocomposites get shifted and observed at 1328, 1591, and 2778 cm^{-1} Raman shift. And

also the calculated disorder parameter was 0.9. The change in the position of the D, G, and 2D bands and also decrease in the I_D/I_G ratio in the Graphene@CuO nanocomposites compared to Graphene, are the confirmation signature of the composite formation [41-43]. The defects (I_D/I_G~0.9) and the presence of CuO nanoparticles at side edges and corners may be responsible for the sensing.

6.5 CO_2 gas sensing application

6.5.1 Sensing mechanism

In the CO_2 sensing mechanism, the adsorbed oxygen on the surface of the sensing material plays an important role. The interaction between adsorbed atmospheric oxygen and sensing surface is depicted by the Eqns 6.4, 6.5, and 6.6.

$$O_2(air) \leftrightarrow O_2(ads) \qquad (6.4)$$

$$O_2(ads) + e^- \leftrightarrow O_2^-(ads) \qquad (6.5)$$

$$O_2^-(ads) + e^- \leftrightarrow 2O^-(ads) \qquad (6.6)$$

The defects present in the synthesized materials through the oxygen vacancies act as the adsorption sites for atmospheric oxygen. Therefore, a large number of defects adsorbed more atmospheric oxygen and ionic oxygen species have been formed. When CO_2 interacts with sensing material, it is initially adsorbed on pre-adsorbed oxygen (ionic oxygen) and forms the surface carbonate which is shown in the Eqns. 6.7 and 6.8.

$$CO_2 + 2O^-(ads) \leftrightarrow CO_3^{2-} \qquad (6.7)$$

$$CO_2 + O^- (ads) \leftrightarrow CO_3^- \qquad (6.8)$$

These surface carbonates capture certain electrons from the sensing material, resulting in an increase in resistance of the sensing material. This shows that the formation of surface carbonates was responsible for CO_2 detection through the resistance change [37].

6.5.2 CO_2 sensing characteristics of Graphene@CuO

The CO_2 sensing characteristics of the thin film of Graphene@CuO nanocomposites are illustrated in Fig. 6.10. The resistance of the sensing material has been recorded with the exposure of 0.5, 1.0, 1.5, and 2.0 vol.% CO_2 gas in the vacuum assisted chamber. For each concentration of the gas, the obtained respective cycle has been shown in Fig. 6.10.

For every cycle, as the CO_2 is exposed to the sensing element inside the vacuum assisted chamber, the resistance of the sensor getting rises and achieved a stable state of resistance and this corresponds to sensor response. Also as the CO_2 is removed from the chamber, the resistance starts decreasing to achieve the initial state of the resistance and this relates to the recovery of the sensor. The sensitivity and %S.R. for every cycle of the gas were calculated according to the definition and Eqn 6.1 detailed in section 6.2.2 and also shown in Table 6.2. The variation in the resistance takes place from 2.59×10^6 to 2.59×10^6 with the exposure of the 0.5 vol.% concentration of the CO_2. The %S.R. for the same was calculated as 133.33. The exposure of 1.0 vol.% concentration of the CO_2 causes the change in the resistance from 2.87×10^6 to 1.06×10^7 and the calculated %S.R. was found as 267.94. The change in the resistance was recorded from 2.86×10^6 to 2.12×10^7 and from 2.95×10^6 to 3.77×10^7 for the 1.5 and 2.0 vol.% concentration along with

%S.R. 641.96 and 1178.31 respectively. The nature of the CO_2 gas sensor for the repeatability was investigated and found to be repeatable and also the repeatability curve for the 0.5 vol.% gas is shown in Fig. 6.11 (a). From the observation of Fig. 6.11 (b), it is clear that the % S.R. of the sensor varies linearly with the variation in the concentration of the gas. The response and recovery times of the sensor were calculated with the exponential fitted curve according to Eqns. 6.2 and 6.3 respectively. The exponential growth and decay fitted curves for 1.5 and 2.0 vol.% gas are shown in Figs. 6.11 (c) and (d) respectively. The calculated response and recovery time for each cycle are shown in Table 6.2.

6.6 Humidity sensing application

The humidity sensing application of the thin film of Graphene@CuO nanocomposites also has been performed. The setup for humidity sensor characterization has already described in **Chapter 2**. All the data related to this experiment have been recorded using this setup and plotted the same as shown in Fig. 6.12. Curve (a) of Fig. 6.12 (a) shows the plot for sensitivity versus %RH and the related data may be found in Table 6.3. The slope of this curve is defined as the sensitivity of the humidity sensor. Humidity sensor attributes are defined in **Chapters 2 and 3**. The detailed descriptions of the sensing mechanism of the impedance-based humidity sensor have been discussed in **Chapter 2**. The experiment was performed in the 10-95 %RH range and the calculated sensitivity of the sensor was 1.55 MΩ/%RH. The response-recovery times of a sensor are important parameters and the calculated response and recovery time for the Graphene@CuO nanocomposites-based humidity sensor was found as 12 and 9 s respectively. The response and recovery time curve has been shown in Fig. 6.12 (b) and

related data has been shown in Table 6.4. The repeatability curve for the humidity sensor has been shown in Fig. 6.12 (c) and the sensor has found 85.19% repeatable nature. The ageing effect of a sensor shows the life of the sensor as well as its accuracy after a long time. The ageing effect analysis curve after 3, 7, and 15 days for the humidity sensor have been shown in Fig. 6.12 (d) and these results show good stability after the same days. The related data of the repeatability and ageing effect have been depicted in Table 6.5.

6.7 Selectivity of the sensor

A sensor may not be good for every sensing species but it may be good for a particular species. The criteria by which a good sensor is chosen for a particular sensing species, known as selectivity of the sensor. The selectivity is an important parameter for a sensor. The selectivity of the CO_2 sensor was investigated concerning LPG, humidity, acetone, ethanol and the related plot is shown in Fig. 6.13. In this figure, the %S.R. for 2.0 vol.% CO_2 gas was found maximum in comparison of 2.0 vol.% LPG, 95% relative humidity, 2.0 vol.% acetone, and ethanol. The Graphene@CuO based sensor showed good diffusibility with the CO_2 gas.

6.8 Conclusion

The Graphene and Graphene@CuO nanocomposites have been successfully synthesized through the chemical vapor deposition technique. The surface morphology and elemental analysis confirmed that the synthesized materials were the Graphene and Graphene@CuO nanocomposites. The average crystallite size of the Graphene was calculated as 1.29 nm while Graphene@CuO was 26.07 nm. The presence of the Cu

metal was confirmed via the XRD pattern of the Graphene@CuO nanocomposites. The FTIR exhibited the presence of the bond vibrations and stretching between the constituent elements in the synthesized materials. The Raman spectrum of the Graphene revealed the I_D/I_G ratio 1.1 confirming the defects present in the same and the I_D/I_G ratio of Graphene@CuO nanocomposites as 0.9. The defects and attached metal nanoparticles in the Graphene were found responsible for the sensing. The Graphene@CuO nanoparticles-based CO_2 sensor showed the minimum response and recovery times as 1.3 and 1.5 for 0.5 vol.% concentration respectively and the maximum %S.R was found as 1178.31 for the 2.0 vol.% concentration. The selectivity of the CO_2 gas sensor based on Graphene@CuO nanocomposites was checked with respect to LPG, humidity, acetone, and ethanol and found that the sensor was highly selective for CO_2. The results of Graphene@CuO nanoparticles-based CO_2 gas sensor are innovative and the lab model of the sensor developed here can be proposed for commercial development.

References

[1] P. G. Collins, K. Bradley, M. Ishigami, A. Zettl, Extreme oxygen sensitivity of electronic properties of carbon nanotubes, Science 287 (2000) 1801–1804.

[2] J. Kong, M. G. Chapline, H. Dai, Functionalized carbon nanotubes for molecular hydrogen sensors, Adv. Mater. 13 (2001) 1384–1386.

[3] K. G. Ong, K. Zeng, C.A. Grimes, A wireless, passive carbon nanotube-based gas sensor, IEEE Sens. J. 2 (2002) 82–88.

[4] C. Cantalini, L. Valentini, L. Lozzi, I. Armentano, J. M. Kenny, S. Santucci, NO_2 gassensitivity of carbon nanotubes obtained by plasma enhanced chemical vapor deposition, Sensors and Actuators B: Chemical 93 (2003) 333–337.

[5] S. Chopra, K. McGuire, N. Gothard, A. M. Rao, Selective gas detection using a carbon nanotube sensor, Appl. Phys. Lett. 83 (2003) 2280–2282.

[6] S. G. Wang, Q. Z. Zhang, D. J. Yang, P. J. Sellin, G. F. Zhong, Multi-walled carbon nanotube-based gas sensors for NH_3 detection, Diamond Relat. Mater. 13 (2004) 1327–1332.

[7] J. Suehiro, G. Zhou, H. Imakiire, W. Ding, M. Hara, Controlled fabrication of carbon nanotube NO_2 gas sensor using dielectrophoretic impedance measurement, Sensors and Actuators B: Chemical 108 (2005) 398–403.

[8] Y. Murata, E. Starodub, B. B. Kappes, C. V. Ciobanu, N. C. Bartelt, K. F. McCarty, S. Kodambaka, Orientation-Dependent Work Function of Graphene on Pd(111), Appl. Phys. Lett. 97 (2010) 143114.

[9] P. W. Sutter, J. I. Flege, E. A. Sutter, Epitaxial Graphene on Ruthenium, Nat. Mater. 7 (2008) 406−411.

[10] S. Yoshii, K. Nozawa, K. Toyoda, N. Matsukawa, A. Odagawa, A. Tsujimura, Suppression of Inhomogeneous Segregation in Graphene Growth on Epitaxial Metal Films, Nano Lett. 11 (2011) 2628−2633.

[11] J. Coraux, A. T. N'Diaye, C. Busse, T. Michely, Structural Coherency of Graphene on Ir (111), Nano Lett. 8 (2008) 565−570.

[12] Q. Yu, J. Lian, S. Siriponglert, H. Li, Y. P. Chen, S. S. Pei, Graphene Segregated on Ni Surfaces and Transferred to Insulators, Appl. Phys. Lett. 93 (2008) 113103.

[13] A. Reina, X. Jia, J. Ho, D. Nezich, H. Son, V. Bulovic, M. S. Dresselhaus, J. Kong, Large Area, Few-Layer Graphene Films on Arbitrary Substrates by Chemical Vapor Deposition. Nano Lett. 9 (2009) 30−35.

[14] K. S. Kim, Y. Zhao, H. Jang, S. Y. Lee, J. M. Kim, K. S. Kim, J. H. Ahn, P. Kim, J. Y. Choi, B. H. Hong, Large-Scale Pattern Growth of Graphene Films for Stretchable Transparent Electrodes. Nature 457 (2009) 706−710.

[15] C. M. Orofeo, H. Ago, B. Hu, M. Tsuji, Synthesis of Large-Area, Homogeneous, Single Layer Graphene by Annealing Amorphous Carbon on Co and Ni, Nano Res. 4 (2011) 531−540.

[16] X. Li, W. Cai, J. An, S. Kim, J. Nah, D. Yang, R. Piner, A. Velamakanni, I. Jung, E. Tutuc,. Large-Area Synthesis of High-Quality and Uniform Graphene Films on Copper Foils, Science 324 (2009) 1312−1314.

[17] Y. Lee, S. Bae, H. Jang, S. Jang, S. E. Zhu, S. H. Sim, Y. I. Song, B. H. Hong, J. H. Ahn, Wafer-Scale Synthesis and Transfer of Graphene Films. Nano Lett. 10 (2010) 490−493.

[18] S. Bhaviripudi, X. Jia, M. S. Dresselhaus, J. Kong, Role of Kinetic Factors in Chemical Vapor Deposition Synthesis of Uniform Large Area Graphene Using Copper Catalyst. Nano Lett. 10 (2010) 4128−4133.

[19] C. Mattevi, H. Kim, M. Chhowalla, A Review of Chemical Vapour Deposition of Graphene on Copper. J. Mater. Chem. 21 (2011) 3324−3334.

[20] H. Ago, Y. Ito, N. Mizuta, K. Yoshida, B. Hu, C. M. Orofeo, M. Tsuji, K. Ikeda, S. Mizuno, Epitaxial Chemical Vapor Deposition Growth of Single-Layer Graphene over Cobalt Film Crystallized on Sapphire. ACS Nano 4 (2010) 7407−7414.

[21] A. Varykhalov, O. Rader, Graphene Grown on Co (0001) Films and Islands: Electronic Structure and its Precise Magnetization Dependence. Phys. Rev. B 80 (2009) 35437.

[22] H. Ago, Y. Ogawa, M. Tsuji, S.Mizuno, and H. Hibino, Catalytic Growth of Graphene: Toward Large-Area Single-Crystalline Graphene, J. Phys. Chem. Lett. 3 (2012) 2228−2236.

[23] A. Guermoune, , T. Chari, F. Popescu, S. S. Sabri, J. Guillemette, H. S. Skulason, T. Szkopek, and M. Siaj, Chemical vapor deposition synthesis of graphene on copper with methanol, ethanol, and propanol precursors, Carbon 49 (13) (2011) 4204-4210.

[24] H. J. Yoon, J. H. Yang, Z. Zhou, S. S. Yang, and M. M.-C. Cheng, Carbon dioxide gas sensor using a graphene sheet, Sensors and Actuators B: Chemical 157 (1) (2011) 310-313.

[25] K. R. Nemade and S. A. Waghuley, Carbon dioxide gas sensing application of graphene/Y_2O_3 quantum dots composite, In International Journal of Modern

Physics: World Scientific Publishing Company, 2013, Conference Series, vol. 22, 380-384.

[26] K. R. Nemade and S. A. Waghuley, Chemiresistive gas sensing by few-layered graphene, Journal of electronic materials 42 (10) (2013) 2857-2866.

[27] K. R. Nemade, and S. A. Waghuley, Role of defects concentration on optical and carbon dioxide gas sensing properties of Sb_2O_3/graphene composites, Optical Materials 36 (3) (2014) 712-716.

[28] K. R Nemade and S. A. Waghuley, Highly responsive carbon dioxide sensing by graphene/Al_2O_3 quantum dots composites at low operable temperature, Indian Journal of Physics 88 (6) (2014) 577-583.

[29] S. M. Hafiz, R. Ritikos, T. J. Whitcher, N. M. Razib, D. C. S. Bien, N. Chanlek, H. Nakajima, A practical carbon dioxide gas sensor using room-temperature hydrogen plasma reduced graphene oxide, Sensors and Actuators B: Chemical 193 (2014) 692-700.

[30] G. Jimenez-Cadena, J. Riu and F. X. Rius, Gas sensors based on nanostructured materials, Analyst 132 (2007) 1083-1099.

[31] G. Telipan, M. Ignat, C. Tablet and V. Parvulescu, Synthesis, characterization and gas sensing properties of rutile TiO_2 doped with Pt obtained by sol-gel method, Journal of optoelectronics and advanced materials 10 (8) (2008) 2138-2141.

[32] G. Y. Chai, O. Lupan, E. V. Rusu, G. I. Stratan, V. V. Ursaki, V. Şontea, H. Khallaf, and L. Chow, Functionalized individual ZnO microwire for natural gas detection, Sens. Actuators A: Physical 176 (2012) 64-71.

[33] M. Mahdizadeh-Rokhi, Investigation of structural and gas sensing characteristics of un-doped and Co-doped SnO_2 nanostructured thin films, Indian J. Phys. 87 (2013) 517-522.

[34] S. A. Waghuley, Synthesis, characterization and CO_2 gas sensing response of SnO_2/Al_2O_3 double layer sensor, Indian J. Pure Appl. Phys. 49 (2011) 816-820.

[35] R. Chapelle, F. Oudrhiri-Hassani, L. Presmanes, A. Barnabe, P. Tailhades, CO_2 sensing property of semiconducting copper oxide and spinal ferrite nanocomposite thin film, App. Surf. Sci. 256 (2010) 4715–4719.

[36] J. Herra n, G. G. Mandayo, I. Ayerdi, E. Castan ˜o, Influence of silver as an additive on $BaTiO_3$ –CuO thin film for CO_2 monitoring. Sens. Actuators B: Chem. 129 (2008) 386–390.

[37] K. Fan H. Qin, L. Wang, L. Ju, J. Hu CO_2 gas sensors based on La_{1-x} Sr_xFeO_3 nanocrystalline powders, Sensors and Actuators B: Chemical 177 (2013) 265–269.

[38] T. Krishnakumar, R. Jayaprakash, T. Prakash, D. Sathyaraj, N. Donato, S. Licoccia, M. Latino, A. Stassi, G. Neri, CdO-based nanostructures as novel CO_2 gas sensors, Nanotechnology 22 (2011) 1-9.

[39] U. Kumar and B. C. Yadav, Synthesis of carbon nanotubes by direct liquid injection chemical vapor deposition method and its relevance for developing an ultra-sensitive room temperature based CO_2 sensor, Journal of the Taiwan Institute of Chemical Engineers, 96 (2019) 652-663.

[40] R. Udayabhaskar, R. Suresh, R. V. Mangalaraja, J. Yáñez, B. Karthikeyan, and D. Contreras, Unraveling the synergistic influences of graphene and CuO on the

structural, photon and phonon properties of graphene: CuO nanocomposites, Carbon 152 (2019) 766-776.

[41] A. C. Ferrari, Raman spectroscopy of graphene and graphite: Disorder, electron–phonon coupling, doping and nonadiabatic effects, Solid State Communications 143 (2007) 47-57.

[42] V. B. Mohan, M. Nieuwoudt, K. Jayaraman, and D. Bhattacharyya, Quantification and analysis of Raman spectra of graphene materials, Graphene Technology 2 (2017) 47-62.

[43] H. Wang, Z. Maiyalagan, X. Wang, Review on recent progress in nitrogen-doped graphene: synthesis, characterization, and its potential applications, ACS Catal. 2(5) (2012) 781-794.

Figures

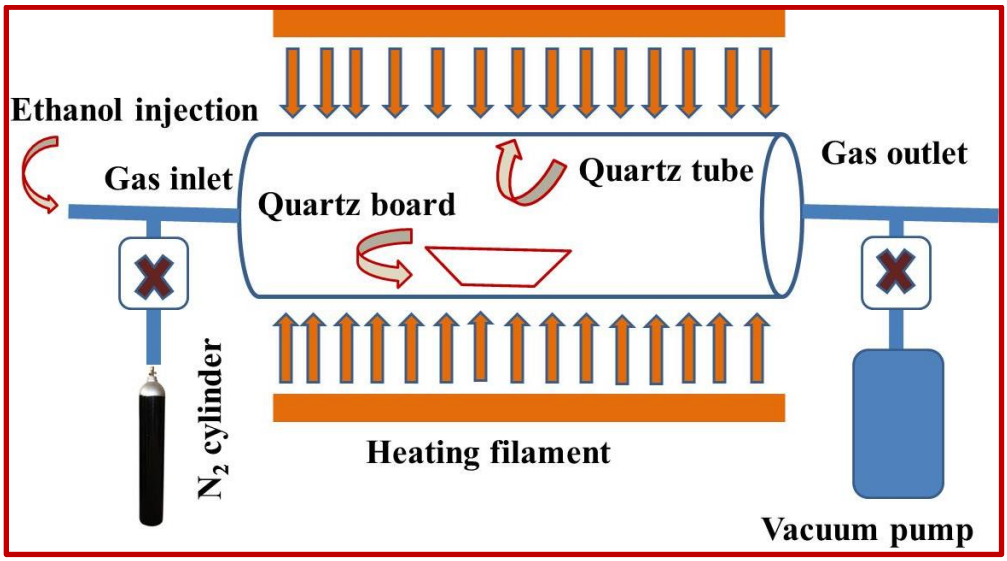

Fig.6.1 Schematic of a typical DLICVD

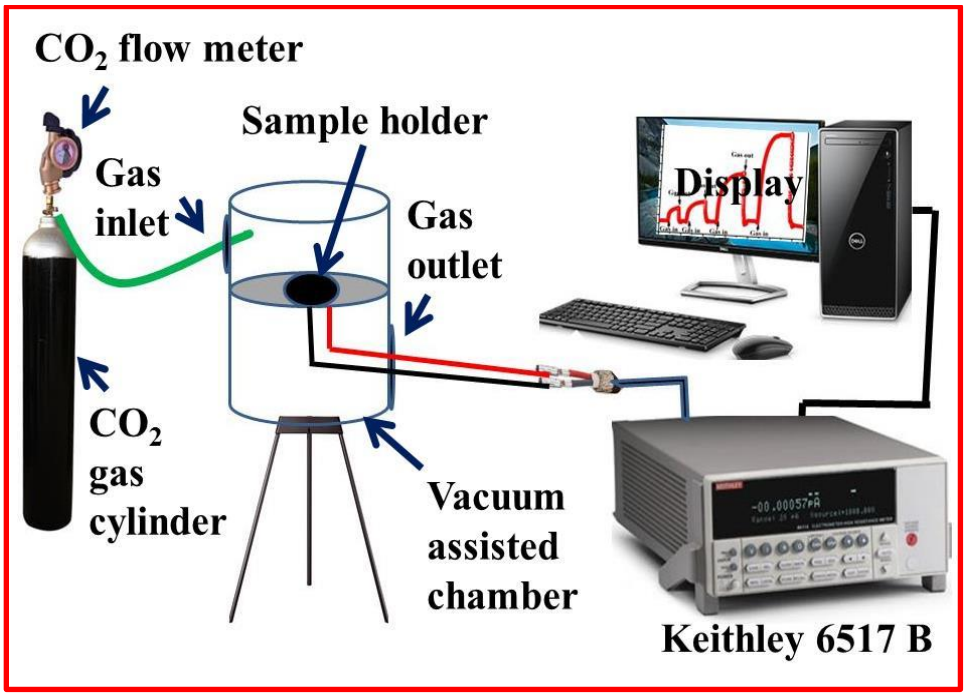

Fig. 6.2 CO_2 gas sensor characterization setup

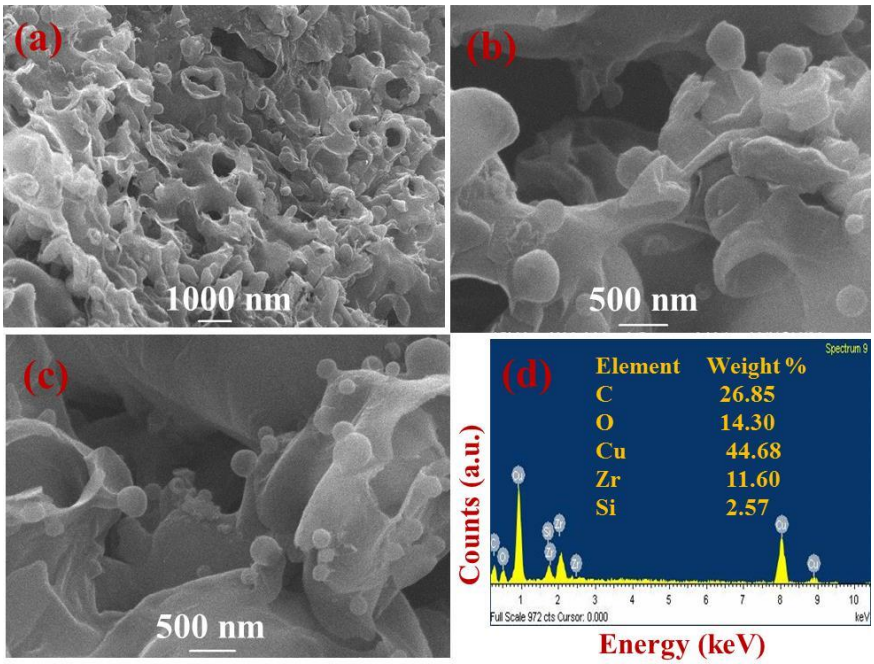

Fig. 6.3 (a)-(c) SEM micrographs and (d) EDX spectrum of Graphene@CuO nanocomposites

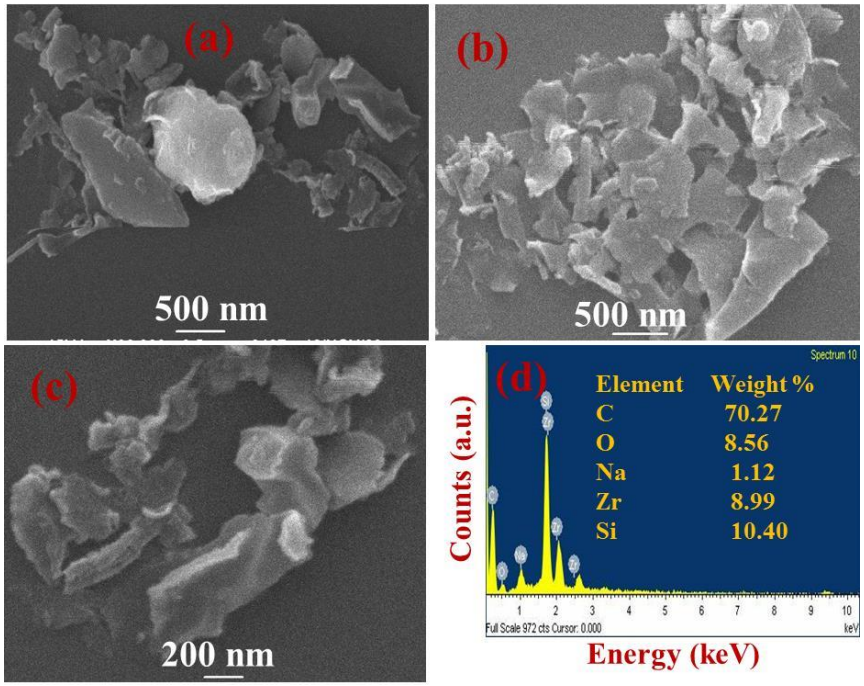

Fig. 6.4 (a)-(c) SEM micrographs and (d) EDX spectrum of synthesized Graphene

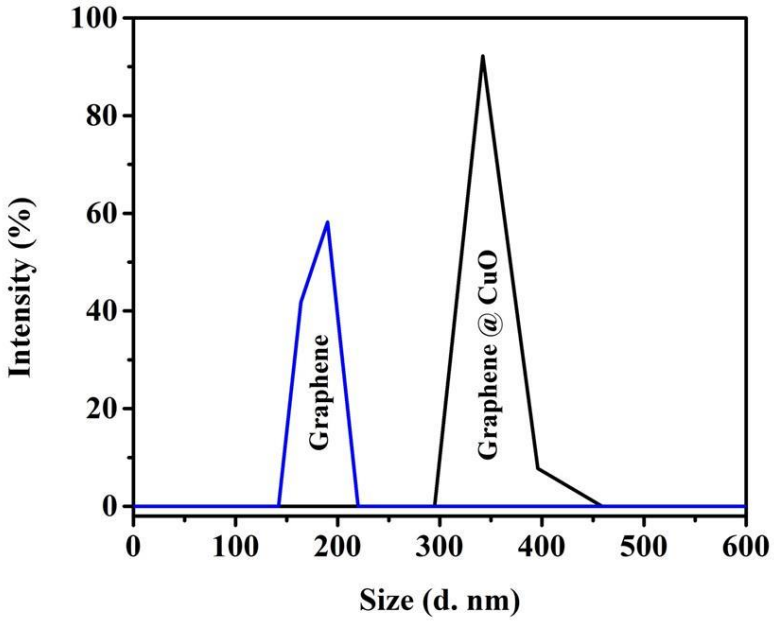

Fig. 6.5 Particle size distribution of Graphene and Graphene@CuO nanocomposites

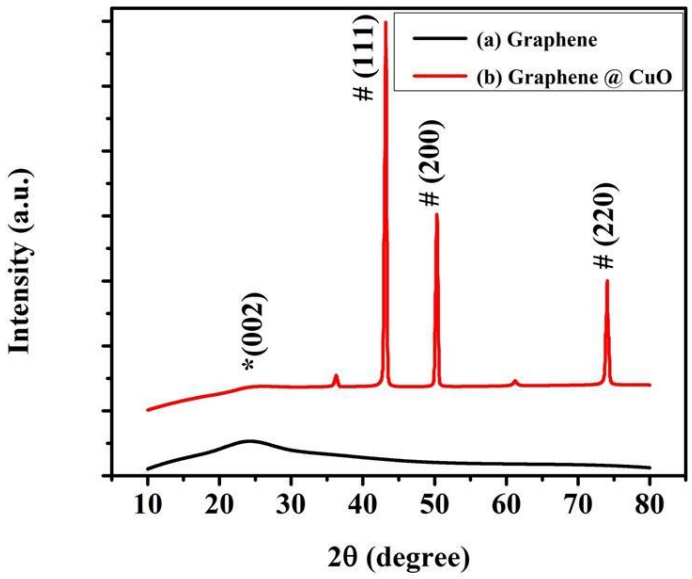

Fig. 6.6 XRD pattern of (a) Graphene and (b) Graphene@CuO nanocomposites

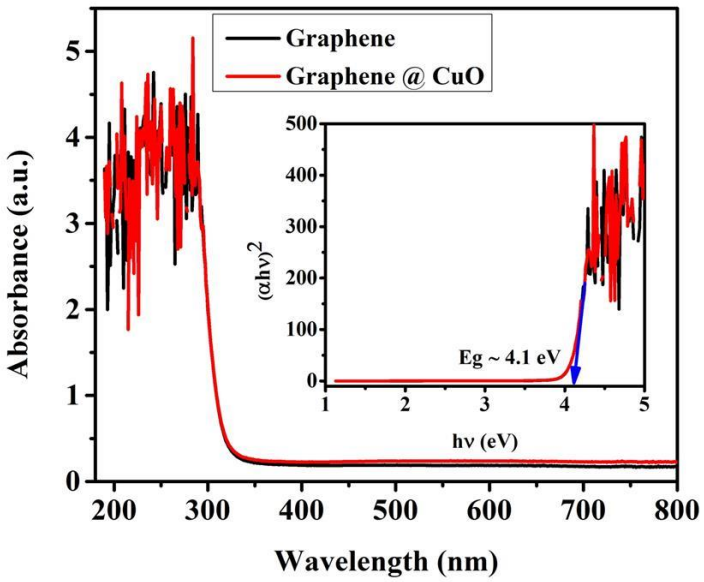

Fig. 6.7 Optical absorption of Graphene and Graphene@CuO nanocomposites along with inset Tauc plots of the same

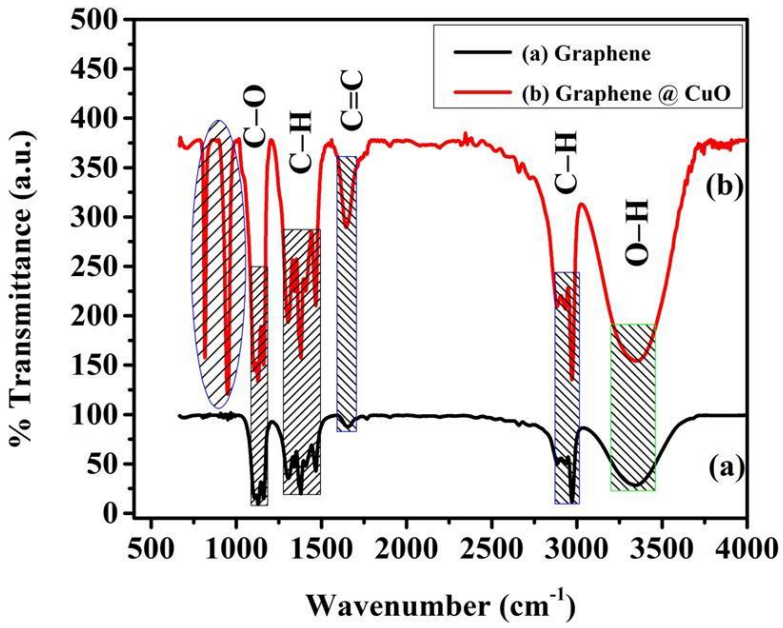

Fig. 6.8 FTIR spectrum of (a) Graphene and (b) Graphene@CuO nanocomposites

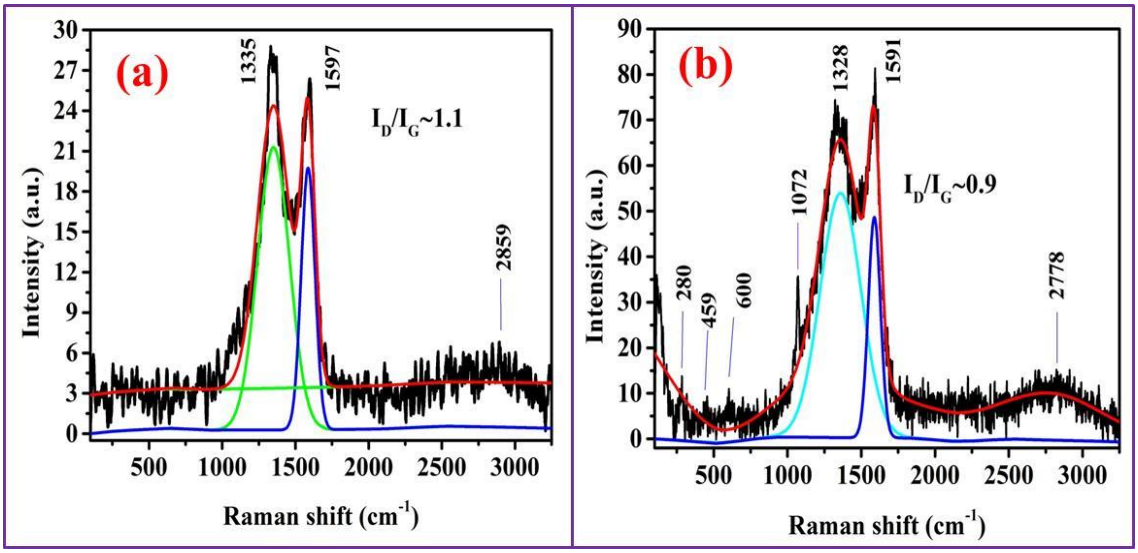

Fig. 6.9 Raman spectrum of (a) Graphene and (b) Graphene@CuO nanocomposites

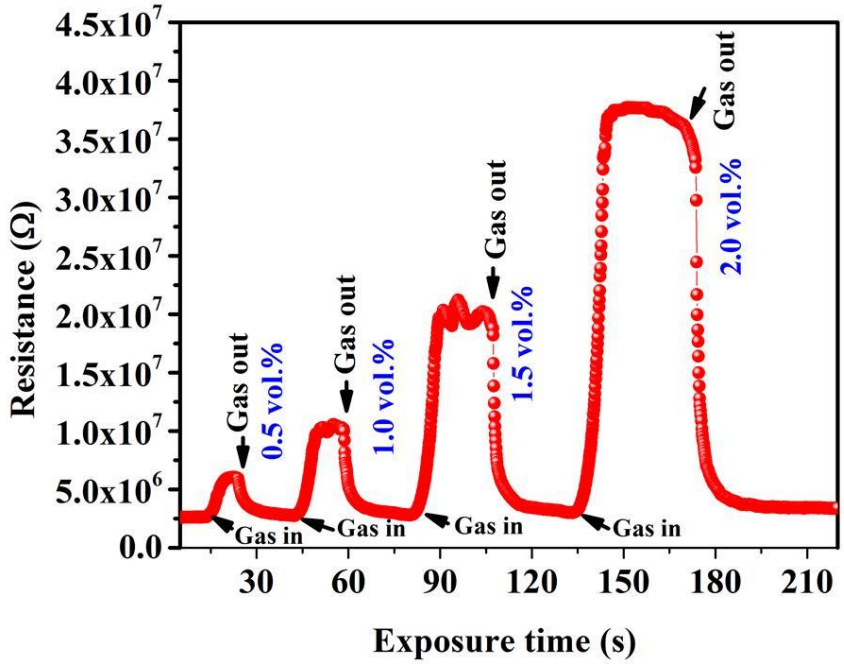

Fig. 6.10 CO_2 sensing characteristics of the Graphene@CuO nanocomposites

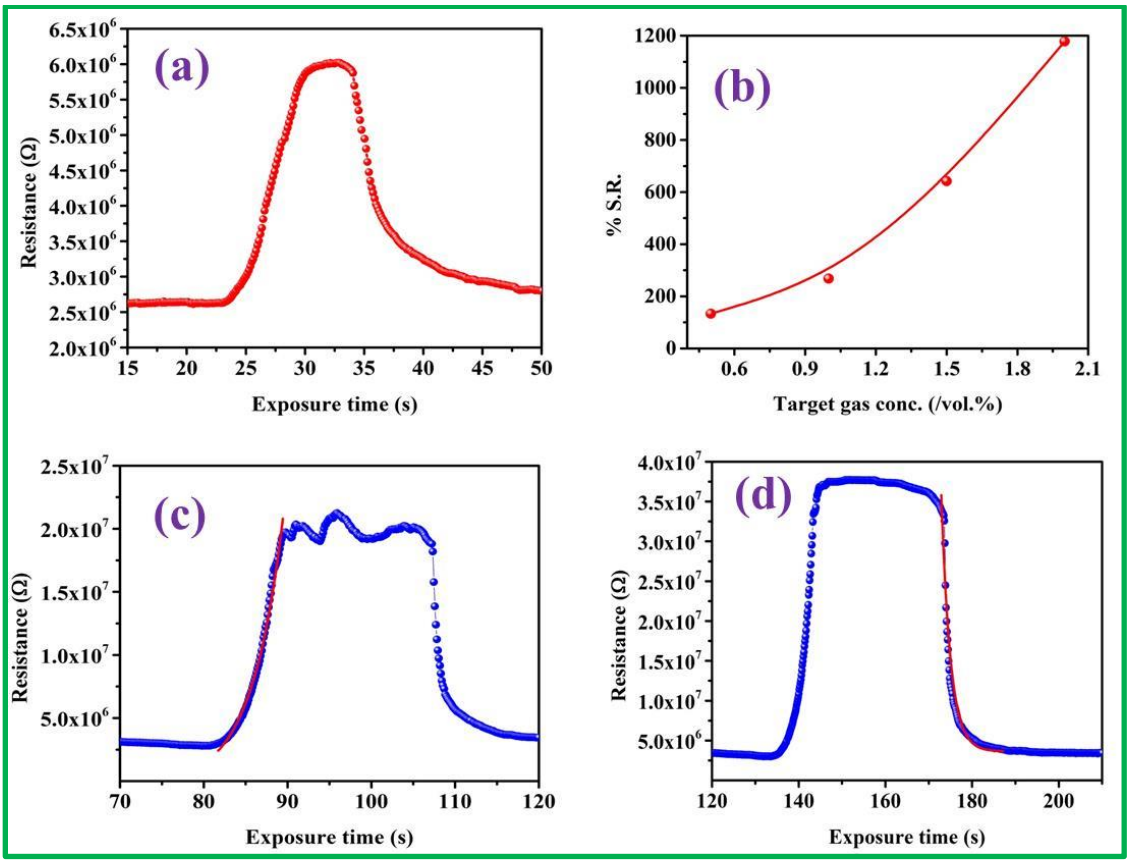

Fig. 6.11 CO_2 sensor attributes: (a) Repeatability curve for 0.5 vol.%, (b) %S.R. versus target gas concentration curve, (c) Exponentially growth fitted curve for the 1.5 vol.% and (d) Exponentially decay fitted curve for the 2.0 vol.%

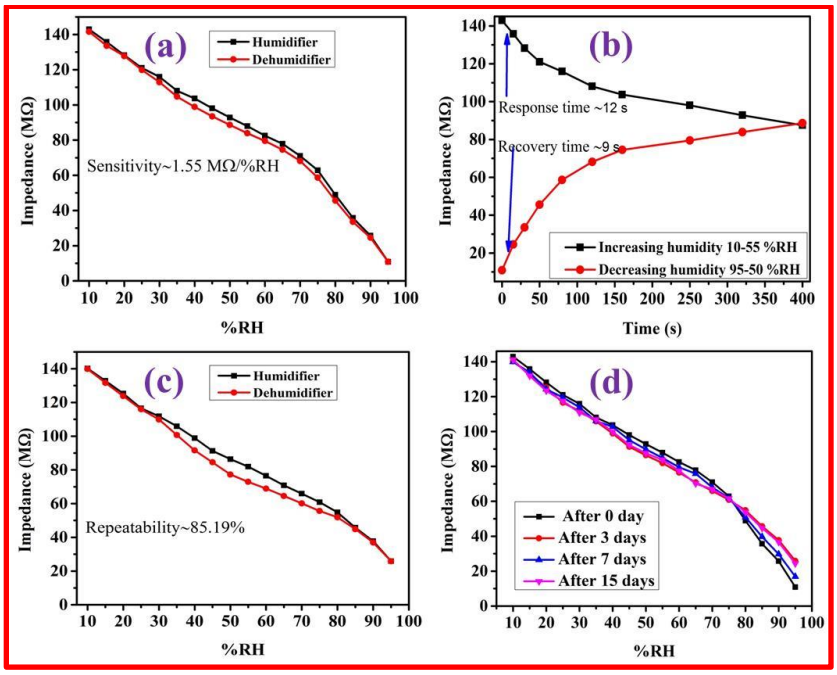

Fig. 6.12 Humidity sensor attributes (a) sensitivity curve, (b) response-recovery time curve, (c) repeatability curve, and (d) ageing effect

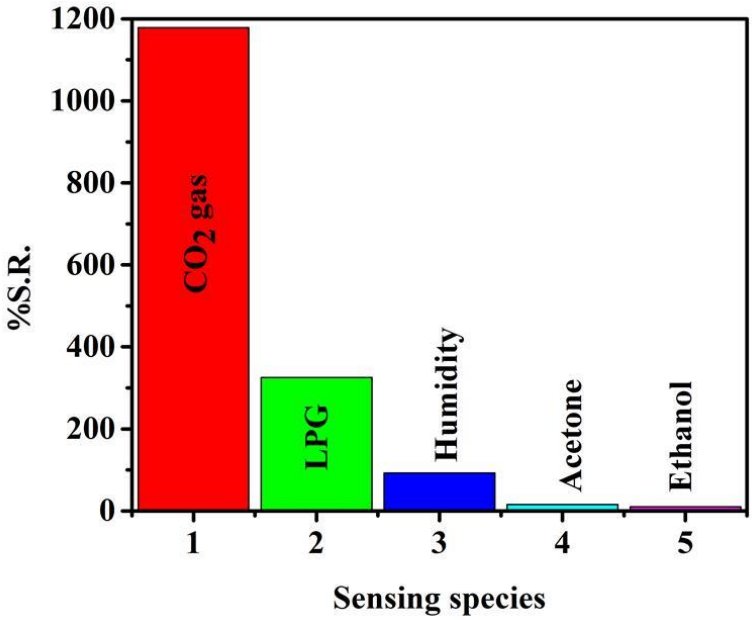

Fig. 6.13 Selectivity of the sensor towards CO_2, LPG, humidity, acetone, and ethanol

Tables

Sr. No.	Sensing materials	Sensor response/ Sensitivity	$T_{Res.}$ (s)	$T_{Rec.}$ (s)	References
1.	Graphene	--/0.17%/ppm	8	-	23
2.	Graphene/Y_2O_3 quantum dot	1.08/--	-	-	24
3.	Few layered Graphene	3.83/--	11	14	25
4.	Sb_2O_3/Graphene quantum dot	--/--	16	22	26
5.	Graphene/Al_2O_3 quantum dot	10.84/--	14	22	27
6.	H_2 plasma reduced GO	71%/--	240	240	28

Table 6.1 Sensing attributes for Graphene-based CO_2 sensor

CO_2 gas Conc. / **Sensor Attributes**	**0.5 vol.%**	**1.0 vol.%**	**1.5 vol.%**	**2.0 vol.%**
Sensitivity (/vol.%)	266.66	267.94	427.97	589.16
% S.R.	133.33	267.94	641.96	1178.31

Response time (s)	1.3	2.8	3.8	4.8
Recovery time (s)	1.5	1.8	1.9	2.1

Table 6.2 CO_2 gas sensor attributes based on the synthesized Graphene@CuO nanocomposites

%RH	**Impedance (MΩ)**	
	Increasing mode	**Decreasing mode**
10	142.89	141.60
15	135.79	133.65
20	128.24	127.79
25	121.03	119.88
30	115.92	112.90
35	108.07	104.70
40	103.68	98.86
45	98.05	93.50
50	92.82	88.66
55	87.91	83.91
60	82.55	79.53
65	77.84	74.55
70	70.97	68.15
75	62.86	58.64
80	48.88	45.59
85	35.73	33.55
90	25.75	24.55
95	10.88	10.88

Table 6.3 Variation in the impedance as per increasing and decreasing humidity at 100 Hz

	Impedance (MΩ)	
Time (s)	**Response (10-55 %RH)**	**Recovery (95-50 %RH)**
0	142.89	10.88
15	135.79	24.55
30	128.24	33.55
50	121.03	45.59
80	115.92	58.64
120	108.07	68.15
160	103.68	74.55
250	98.05	79.53
320	92.82	83.91
400	87.55	88.66

Table 6.4 Time measured along with variation in the impedance as per increasing humidity (10-55 %RH) and decreasing humidity (95-50 %RH) at 100 Hz frequency

%RH	**Impedance (MΩ)**				
	Repeatability		**Ageing effect**		
	Increasing mode	**Decreasing mode**	**After 3 days**	**After 7days**	**After 15 days**
10	140.19	139.87	140.19	139.90	141.19
15	132.89	131.65	132.89	133.79	131.89
20	125.34	123.79	125.34	124.24	123.34
25	116.53	115.98	116.53	119.53	117.53
30	111.84	109.9	111.84	113.92	110.84
35	105.87	100.7	105.87	106.07	106.87
40	98.88	91.56	98.88	102.68	99.88
45	91.25	84.50	91.25	95.05	92.35
50	86.42	77.26	86.42	89.82	87.52
55	81.91	72.91	81.91	84.91	83.81
60	76.5	68.93	76.5	79.55	77.53
65	70.84	64.55	70.84	75.84	70.18
70	65.97	60.15	65.97	67.97	66.87

75	60.86	55.64	60.86	61.86	61.66
80	54.88	51.89	54.88	50.88	53.78
85	45.73	44.85	45.73	39.73	44.63
90	37.75	36.95	37.75	29.75	36.65
95	25.88	25.88	25.88	16.88	24.28

Table 6.5 Recorded data of repeatability and ageing effect after 3, 7, and 15 days

CHAPTER 7

CONCLUDING REMARKS AND FURTHER RESEARCH SCOPE

A study of synthesis, characterization and sensing properties of modified Graphene and its nanocomposites is summarized in the present chapter. This chapter also gives the guidelines for further research work in the field of carbon nanostructure and its nanocomposites films as efficient humidity and gas sensors.

CHAPTER 7

Concluding remarks and scope of further research

7.1 Conclusion

The materials having a dimension of nanometer at least in one direction are dealt with the Nanoscience, however, the application and engineering of nanomaterials are covered in Nanotechnology. Also, Nanoscience and Nanotechnology deal with the novel phenomenon of preparing, measuring its property, and manipulating the dimension of an object up to the order of nanometer scale and to develop the products for practical application and miniaturization of electronic devices. The application of nanotechnology in engineering the materials for sensor developments improve the working, detection limit of the humidity and gas sensors at room temperatures. This must be achieved predominantly by alterations of the space charge layers for each grain and enhancing the electronic properties of the material. The large surface to volume ratio of nanomaterials can be used as a prominent parameter to contribute in the era of sensor developments. The surface reaction on the sensor gets improved when the number of defect sites for the reaction is increased. The larger surface to volume ratio of nanocrystalline structures enhances the opportunity for the occurrence of this surface reaction. This turn will increase the sensitivity of the sensors.

The carbon nanomaterial like Graphene is one of the most important nanomaterials used in technology having extraordinary properties. In the field of sensors, they have played a much efficient role by providing an enhanced surface area or high aspect ratio. Carbon nanomaterials are among the most broadly discussed researched and

applied materials for synthetic nanomaterials. The structural diversity of this material provides an array of unique electronic, magnetic, and optical properties, which when combined with their robust chemistry and ease of manipulation, makes them an attractive candidate for sensor application. Generally, metal oxide-based sensors are used in sensing applications but when these nanomaterials are doped with carbon nanomaterials then their sensing capability, response, and recovery time are improved many times.

Chapter 1 addresses the introduction of different synthesis techniques used for the synthesis of Graphene and its derivatives along with their sensing applications. The sensing principle and extensive survey of literature on the development of carbon-based humidity and gas sensors and their present status have been discussed. The orientation and objectives of the present research investigation are included at the end of the Chapter. **Chapter 2** addresses the synthesis and characterization techniques (BET, SEM, EDX, UV Visible spectroscopy, particle size analysis, FTIR, and Raman spectroscopy) for the synthesized oxygen functionalized Graphene (modified Graphene). The thin film of modified Graphene was used for humidity sensing at different frequencies 100 Hz, 1 kHz, and 10 kHz. The chapter also discussed the impedance-based humidity sensing mechanism at an optimized 100 Hz frequency. To get the higher sensitivity the five-layered Graphene Oxide was functionalized with iron oxide nanoparticles. So **Chapter 3** describes the synthesis of five-layered GO and its functionalization with iron oxide nanoparticles for humidity detection. The thin film of Fe-GO shows the unique flower-like SEM micrographs which are much useful for humidity detection. The capacitance-based humidity sensing mechanism has also been discussed in this Chapter. The Fe-GO based sensor shows the maximum sensitivity in the higher humid region, so such a type

of sensor is used where the level of the humidity is much higher. The maximum sensitivity in the high humid region is attributed due to the dangling bonds formed during the functionalization with the iron oxide nanoparticles.

In **Chapter 4** an effort has been made to enhance the sensor response via developing the LPG sensor-based thin film of the Graphene functionalized with CuO-SnO_2 nanocomposite. The sensitivity of the sensor was increased in comparison to the previously reported two Chapters. Further, to increase the sensitivity the next chapter has been designed as **Chapter 5** in which the development of the LPG sensor based on the GO functionalized with PPdAAm/SnO_2 nanocomposites was described. The development of ultra-fast sensitive and selective CO_2 gas and humidity sensors based on the thin film of Graphene@CuO nanocomposites were described in **Chapter 6**. **Chapter 7** deals with a brief report of the work done including the concluding remarks. Also, this chapter of the Thesis.

Future scope for further research work in the field of carbon nanomaterials and their composites as the electrochemical sensor has been depicted in the last chapter

A study of synthesis, characterization, and sensing properties of Graphene functionalized with metal oxide is summarized as below:

7.1.1 Modified Graphene as a moisture sensor at an optimized frequency

The Graphical Abstract of synthesis, characterization, and humidity sensing of oxygen functionalized Graphene has been depicted in Fig. 7.1. To obtain the oxygen functionalized Graphene the synthesis was performed by the modified Hummer method

followed by the thermal reduction at 600 °C. To characterize the synthesized material different characterization tools were used. The BET surface area of the synthesized material was found as 10.55 m^2/g and the pore size distributions ranging from 10.34 to 97.44 nm confirming the mesoporous nature of the material. The surface morphology of the material revealed the wrinkles, defects, and dangling bonds present in the synthesized layered sheet-type structure. The I_D/I_G ratio of the m-Graphene is calculated as 1.55 along with crystallite size 10.81 nm with the help of the Raman spectrum.

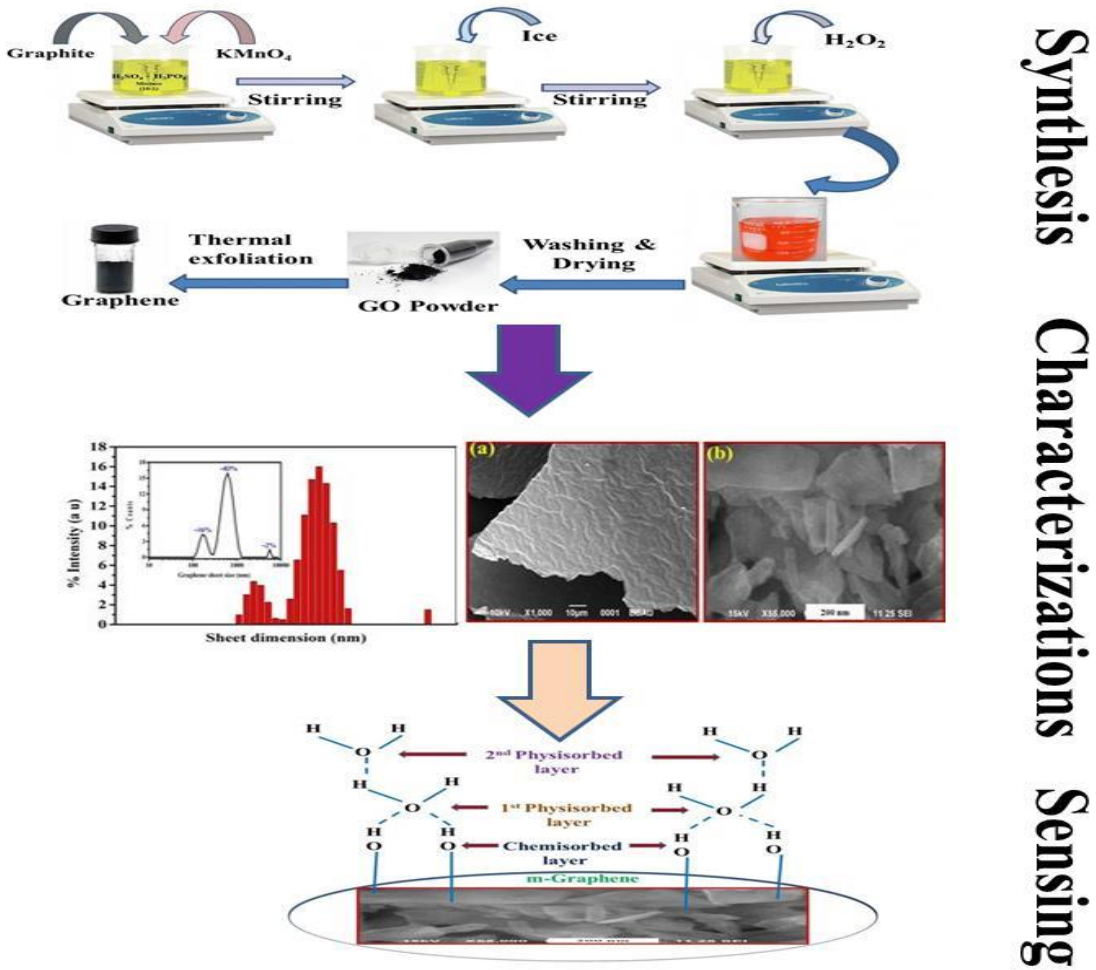

Fig. 7.1 Schematic showing the Graphical Abstract of synthesis, characterization, and humidity sensing

The thin film of m-Graphene was employed as the moisture sensing at different frequencies and optimized as 100 Hz for maximum sensitivity. The humidity sensor showed the sensitivity as 2.51 MΩ/%RH along with the calculated repeatability, response, and recovery time are 96.05%, 24, and 13 s respectively at room temperature. Such type of sensitivity was attributed due to the wrinkles, defects, and dangling bonds present in the synthesized material.

7.1.2 Fabrication of humidity sensor based on thin-film of Graphene functionalized with iron oxide nanoparticles

The work performed for the Fe-GO based sensor has been represented in Fig. 7.2 which is showing the synthesis of GO functionalized with the iron oxide nanoparticles for humidity detection. The synthesis of the GO and Fe-GO were performed with the wet chemical method. Thin films of GO and Fe-GO were fabricated by using the spin coating technique at the rate of 1500 rpm. The thin film of Fe-GO was characterized by various techniques and a unique flower-like structure was found after the functionalization of GO with iron oxide nanoparticles. The XRD revealed that the GO consists of a minimum of 5 layers of Graphene. BET surface analysis confirmed that the synthesized Fe-GO is the mesoporous material partaking the surface area 45.23 m^2/g together with a mean pore diameter of 32 nm. The defect ratio I_D/I_G was calculated as 1.41. After the fabrication of thin-film, variations in capacitance of the film with relative humidity (%RH) were recorded at an optimized frequency of 100 Hz. The sensitivity of the Fe-GO-based sensor was found as 14.12 pF/%RH for higher humidity (70-95 %RH) region and also the average sensitivity, response, and recovery time were observed as 5.18 pF/%RH, 31 and 11 s respectively at room temperatures in the 10-95 %RH humidity region. The Fe-GO

based sensor showed the best sensitivity in the higher humidity region (14.66 pF/%RH) as compared to the lower (0.26 pF/%RH) and mid humid region (0.61 pF/%RH). The Fe-GO based sensor exhibited good sensitivity due to the metallic dangling bonds of iron oxide nano metal present in the flower-like unique morphology.

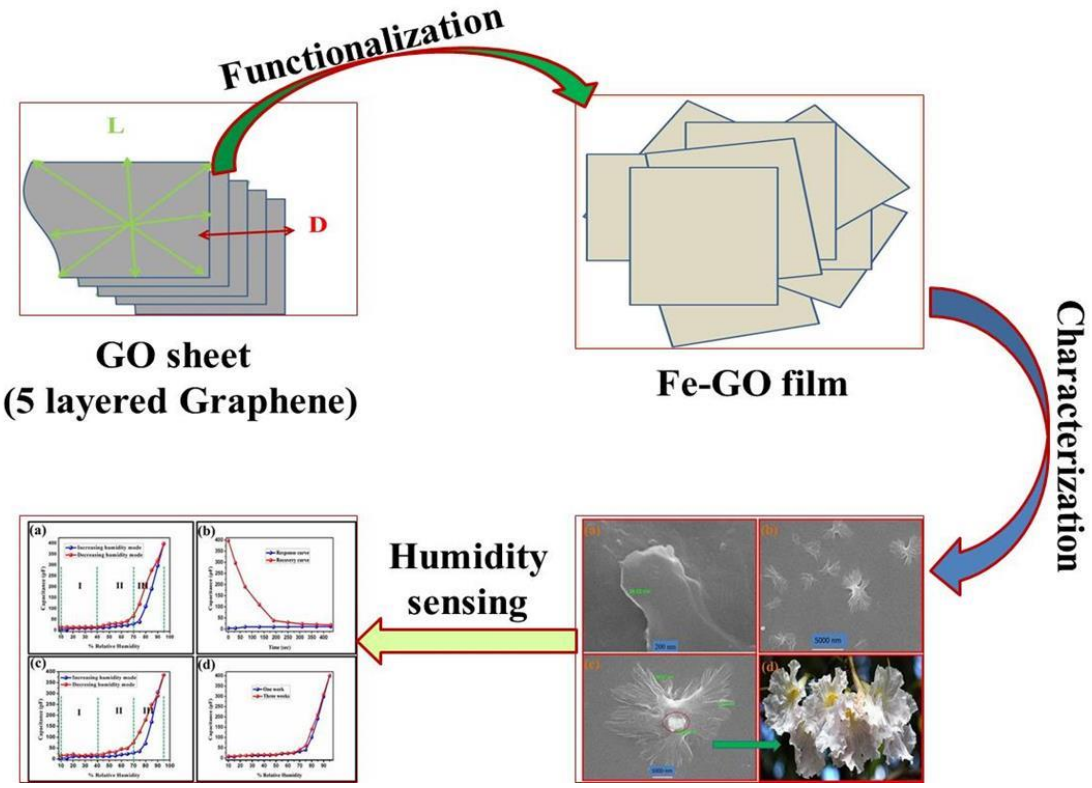

Fig. 7.2 Schematic showing the summary of synthesis, characterization, and humidity sensing application of Fe-GO based humidity sensor

7.1.3 Design and fabrication of Graphene functionalized with CuO/SnO_2 nanocomposites based LPG and humidity sensor

The thin film of the Graphene functionalized with CuO/SnO_2 nanocomposite (GCS) synthesized via Hydrothermal was fabricated on the silica glass substrate. The

morphology of the synthesized material showed that metal nanoparticles were attached at the side edges, corners and distributed over the basal plane of the Graphene. The optical bandgap of the synthesized material was calculated as 4.1 eV from the absorption spectrum.

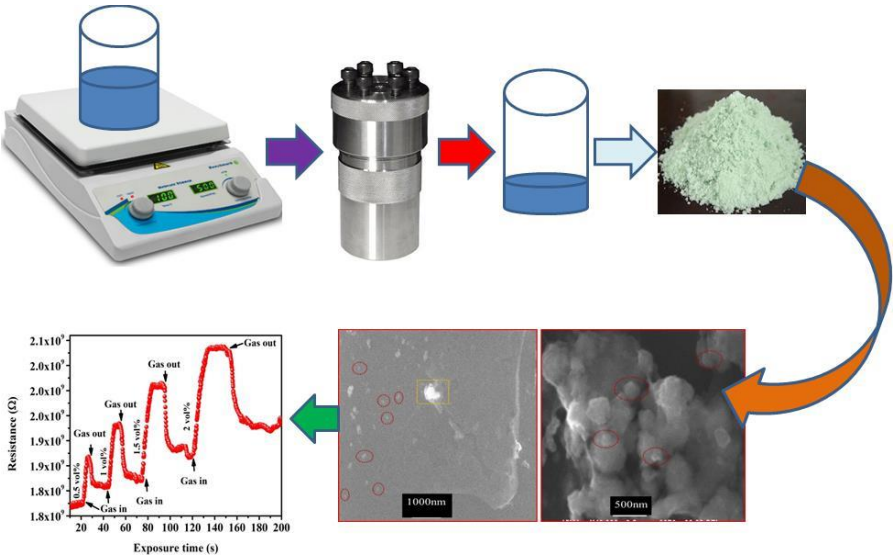

Fig. 7.3 Schematic showing the Graphical Abstract of synthesis and characterization of GCS based LPG sensor

The thin film of the material was employed as the LPG sensor. The concentration 0.5, 1.0, 1.5, and 2.0 vol.% of the LPG was detected with the GCS based sensor. The sensor showed the minimum % sensor response (5.35) for the 0.5 vol.% with the lowest response and recovery time (1.7 and 1.2 s) while the maximum % sensor response (11.76) for the 2.0 vol.% having long response and recovery time (7.6 and 4.8 s). The metallic dangling bonds are much useful for the sensor response as well as response-recovery time. The Graphical Abstract of GCS based work has been depicted in Fig. 7.3. The thin film was also used for humidity sensing and the observed sensitivity was 1.20

MΩ/%RH. The selectivity of the sensor was investigated towards the humidity, ethanol, acetone, and CO_2 gas and was found appropriate for the LPG. The linear characteristics of Graphene/CuOSnO_2 nanocomposite based LPG sensor was rather appropriate for emerging a commercial LPG sensor operable at room temperature.

7.1.4 Development of Graphene oxide functionalized with poly palladium acryl amide SnO_2 nanocomposites for LPG and humidity sensing

Synthesis and characterization of Graphene oxide (GO) functionalized with poly Pd acryl amide SnO_2 (PPdAAm/SnO_2) nanocomposites and their relevance for detecting the liquefied petroleum gas at room temperature are summarized in Fig.7.4. For surface morphological observation and elemental mapping, a thin film of the material was investigated through the Scanning Electron Microscope, and further for optical characterization, UV-Vis spectrophotometer and Particle size analyzer were used. The minimum crystallite size of the material was found as 19.14 nm from the X-Ray Diffraction analysis and also confirmed the presence of the Palladium (Pd) nanoparticles. The peaks corresponding at 465 and 507 cm^{-1} in the Raman spectrum confirmed the stretched bond vibrations of the SnO_2 nanoparticles. The average size of the synthesized material was found as 118 nm through the Dynamic Light Scattering technique and the Tauc plot gave the bandgap as 5.3 eV in from the absorption spectra. The N-H vibrations of the amide group present in the FTIR spectrum confirmed the formation of acrylamide in the synthesized material. The LPG detection was studied for 0.5, 1.0, 1.5, and 2.0 vol.% concentration with the typical operable voltage of 40 V at 27 °C and found as the

%sensor response of the sensor 120.90, 163.33, 373.25, and 570.58 respectively. The response and recovery time was observed shorter (7.8 and 3.3 s) for the 0.5 vol.% and longer (18.9 and 5.2 s) for the 2.0 vol.% concentration of the LPG. Also, the results were found reproducible and no aging effect was observed. Thus the lab model of sensor developed here may be proven robust for outdoor applications and can be fabricated at the commercial level.

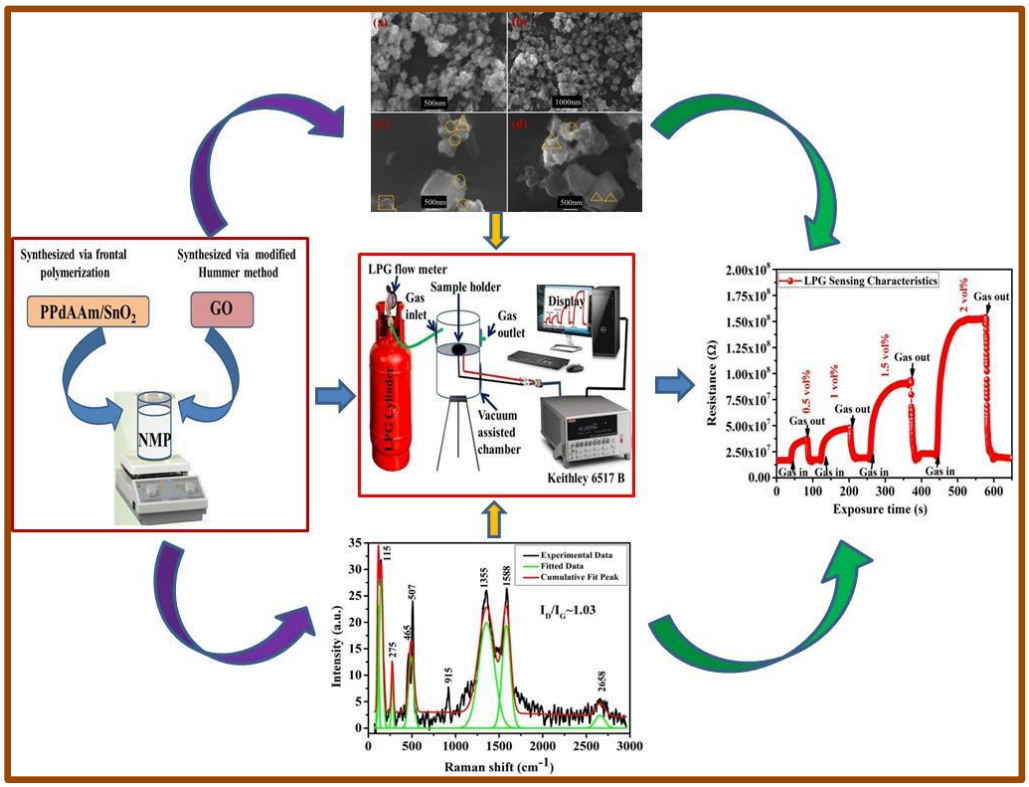

Fig. 7.4 Schematic showing the Graphical Abstract of synthesis and characterization of MP-GO based LPG sensor

7.1.5 Development of ultrafast sensitive and selective CO_2 gas sensor based on the thin film of Graphene @ CuO nanoparticles

Synthesis and characterization of Graphene grown on CuO nanoparticles and its relevance for detecting the CO_2 gas at room temperature are summarized in Fig. 7.5. For surface morphological observation and EDX spectrum, a thin film of the material has been inspected through the Scanning Electron Microscope, and also for optical characterization, UV-Vis spectrophotometer and Particle size analyzer have been used. The average size of the synthesized material was found as 341.18 nm through the Dynamic Light Scattering technique and the Tauc plot gave the bandgap as 4.1 eV in from the absorption spectra. The CO_2 detection was studied for 0.5, 1.0, 1.5, and 2.0 vol.% concentration with the typical operable voltage of 10 V at 27 °C and found as the %sensor response of the sensor 133.33, 267.94, 641.96, and 1178.31 respectively. The response and recovery time was observed shorter (1.3 and 2.3 s) for the 0.5 vol.% concentration of the CO_2 gas. Also, the results were found reproducible and no aging effect was observed. The selectivity of the sensor was tested toward the acetone, ethanol, humidity, and LPG and the sensor was selected for the CO_2 gas. The sensor is quite sensitive and can be used for commercial production.

The complete overview of the Thesis including the sensing materials, dopants, bandgap, sensitivity, crystallite size, average grain size, pore size is depicted in Table 7.1. The main target of our research work was to design and fabricate the different types of sensors using carbon nanomaterials which would be robust, cost-effective, and more sensitive than previously reported sensors.

From Table 7.1, it is clear that in comparison to the modified Graphene and Fe-GO-based humidity sensor, the later one shows better results. The reason behind it is in the Fe-GO there are more dangling bonds are present which are of the breakage of the

GO sheets as well as metallic bonds in comparison to m-Graphene. The 4th and 5th Chapters are of LPG sensors which are based on GCS and MP-GO. In the comparison of these two LPG sensors, the MP-GO-based LPG sensor shows better results. In the MP-GO based LPG sensor, the Pd plays a prominent role in enhancing the sensor response as well as shorter response-recovery times.

Chapters	**Materials**	**Synthesis Method**	**Disorder Parameter (I_D/I_G)**	**Type of sensor**	**Sensitivity/ %Sensor Response**	**Response time (s)**	**Recovery time (s)**
Chapter 1	**Introduction**	-	-	-	-	-	-
Chapter 2	**M-Graphene**	Wet chemical method	1.55	Humidity	2.51 MΩ/%RH	24.0	13.0
Chapter 3	**Fe-GO**	Wet chemical method	1.53	Humidity	5.18 pF/%RH	31.0	11.0
Chapter 4	**G-CuO/SnO_2**	Hydrothermal method	1.09	LPG	5.4	1.6	1.2
Chapter 5	**MP-GO**	Wet chemical method	1.03	LPG	120.90	7.8	3.3
Chapter 6	**Graphene@Cu nanocomposites**	Chemical Vapor Depostion	0.90	CO_2	133.33	1.3	2.3

Table 7.1 Summary of the research work performed Chapter-wise in the entire Thesis

The 6th chapter reveals the CO_2 sensor based on the thin film of the Graphene@CuO nanocomposite synthesized by Chemical vapor deposition technique. The CO_2 sensor has the ultra-high %sensor response as 1178.31 for the 2.0 vol.% concentration of the CO_2 gas and minimum response/recovery times were calculated as

1.3/2.3 s respectively. As the I_D/I_G ratio get decreasing the sensitivity is going to increase. The disorder parameters are getting decrease with the functionalization of the Graphene sheets with the metal oxides nanoparticles. After optimization, these materials may be useful for a commercialized model of sensor applicable for both indoor and outdoor detection of LPG/ humidity/CO_2. Thus different configurations/systems described in the thesis and the detailed specifications are given for each of them are expected to prove useful in fabricating sturdy, robust, and cost-effective sensors suitable for operation at room temperature.

7.2 Scope of further research

Future inspections that would be fruitful in further understanding the role of carbon nanomaterials for more applications in the sensor at high and below room temperature are needed. These include incorporation of the recovery aspects achieved from the incorporation of catalyst onto the surface of carbon nanomaterials being used to detect a reducing gas. Spectroscopic evaluation and surface nanoscale engineering of the sensing mechanism would be very fruitful in the selection of the material to be used for the fabrication of cost-effective sensors in the future. The future scope of carbon nanomaterials can be understood as follows:

- A comprehensive investigation of the evolution of the surface reactions for the temperature regarding to understand the reaction products from the surface interaction needs to be carried out. Temperature Programmed Desorption (TPD) experiments give valuable information on the formation and desorption of reaction products on the surface.

- The manifestation of crystallographic defects affects the sensing mechanism of gas sensors. An in-situ XPS with gas atmosphere control would give a better idea as to what happens to the electronic structure of the carbon nanomaterials and its nanocomposite during high-temperature gas interaction and also an idea of how the shear planes grow and whether this leads to an increase in the density of states in the gap.
- Theoretical modeling on the sensing mechanism of Graphene-based humidity, LPG, and other oxidizing/ reducing gases may be undertaken for further research.
- Carbon nanostructured materials may be very useful in biomedical applications such as drug delivery systems, cancer cell detection, and treatment, etc. The related Physics may be studied.
- Graphene is a 2D material that can be used in flexible electronics to develop flexible sensors and other electronic devices.

Development of sensitive and peer selective LPG sensor based on Graphene functionalized with CuO/SnO_2 nanocomposites

Kuldeep Kumar, B. C. Yadav

Nanomaterials and Sensors Research Laboratory, Department of Physics,

Babasaheb Bhimrao Ambedkar University, Lucknow-226025, U.P., India

*Corresponding author's email: balchandra_yadav@rediffmail.com

Mob. No.: +91 9450094590

Abstract

The present article addresses the design and fabrication of the LPG sensor at room temperature based on the Graphene functionalized with CuO/SnO_2 (GCS) nanocomposites synthesized with temperature-controlled hydrothermal technique. The surface morphological investigations, as well as elemental mapping analysis details as the metal nanoparticles, are attached with Graphene sheet at the side edges, corners, and basal planes. Confirmation of the nano-sized distribution has been done with the particle size analysis. The bandgap of the synthesized nanomaterials was found as 4.1 eV. The presence of the oxygen-containing functional groups in the material was confirmed with the FTIR. The Raman spectrum was used to describe the nature of the synthesized Graphene as well as GCS. The %maximum sensor response of the LPG sensor was found as 11.76 for the 2.0 vol.% LPG and also the response and recovery time for the 0.5 vol.% LPG are 1.7 and 1.2 s respectively. Further, the effect of relative humidity on room temperature LPG sensing has been investigated.

Keywords: LPG sensor, Graphene, CuO/SnO_2 nanocomposites, sensitivity, surface adsorption

Development of Graphene oxide functionalized with PPdAAm/SnO_2 nanocomposite for Liquefied petroleum gas sensing

Kuldeep Kumar[1], Utkarsh Kumar[1], B. C. Yadav[1*], Vitaly A. Shershnev[2], Rose K. Baimuratova[2], Rajeev Kumar[3], Lava Kumar Gupta[4], Gulzhian I. Dzhardimalieva[2,5]

[1]Nanomaterials and Sensors Research Laboratory, Department of Physics,

Babasaheb Bhimrao Ambedkar University, Lucknow-226025, U.P., India

[2]Laboratory of Metallopolymers, Institute of Problems of Chemical Physics, Russian Academy of Sciences, Chernogolovka, Moscow Region 142432, Russia

[3]CSIR-Advanced Materials and Processes Research Institute, Bhopal-462026, M.P., India

[4]Department of Physics, P.P.N. College, CSJM Kanpur University, Kanpur, U.P., India

[5]Moscow Aviation Insitute (National Research University), Volokolamskoe Shosse, 4, 125993 Moscow, Russia

[*]Corresponding author's email: balchandra_yadav@rediffmail.com

Mob.No.: +91 9450094590

Abstract

The present article reports the synthesis and characterization of Graphene oxide (GO) functionalized with poly Pd acryl amide SnO_2 (PPdAAm/SnO_2) nanocomposites and its relevance for detecting the liquefied petroleum gas at room temperature. The minimum crystallite size of the MPGO was found as 19.14 nm from XRD. The peaks corresponding at 465 and 507 cm^{-1} in the Raman spectrum confirmed the stretched bond vibrations of the SnO_2 nanoparticles. The average size of the synthesized material was found as 118 nm through the DLS technique and the Tauc plot gave the bandgap as 5.3 eV. The N-H vibrations of the amide group present in the FTIR spectrum confirmed the

formation of acrylamide in the synthesized material. The LPG detection was studied for 0.5, 1.0, 1.5, and 2.0 vol.% concentration with a typical operable voltage of 40 V at 27 °C. The maximum %sensor response of the sensor was found as 570.58 for 2.0 vol.% of LPG.

Keywords: Graphene oxide, Poly Pd acryl amide SnO_2 nanocomposites, sensitivity, surface adsorption, LPG sensor

Development of ultra-fast sensitive and selective CO_2 sensor based on Graphene@CuO nanocomposites

Kuldeep Kumar, B. C. Yadav

[1]Nanomaterials and Sensors Research Laboratory, Department of Physics,

Babasaheb Bhimrao Ambedkar University, Lucknow-226025, U.P., India

[2]CSIR-Advanced Materials and Processes Research Institute, Bhopal-462026, M.P., India

[*]Corresponding author's email: balchandra_yadav@rediffmail.com

Mob.No.: +91 9450094590

Abstract

The present paper reports the development of the CO_2 gas and humidity sensor at room temperature based on the Graphene@CuO nanocomposites, synthesized through the Chemical Vapor Deposition (CVD) route. The synthesized materials have been characterized with several techniques such as Scanning electron microscopy (SEM), Electron dispersive X-rays (EDX), Ultraviolet-visible (UV-Vis.) spectroscopy, X-ray Diffraction (XRD), Fourier Transform Infrared (FTIR), and Raman spectroscopy. The surface morphological investigations as well as elemental mapping analysis confirmed that the CuO metal nanoparticles are attached with Graphene sheets at the side edges, corners, and basal planes. Investigation of the nanosize distribution has been carried out with the particle size analysis. The bandgap of the synthesized nanomaterials was estimated as 4.1 eV. The presence of the oxygen-containing functional groups in the material was confirmed with the FTIR. The Raman spectrum described the nature of the synthesized Graphene as well as Graphene@CuO nanocomposites. The % sensor response of the CO_2 sensor was found maximum as 1178.3) for the 2.0 vol.% and also

the response and recovery time for the 0.5 vol.% were found 1.3 and 1.5 s respectively.

Keywords: CO_2 gas sensor, Graphene@CuO nanocomposites, Chemical Vapor Deposition, Sensor response